Computational modelling of monocyte deposition in abdominal aortic aneurysms

David Hardman

A thesis submitted for the degree of Doctor of Philosophy.
The University of Edinburgh.
May 2010

Abstract

Abdominal aortic aneurysm (AAA) disease involves a dilation of the aorta below the renal arteries. If the aneurysm becomes sufficiently dilated and tissue strength is less than vascular pressure, rupture of the aorta occurs entailing a high mortality rate. Despite improvements in surgical technique, the mortality rate for emergency repair remains high and so an accurate predictor of rupture risk is required. Inflammation and the associated recruitment of monocytes into the aortic wall are critical in the pathology of AAA disease, stimulating the degradation and remodeling of the vessel wall. Areas with high concentrations of macrophages may experience an increase in tissue degradation and therefore an increased risk of rupture. Determining the magnitude and distribution of monocyte recruitment can help us understand the pathology of AAA disease and add spatial accuracy to the existing rupture risk prediction models. In this study finite element computational fluid dynamics simulations of AAA haemodynamics are seeded with monocytes to elucidate patterns of cell deposition and probability of recruitment.

Haemodynamics are first simulated in simplified AAA geometries of varying diameters with a patient averaged flow waveform inlet boundary condition. This allows a comparison with previous experimental investigations as well as determining trends in monocyte adhesion with aneurysm progression.

Previous experimental investigations show a transition to turbulent flow occurring during the deceleration phase of the cardiac cycle. There has thus far been no investigation into the accuracy of turbulence models in simulating AAA haemodynamics and so simulations are compared using RNG $\kappa - \epsilon$, $\kappa - \omega$ and LES turbulence models. The RNG $\kappa - \epsilon$ model is insufficient to model secondary flows in AAA and LES models are sensitive to inlet turbulence intensity.

The probability of monocyte adhesion and recruitment depends on cell residence time and local wall shear stress. A near wall particle residence time (NWPRT) model is created incorporating a wall shear stress-limiter based on in vitro experimental data. Simulated haemodynamics show qualitative agreement with experimental results. Peaks of maximum NWPRT move downstream in successively larger geometries, correlating with vortex behaviour. Average NWPRT rises sharply in models above a critical maximum diameter.

These techniques are then applied to patient-specific AAAs. Geometries are created from CT slices and velocity boundary conditions taken from Phase Contrast-MRI (PC-MRI) data for 3 patients. There is no gold standard for inlet boundary conditions and so simulations using 3 velocity components, 1 velocity component and parabolic flow profiles at the inlet are compared with each other and with PC-MRI data at the AAA midsection. The general trends in flow and wall shear stress are similar between simulations with 3 and 1 components of inlet velocity despite differences in the nature and complexity of secondary flow. Applying parabolic velocity profiles, however, can cause significant deviations in haemodynamics. Axial velocities show average to good correlation with PC-MRI data though the lower magnitude radial velocities produce high levels of noise in the raw data making comparisons difficult. Patient specific NWPRT models show monocyte infiltration is most likely at or around the iliac bifurcation.

Declaration of originality

I hereby declare that the research recorded in this thesis, and the thesis itself, was composed and originated entirely by myself, except where explicitly stated otherwise, in the Department of Medical Physics and the Institute for Materials and Processes at The University of Edinburgh and has not been submitted for any other degree or professional qualification

David Hardman

Acknowledgements

This thesis would not have been possible without the kind help and support of so many people.

Firstly, thanks to my supervisors, Pete Hoskins and Bill Easson for their help and advice throughout. Pete's speedy proof-reading skills deserve special mention.

Thanks also to Scott Semple and Jenny Richards for their help in obtaining clinical data throughout the project.

Irene deserves a special mention for sorting all the paperwork and providing a constant source of cake and gossip.

To the MRC for funding me during the project.

To all of the staff and students in Medical Physics and especially the past and present members of the esteemed club that is the Broomcupboard for moral support and Friday Pints. Special thanks to Kate and James for their invaluable advice and taking the time to solve the many problems I threw their way.

Thanks also to Mairéad and Michael for making sure my inbox was always full during the ups and the downs, Antonios for teaching me the truth about white chocolate, Steven Hammer for his help with geometry creation, Adele for bringing a sense of order to the chaos and Gavin for teaching me the benefit of regularly saving simulations.

A huge thanks to my parents who have supported and encouraged me throughout and to Pat and Geoff for all of their support.

The biggest thanks go to Andrea for her constant support and epic proof-reading. This thesis is dedicated to her.

Contents

List of figures

List of tables

Abbreviations

1DV	Axial velocity only	MMP	Matrix Metalloproteinase
3DV	Axial and radial velocities	NO	Nitric Oxide
AAA	Abdominal Aortic Aneurysm	N-S	Navier-Stokes Equations
BBO	Basset-Boussinesq-Oseen	NWPRT	Near-Wall Particle Residence Time
BCD	Bounded Central Difference	PC-MR	Phase Contrast Magnetic Resonance
CFD	Computational Fluid Dynamics	RANS	Reynolds Averaged Navier-Stokes Model
DNS	Direct Numerical Simulation	RMS	Root Mean Squared
DPM	Discrete Phase Model	SMC	Smooth Muscle Cell
ECM	Extra-Cellular Matrix	SNR	Signal to Noise Ratio
FDG	Fludeoxyglucose	SPIO	Superparamagnetic Iron Oxide
FEM	Finite Element Method	TI	Turbulence Intensity
FSI	Fluid-Structure Interaction	TIMP	Tissue Inhibitor of Matrix Metalloproteinase
GCI	Grid Convergence Index	UDF	User Defined Function
HFI	Helical Flow Index	USPIO	Ultrasmall Superparamagnetic Iron Oxide
ICAM	Inter-Cellular Adhesion Molecule	VRT	Volumetric Residence Time
ILT	Intra Luminal Thrombus	VCAM	Vascular Cell Adhesion Molecule
LES	Large Eddy Simulation	WSS	Wall Shear Stress

Nomenclature

$\vec{A}$	Surface area vector
a_p	Cell radius
C_d	Drag coefficient
d	Inlet radius
D	Maximum AAA radius
h_p	Distance between cell centre and wall
H_k	Kinetic helicity density
L	Vessel length
m	Mass
P	Pressure
Q	Flow rate
Re	Reynolds Number
R	Vessel radius
T	Time to complete full wave cycle
u, v, w	Velocity in x, y (radial) and z (axial) directions respectively
V_e	Volume of finite element e
V_p	Volume of cell p
α	Womersley number
ϵ	Dissipation rate
Γ_v	Vorticity
κ	Turbulent kinetic energy
μ	Dynamic viscosity
ν	Kinematic viscosity
ω	Specific dissipation rate
Ψ	Local normalised helicity
ρ	Density
τ_w	Wall shear stress
τ_p	Particle momentum response time

Chapter 1
Introduction

1.1 Abdominal Aortic Aneurysm Disease

An aneurysm is formed when a blood vessel becomes dilated or distorted causing it to expand to a size greater than its original diameter. Aneurysms can occur in a variety of blood vessels though they are most commonly found in the intracranial arteries and in the aorta. An abdominal aortic aneurysm (AAA) is defined clinically as a focal dilation of the aorta below the renal arteries exceeding 150% of the normal arterial diameter [8](figure 1.1). The general pathogenesis of AAAs is denoted by the degradation of both elastin and collagen in the media and adventitia of the aortic wall. This results in the expansion of the aneurysm sac until wall stresses exceed wall strength and sac rupture occurs. Elderly males are most at risk from AAA with rupture accounting for 1.5% of the total mortality in males over 55 years old [23]. Post rupture AAA mortality rate is up to 90%, including patients who do not reach hospital [150]. Despite improvements in surgical techniques, including the use of endovascular stenting, the mortality rate for emergency AAA repair remains high. It is therefore important to assess a critical time at which to operate on AAA and minimise the risks involved.

Currently, aneurysms with a maximum anterior-posterior diameter greater than 5.5 cm, a growth rate greater than 0.5cm/year [54] or which exhibit symptoms such as abdominal pain are considered at risk of rupture and emergency operation is required. The critical diameter of 5.5 cm is based on data from the United Kingdom Small Aneurysm Trial [128], though in practise it is inefficient in many cases. 60% of AAAs with diameters greater than the critical limit do not [83] rupture while rupture occurs in 10% with diameters less than or equal to 5.5cm. A more accurate method of rupture risk prediction would save unnecessary surgery while maintaining, or even improving the current mortality rate.

The mechanisms which instigate and exacerbate AAA are still relatively poorly understood. Previous studies have revealed a significant percentage of men with small AAAs show signs of Chlamydia pneumonia infection [90] which suggests Chlamydia infection may initiate AAA formation although a definite link remains inconclusive [6]. Others have attributed AAA ini-

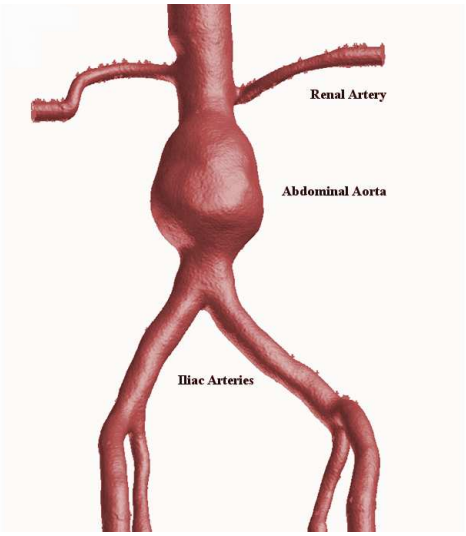

Figure 1.1: *Abdominal aortic aneurysm*

tiation to atherosclerosis. While both AAA and atherosclerosis share many aspects of their pathology and risk factors [84] there is no definitive evidence that atherosclerosis is a causative factor in aneurysm formation.

The pathology of AAA disease involves the expansion of the aortic wall. The underlying mechanisms responsible for the breakdown of the wall itself are inflammation and neovascularisation, the creation of new microvessels within the aortic wall. These mechanisms break down the extra-cellular matrix and cause the disappearance of smooth muscle cells [143] and are, in turn, regulated by the haemodynamic conditions present in the abdominal aorta. To understand how AAA disease develops, the interplay between inflammation and haemodynamics must be understood in both the healthy and diseased aorta and how this leads to tissue damage, expansion and the eventual rupture of the vessel.

1.1.1 Changes in the extra cellular matrix (ECM)

The mechanical characteristics of the aortic wall are defined by the make up of the ECM. Elastin fibres account for the visco-elastic properties of the vessel while collagen fibres provide tensile strength. In healthy tissue, elastin is arranged in strong cross-linked formations and collagens, of which collagen I and III are most prevalent in the aorta, are arranged circumferentially to effectively contain high loads acting on the vessel wall. Over time, elastin throughout the body becomes degraded through calcification, lipid fixation and proteolytic degradation leading to a

loss of tissue elasticity. In AAA disease, calcification and proteolysis degrade the structured ECM. Elastin and collagen are still produced in smooth muscle cells (SMC) in the media and fibroblasts in the adventitia of the aorta, but this replacement tissue is unstructured and therefore does not protect the wall from stresses and strains. Dobrin et al [36] suggest that the stiffening and expansion of the AAA is due to the degradation of organised elastin fibres while rupture occurs due to the degradation of collagen. There has been considerable interest in applying these observations to aneurysm wall stress models. Constitutive models of strain energy density have been created which account for the mechanical effects of the ECM on wall stresses.

Calcification is present in around 80 % of AAAs forming discrete, heterogeneously distributed areas of solid, inert tissue. Maier et al [100] suggest that it is necessary to include areas of calcification in AAA wall stress analysis studies though their presence is not thought to affect aneurysm rupture risk.

1.1.2 Inflammation

The breakdown of the AAA wall is generally attributed to inflammation and inflammatory infiltrates [137]. This phenomenon is exemplified by a distinct sub category of AAA known as inflammatory AAA (IAAA) where evidence of intense inflammation prevails. IAAA are defined by dense fibrosis which spreads to the surrounding organs and make up around 3% to 10% of all AAAs [168]. As IAAA make up a minority of AAAs, this study will focus on regular AAAs though the principals of disease progression are believed to be similar. Proteolytic enzymes are responsible for degrading the collagen and elastin which constitute the ECM of the aortic wall and so are of particular interest when elucidating aneurysm histology. In particular, a family of elastinases and collagenases known collectively as matrix-metalloproteinases (MMPs) and their inhibitors (TIMPs) are thought to play a major role in ECM breakdown. It has been postulated that the degradation of elastin via elastolytic MMPs (MMP-2,-7,-9) is responsible for the initial expansion and deviation from linear elasticity in AAAs, whereas collagen degradation via MMP-1,-8 and -13 may weaken the structure of the wall sufficiently to cause rupture [36]. While the details of the pathways leading to MMP activation are little understood, they are thought to be products of a pro-inflammatory cytokine cascade instigated by smooth muscle cells and macrophages within the aortic wall [23]. Experiments by Anidjar and Dobrin et al. [36] among others have shown that areas of matrix degradation are accompanied by inflammatory infiltrates, strongly suggesting a correlation between inflammation, proteolysis and AAA

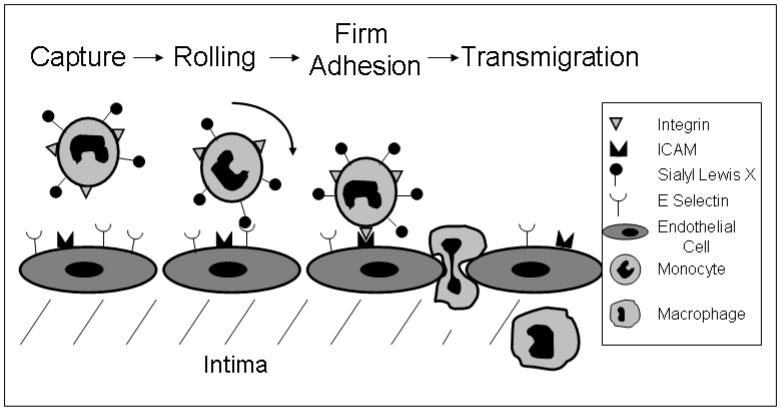

Figure 1.2: *Leukocyte migration to the endothelium*

development.

During inflammation, monocytes (and other leukocytes) migrate from the lumen through the endothelium and into the vessel wall. As they pass through the endothelium they lose their hard exterior, becoming macrophages which then migrate along a chemotactic gradient to the area of inflammation. While inside the vessel wall, macrophages release cytokines which enable MMP release. Extravasation of leukocytes involves a three stage process as shown in figure 1.2. When leukocytes become proximal to the endothelium, chains of the cell adhesion molecule L-selectin found on the leukocyte attach to P and E-selectins on endothelial cells. These bonds are weak and continually break and reattach, allowing the cell to roll along the lumen surface. Having been slowed by this process, the leukocytes then firmly attach to the endothelium via activated integrin molecules on the endothelium. Once firm adhesion occurs, the leukocyte transmigrates through the endothelium into the vessel wall. While there is much literature concerning rolling, tethering and transmigration of leukocytes, the margination of leukocyctes in blood flow in large arteries has received little attention. A study by Phibbs [126] indicates that maximum leukocyte concentration lies at a distance of around 80-90% of the vessel radius. In AAA disease, leukocytes tend to localise in the medial and adventitial layers of the aortic wall [13]. This is in contrast with inflammation during atherosclerosis in which cells aggregate in the intimal layer of the wall [89]. The traditional model of inflammation involves cells migrating from the lumen to the intima where inflammation is then initiated. In spatial terms this is an 'inside-out' model of inflammation. In certain cases of disease in larger arteries an 'outside-

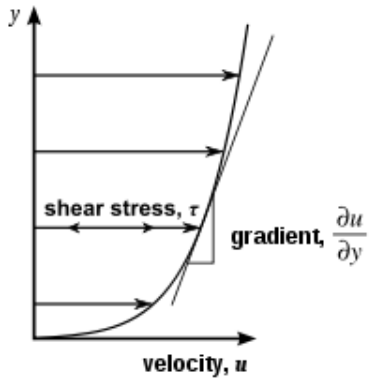

Figure 1.3: *Wall shear stress (WSS),* τ_w

in' model has been proposed [99] whereby inflammation is initiated in the adventitia and then migrates towards the intima. The aggregation of leukocytes and inflammatory indicators in the outer layers of the aortic wall in AAA suggests that the 'outside-in' inflammatory pathway plays a role in aneurysm formation. More developed AAAs have been shown to have a denser network of microvessels due to neovascularisation of the wall during aneurysm growth [151]. In mouse models, macrophages expressing 5-lipoxygenase (5-LO), an enzyme involved in the synthesis of proinflammatory leukotrienes, were found to be abundant in the adventitia and almost entirely absent from the intima of the aorta in animals with AAA [193] providing further evidence of the role of both the adventitia and macrophages in AAA development. By observing the behaviour of inflammatory cells in the aorta the route by which they enter the AAA wall can be determined, whether it be inside-out or outside-in, and determine the area in which they will inflict the most damage.

1.1.3 Haemodynamic Effects

Hemodynamic forces have a regulatory effect on vessel dynamics, leukocyte recruitment and infiltration and on neovascularisation and progenitor cell recruitment. Haemodynamic variables which control physiological behaviour include the magnitude and direction of flow velocity, the presence of turbulent and non-linear flow and the nature of wall shear stress (WSS). WSS, τ_w is described in figure 1.3 and can be expressed

$$\tau_w = \mu \left(\frac{\partial u}{\partial y} \right)_{y=0}, \tag{1.1}$$

where μ is the dynamic viscosity, u is the flow velocity parallel to the wall and y is the distance to the wall. *In vitro* studies have shown biological and physiological changes occurring in endothelial cells when exposed to differing shear stresses, potentially affecting their rates of mass transfer. Endothelial cells have been shown to align with blood flow in healthy arteries and remain unaligned in the presence of turbulent flow [30]. Responses to shear stress include increased expression of cytokines and guanine triphosphate (GTP) binding proteins, K+ and Cl- channel activation and the release of neurotransmitters and vasodilators including nitric oxide (NO). Sho et al. [150] found that luminal flow conditions regulate macrophage infiltration in animal models with the concentration of medial macrophages varying inverslely to the volume of flow and WSS magnitude proximal to the lumen. So far data has been obtained from *in vivo* animal models and *in vitro* tissue testing of humans and animals. Physiological, mechanical and chemical effects of shear stress on leukocytes and the endothelium dictate the efficiency of cell adhesion at different WSS environments. The expression of vascular cell adhesion molecule-1 (VCAM-1) and intercellular cell adhesion molecule-1 (ICAM-1) are altered at different WSS magnitudes, changing the adhesion dynamics between leukocytes and the lumen. At low shear rates [117] VCAM-1 expression is high, whereas ICAM-1 expression is low. Selectin bonds are formed easily and are less prone to detachment allowing leukocytes to roll in a controlled and slow manner across the endothelium [71, 82]. As shear rates and shear stresses increase, leukocytes retract their pseudopodia making bond formation less likely [50]. VCAM-1 levels drop then plateau with increasingly higher WSS while ICAM-1 levels increase and selectin bond detachment becomes more frequent [71]. With less stable selectin bonds, leukocyte rolling becomes faster and more erratic making adhesion less likely. While higher shear stresses prevent leukocytes from adhering, once a cell is attached to the endothelium it takes a much higher WSS to dislodge it. Taylor et al. [164] found that the efficiency of attachment of pre-attached cells actually increases between 0 and 0.5 Pa before decreasing. This may be due to changes in expression of cell adhesion molecules. Prolonged exposure to oscillatory shear stress has been shown to upregulate adhesion molecules and thus increase leukocyte adhesion probability [63].

1.1.4 Thrombus Formation

Around 75% of AAAs have been found to contain intraluminal thrombi (ILT), described by Wang et al [180] as 'an accumulation of fibrin, blood cells, platelets, blood proteins and cellular debris adhering to the AAA inner wall'. Although the formation of the thrombus is generally anisotropic, the ILT present in established aneurysms consists of three distinct layers. The

luminal layer, in contact with the bulk blood flow, forms a soft, spongy layer in which a well structured fibrin matrix is present. This luminal layer appears as a reddish colour in excised ILT indicating that fresh blood is still present in this layer [179]. Behind this, a medial layer of thrombus consisting of less structured fibrin bundles is present which appears white in the excised tissue. The furthest, and oldest, layer is an abluminal layer in contact with the wall in which the fibrin structure breaks down completely producing a darker layer of tissue. The build up of ILT is believed to be caused by platelet deposition and aggregation [169].

There is as yet no consensus on the effects of the ILT on wall stresses and AAA rupture risk though given the nature of thrombus formation the effects are likely to be complex. Vorp et al. [177] found the AAA wall to be weaker in areas of ILT, corroborated by the findings of Kazi et al [69] that the wall around ILT is thinner. Hans et al.[57] found no correlation between sites of ILT and sites of rupture.

Elucidating the effects of thrombus on the vessel wall and on rupture risk has involved observation of the underlying biology. Vorp et al. investigated the hypothesis that ILT causes local hypoxia which could increase inflammatory response, enhance macrophage bio reactivity and thus catalyse proteolytic degradation [177]. *In vitro* studies [69] show a fragmentation of elastin fibres, a decrease in collagen synthesis and smooth muscle cell (SMC)/fibroblast activity as well as increased infiltration of inflammatory cells in areas of ILT. These findings prompted the hypothesis that areas of thrombus act as sinks for inflammatory cells and other agents of AAA wall degradation. The build up of thrombus has been attributed, at least in part, to the rate of platelet deposition [182] which, as with the inflammatory process, is regulated by vessel haemodynamics [9]. The body naturally prevents platelets from aggregating and forming a clot and so before platelets can bind to the AAA lumen, they must first be activated. Activation occurs when the platelets experience a high level of WSS [120]. The haemodynamics of the vessel not only activate platelets, but also dictate the concentration of cells at the wall and the local shear stresses experienced by the cells near the wall. Investigations using generic aneurysm models have shown that the haemodynamics of flow in the cavity, which shall discuss later, are likely to enhance platelet deposition [9] and thus increase thrombus formation. While haemodynamics play a role in thrombus formation, the growing thrombus will in turn affect vessel haemodynamics by narrowing the cavity or obstructing flow. Previous computational investigations have also suggested that the ILT may actually be beneficial by reducing stress on the wall and so reducing rupture risk [10, 180].

1.1.5 Neovascularisation

Large arteries such as the aorta have relatively thick walls through which diffusion of nutrients becomes difficult and so they often exhibit a microvasculature of much smaller vessels throughout the wall known as the vasa vasorum. The vasa vasorum transport solutes to the medial layer of the wall and aid diffusion [136]. They consist of 3 types of vessel; vasa vasorum intima which enter the wall from the main artery lumen, vasa vasorum externa which enter from the lumen of arteries branching from the main artery and venous vasa vasorum which drain into veins surrounding the main artery [116]. The healthy abdominal aorta appears to have a relatively small number of vasa vasorum [187] while aneurysmal aorta has been found to contain significantly more, with the density of vessels increasing in correlation with AAA size [151]. The formation of these new vessels, termed angiogenesis, is a complex process which is not yet fully understood, though it is known that macrophages are a significant agent involved in all stages of angiogenesis via the cytokine pathways which they enable [161]. Experiments with neoplastic tissues [113] show angiogenesis is only observed when macrophages are present and further studies by Polverini et al [127] using a cornea assay revealed that macrophages must be activated via chemical signals before angiogenesis can be initiated. As well as medial angiogenesis, neovascularisation also occurs in the ILT. The structured luminal and medial layers of thrombus in AAAs are permeated by a network of tunnels or canaliculi which trap cellular infiltrates [1]. As with angiogenesis in the wall, macrophages play an important role in the formation of microvessels throughout the thrombus. Macrophages have been shown to work with endothelial progenitor cells to tunnel through the fibrin network of occlusive thrombus [108], eventually allowing blood flow to bypass the occlusion. The recanalization of thrombus in AAA may enable the transport of species to the aortic wall.

1.1.6 ILT, Neovascularisation and Inflammation

Both the neovascularisation and growth of ILT create complexities in the standard model of inflammation in AAA disease. The vasa vasorum is a candidate for conveying inflammatory cells into the outer wall of the AAA, which could allow for an outside-in inflammatory pathway. Technically this blurs the distinction between 'inside-out' and 'outside-in' hypotheses as the vasa vasorum are supplied by either the main arterial blood or from one of the major tributary vessels and so inflammatory cells will have to be sourced from the bulk aortic blood flow. Inflammation and neovascularisation appear to be intrinsically linked. The presence of

macrophages is essential for the formation of neovascularisation and the inhibition of neovascularisation has been shown to reduce macrophage accumulation in atherosclerosis [114]. The formation of thrombus creates a physical barrier between the lumen and the vessel wall and can cause dysfunction of the endothelium without causing physical loss of endothelial cells [67], disrupting the classical mechanisms inflammation. However, the inside-out concept of inflammation should not be entirely disregarded when accounting for the network of canaliculi found in the thrombus. These networks of tunnels are large enough to allow macromolecules to permeate through the ordered luminal and medial layers of the thrombus and enter the unstructured fibrous mesh of the abluminal layer through which it is theoretically possible for inflammatory cells including macrophages to enter the aortic wall, though there has been no conclusive study to the author's knowledge. Investigations by Fontaine et al [43] and Adolph et al [1] show that inflammatory cells become trapped in the improvised vasculature of the ILT creating 'sinks' of inflammatory infiltrates.

1.1.7 Summary

The initiating factors of AAA disease are yet to be determined yet it is clear that inflammation plays a key role in the development of the disease in terms of wall structure degradation, thrombus formation and neovascularisation. It follows that haemodynamics must also play an important role in terms of the activation, aggregation and displacement of both inflammatory cells and platelets. The formation of thrombus and the microvasculature of the vessel wall complicate the process of inflammation in ways which are still not fully understood. Endothelial dysfunction and the physical barrier created by thrombus formation will affect the recruitment of inflammatory cells though the canalisation of the thrombus provides an alternative passage for cell transport and may allow cells to enter the wall of the aorta. Inflammatory cells are responsible for the the creation of new microvessels both in the thrombus and in the form of vasa vasorum, which in turn have a role in transporting cells and infiltrates throughout the wall. While investigations have shown that inflammation and inflammatory infiltrates reside in the middle to outer layers of the wall, the method by which they arrive there is yet to be elucidated. By studying the behaviour of inflammatory cells in the bulk blood flow, more may be learned about the pathways of inflammation and the areas most affected by the subsequent wall degradation will be able to be ascertained.

1.2 Strategies in Rupture Risk Prediction

Research into AAA disease focuses on understanding the underlying pathology and nature of the disease and improving methods of predicting the risk of aneurysm rupture. While the current index for assessing surgical intervention based on measurement of AAA diameter has a sound basis in literature [146], it is not ideal. While AAAs are most likely to rupture when they become large, smaller aneurysms have also been found to rupture. A study by Nicholls et al [119] shows 10% of the AAAs which ruptured were smaller than 5 cm in diameter [68]. Conversely, AAAs have been found unruptured with diameters greater than 6 cm. Given the costs and risks [25] associated with open surgery and given that around 85% of patients with AAA die of causes unrelated to the aneurysm [5], surgical intervention may introduce unnecessary risk. A more robust method of rupture prediction is required to both reduce mortality and increase the cost-effectiveness of surgery. Recent investigations of AAA disease can be divided into two strategies; those which focus on the physical effects of AAA expansion such as stresses, strains and strength of the wall to predict the risk of AAA rupture and those which observe the underlying pathology of AAA disease in terms of inflammation its role in the biochemical degradation of the wall.

1.2.1 Pathology

By observing the concentrations of species such as inflammatory infiltrates in the wall and in the blood of AAAs which progress to either rupture or elective repair it is hoped that biological indicators of rupture risk can be found. The destructive properties of MMPs make them a candidate for study. Wilson et al [185] found that levels of MMP-1 and MMP-9 in the blood serum were significantly higher in ruptured AAAs than unruptured. Peterson et al [125] found MMP-9 to be significantly higher in ruptured AAAs while MMP-2 was significantly higher in electively repaired AAAs. Wilson et al [186] found high concentrations of MMP-8 and -9 at the site of rupture. These studies indicate that MMP distribution is not homogenous and suggests that the distribution of these infiltrates is key to predicting whether an aneurysm will rupture and the location of the point of rupture. If biomarkers are to be used to predict rupture risk, they must be found and quantified using the least invasive methods possible. Finding biomarkers in the blood serum is feasible, but gives no information on their levels and distribution in the AAA itself. The studies mentioned above all rely on histological data which while undeniably informative is an extremely invasive method if used prospectively. More recent research has

taken advantage of advances in non-invasive imaging techniques to monitor recruitment of biomarkers in aneurysms. The uptake of the PET contrast agent ^{18}F-fluorodeoxyglucose (FDG) in cells is a marker of glucose metabolism and thus indicates areas of high metabolic activity in tissue. A study by Reeps et al [135] has shown areas of FDG uptake to be significantly correlated with areas of inflammation and MMP expression. This has led to investigating the use of FDG-PET imaging combined with CT scanning to highlighting areas of inflammation [75].

1.2.2 Wall Stress Studies

By studying the stresses exerted on the AAA wall, along with the corresponding mechanical strain and tissue strength of the wall, models can be built expressing the likelihood of rupture based on the mechanical properties of the vessel. Numerical models of stress distribution in generic AAA shaped geometries were created by Vorp et al [178]. Realistic maximum pressure loads were applied to the geometries which were attributed a linear elastic stress-strain relation. The shape of the model was found to significantly affect the distributions of wall stress. *Ex vivo* investigations have shown that under pulse pressure and at critical AAA diameters large strains are observed before rupture [58, 131]. Since linear elastic models only account for small strains it is clear that a large strain non-linear elastic model must be found. To achieve this, tensile testing was performed on excised strips of AAA wall in order to find their constitutive properties. Excising human AAA tissue has limitations as only the anterior section is generally available in patients undergoing operations and mechanical properties may be compromised when compared to *in vivo* tissue. Tensile tests conducted by Di Martino et al [33] indicate AAA size may not be correlated with wall strength and that tissue which is thicker and more compliant is weaker and so an alternative rupture risk index to size alone is required accounting for wall strength. The responses to tensile testing of tissue have been used to create constitutive models of stress-strain behaviour. Holzapfel [60] provides a summary of many of the proposed non-linear and constitutive models in healthy arteries, many of which were developed to account for compliance in AAA models. More recent investigations have addressed the complex non-linear elastic properties of the AAA wall by proposing constitutive models based on the strain energy density function. These models relate the strain energy density of the tissue to the gradient of deformation to account for the rearrangement of the microstructure of the wall with AAA development [130]. Models of wall compliance have been simulated using numerical models with fixed pressure boundary conditions [40] to determine the stresses acting on the

walls during the cardiac cycle. Fixed pressure boundary conditions do not take into account the spatial pressure variations caused by secondary flow features. As complex secondary flows are common in AAAs, studies have combined compliant wall models with numerical models of haemodynamics to observe fluid-structure interactions (FSI) in aneurysms. Li and Kleinstreuer [88] developed FSI models of simplified asymmetric AAA geometries. FSI has been applied to patient specific AAAs with physiological blood flows to gain a more complete picture of haemodynamics and wall shear stresses in AAA. Scotti and Finol [148] found that maximum wall stress varied by 3 to 25% between solid modelling alone and compliant wall FSI models. FSI modelling has also been used to test the efficiency of stent grafts within AAA [87]. Numerical indices of rupture risk tend to assume isotropic conditions throughout the AAA wall. Raghavan [129] showed through tesile testing that wall thickness and tensile properties are distributed heterogeneously throughout the AAA.

1.2.3 Summary

While wall stress studies have shown the potential to improve the current clinical protocol for rupture risk by including tissue stress, strain and strength variables, current models assume that AAA disease will affect all areas of the wall equally. In a study by Vallabhaneni et al [171] tensile testing was applied to sections of AAA and showed the inhomogeneous nature of the mechanical properties of AAA disease both between patients and in individual aneurysms. Such heterogeneity means that current rupture risk predictors based on mechanical wall properties will fail. It therefore the becomes necessary to observe the causes of wall breakdown to try and predict the patterns in wall properties. Pathological approaches can be used to define the root cause of AAA disease in terms of recruitment of inflammatory cells and the subsequent activation of MMPs. The Vallabhaneni study has been the first to test MMP levels alongside tensile testing of AAAs. The study showed significant heterogeneity in levels of MMP-2 and MMP-9 in samples taken from AAA walls. While the study did not find any significant correlation between areas of high MMP activity and wall properties, the authors suggest that hotspots of MMP hyperactivity could cause focal weakening of the wall, resulting in areas prone to rupture risk.

A method of predicting where inflammation will occur would combine the two strategies of wall stress and pathology. By predicting where hotspots of inflammation will occur and conversely where inflammation is unlikely to occur, the distribution of areas with severe wall degradation

can be predicted and so add a level of spatial accuracy to the existing rupture risk prediction models.

The literature presented so far has identified the need to model monocyte dynamics in flow. This will provide further understanding of the likely sites of deposition of monocytes which may be used as a tool for future clinical studies to explore the relationship between monocyte dynamics, inflammation measured *in vivo* using imaging systems, and occurrence of rupture. The remainder of this chapter is devoted to descriptions of the literature relating to the methods to be used in this thesis.

1.3 A Monocyte Deposition Model Approach

This study proposes a method of predicting areas of inflammation in AAA disease through the tracking of monocyte deposition and observation of AAA haemodynamics. To achieve a model of cell deposition, information is required on the geometry of the aneurysm, the haemodynamics of blood in the aneurysm and the physical and biochemical responses of monocytes to the aneurysm haemodynamics. The different techniques by which this information can be obtained are discussed below.

1.3.1 Choice of Candidate Leukocyte Species

While other species of leukocytes are present in the AAA wall, this study is specifically concerned with monocytes. When deciding a candidate white blood cell to model, two things were taken into account; the quantity of literature describing the cells and their link to AAA pathology and the relative concentrations of the cells in the the bloodstream. Having more information on the effects of the cells allows more accurate modelling and more clinical relevance. Choosing a species with lower concentrations will allow for more efficient modelling. The link between monocyte derived macrophage infiltration and MMP expression and the subsequent wall degredation has been studied [53] whereas the extent to which T-cells affect AAA disease has yet to be well described [44]. Neutrophils have been linked to MMP production in experimental AAAs [38] despite this, they have not been used in this investigation as current literature suggests macrophages have more of an effect on wall degradation. The high concentration of neutrophils in the blood stream compared to monocytes would provide further challenges for numerical modelling. Although only monocytes will be studied here, the techniques used can

easily be applied to other leukocyte species in future works.

1.3.2 Geometry

While generic geometries can be created by hand using CAD software, patient-specific geometries require input from scans by imaging modalities such as Computed Tomography Angiography (CTA) or Magnetic Resonance Angiography (MRA). The vessel lumen is segmented from each slice of the scan and compiled to form the three-dimensional geometry. During CTA a bolus of contrast agent is perfused into the target artery during scanning. The resulting high contrast between blood and lumen in CTA scans increases the accuracy in defining the lumen for segmentation. There are a variety of techniques for acquiring data through MRA. Contrast enhanced MRA (CE-MRA), as with CTA, involves scanning while a contrast agent is perfused into the blood either as a first pass perfusion or a longer term blood-pool agent. Time of flight MRA (TOF MRA) Provides high contrast images of areas of flowing blood. Areas of slower flow, which occur in large arteries, may result in inferior image quality using this method.

1.3.3 Measuring Haemodynamics

1.3.3.1 *In Vitro*

The haemodynamics of flow in AAAs can be assessed *in vitro* using transparent models of either generic aneurysm geometries or casts of patient aneurysms. Blood or, more usually, blood mimicking fluid can be pumped through the model using physiologically realistic flow magnitudes. Visualising and recording the resulting flow dynamics can be achieved through a number of methods including most of those used for *in vivo* measurements though there are a few methods solely used for measuring velocity *in vitro*. By injecting contrast agents such as dye into the model [132] a qualitative observation of flow behaviour can be obtained. If the flow is seeded with neutrally buoyant particles, laser Doppler anemometry (LDA) or particle image velocimetry (PIV) can be applied to obtain flow velocity information. LDA uses two laser beams which are intersected, creating fringes of overlap running perpendicular to the flow. When a particle passes through the beams all three components of velocity can be calculated by recording the frequency of the reflected light signal given off by the particle while passing through the fringe. PIV uses another laser technique to determine particle velocity. A sheet of laser light is flashed twice in the direction of flow and the corresponding illumination of the

seeded particles is recorded on camera. The images can be converted into vector plots by observing how far the particles move in the given time interval between flashes. Particle tracking velocimetry (PTV) uses similar principals to PIV and, using optical and ray-tracing techniques, can track discrete particles throughout a flow. PTV has been used previously [12] to validate flow in a physiologically realistic model of an AAA in order to validate CFD simulations of blood flow. *In vitro* methods allow a large amount of control over the experimental setup but require simplified parabolic flow profiles at the inlet and the creation of patient specific casts is not trivial.

1.3.3.2 Imaging

Imaging techniques using Doppler ultrasound, CT and MRI based methods can be used to measure blood velocity. The velocity data obtained from Doppler ultrasound can be displayed as either spectral Doppler, whereby the frequency spectrum is displayed in the y-axis with time along the x-axis, or colour Doppler where the velocity magnitude and often direction is superimposed on the ultrasound image. Doppler ultrasound has been used previously to study the healthy aorta [176] though the technique is dependent on the positioning of the transducer and the movements of the operator. There are also difficulties in resolving low and retrograde flows present in AAA [4] and so other methods are generally prefered for rigorous quantitative analysis of blood flow velocity in the aorta.

Injecting a bolus of iodine-based CT contrast agent into a blood vessel allows the flow velocity to be observed via CT angiography. Images of the vessel are recorded at discrete time intervals and the motion of the bolus analysed to determine flow velocity [24]. The injection of the bolus and radiation dose associatied with CT angiography mean this technique is used less frequently than non-invasive MRI techniques.

Tissue moving with uniform motion within a magnetic field gradient produces a change in the MR signal phase which is proportional to the tissue velocity [124]. By finding the difference in phase between scans taken at consecutive time intervals the x, y and z components of velocity can be obtained. Since the velocity of blood is significantly higher than that of the surrounding tissue, phase contrast MRI (PC-MRI) becomes a non-invasive method of gauging blood velocity. There are two methods by which PC MRI can be used to elucidate haemodynamics in a vessel. The first is by obtaining three dimensions of blood velocity over a designated inlet plane and extrapolating the flow dynamics using CFD. The second is to directly measure

velocity throughout the vessel by obtaining all three directions of flow velocity over all three coordinate axes at each timestep, known as 7D-MR velocimetry.

PC-MRI has been used extensively in image guided CFD modelling. It has been shown to produce accurate results under uniform flow conditions [47], though can be distorted by various artifacts in more complex flows [157]. This makes it a viable modality for providing inlet data in large, straight vessels such as the aorta. Most studies which use PC-MRI data to derive velocity inlet boundary conditions obtain transverse slices of flow in the through-plane direction (the 'head to foot' component in the case of the aorta). CFD simulations of large arteries and AAA generally interpolate the velocity data from the image to create Womersley inlet flow profiles [74, 86, 163].

Determining magnitudes of WSS using PC-MRI data requires near wall data to be obtained with a high degree of accuracy, which has proven to be problematic due to image resolution, partial volume effects and velocity to noise ratio present in PC-MR data [51, 64, 124]. These factors are especially apparent in smaller vessels and areas of low-velocity blood flow. It should also be remembered that wall motion may add velocity artefacts to the velocity data in the radial directions. Methods for allowing WSS to be obtained have been proposed by fitting the PC-MRI data to a fifth order three dimensional polynomial [140] or, alternatively, elements near the vessel lumen can be interpolated from surrounding pixels [20]. PC-MRI has been used previously to observe flow velocities in healthy [122] and aneurysmal [165] [46] aortas. Despite current limitations in image resolution, attempts have been made using PC-MRI to discern WSS magnitudes in healthy aorta [165].

1.3.3.3 Numerical Modelling

Numerical methods of modelling blood flow have evolved to be more powerful and more efficient as computing power has increased. Modelling software and techniques are versatile and can be edited to account for biological and chemical factors influencing flow in the vessel. Computational fluid dynamics (CFD) has the potential to be a useful clinical tool in observing vascular flow and disease pathology. Advances in medical imaging allow the creation of more accurate and detailed patient specific models of the vasculature [156] and for the capturing of velocity profiles of blood flow within vessels. Combining this data with numerical methods gives non-invasive and repeatable models of the vasculature.

Numerical modelling of the vasculature can be achieved through three different scales of models namely 0-D, 1-D or 2 and 3-D models. The choice of model depends on the complexity needed and parameters available. Lumped parameter, or 0-D models, consist of ordinary differential equations pertaining to viscous resistance, vessel capacitance and fluid inertia. 0-D models are generally used to describe the vascular system as a whole in a numerically efficient way [149]. 1-D models solve the governing Navier-Stokes equations of flow for generic vessel geometries. They are computationally cheap to run, but incorporate many assumptions of the vessels being observed. While they are a good indicator of averaged flow values in healthy vessels, they cannot accurately account for complex flow in the vessel as witnessed in AAA disease [45].

2-D and 3-D models use numerical methods to solve the partial differential equations found in the governing equations. The finite difference method (FDM) converts the continuum to be solved into a structured grid of discrete points. Inlet and/or outlet boundary conditions such as velocity or pressure magnitude are added to the model and the governing equations are solved over the grid via a choice of iterative processes. The finite element method (FEM) uses similar principles to the FDM whereby the geometry of the vessel is split into discrete points. FEM allows more flexibility in the formation of the grid, especially at boundaries and in complex geometries. The finite volume method (FVM) divides the geometry into a mesh of discrete volumes. The partial differential equations are solved across these volumes by first converting them to surface integrals and then solving iteratively. Unlike FDM and FEM, FVM does not require a structured grid and so complex geometries become easier to discretise, making solutions for the equations flow more attainable. Because of the flexibility in mesh generation afforded by the FVM it is used by most CFD software packages and has been used throughout this study. 0-D and 1-D models have been used as boundary conditions for input into 2-D and 3-D models [45].

FEM models have been used previously to great affect in determining the haemodynamics and wall properties of healthy arteries and aortic and cerebral aneurysms. Early models of large arteries such as the carotid [77] and the healthy abdominal aorta [109] found a correlation between areas prone to atherosclerosis and low and oscillating WSS. Numerical modelling has since proven to be a useful tool in investigating areas of the vasculature prone to atherosclerosis [14].

The first numerical models of AAA disease examined haemodynamics in generalised rigid

walled models [9, 15] using 2-D axisymmetric models of simple bulge shapes with sizes similar to AAAs to obtain velocity and WSS data under steady flow conditions. The simplified geometries meant that flow characteristics could be validated against experimental setups with matching geometries [4, 37]. These models were extended by applying pulsatile flow regimes [41] and experimenting with more realistic, asymmetric geometries [42] requiring a move to 3-D modelling. As imaging technology and computational efficiency have progressed, the ability to model patient-specific aneurysms has become available leading to two strategies of patient specific aneurysm research. FEM solid modelling of stresses, strains and tissue compliance in the aneurysm wall were simulated [130, 178] to identify areas of potential weakness and therefore rupture risk in the wall and the haemodynamics of flow inside the aneurysm were modelled using CFD to identify the patterns in WSS and flow characteristics which affect aneurysmal disease through biomechanical processes.

1.3.4 Physical and biochemical responses of monocytes to aneurysm haemodynamics

1.3.4.1 *In vitro*

Previous investigations have isolated monocytes and other leukocytes for *in vitro* analysis of their physical properties and the effects of shear stresses on their adhesion and transmigration. By placing the cells in a flow chamber and subjecting them to flows of varying magnitudes, the adhesive properties of cells under various shear stresses can be observed. Shear stress tests can be performed with cells attached to medium and in the presence of an endothelial cell culture [80, 81]. The data from *in vitro* testing can be used to improve the accuracy of numerical simulations.

1.3.4.2 Histology

Histological techniques have been used previously to visualise monocytes in atherosclerotic plaque [91]. Bylock and Gerrity [17] isolated swine monocytes, labelled them with fluorescence and injected them back into the animal where histological analysis revealed an aggregation of monocytes in the intima of the plaque. Steinberg et al [155] conducted polymerase chain reaction (PCR) analysis to determine rates of leukocyte recruitment in aortic atherosclerotic plaques. While histology gives spacially detailed insights into the recruitment of inflammatory

cells, it is extremely invasive and only gives a snapshot of disease *in situ* so is not suitable for rupture risk prediction.

1.3.4.3 Imaging

Through the use of contrast agents, imaging techniques can be used to observe monocytes in the thrombus and aortic wall. Recent experiments in echocardiography have studied the use of lipid microbubbles as an ultrasound contrast agent [85]. The microbubbles are targeted to activated leukocytes and have been used to visualise inflammation in myocardial tissue. The PET contrast agent ^{18}F-FDG is commonly used as an indirect marker of inflammation. When superimposed onto CT scans the combined PET/CT image gives a visualisation of the spatial distribution and the magnitude of inflammation. PET/CT scans have been used by Kotze et al [75] to observe metabolic activity in AAAs. Alongside PET/CT imaging, the MRI contrast agents superparamagnetic iron oxide (SPIO) and ultrasmall-SPIO (USPIO) may be useful tools in assessing the distribution of macrophage infiltration in AAA. SPIOs are nanoparticles which cause MR signal dropout in tissue. They can be ingested by macrophages [134] and so areas of high macrophage concentration can be identified by the loss of signal in the MR image. They have previously been used to quantify monocyte recruitment in atherosclerotic lesions [91] and feasibility studies have been conducted on murine AAA models [170] with encouraging results for the future use of USPIOs in non-invasive quantification of inflammation in AAAs. Recent advances in imaging techniques may provide a non-invasive method of observing the recruitment of inflammatory cells in AAA. While such techniques would be extremely useful, so far they can only ascertain areas of inflammation at a given timepoint and do not have the capacity required to assess the origin or evolution of inflammatory infiltrates in the wall. They can also provide information on local haemodynamic conditions which are inextricably linked with cell recruitment. Other potential downsides of imaging are the invasive aspect of injecting contrast agents and the dose of radiation associated with CT and PET scanning.

1.3.4.4 Numerical modelling of species in blood

Once the underlying flow in a vessel has been modelled to a desired degree of accuracy, models can be created which map the transport of blood borne species. Tracking species has a number of clinical uses including simulating platelet activation and deposition [9] which can be used to predict thrombus formation, elucidating the distribution of LDL cholesterol [92], a target

species in atherosclerotic disease, modelling oxygen distribution to predict areas of hypoxia and the tracking of white blood cells to predict areas of inflammation which is the focus of this study. Several methods exist for species modelling and the choice of method depends on the size and concentration of the species and the size of the vessel in which it resides.

The efficiency of numerical modelling is affected by the number of mesh volumes in a model, with a denser mesh resulting in increased processing time. Modelling small blood vessels gives the opportunity to apply a much higher grid resolution than large arteries, allowing for detailed modelling of particles within blood flow. This micro-scale modelling has been used with great effect to simulate the complex binding process of leukocytes on endothelial cells [70, 118, 160]. An investigation by Migliorini et al [104] modelled leukocytes as single, solid particles with a coupled receptor-ligand binding model which they extended to account for the hypothesised effects of red blood cells on leukocyte-wall interactions. These studies assume the leukocyte remains a solid sphere, which would be a reasonable assumption when in the bulk flow, but as the cells make contact with the wall a change in their viscoelastic properties becomes apparent. Other models divide the cells into smaller elements and model the leukocyte as a viscoelastic drop which becomes deformed upon contact with the endothelium [70]. Micro-scale models are an opportunity to assess individual cell behaviour with a high degree of accuracy, but the computational power required to include these models in simulations with large concentrations of particles in large arteries is currently too large to be feasible.

The transport of solutes and macromolecules with very low molecular weights such as oxygen, carbon dioxide and LDL cholesterol can be modelled in large arteries by applying an equation of mass transport to the solved Navier-Stokes equations [133]. How mass transport is modelled using this 'continuum' approach is dependent on the values of three non-dimensional parameters. Namely the Reynolds, Schmidt and Péclet numbers. The Reynolds number (Re) describes the ratio of inertial to viscous force. The Schmidt number (Sc), which expresses the ratio of momentum diffusivity to mass diffusivity, can be written: $Sc = \mu\ \rho D$ where D is the mass diffusion coefficient. Multiplying these numbers together gives the Péclet number (Pe) which relates the rate of advection to diffusion. Mass transport is modelled through the addition of an advection-diffusion equation which tends to break down when modelling solutes with large Péclet numbers. Most of the species of interest have Péclet numbers in the region of 10^5 to 10^8 [154] causing instabilities when standard numerical techniques are used. Despite this, investigations have used stabilisation techniques and very fine near-wall meshes to elimi-

nate numerical instability. These methods make modelling species in this way computationally expensive but allows models of species transport in blood flow to be coupled with models of transport through the vessel wall [3].

The high concentration of red blood cells in whole blood (around 45%) makes the modelling of individual particles in large arteries difficult as described below. Recent investigations [65] have attempted to bypass the need to model individual cells by treating the blood cells and blood plasma as two distinct fluid phases within the same domain. While the solid properties of the cells mean this will be unrealistic on a micro-scale, on a macroscopic scale the high density of red blood cells may act more like a non-Newtonian fluid.

The modelling of larger particles can be achieved via discrete phase modelling (DPM) by seeding the solved background flow and tracking the particle paths at each time point. Previous particle tracking studies have seeded flow using either individual particles [16, 95] or as a 'packet' of multiple particles contained within a single fluid volume [78] depending on the concentration of the particles in the blood. Since the background flow is modelled using fixed-grid Eulerian methods and the particles or fluid volume motion is tracked with the flow, these tracking methods are termed Eulerian-Lagrangian methods. The first ventures into Eulerian-Lagrangian modelling in vessels concerned the simulation of platelet motion [9] with the aim of predicting thrombus formation. Platelets were considered neutrally buoyant particles, seeded at a given concentration into fluid volumes. These platelet models gave rise to the use of residence time models in blood species tracking to give a statistical method of calculating particle-wall interaction negating the need for micro-scale analysis. Applying Eulerian-Lagrangian modelling to single white or red blood cells proved to be non-trivial as, given the size and density of the cells, it is not sufficient to assume they will follow the bulk fluid flow. Calculation of lift, drag and near-wall viscous forces becomes necessary as well as factors such as cell shape and stability. Numerical models have, however been formulated to account for these factors and have been validated for single cells against the experimental findings of Karino and Goldsmith [66]. The feasibility of modelling single particles using an Eulerian-Lagrangian method depends upon the concentration of particles in the blood. Using this technique to model red blood cells is currently unfeasible due to the high concentration of cells. The increasing number of particle paths needing to be solved requires a two-way solution as the cells will interact with each other and change the characteristics of the surrounding plasma phase. Leukocytes are found at much lower concentrations allowing the assumption of one-way modelling as the cell phase is un-

likely to affect the bulk flow and the tracking of physiologically realistic concentrations even in large arteries. Modelling white blood cells in large arteries has been studied by Longest et al [95] using a near wall residence time approach.

1.3.4.5 Residence Time Models

One of the challenges in modelling leukocytes in large arteries is accounting for the complex near-wall behaviour within the mesh resolution and computational limits available. Accounting for these micro-scale effects on the macro-scale models has been achieved through the use of statistical particle residence time models. Volumetric residence time models used in platelet modelling [78] use the integral of the time a particle spends in a given mesh volume during its time in the flow. The sum of this integral for all particles in the flow is normalised by dividing by the concentration of platelets, element volume and a normalisation factor based on the ratio of activated platelets to total platelets at inlet

$$VRT = \frac{1}{CV_e f} \sum_{i=1}^{n} \int_{path,i} H_i^e(t) dt, \tag{1.2}$$

where V_e is the volume of finite volume e, C is the concentration of platelets, f is ratio of active to innactive platelets and $H_i^e(t)$ is a function equal to 1 if platelet j is in volume e at time t and 0 if the platelet is not present.

Kunov et al use the photographic analogy of the exposure time of platelets in each volume. A similar technique has been used for leukocytes. Whereas for activated platelets, the volumetric residence time should theoretically correlate with the wall deposition rate, leukocyte adhesion is a more complex process and so the model needs to be adapted to account for their deposition. Longest et al [95], formulated a near wall particle residence time model (NWPRT) which accounts for the ratio of particle radius to distance from wall and the particle velocity within a volume and can be written

$$NWPRT = \frac{Q}{n_{tot} V_{nw}} \sum_{i=1}^{n} \int_{path,i} \left(\frac{a_p}{h_p}\right)^s \frac{1}{|v_i|} dr. \tag{1.3}$$

The average flow rate Q, the total number of cells n_0 and the near wall volume V_{nw} are used to normalise the equation as a non-dimensional parameter. V_{nw} is calculated by multiplying

the surface area by the fixed value chosen as edge of the near wall region. The ratio of cell radius to the distance from the cell centre to the wall, a_p/h_p provides a statistical parameter governing the likelihood of cell attachment when divided by particle velocity magnitude v_i. Longest et al [95] apply a correction factor s to the model wich is assigned a value depending on the species of cell being tracked. For monocytes, the suggested value is $s = 1$. The Longest et al NWPRT model has been used to model monocytes in femoral bypass anastomosis and an idealised rabbit aorto-celiac junction [96]. A similar model has been used by Kim et al [72] to simulate monocyte and platelet behaviour.

1.3.5 Summary

This study uses finite volume numerical models to determine the haemodynamics of AAAs and the behaviour and deposition of monocytes within the flow. FEMs have been used previously to great effect in modelling flow and tracking particles in a variety of vessels. FEM has an advantage over *in vitro* methods in that it can be applied directly to patient specific models, it is also minimally invasive when compared to histological techniques in which tissue samples are required. Geometries can be built using CAD software for simple models but for patient specific models imaging techniques are generally used. CT scans have been used in this study as they provide a higher contrast between the blood and the lumen than available MRI techniques. The patient-specific inlet velocity boundary conditions are obtained via PC-MR, a robust technique which has been used previously on large arteries [46, 98]. The use of contrast enhanced imaging techniques to determine monocyte deposition has been neglected in this study. As the focus of this study is as much on the journey of the monocyte from the aorta to to wall and the haemodynamic properties it encounters at its final destination within the wall, the *in situ* data provided by MRI or PET/CT scanning are less useful. These imaging techniques could feasibly be used in parallel with this study as a method of validating the numerical models. To apply models of monocyte motion and deposition to the FEM model we must obtain the physical properties of the cells and the effects of flow haemodynamics on the cells when they are in the bulk blood flow and when attaching to the wall. These properties have been taken from the literature, from studies using the *in vitro* techniques above. A NWPRT model is applied to the FEM model to model particle deposition at the wall.

1.4 Haemodynamics in Healthy and Diseased Aorta

Aortic haemodynamics differ between patients though the general characteristics of flow are retained in healthy vessels. The onset of disease can cause flow dynamics to diverge from these characteristics, introducing non-linear secondary flows. The deposition of monocytes in AAA disease is dependent on the underlying haemodynamics of the vessel and so an understanding of haemodynamics in both healthy and diseased aorta is required to describe observations of cell behaviour. While, in this study, the abdominal aorta is modelled as a discrete entity from the rest of the vasculature the characteristics of flow entering the model are important in dictating the patterns of flow within the AAA. It is therefore important to understand the flow characteristics not only within the AAA cavity, but throughout the aorta.

1.4.1 Haemodynamics of Healthy Aorta

As blood flows over the aortic arch, a high degree of secondary flow effects are created. The bulk flow exhibits a helical motion as it transcends the superior aorta [62]. These effects become damped as the blood descends the aorta due to viscous effects and the compliance of the vessel but are still present as far down as the renal arteries [48]. The degree of this secondary flow reaching the abdominal aorta is uncertain, as discussed in Chapters 4 and 5. As the flow passes the renal arteries, *in vitro* aortic models [109, 163] show that under resting conditions the flow becomes more complex with two vortices forming during the deceleration phase of systole on the anterior and posterior walls which then translate downstream. Despite the downstream motion of the bulk of the blood flow, a thin area of transient retrograde flow was noted on the posterior wall creating high residence times. Helical flow was observed in the iliac bifurcations during mid-systole with flow reversal occurring at the posterio-lateral regions of the bifurcation during the backstroke of systole. Under exercise conditions much of the secondary flow characteristics are absent and flow is generally laminar in nature [110] although the spiral flow entering the bifurcation is still prevalent. Pederson et al [123] and Taylor et al [165] show WSS is significantly lower in the infrarenal aorta than the downstream superceliac region with oscillatory flow only occuring in the infrarenal aorta. A study detailing flow in the abdominal aorta by Bonert et al [11] found vessel cross-sectional area and curvature to be influential in the distribution of WSS magnitude. Intimal thickening was found to correlate with regions of low and oscillating WSS [11, 123, 165] indicating that these regions are the most prone to atherosclerotic disease.

1.4.2 AAA haemodynamics

1.4.2.1 Generic AAA Geometries

Vortex formation has been shown to be a defining feature in AAA haemodynamics. Annular vortices are present in generalised AAA models subject to steady and turbulent flows [9, 15, 42, 191]. In steady flow models a stationary vortex is formed, filling a larger volume of the cavity as Reynolds numbers increase above 300 then shrinks to a much thinner vortex close to the wall around a Reynolds number of 3600 [9]. Low and negative WSS are found throughout the cavity with a large spike of WSS occurring at the flow reattachment point downstream of the vortex [4]. Under pulsatile flow conditions in the generalised AAA models an annular vortex forms at the proximal end of the cavity during the back stroke of systole and translates downstream. It then dissipates at the distal end of the cavity at the beginning of systole in the next cycle [37, 42, 144, 191]. The motion of the vortices dictates the temporal WSS magnitudes. As in the steady state models, WSS remains low compared to the inlet length throughout much of the cavity with a spike in WSS occurring at the vortex reattachment point at the distal end of the cavity. Maximum WSS occurs at the peak flow timepoint where the dissipating vortex is forced down the distal neck of the AAA. While the flow was found to be laminar for the majority of the pulsatile cycle, turbulence has been shown to occur even in simple aneurysm models during the deceleration phase of systole [191]. Salsac et al [144] investigated variation in WSS patterns with aneurysm size, showing flow separation to be present in all of the bulge diameters used (smallest bulge diameter to inlet diameter being D/d=1.3 and largest being D/d=2.4), the mean WSS magnitude was found to decrease with AAA dilation ratio. While many of the generalised AAA simulations and experiments are axisymmetric in shape, Finol et al [42] observed the effects of asymmetry on flow under pulsatile conditions. The general trends of vortex formation and dissipation were preserved with asymmetry, though interestingly the peak WSS at the distal end of the cavity was significantly higher in asymmetrical models when compared to an axisymmetric model.

1.4.2.2 Patient Specific Geometries

Relatively few numerical haemodynamic studies have been carried out on rigid walled anatomical AAA models, especially when compared to studies of intractranial aneurysms. When extrapolating flow dynamics to patient specific geometries it must be remembered that AAAs develop in a variety of shapes and sizes, with differing angles of inlet and outlet aorta. While

analysis of flow in one patient may not hold for another, all AAAs share the same expanded interior geometry and it is important to assess to what degree the flow dynamics observed in generalised models are present in anatomical models. The study of a rigid-walled anatomical model with a single pipe outlet is presented by Finol and Amon [42]. Flow separation was shown to begin during the deceleration phase and vortex formation and translation is present during late systole and diastole as in generic models. The nature of the vortex formation however is different from that observed in simplified models with the angle of the AAA sac inducing the formation of a single, central vortex rather than torus shaped vortices. As geometric complexity is increased, so too is complexity of WSS variation. Peak WSS was found to occur in a localised area at the proximal neck of the model and was significantly higher than under healthy aortic conditions. Low WSS was observed over the more rounded anterior wall with oscillating WSS occurring at the posterior wall during late diastole. This model had straight inlet and outlet tubes leading from the AAA sac and does not account for thrombus layers and so may not be physiologically realistic. More realistic models were examined by Fraser [46] in a study which confirmed that vortex shape depends upon aneurysm geometry. Toroidal vortices formed in AAAs with large bulge to inlet ratios and were more crescent shaped with smaller bulges. Helical flow in the AAA was present only in geometries whereby the inlet joined the sac at an angle. These studies highlight the potentially significant differences in haemodynamics occuring with differing geometry.

1.4.3 Effects of Turbulent Flow

Regions of disturbed flow in arteries are closely correlated with damage to the endothelial lining [31] and regions of arterial disease. Whether it is the perturbations in flow which cause the initiation of disease or vice versa is yet to be fully understood, though it is generally agreed that the presence of disturbed flow exacerbates disease formation. Non-linear near wall flows create changes in local WSS gradients resulting in changes to biochemical signalling in endothelial cells. Changes in endothelial cell signalling can result in the production of the vasoconstrictors such as NO and cellular realignment. In areas of oscillating shear-stress endothelial cells have been observed to align in a less uniform manner than in laminar flow [30], increasing the probability of mass transport between blood and wall through gaps between the cells. Turbulent mixing of cells near the wall alters both cell residence times and cell mixing behaviour. Recirculation regions near the wall may promote cell adhesion [22] and increased mass transfer to the wall. Turbulent shear stresses have been shown to induce high endothelial cell turnover

compared to laminar shear stresses [31] and cause endothelial cell loss after prolonged exposure to turbulent flows [191]. Microscale turbulent eddies are thought to be responsible for both damaging red blood cells and activating platelets which may in turn lead to an increased probability of thrombus formation in turbulent regions.

The formation of turbulent perturbations is due to vessel surface roughness, pre-existing upstream perturbations and the Reynolds number of the flow [120]. At low Reynolds numbers the viscous properties of the fluid are dominant and so perturbations cannot form, giving the flow a smooth, laminar characteristic. At high Reynolds numbers, inertial forces dominate allowing the formation of turbulent perturbations in the flow. Between these two extremes there is a transitional phase in which the flow is not fully turbulent. In pipe flow this region is at Reynolds numbers of around 2000 to 2300. In healthy arteries, blood flow is regulated to reduce perturbations and can generally be modelled as laminar fluid motion [120]. By expanding or contracting vessels through the use of vasodilators and vasoconstrictors, low Reynolds numbers can be maintained in an artery. Disruption of signalling pathways, degradation of the ECM and occlusion or deformation of the artery may cause the regulatory mechanisms fail leading to a transition to turbulent flow.

Since AAA disease is characterised by an expansion in the vessel wall, the fluid dynamics will be different from those observed in pipe flow and so the range of Reynolds numbers at which transition to turbulence occurs may also differ and should not be assumed to be the same as pipe flow.

Simplified models of AAA disease exhibit a transition to turbulence during the deceleration phase of the cardiac cycle [191]. Since turbulent flows affect WSS as well as endothelial and blood-species behaviour it is important when modelling arterial blood flow and the motion of white blood cells that turbulent effects should be adequately accounted for.

1.4.4 Blood properties

Throughout this study, the density of blood is taken to be 1059 kg/m^3 and the viscosity to be 3.5x10$^-$3 kg/ms. Because of the large diameter of the abdominal aorta, blood is modelled as a Newtonian fluid as described above.

Property	Modelling Values (Physiological Range)
Diameter	16μm (14-17 μm) [29])
Concentration (Adult)	3×10^5/ml ($0 - 8 \times 10^5$/ml)[29]
Density	1070 kg/m^3 [152]
Volume Fraction	6.43×10^{-2}%

Table 1.1: *Monocyte Properties*

1.4.5 Monocyte Properties

The physical properties of monocytes used in this study have been taken from the literature and are shown in table 1.1. Where a range of values exist, the median value has been taken. The effects of WSS on monocyte binding are covered in greater detail in Chapter 4.

1.5 Proposed Solution

To create a model of monocyte deposition, finite volume CFD techniques will be used to simulate the flow of blood within AAAs. These models will be seeded with discrete virtual particles with the physiological properties and concentration of monocytes. Modelling cells using a one-way Lagrangian approach can be used to predict how the monocytes will be transported by the blood flow. Monocyte deposition is a function of cell residence time and the distance of the cell from the wall as well as the haemodynamic and biochemical effects on the cell and the wall. To account for the complex biochemical interactions of monocytes at the vessel lumen, cell residence time is calculated using a statistical approach via a NWPRT model. The NWPRT model accounts for the time each monocyte spends in a given mesh volume in the near wall region, the volume of the element and the distance of the particle from the wall to provide a probability of firm cell adhesion.

1.5.1 Generic AAAs

In order to calibrate the CFD models, definitions of the AAA geometry and boundary conditions are required. With any computational simulation it is necessary to begin with simplified models to prove that the initial concepts are sound and then add more complex traits to the models. In this respect, the CFD models shall use generic, bulge shaped AAA geometries with simple, fully-developed inlet velocity boundary conditions with magnitudes taken from patient data used in previous studies [46]. Using simplified AAA geometries allows the underlying

haemodynamics to be validated against existing experimental models. By comparing simulations of various AAA diameters the changes in haemodynamics and monocyte residence time can be observed as AAAs become more developed. The monocyte behaviour in generic AAAs can also be compared with that in a straight control tube, simulating a healthy aorta.

1.5.2 Patient Specific AAA

The next step towards a clinically relevant model is to apply physiologically realistic geometries and boundary conditions to the CFD model. CT scans provide a high contrast between blood and the vessel lumen making them ideal candidates for segmentation and stitching together to create patient specific geometries. PC-MRI can provide physiologically realistic inlet velocity boundary conditions which can then be applied to the patient specific geometry. PC-MRI can also be used to validate the haemodynamics predicted by CFD models. Once validated patient-specific models of AAA haemodynamics have been created, monocyte particles can then be seeded, the NWPRT model applied and the end result of a patient-specific model of monocyte deposition model achieved. Before the simulation of monocyte behaviour in AAA can be achieved there are areas of modelling methodology absent from the literature which need to be assessed in order to create physiologically realistic models. The first is how the transition to turbulent flow present in AAAs is modellid and the second is what level of detail is required when applying physiologically realistic boundary conditions.

1.5.3 Turbulence Modelling

1.5.3.1 Transition to turbulence in vascular disease

Reynolds numbers throughout the vasculature range from less than 10 in the microvasculature to a maximum of around 4000 in the aorta during peak systole [76] which means it is unlikely that blood flow would become fully turbulent during a normal human cardiac cycle for any significant period of time. Instead the laminar flow partially breaks down into a state described as a transition to turbulence [18]. Significantly for this study, transitional flows have been observed in haemodynamic analysis of *in vitro* AAA. Studies by Yip and Yu [191] observed that while the flow remains laminar during the beginning of systole and the end of diastole, perturbations become endemic during the back-stroke of systole and early diastole.

To preserve accuracy in the modelling of AAA haemodynamics a method of effectively mod-

elling the transition to turbulence is required. The need for modelling turbulent behaviour is particularly necessary for the purposes of this study as the end goal of modelling monocyte behaviour involves tracking individual particles through near-wall regions prone to turbulent perturbations. Several methods of numerically modelling turbulent flow exist yet no previous studies have been conducted to compare the extent of variability in haemodynamics and wall shear stresses which arise through the use of these different methods. Chapter 3 compares the effectiveness of a variety of turbulence models by comparing differences in haemodynamics and WSS in generalised AAA geometries experiencing steady and pulsatile flows. Analysis of the effects of turbulence models on flow can determine the most appropriate model to use when simulating haemodynamics in AAA.

1.5.4 Boundary Conditions

Dynamics of the fluid within the geometry are determined by the inlet and/or outlet boundary conditions applied to it. The accuracy of simulation therefore relies heavily on the information carried in the boundary conditions which can be either velocity, pressure or mass flow conditions. In simulations with compliant walls it is necessary to include pressure boundary conditions as the pressure wave is the driving force behind wall motion. As this study uses only rigid wall models, the inclusion of pressure boundary conditions is no longer necessary and so velocity inlet conditions will be sufficient. Velocity data for blood flows can take the form of *in vivo* measurements from techniques such as MRI, ultrasound, X-ray angiography. *In vitro* data can be aquired by applying realistic flow to transparent casts or models of vessels and aquiring velocity data through techniques such as LDA PIV. If the inlet velocity data has sufficient resolution to provide spatial differentiation of velocities over the inlet plane it can be applied directly from measured velocity data. Velocity boundary conditions can use one or three directions of flow, uni-directional velocity accounting for flow in the direction of highest velocity magnitude and three directional flow accounting for additional radial velocity components. When limited or no velocity data is available, or if computational constraints are required or allowed, it is common to assume that the flow is a fully developed at the inlet and a time varying parabolic profile is attached [46]. More detailed methodology of boundary condition formulation is found in Chapters 5 and 6.

The physical properties of whole blood can be taken from literature. The viscosity of blood depends upon its percentage of red blood cells, or hermatocrit which, while variable, is generally

between 38% and 46%. In this study, a blood viscosity of 3.5×10^{-3} has been used, derived by Cox [27]. The decision to use either parabolic flow profiles, uni-directional measured flow or tri-directional measured flow will effect the outcome of the numerical simulation. These effects have yet to be quantified for AAA models and Chapters 4 and 5 provide an investigation into the most suitable boundary condition to use.

1.5.5 Effects of Fluid-Structure Interaction (FSI)

Di Martino et al [35] began the first investigations into the interactions between fluid dynamics and wall structure with the aim of creating a more accurate model of AAA rupture risk. Previous models had not accounted for complex flows when modelling wall stresses. The study worked on the hypothesis that the haemodynamics would affect wall motion which would in turn affect the haemodynamics. FSI models have subsequently been used to model simplified AAAs with both axisymmetric and asymmetric geometries [88, 148]. These studies show that vortex formation is an integral part of AAA haemodynamics, but did not compare their results with rigid wall models. As an aside, Kleinstreuer noted that the angle of entry of the neck into the AAA cavity caused a significant difference in vortex structure. Experimental models of simple, asymmetric AAAs were created by Deplano et al [32] with rigid and compliant walls. Each model was tested using inlet waveforms analogous to resting and exercise conditions and flow characteristics observed with PIV of seeded particles. They state a significant difference between vortex behaviour in rigid and compliant walls, thought to be due to the energy stored in the compliant wall during peak flow being released during the deceleration phase which boosts the formation and translation of vortices. While compliance has some effect on flow, the rigid walled models used in the Deplano et al investigation show the vortex remaining at the proximal end of the aneurysm whereas previous investigations have shown translation of the vortex. This suggests that the difference in flow dynamics due to compliance may not be as significant as stated.

1.6 Thesis Outline

1.6.1 Aims and Objectives

The key aims of this study are, firstly, to develop the methods of numerical modelling of AAA haemodynamics through novel investigations of turbulence models and inlet velocity boundary

condition methods. Secondly, to further the understanding of AAA disease by observing the behaviour and adhesion probability of inflammatory cells in flow. It has been postulated that inflammation occurs in specific focal areas in the AAA wall causing hotspots of wall degradation leading to a weakening of the wall. Previous studies have shown [34] that areas of decreased tissue strength are prone to rupture. By identifying the areas of high inflammatory infiltrate it is hoped that the numerical modelling protocol can provide the first steps towards a clinical indicator of AAA wall weakness and thus improve rupture risk prediction.

1.6.2 Thesis Structure

- Before simulating haemodynamics and probability of cell adhesion in patient specific AAA geometries, a protocol for simulation was established in simplified, axisymmetric aneurysm geometries. Geometries were created with a range of bulge sizes in order to observe the general trends in haemodynamics and monocyte adhesion in developing and fully developed AAAs. An averaged patient pulsatile flow waveform was applied as the inlet boundary condition for each geometry.

- The modelling procedure was calibrated through mesh and timestep refinement studies, a cycle independence study and a comparison of first and second order solutions. A fine near wall boundary layer of volumes was added to the models in order to model WSS and particle behaviour in the near wall region.

- Previous investigations have shown that blood flow in AAAs undergoes a transition to turbulence during each pulsatile cycle [191]. Laminar flow modelling does not account for the changes in haemodynamics caused by turbulence in a vessel and so a turbulence model is required. The accuracy and efficiency of relevant turbulence models of varying complexity were investigated by simulating haemodynamics in an axisymmetric AAA geometry. Haemodynamics and WSS were compared between simulations and compared with previous experimental findings to assess which turbulence model is the most appropriate.

- Once the axisymmetric models were calibrated and turbulence models investigated, the probability of monocyte adhesion to the lumen was determined through the use of a near wall particle residence time (NWPRT) model based on previous work by Longest et al [95]. The NWPRT model was applied to monocyte particles seeded into the blood. A

novel variable WSS limiting factor based on *in vitro* experimental adhesion properties was created and applied to the NWPRT model. Residence times were compared with trends in haemodynamics and WSS which was found to be an indicator of vortex behaviour.

- Simulations were then conducted in patient-specific geometries. Geometries were created from segmented CT scans and inlet velocities provided by phase contrast-MR (PC-MR) images. Inlet velocity boundary conditions can be applied using axial and radial components of velocity, axial velocity alone or as fully developed flow profiles based on the inlet centreline velocity. There is no previous literature detailing which method is most appropriate for modelling AAAs and so an inlet boundary condition investigation was required. The investigation consisted of two sections;

  i) Comparing differences in haemodynamics and shear stress properties between simulations.

  ii) Validation of each boundary condition method through comparison of mid-cavity velocities with PC-MR data.

- Finally, the NWPRT model used in axisymmetric AAA simulations was applied to the patient-specific geometries seeded with monocyte particles to determine the probability and distribution of monocyte adhesion. Residence times were compared with values of WSS to determine whether patterns in monocyte adhesion probability are related to secondary flow within the aneurysm.

Chapter 2
Creation and Calibration of Generic AAA Simulations

2.1 Introduction

When creating numerical models of complex systems it is often advantageous to calibrate and trial the numerical techniques in simplified scenarios. Simplifying geometries and solution algorithms increases solution efficiency and therefore errors within the system can be quantified and the most efficient solution strategy obtained. Once the methods of these simple scenarios have been justified, further levels of complexity can be added. Before attempting simulations in patient-specific geometries AAA haemodynamics are simulated in axisymmetric aneurysms of varying cavity diameters, from a straight tube simulating the healthy aorta to a cavity size on the scale of a fully developed AAA. Creating a range of AAA diameters provides an analysis of haemodynamics throughout the development of AAA disease. At the inlet fully developed, parabolic flow profiles are applied to mimic simple yet physically realistic flow conditions.

Previous investigations of axisymmetric AAA geometries by Egelhoff et al [37] and Salsac et al [144] use maximum bulge diameters equating to aneurysms significantly smaller than the critical 5.5 cm cut off point for surgical intervention. The focus of the Salsac et al investigation is on elucidating WSS. The effects of WSS on ILT are not well understood when compared with healthy endothelial cells and so models with a higher probability of an uninterrupted endothelial layer were chosen. Salsac et al used less developed AAAs due to their tendency to contain minimal ILT. Similarly, the effects of ILT on the standard model of monocyte mechanotransduction used in this study are uncertain and so this study has a bias towards smaller aneurysm diameters.

The parameters used to create simulations must be assessed to justify their physiological relevance and calibrated to quantify the magnitude of error present. Despite the need for simplification, the simulation must give a physiologically realistic output and so the dimensions of the geometry and formation of the inlet boundary conditions must strike a balance between

efficiency of simulation and relation to *in vivo* conditions. There is also a balance to be maintained between numerical accuracy and computational efficiency. While accurate solutions are desired, it is also necessary to provide solutions within a manageable time scale and memory usage, especially if these techniques are to be developed for clinical use. The density of the grid used to solve the finite volume equations and the time step used in pulsatile flow studies determine the precision and efficiency of simulation. A study by Roache [138] provides a framework for quantifying errors in grid refinement and has been used in this study to investigate mesh and time step refinement. The solution method and variables used must also be described and justified.

Previous numerical and experimental investigations [15, 37, 144] have used simplified geometries and boundary conditions to elucidate the generalised haemodynamics present in AAAs. The haemodynamics simulated in this study are compared with the results of previous studies in Chapter 4 in order to validate the methods used.

The aim of this chapter is to optimise the mesh and timestep regimes and solver variables used for simulation of AAA. Simplified AAA geometries of varying diameters are constructed and meshed for exporting to CFD solving software. The equations of fluid dynamics to be solved and methods of discretising and solving the equations are described below, as well as justification for the solver variables and the haemodynamic properties used.

2.2 Methods

2.2.1 Geometries

One of the aims of this study is to simulate monocyte recruitment in AAA disease. It is useful to model changes in the patterns of recruitment throughout the progression of an aneurysm and so to achieve this geometries of differing maximum cavity diameter were created.

All of the geometries in this study are modelled with rigid walls. An investigation by Fraser [46] shows that using rigid walled models retains the characteristics of flow but leads to an increase in peak WSS magnitudes when compared to various methods of fluid-structure interaction (FSI). The addition of FSI increases the processing time of simulation and adds an extra unknown variable in the form of the elastic modulus of the wall. As AAAs progress, the wall becomes stiffer [33] and so the haemodynamic differences between compliant and rigid walled

aneurysms may become negligible in larger geometries when compared to the healthy aorta. Because of this, many investigations of flow in simplified geometries [37, 144] use rigid walled geometries, the results of which can be used to validate this study.

Bulge-shaped axi-symmetrical geometries of varying maximum diameter (D) were created in Gambit v. 2.4.6 (Fluent Inc., Lebanon, New Hampshire, USA). The vessel inlet diameter (d) was a physiologically realistic 1.9 cm [121]. The maximum bulge diameters of $D = 1.3d$, $D = 1.5d$, $D = 1.8d$ and $D = 2.1d$ used previously by Egelhoff et al [37] were chosen for the model geometries and a straight vessel of $D = d$ to simulate a healthy aorta. The chosen diameters correspond to varying fixed cavity volumes. If $D = 2.1d$ is 100% cavity volume, $D = 1.8d$ has 80%, $D = 1.3d$ has 20% with D=d having 0% cavity volume. Using dimensions of geometries corresponding to those used by Egelhoff et al allow for validaton by comparison. The investigation of varying vessel diameters can be interpreted physiologically in two different ways; firstly as a measure of AAA progression with $D = 1.3d$ being early stage AAA and $D = 2.1d$ developed AAA. Alternatively, cavity size corresponds to the degree of thrombus, where $D = 2.1d$ is analogous to a fully developed AAA containing no thrombus, in $D = 1.8d$, 20% of the cavity contains thrombus and so on until $D = d$ in which the entire cavity contains thrombus. This second interpretation is relevant when considering the hypothesis that thrombus formation compensates for the expansion of the cavity and is derived from a technique used by Mower et al [115]. While most of the geometries used are analogous to developing AAAs, a final geometry was created with a maximum diameter of $D = 2.9d$ to model a critical AAA with no ILT for comparison. For detailed AAA dimensions see table 2.1.

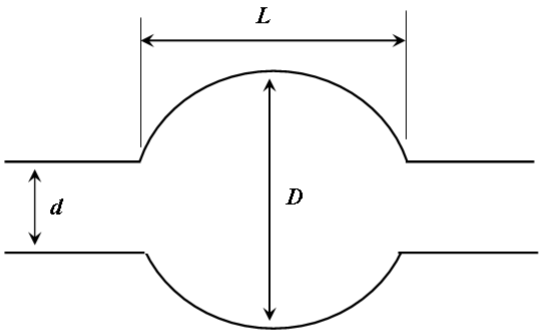

Figure 2.1: *AAA model dimensions*

Model Number	L/d	D/d
0	4.0	1
1	4.0	1.3
2	4.0	1.5
3	4.0	1.8
4	4.0	2.1
5	4.0	2.9

Table 2.1: *AAA model dimensions*

The bulge shape was controlled by the equation

$$R(z) = \frac{d}{2} + \frac{d((D/d) - 1)}{4}\left(1 + \cos\left(\frac{\pi z}{2d}\right)\right) \tag{2.1}$$

as used previously by Bluestein et al [9]. To ensure flow is fully developed when entering the AAA cavity, an inlet of length 3.7d was attached to the geometries and an outlet of length of 11d attached to prevent outlet flow conditions from interfering with flow in the cavity. The inlet and outlet lengths used are suggested by Egelhoff et al [37].

2.2.2 Boundary Conditions

Boundary conditions are required for the inlet, outlet and walls of each simulation. Each boundary condition must be justified in terms of how it relates to physiological patient aneurysms.

Velocity is used as the inlet boundary condition. The simplified models used do not relate to specific *in vivo* aneurysms and so inlet conditions must be prescribed. Flow is therefore assumed to be fully developed when it enters the inlet. For the simplest cases of steady, laminar flow through a tube, a fully developed profile can be derived via the Poiseuille's law

$$Q = \frac{\Delta P \pi R^4}{8\mu L}, \tag{2.2}$$

where Q is flow rate, ΔP is difference in pressure, L is vessel length, μ is dynamic viscosity and R is vessel radius. The velocity at distance r from the centre can then be determined by

$$u_r = \frac{\Delta P\left(R^2 - r^2\right)}{4\mu L}, \tag{2.3}$$

as shown in figure 2.2 Poiseuille's law holds in theory for simple, steady flows but fails when

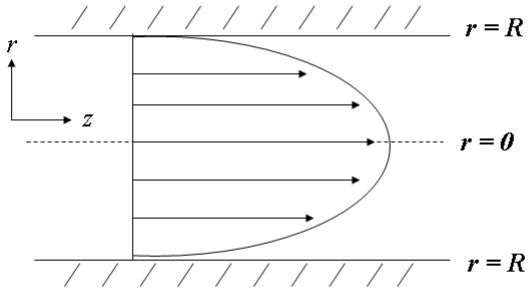

Figure 2.2: *Poiseuille flow in a tube*

accounting for the pulsatile nature of blood flow in large arteries. Where steady flow regimes are required for model calibration, parabolic inlet profiles are created with a user defined function (UDF) and attached at the inlet. The profiles must satisfy Poiseuille flow and give an average inlet flow velocity which satisfies the required Reynolds number. To overcome pulsatility of flow, fully developed flow profiles are calculated which adhere to the Womersley number, a non-dimensional number denoting the ratio of pusatile flow frequency to viscous effects

$$\alpha = r(\frac{2\pi}{T\nu})^{1/2} \tag{2.4}$$

Where T is the time taken to complete a cycle of pulsatile flow and ν is kinematic viscosity.

When α is less than unity, flow tends towards Poiseuille flow whereas for high α, of 10 or higher, the velocity profile becomes flattened. The equation of motion of viscous fluids in an oscillatory pressure gradient was found by Womersley to be [188]

$$\frac{\partial P}{\partial z} = Ae^{i\omega t}. \tag{2.5}$$

By incorporating Bessel functions of α, the velocity profile under Womersley flow conditions was found to be

$$v = \frac{A * r^2}{i\mu\alpha^2}\left(1 - \frac{J_0(\alpha r i^{3/2})}{J_0(\alpha i^{3/2})}\right)e^{i\omega t} \tag{2.6}$$

where J_0 is a zeroth order Bessel function of the first kind. An example of Womersley flow

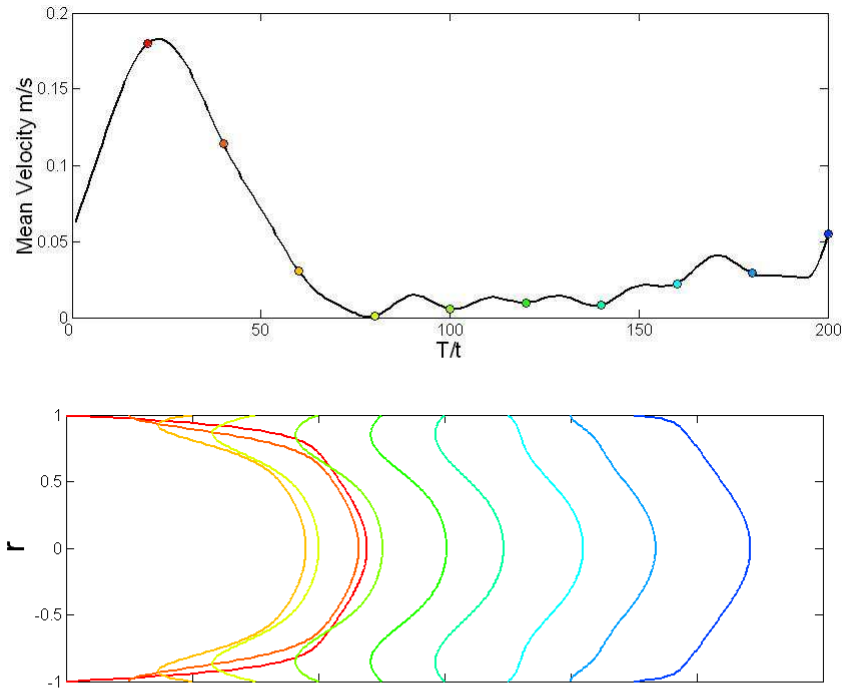

Figure 2.3: *Womersley flow profiles*

profiles obtained from centreline velocities is shown in figure 2.3.

Pulsatile flow inlet boundary conditions were taken from a patient averaged flow waveform compiled by Fraser et al from a study of 20 AAA patient, shown in figure 2.4. The flow waveform was created from aortic centreline velocities at 200 timesteps over a 0.9281 second wave cycle obtained using Doppler ultrasound. To simulate fully developed pulsatile flow in the AAA, the inlet centreline velocity was found at each time step and used to create a set of transient parabolas satisfying the Womersley parameter.

A no slip boundary condition was placed on the wall which requires the flow at the wall to be stationary. Rigid walled models do not require specific pressure outlet conditions as the inlet boundary conditions will create the pressure differentials required to drive the flow. The outlet was prescribed as a simple outflow with no velocity or pressure conditions.

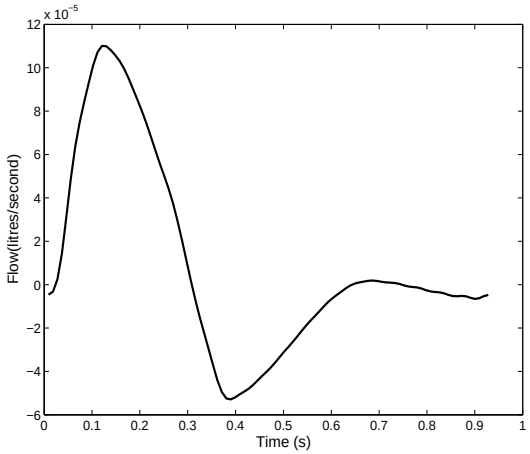

Figure 2.4: *Patient averaged flow waveform*

2.2.3 Governing Equations

To determine the haemodynamics present in each of the AAA models, the equations of mass and momentum conservation over all of the finite volumes are solved. Together these equations constitute the Navier-Stokes (N-S) equations for Newtonian fluids and are the fundamental equations of fluid flow, giving a solution to the flow dynamics in the form of a velocity field. Blood can be assumed to be an incompressible fluid and so the incompressible N-S equations are expressed in the non-linear differential equations below.

Strictly the N-S equations refer only to the conservation of momentum but since these cannot be solved for incompressible flows without the conservation of mass (continuity) equation, it is generally included in any description of the N-S equation and can be described

$$\frac{\partial \rho}{\partial t} + \bigtriangledown \cdot (\rho \vec{v}) = 0 \tag{2.7}$$

where $\vec{v}$ is the velocity vector.

In incompressible flows, ρ is a constant and so this equation can be simplified to $\bigtriangledown \cdot (\vec{v}) = 0$. Which means physically that the volume of interest is neither expanding nor contracting.

The conservation of momentum equations are derived from Newton's second law and can be written;

x momentum

$$\rho\frac{Du}{Dt} = -\frac{\partial p}{\partial x} + \bigtriangledown \cdot (\mu \bigtriangledown \ u) + S_{Mx}, \tag{2.8}$$

y momentum

$$\rho\frac{Dv}{Dt} = -\frac{\partial p}{\partial y} + \bigtriangledown \cdot (\mu \bigtriangledown \ v) + S_{My}, \tag{2.9}$$

z momentum

$$\rho\frac{Dw}{Dt} = -\frac{\partial p}{\partial z} + \bigtriangledown \cdot (\mu \bigtriangledown w) + S_{Mz}, \tag{2.10}$$

where *u*, *v* and *w* are the *x*,*y* and *z* components of velocity respectively, ρ is the fluid density, *p* is the pressure and S_{Mi} are the source terms of other body forces such as gravity. To fully understand the relevance of the N-S equations it is worth relating them back to Newton's second law. The terms on the left-hand side are the inertial terms. Note the use of the substantive derivative

$$\frac{D\theta}{Dt} = \frac{\partial \theta}{\partial t} + \vec{v} \cdot \bigtriangledown\theta, \tag{2.11}$$

where $\bigtriangledown\theta$ is the gradient of θ which can be written as $\frac{\partial \theta}{\partial x}\hat{i} + \frac{\partial \theta}{\partial y}\hat{j}$ for a 2 dimensional case. When expanded, the substantive derivative splits the inertia into unsteady acceleration and convective acceleration within a volume. The terms on the right-hand side are the sum of the forces acting on the fluid within a volume. The middle term describes the viscous stress in terms of the diffusion of momentum. The remaining forces are the gradient of pressure and additional body force, which is generally gravitational force.

2.2.4 Discretisation and Solution of the Navier-Stokes Equations

The N-S equations are solved using Fluent (Fluent Inc., Lebanon, New Hampshire, USA) software which uses a control volume approach to achieve numerical solutions. The geometry is first divided into a mesh of element volumes. Each element can be further divided into element faces, edges and nodes as described in figure 2.5. For each element in the grid, the integral of the governing equations is found over its surface area. Written in volume and surface integral

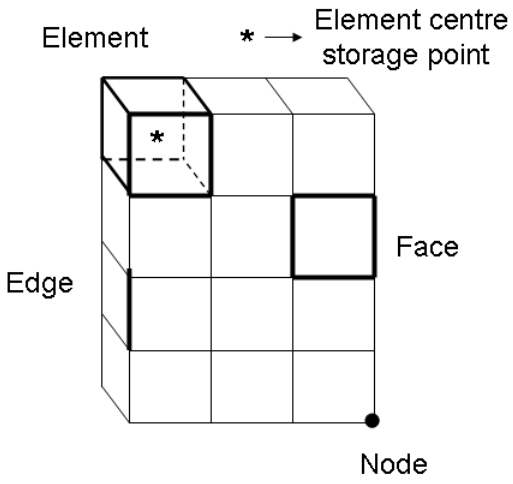

Figure 2.5: *Components of the mesh elements*

form, the continuity equation (equation 2.7) can be described

$$\int_V \frac{\partial \rho}{\partial t} dV + \oint \rho \vec{v} \cdot d\vec{A} = 0 \tag{2.12}$$

and the conservation of momentum (equations 2.8 to 2.10)

$$\int_V \frac{\partial \rho \vec{v}}{\partial t} dV + \oint \rho \vec{v} \vec{v} \cdot d\vec{A} = \oint pI \cdot d\vec{A} + \oint \mu \cdot \bigtriangledown \vec{v} \cdot d\vec{A} + \int_V S_{\vec{v}} dV, \tag{2.13}$$

where $\vec{A}$ is the surface area vector, *V* is the element volume and $S_{\vec{v}} =$ the source of $\vec{v}$ per unit volume.

These integrals are then converted into discrete equations for solving. Each equation is split into spatial and temporal terms. The appropriate method of solution is chosen by weighing up the memory and processing demands of the algorithm against the order of accuracy and the magnitude of error.

2.2.4.1 Temporal Discretisation

The temporal component of the governing equations can be discretised over a time step $\triangle t$. The change in a scalar quantity, $\partial\theta$, is approximated through the use of difference methods. The simplest difference methods are the forward, backwards and central methods which store two levels of information during each iteration. The backwards difference method is calculated by subtracting the previous value of the scalar from the current timestep value and can be described

$$\frac{\partial\theta}{\partial t} = \frac{\theta^{t+\triangle t} - \theta^{t}}{\triangle t} = F(\theta), \tag{2.14}$$

where θ is the scalar quantity, $t + \triangle t$ is the value at the current timestep and t is the value at the previous time step. Forwards difference methods subtract the solution to the current step from that of the next step and central difference methods use an averaged forward and backward step method. Higher order accuracy can be obtained through the use of the Crank-Nicholson method or implicit 3-level methods. The Crank-Nicholson method for solution is based on the trapezoidal rule for integral approximation for transient terms and the central difference method for spatial terms, creating an implicit method which still stores 2 levels of information but gives second order temporal convergence. A 3 level method involving the present, and two previous time steps can be defined by

$$\frac{\partial\theta}{\partial t} = \frac{3\theta^{t+\triangle t} - 4\theta^{t} + \theta^{t-\triangle t}}{2 \triangle t} = F(\theta), \tag{2.15}$$

where $t - \triangle t$ is the value at the previous time step. This method is easy to implement but has a larger truncation error than the Crank-Nicholson method and the extra level of information increases memory usage. The version of Fluent solving software used in this study prevents the trivial application of the Crank-Nicholson method.

2.2.4.2 Spatial Discretisation

The spatial components are converted into a sum of discrete equations for every face of an element. For the continuity equation this can be written

$$\sum_{f}^{N_{faces}} \rho_f \vec{v}_f \cdot \vec{A}_f = 0 \tag{2.16}$$

and for conservation of momentum

$$\sum_{f}^{N_{faces}} \rho_f \vec{v_f} \vec{v_f} \cdot \vec{A_f} = \sum_{f}^{N_{faces}} pI \cdot \vec{A_f} + \sum_{f}^{N_{faces}} (\mu \cdot (\bigtriangledown \vec{v})_n) \cdot \vec{A_f} + S_{\vec{v}} V, \tag{2.17}$$

where $\vec{v_f}$ is the velocity vector at face f and$\vec{A_f}$ is the surface area vector of face f. The scalar values are stored at the centre of each element. For first order accuracy, the face value of a variable can be assumed to be the value stored at the element centre. Fluent uses an upwind scheme whereby the value at a given face of a finite volume is taken to be the value at the centre of the volume immediately upstream. Computing face values at higher order accuracies requires an algorithm which interpolates face values and gradients by averaging the values of the surrounding elements. The second-order upwind scheme used by Fluent to compute element face values can be described for a scalar variable θ via

$$\theta_f = \theta_c + \nabla \theta_c \cdot \Delta \vec{s} \tag{2.18}$$

where θ_c is the element centre value of the variable, $\nabla \theta_c$ is the gradient between the cell centre value and the value of the cell immediately upstream (hence 'upwind' scheme) and $\Delta \vec{s}$ is the displacement vector giving the shortest distance between the upstream cell centre and the element face. Fluent also offers a bounded central-differencing method of calculating face values from averaged upstream and downstream cells. The bounding is required as the central-differencing scheme alone can lead to unbounded solutions and artefacts. The central-differencing scheme and is detailed in Chapter 3 since the choice of this algorithm is dependent on how turbulence is modelled. For higher order solutions, the QUICK scheme offers a method for finding θ_f through quadratic interpolation of upstream and downstream volumes. The QUICK scheme is best suited to structured grids, though Fluent can apply it to unstructured grids also. Higher-order schemes are also available, but the improvements in accuracy have been assumed to be outweighed by the increase in computational resources required and have therefore been omitted from this study.

2.2.5 Solver Variables

A pressure based implicit solver scheme was used for modelling flow in generic AAAs. A node-based gradient solving approach was implemented whereby the variables stored at the element centres are used to calculate values at the element nodes which are in turn used to solve the

discrete N-S equations. A node-based approach adds extra calculations to the solution but the higher number of data points theoretically leads to a more accurate solution.

2.2.5.1 Pressure-velocity coupling

Solving the discretised N-S equations in Fluent requires the continuity equation be used to obtain values of pressure. Equation 2.7 shows that the continuity equation does not contain an explicit pressure term and so to introduce pressure, a pressure-velocity coupling algorithm must be used. These algorithms work via an iterative process whereby for transient simulations; the velocity and pressure at the proceeding timestep are estimated using the current values, the momentum equations are solved to provide an intermediate velocity field, a pressure-correction equation is applied and the corrected pressure is used to obtain a corrected velocity field which satisfies the continuity equation. This process is repeated until the pressure correction is within acceptable bounds before advancing to the next timestep.

In this study the SIMPLE (Semi-Implicit Method for Pressure-Linked Equations) pressure-velocity coupling algorithm was used. The PISO (Pressure Implicit with Splitting Operators) pressure-velocity coupling algorithm offers corrections to the algorithm which are not built into the standard SIMPLE model and which would normally make it the candidate algorithm for transient flow simulations. Due to the small timestep sizes used in this study, it was decided that the advantages in accuracy of the PISO algorithm would not be worth the excess computational expense required for the extra calculations and so the SIMPLE algorithm was preferred.

2.2.5.2 Accuracy of Discretisation

The methods of discretisation must also be chosen. Wherever possible, second order accuracy was preferred in this respect. Second order discretisation methods were chosen for modelling the temporally dependant aspects of the N-S equations (see equation 2.15) and the pressure discretisation. The approach to be used for the discretising of the momentum equation cannot be decided until the turbulence model used is determined, which will be the focus of Chapter 3. For the purposes of calibration, a second-order discretisation approach is used here.

2.2.6 Convergence Index

Reducing the density of a finite volume mesh will in turn increase the average element size. Solving the equations of flow over a larger volume increases the relative error throughout the simulation, especially in the presence of non-linear flows. Increasing mesh density requires an increase in processing power and time taken to complete simulations. With current constraints in computing power, a balance must be made between computational efficiency and the error present in a simulation. It is therefore important to ascertain the level of error present in a given grid density. When defining FVM techniques there are currently few gold standards in terms of model calibration, however Roache et al [138] propose a system for assessing the relative errors involved in refining variables. This technique is used here to calibrate mesh refinement in steady and pulsatile flows and time step size in transient flow.

A scalar variable is required as a cohort in which the magnitude of error is determined. Since WSS plays an integral part in leukocyte adhesion and therefore an important variable in this study it is used in refinement studies throughout this chapter. Three separate simulations are required for each parameter under investigation, in which the parameter is increasingly refined. Below, the techniques used by Roache [138] are applied to a grid refinement study. A coarse, medium and fine grid are modelled and WSS recorded at discrete points in each. The order of accuracy of convergence is evaluated via

$$p = \ln\left(\frac{m_3 - m_2}{m_2 - m_1}\right) / \ln\left(r\right) \tag{2.19}$$

where m_n is the solution of a given variable on mesh n and r is the refinement ratio. Ideally, convergence of at least second order is preferred in this study. Estimations of error for each grid can then be calculated via

$$\epsilon = \frac{m_1 - m_2}{m_1} \tag{2.20}$$

which can be translated into a scale of error magnitude in terms of the grid convergence index (GCI) via

$$GCI_{fine} = \frac{F_s \epsilon}{r^p - 1} \tag{2.21}$$

$$GCI_{coarse} = \frac{F_s \epsilon r^p}{r^p - 1} \tag{2.22}$$

Where F_s is a safety factor added to counter uncertainty in convergence. In this study a safety factor of $F_s = 1.25$ is used [139]. The GCI provides an error band which can be used to analyse

confidence in simulation results and can be calculated post-simulation allowing a comparison of GCI between investigations. The WSS obtained with an infinitely small mesh size can be estimated via a Richardson extrapolation of the three mesh sizes defined by

$$m_0 = m_1 + \frac{m_1 - m_2}{r^p - 1}. \tag{2.23}$$

Defining an asymptotic range of convergence provides a quantitative value based on GCI from which grid density can be judged to be sufficient for modelling. The asymptotic range of convergence is achieved when

$$\frac{GCI_{23}}{r^p GCI_{12}} \simeq 1 \tag{2.24}$$

2.2.7 Mesh

When splitting the geometry into a mesh of finite volumes, the number of elements used must strike a balance between the accuracy of simulation and the computational effort involved. Using simple geometries permits the use of simplified meshing which in turn increases the efficiency of computation. The smooth geometries allow larger mesh elements to be used more effectively when compared with complex patient specific geometries and provide a reduction in skewed and irregular mesh elements. To resolve the number of elements required for an effective balance, a mesh independence study was performed.

2.2.7.1 Mesh Convergence Steady Flow

The grid convergence index method outlined in section 2.2.6 was used to assess the relative errors arising from the use of differing mesh densities. The three mesh densities were created by dividing the perimeters of the inlet and outlet faces into 30, 60 and 120 mesh points. The use of perimeter meshing to define the mesh refinement index has previously been used by Varghese and Frankel [172]. Both faces were meshed using a paved quad scheme and the volume of the geometry then meshed with hex elements based on the inlet and outlet meshes. This created volume meshes with $n1 = 10540$, $n2 = 83820$ and $n3 = 731162$ elements. Since WSS is a sensitive variable which is integral to this study, the magnitude of WSS in steady flow at the cavity centre-point was used as the m value and recorded at the central point of the cavity in the $D = 2.1d$ and $D = d$ models. The inlet flow was set to a Reynolds number of 900, a mid-range value for aortic flow [9]. By comparing all 3 mesh densities using the Roache refinement

method, the WSS at m_∞ can be obtained and the GCI for the fine grid determined.

2.2.7.2 Mesh Convergence Pulsatile Flow

To investigate grid convergence in pulsatile flow, the fully developed Womersley inlet flow profile boundary condition was applied to the $D = 2.1d$ geometry discretised into the 3 mesh densities used for analysing steady flow ($n1$, $n2$ and $n3$). A time step size of T/100 (4.281×10^{-3} seconds) was used. To study grid density convergence on a diverse array of flow dynamics, data was collected from time points corresponding to mid systole (t=16T/100) and the end of diastole (t=T) at central and distal points on the wall (z=0 and 0.038m). All measurements were taken on the third pulsatile cycle to allow for cycle independence to occur. Contours of velocity were defined for the fine and coarse meshes at both time points to visually portray the effects of grid refinement. WSS values for m_∞ were determined and the GCI for each of the fine grid densities derived.

2.2.8 Transient Flow Calibrations

When simulating pulsatile flow, the solutions must be assessed to determine whether they are independent of the size of the time step $\triangle t$ and that solutions are the same over consecutive pulsatile cycles. If the time step is too large there is a risk that subtleties in the flow dynamics occurring between time steps will be discounted. If it is too small the computational effort required becomes unfeasible.

Secondary flows, such as the vortices present in AAAs, often overlap between cycles which prevents the dynamics of the flow from being discretely packaged into individual cycles. It often takes a number of cycles before the flow becomes completely cycle independent and so pulsatile flow simulations must be assessed to discover when cycle independence occurs.

2.2.8.1 Time Step Convergence

To assess time step independence, the convergence method was extended to use time step size ($\triangle t$) in place of grid density. Model $D = 2.1d$ was meshed with grid density $n3$ and simulated using $\triangle t$ values of T/50 (1.8562×10^{-2} seconds), T/100 (9.281×10^{-3} seconds) and T/200 (4.6405×10^{-3} seconds), giving a time step refinement ratio of $r = 2$. Values of WSS were used as the variable for comparison with data taken from points on the wall at the the cavity

centre and at the distal end of the cavity with time points at the end of diastole (t=0) and mid systole (t=16T/100) on the third pulsatile cycle. GCI was calculated using equations 2.21 and 2.22 and the asymptotic range of convergence was calculated using equation 2.24

2.2.8.2 Cycle Independence

Using AAA geometry, $D = 2.1d$ with grid $n3$ and $\triangle t = T/200$, longitudinal Z-directional WSS profiles were obtained every tenth of a cycle over four pulsatile cycles. By comparing profiles between cycles, cycle independence can be ascertained.

2.2.9 Unsteady Solver Order

Higher order solutions are generally assumed to increase simulation accuracy, especially in complex flows, though this comes at the cost of the increased processing power required. First and second order unsteady solvers were compared by observing longitudinal plots of z-directional WSS magnitude at timepoints throughout the cardiac cycle and recording the time taken to solve a pulsatile cycle. If the difference in WSS is sufficiently small and the saving in simulation time sufficiently large, a first order solver will be chosen above the current second order solver.

2.2.10 Boundary layer

This study models the behaviour of individual cells in flow and so to acheive this flow must be resolved on a scale of the same order of magnitude as the cells. Monocytes have an average diameter of $16\mu m$, much smaller than the mesh elements described above (450-500 μm). To mesh the whole geometry with a $10\mu m$ grid would require large amounts of computational effort. Such a mesh would be unnecessary as the difference in densities between monocytes and whole blood (see Chapter 4) is such that for the bulk of the flow it is assumed that cell motion will not deviate significantly from that of the underlying flow and so can be resolved at the given mesh density. The focus of this study is simulating the adhesion of cells to the artery wall and obtaining accurate values of WSS. At the near-wall region it becomes necessary to model both flow and cell dynamics at a cell-diameter scale. A boundary layer of hex elements was added to the mesh at the near-wall region. These elements get progressively smaller nearer to the wall. Details of the boundary layer are given in table 2.2.

First layer height	30μm
Growth Factor	2
Number of Rows	4
Total Depth	450μm

Table 2.2: *Boundary Layer Properties*

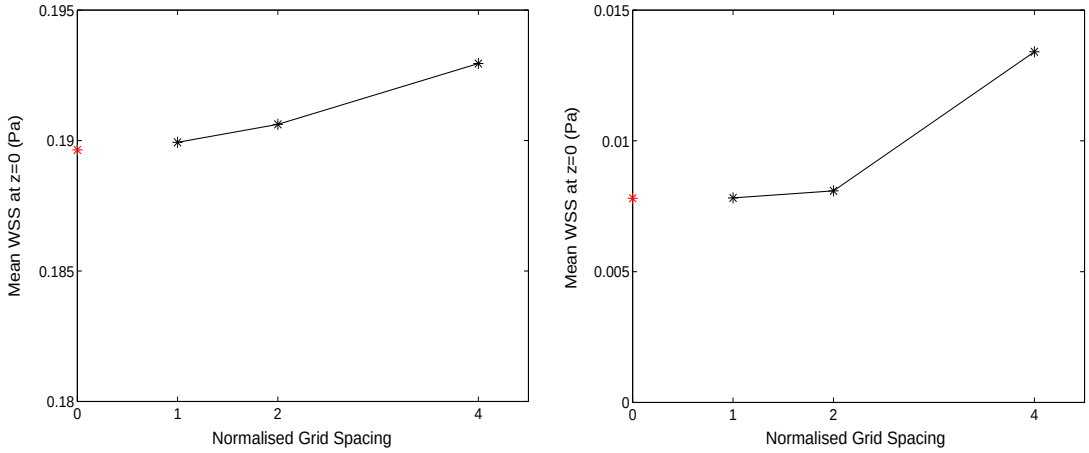

(a) Model D=d, p=4.317, $GCI_{12} = 0.225\%$ (b) Model D=2.1d, p=1.7567, $GCI_{12} = 0.191\%$

Figure 2.6: *Mesh convergence plots for steady flow at cavity centre*

2.3 Results

2.3.1 Mesh Refinement

2.3.1.1 Steady Flow

Figures 2.6(a) and 2.6(b) show that for the 120 point perimeter mesh, corresponding to a normalised grid spacing of 1, GCI for both models is within the asymptotic range of convergence (range of convergence is 0.996 for $D = d$, 0.967 for $D = 2.1d$). This implies that grid $n3$ (containing 731162 elements) is a sufficient density to efficiently solve the steady flow to at least a second order degree of accuracy.

2.3.1.2 Pulsatile Flow

The velocity contour plots in figure 2.7 show that refining the grid changes vortex dynamics in the aneurysm at the end of diastole. During the higher inlet flows of mid systole the differences are less extreme though still noticeable, as described in figure 2.9. When defining the order of

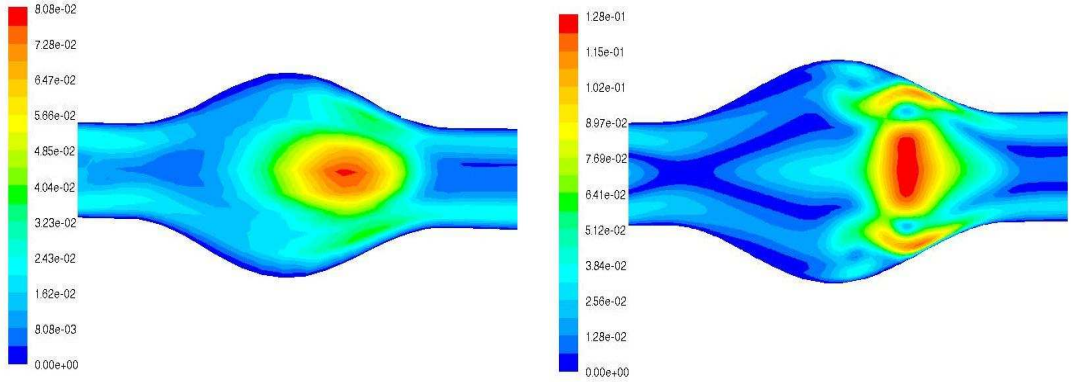

(a) Normalised Grid Density = 4 (b) Normalised Grid Density = 1

Figure 2.7: *Contours of velocity magnitude (m/s) at time* $T/t = 0$

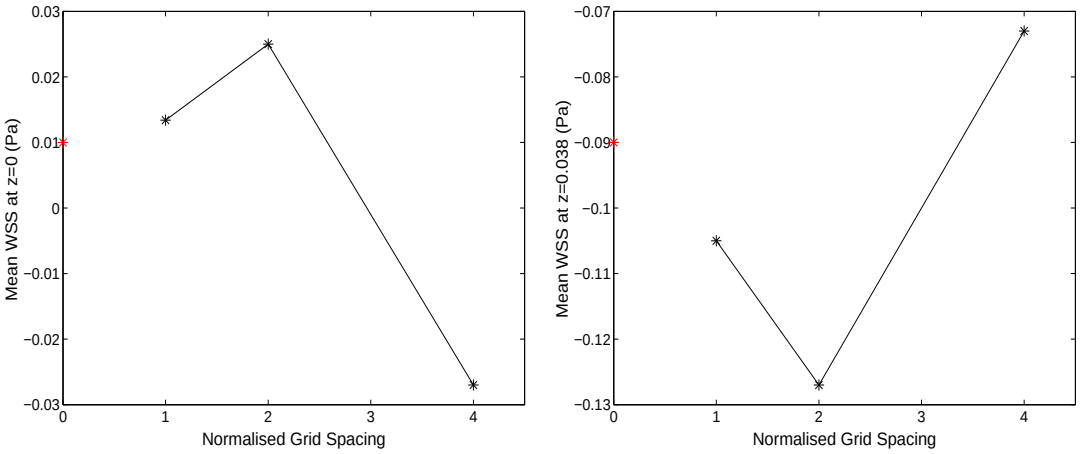

(a) Distance from centre z = 0m ($GCI_{12} = 34\%$) (b) Distance from centre z = 0.038m ($GCI_{12} = 8.7\%$)

Figure 2.8: *Pulsatile flow mesh convergence at time* $T/t = 0$

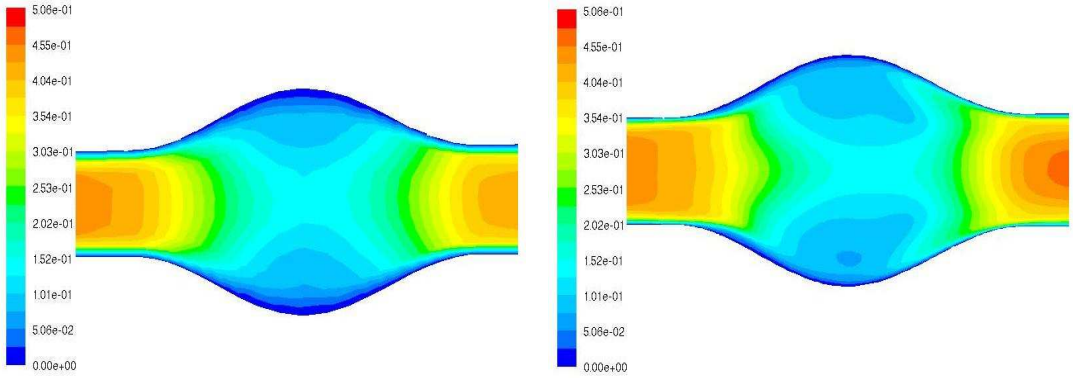

(a) Normalised Grid Density = 4 (b) Normalised Grid Density = 1

Figure 2.9: *Contours of velocity magnitude (m/s) at time* $T/t = 0.08$

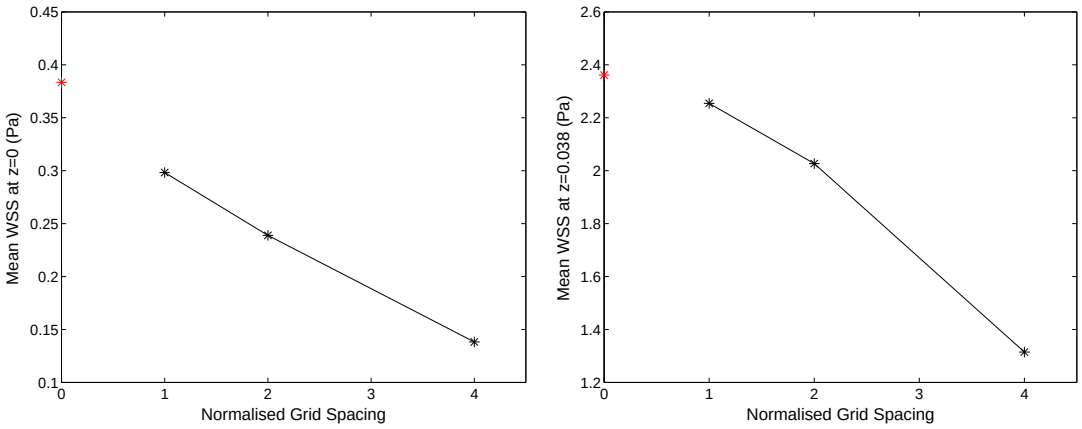

(a) Distance from centre z = 0m ($GCI_{12} = 8.3\%$) (b) Distance from centre z = 0.038m ($GCI_{12} = 4.2\%$)

Figure 2.10: *Pulsatile flow mesh convergence at time* $T/t = 0.08$

mesh convergence for pulsatile flow, the computed p values for points towards the distal end of the cavity vary significantly from the ideal value of 2, possibly because the reattachment point changes with grid refinement as observed in figure 2.9 and described below. Because of this the convergence order used to extrapolate WSS on an infinitely small grid (m_0) was set to 2, a reasonable assumption [138] since the solver is set to second order. By applying a pre-defined value to p, the value of m_3 is excluded from the calculation of m_0 and so grid convergence cannot be ascertained in this instance. The original convergence indices with p defined by the WSS values have been included in Appendix A for comparison. The shift in vortex reattachment points during diastole caused by grid refinement creates the fluctuations in WSS magnitude observed in figures 2.8(a) and 2.8(b) which may lead to the significantly large GCI of 34% observed at the cavity centre (figure 2.10). The systolic values (figure 2.10) show a more linear convergence, though the GCI magnitudes (8.3% and 4.2%) are still outside of the asymptotic range of convergence. Large differences in error magnitude indicate that a finer grid may be required. The computational power required to solve a grid with normalised grid spacing of 0.5 (over 6 million elements) would not be feasible.

Refining the time step $\triangle t$ may reduce the magnitude of error. One solution is to apply adaptive meshing whereby points of interest or areas which require higher degrees of accuracy in solving are given a finer mesh density. Accuracy in obtaining WSS is necessary and so the near-wall region is of significant interest. The addition of a boundary layer of fine elements near to the wall should increase the solver accuracy in the near wall area. The inclusion of a near wall boundary layer is also beneficial in turbulence modelling, investigated in Chapter 3, and in accurately modelling particle behaviour near the wall.

2.3.2 Time Step Refinement

As in the diastolic pulsatile flow grid convergence, the WSS values for the timestep sizes used do not appear to converge (figures 2.12 and 2.14). During diastolic flow this may be due to changes in the flow reattachment regions between timestep sizes. It may also be that timestep m_3 is too long to provide reasonable simulation. The order of convergence p used to define m_0 has been fixed at 2, which excludes m_3 from the calculation. To determine the extent of timestep convergence, further trials are required using a normalised timestep of 0.5.

Figures 2.12(b) and 2.14(b) show the timestep convergence index values are low for values at the distal end of the aneurysm (1.58% during mid systole, 1.025% at the end of diastole)

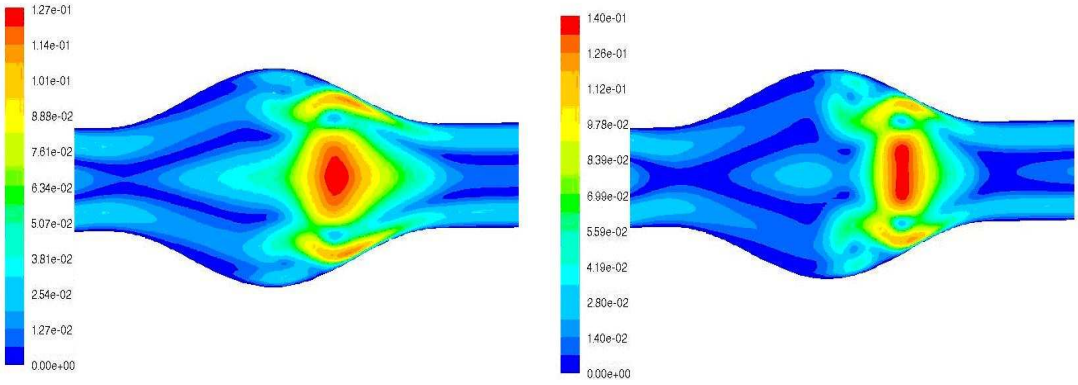

(a) $\triangle t = 1.8562 \times 10^{-2}$ (b) $\triangle t = 4.6405 \times 10^{-3}$

Figure 2.11: *Contours of velocity magnitude (m/s) at time* $T/t = 0$

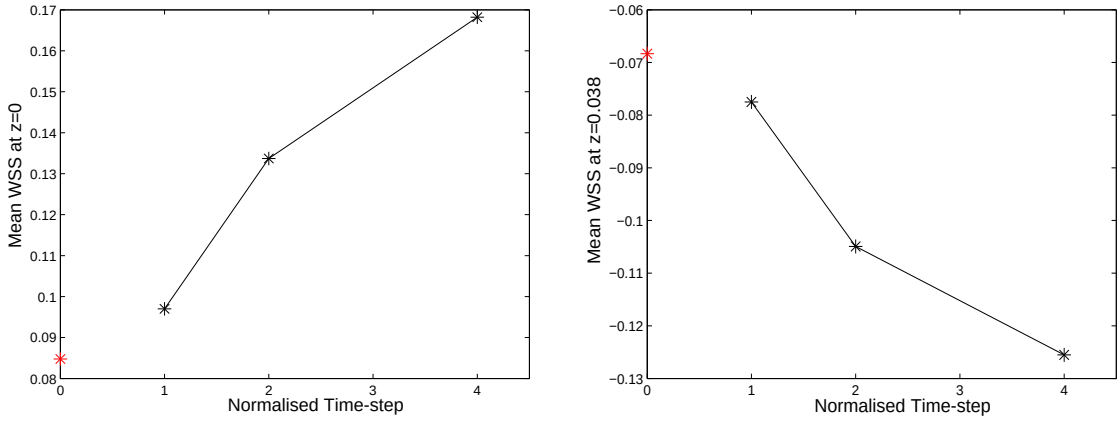

(a) Distance from centre z = 0m ($GCI_{12} = 15.46\%$, Error Convergence=0.713) (b) Distance from centre z = 0.038m ($GCI_{12} = 1.58\%$, Error Convergence=1.5738)

Figure 2.12: *Timestep convergence at time* $T/t = 0$

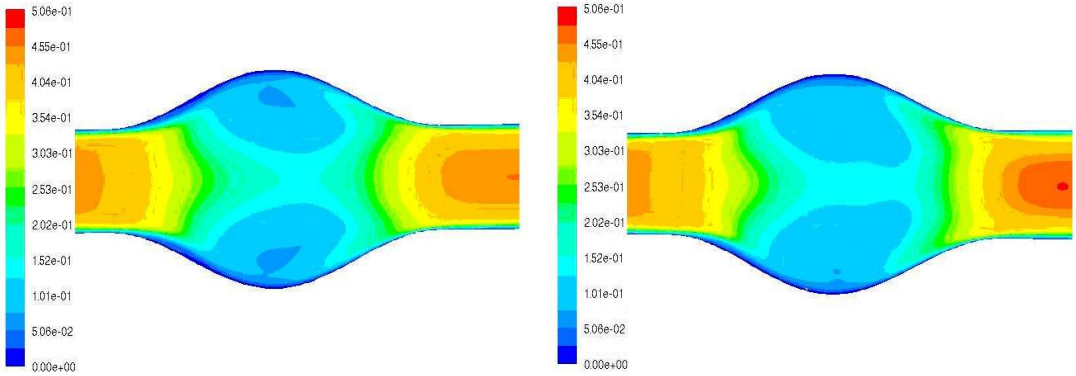

(a) $\triangle t = 1.8562 \times 10^{-2}$ (b) $\triangle t = 4.6405 \times 10^{-3}$

Figure 2.13: *Contours of velocity magnitude (m/s) at time* $T/t = 0.08$

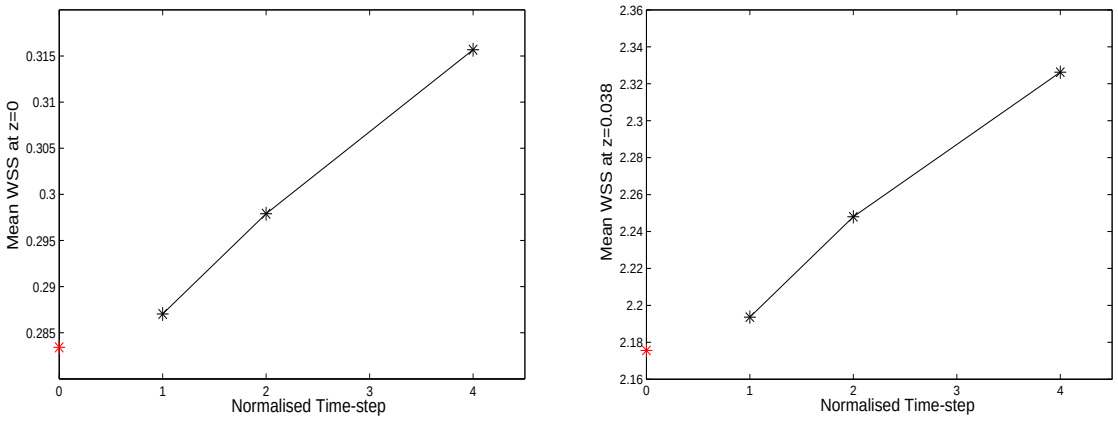

(a) Distance from centre z = 0m ($GCI_{12} = 14.78\%$, Error Convergence=0.55) (b) Distance from centre z = 0.038m ($GCI_{12} = 1.025\%$, Error Convergence=1.41)

Figure 2.14: *Timestep convergence at time* $T/t = 0.08$

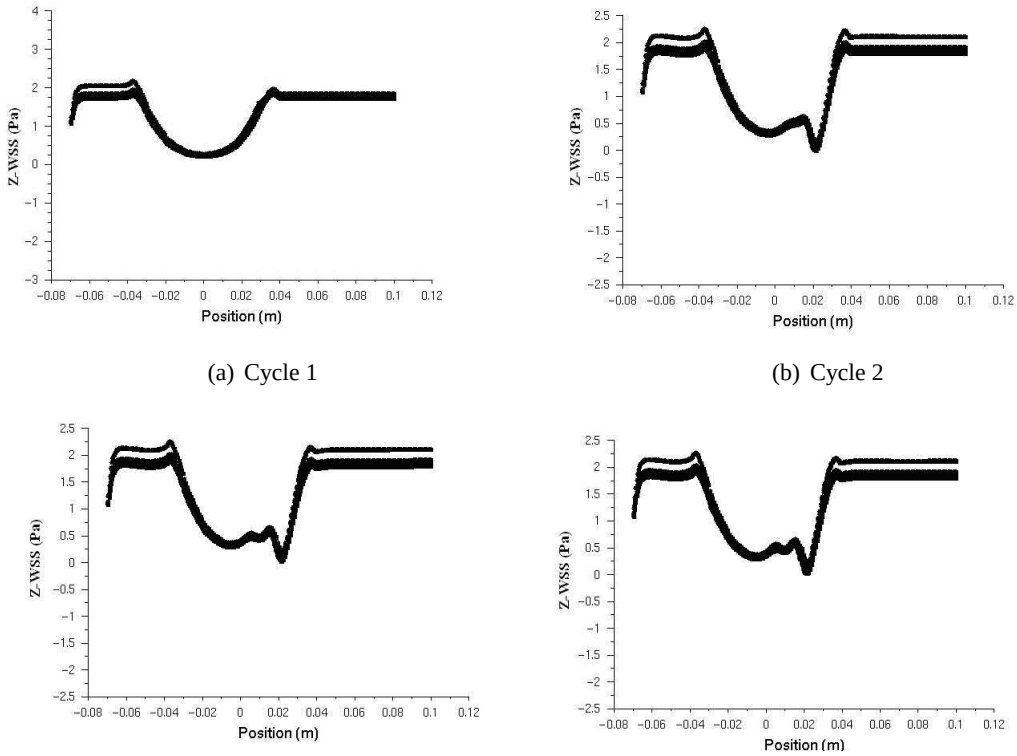

(a) Cycle 1

(b) Cycle 2

(c) Cycle 3

(d) Cycle 4

Figure 2.15: *z-WSS plots at* $T/t = 0.2$ *over 4 cardiac cycles*

while figures 2.12(a) and 2.14(a) show higher values at the AAA cavity centre (both around 15%). This is similar to the findings of the pulsatile mesh convergence study and so higher error values may be associated with changes in vortex reattachment points. The average of the 4 error convergence rates (equation 2.24) is 1.0615 which is within the asymptotic rate of convergence and so a time step of $\triangle t = T/200$ using a grid of at least 731162 elements will be sufficient for use in this study. The inclusion of a near-wall boundary layer will further decrease the convergence index values.

2.3.3 Cycle Independence

With the exception of the first time point (T/10) all WSS profiles show cycle independence by the second cycle. For that reason, only results for T/10 are shown in figure 2.15. While there are minor differences in WSS between cycles 2 and 3 at the first time point, there are no such differences between cycles 3 and 4 at the same time point and so the simulation can be said to be entirely cycle independent by the third cycle.

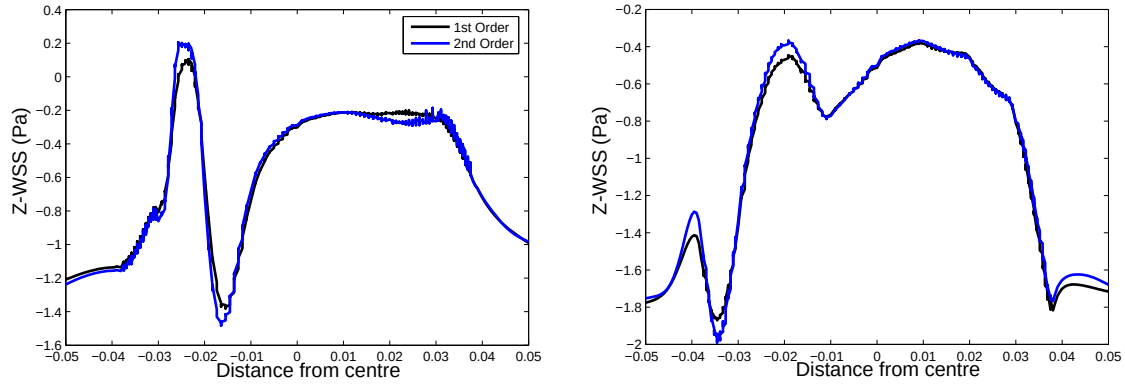

(a) time $T/t = 0.3$ (b) time $T/t = 0.4$

Figure 2.16: *Longitudinal Z-WSS plots using transient solvers with 1st and 2nd order accuracy*

2.3.4 Unsteady Solver Order

The largest differences in WSS between orders were found at timesteps T/t=40 and T/t =60, corresponding to the deceleration phase (figures 2.16(a) and 2.16(b)). At these points, both first and second orders follow the same trends in WSS but the first order model produces more blunted peaks in WSS. Maximum and minimum WSS differ by around 0.1 Pa between orders which is 6% of the total WSS range for the second order model at both timesteps. Since there is very little difference in patterns of WSS between the orders, these differences in maximum and minimum WSS could be overlooked if there is a substantial saving in processing time by using a first order model. The difference in time taken to solve a full cardiac cycle was similar for both the first and second order solvers and so the second order solver is used throughout this study.

2.4 Discussion and Conclusions

Generic AAA models were created based on physiologically realistic dimensions. A range of geometries were created from a straight tube modelling the healthy aorta to a fully developed aneurysm, simulating various stages of aneurysm development. The geometries were meshed in Gambit software using a structured quad mesh and exported to Fluent for solving with an implicit finite volume solver with second order temporal and momentum solvers and SIMPLE pressure-velocity coupling. A patient averaged flow wave form defined by Fraser [46] was

converted to fully developed Womersley velocity profiles and attached as an inlet boundary condition. Meshing and time step parameters were found which produce results independent of grid size, time step and fully cycle dependent by the third cycle. The finest mesh density feasible (731162 elements) was sufficiently accurate in steady flow conditions but outside of the required convergence criteria in pulsatile flow. This was not unexpected as previous studies [86] have failed to reach a sufficient convergence for WSS using meshes far finer than would be computationally feasible in this study. The convergence error was reduced by refining the time step size and a convergence investigation using the fine mesh model found that a $\triangle t$ of T/200 (4.6405×10^{-3} seconds) reduced the magnitude of error to within the asymptotic range of convergence, making it sufficient for the purposes of this study. Further study is required to examine the nature of grid and timestep convergence. A more rigorous grid and timestep refinement study would use normalised spacing 0.5, or possibly even finer if the variables are still not found to converge. In order to prepare the AAA models for turbulence and particle motion simulation, a fine near-wall boundary layer of elements is necessary. Applying a boundary layer will further reduce errors in WSS estimation.

Chapter 3
Turbulence Investigation

3.1 Introduction

AAAs experience a transition to turbulence during the deceleration phase of the cardiac cycle [191]. Turbulent flows affect patterns in WSS as well as endothelial cell and leukocyte behaviour as discussed in Chapter 1. It is therefore important when modelling arterial blood flow and the motion of white blood cells that turbulent effects should be accounted for through the use of a turbulence model. A wide range of numerical turbulence models exist however there have as yet been no investigations into which models are appropriate for modelling turbulence in AAA disease in terms of accuracy and computational efficiency. In this chapter velocity and WSS magnitudes in AAAs with steady and pulsatile flow regimes are obtained to investigate the effectiveness of commonly used turbulence models. The aims of this chapter are to compare each of the turbulent models with experimental results to validate their accuracy and to observe the differences in haemodynamics arising from the use of different methods of modelling turbulence.

3.2 Turbulence models

Due to the importance of obtaining accuracy in turbulence modelling and the variety of flow regimes which encounter turbulence, there are a variety of turbulence models available. Some of the models most appropriate for modelling blood flow in a large artery are reviewed below. These models can be broken down into direct simulation, Reynolds-averaged Navier-Stokes (RANS) models and large eddy simulation (LES) models.

3.2.1 Direct Numerical Simulation (DNS)

Turbulent perturbations can be solved directly via the Navier-Stokes equations, negating the need for a specific turbulence model. To achieve the required accuracy, turbulent eddies must

be solved down to the smallest microscale. Using FVM would require the size of all volumes within the turbulent region to be on the order of the Kolmogorov microscale defined by $\eta = \left(\nu^3/\epsilon\right)^{1/4}$. This method of direct numerical simulation (DNS) requires the least modelling assumptions and so should provide a high degree of accuracy but the fine meshes required are generally not computationally viable with the efficiency and computing power of current technology. A review by Moin and Mahesh [106] suggests that for moderate Reynolds number flows in transition to turbulence, DNS modelling is achievable for macroscopic measurements. Recent studies using spectral element methods have modelled flow in an idealised stenosis with maximum Reynolds numbers of around 1000 [173, 174]. The higher Reynolds numbers encountered in the aorta make DNS prohibitively computationally demanding for this study.

3.2.2 Reynolds-averaged Navier-Stokes (RANS) Models

Difficulties presented by turbulence modelling arise when the length of turbulent eddies are smaller in scale than the elements used to model the flow. RANS methods offer a way of bypassing the need to directly solve small-scale turbulent perturbations by adding averaged flow transport equations to the Navier-Stokes equations. The components of velocity and pressure are split into an ensemble-averaged or time-averaged component and a fluctuating component. For velocity this can be written

$$u_i = \bar{u}_i + u_i', \tag{3.1}$$

where $\bar{u}_i$ is the mean and u_i' the fluctuating velocity component.

If the flow is statistically steady, $\bar{u}$ is found by taking a time-average of the equations of motion. It can also be averaged over a specific point in space if the mean flow in that region does not vary with time. The unsteady cardiac cycles used in this study are not statistically steady and mean flow varies on a timescale below that of the cardiac cycle. $\bar{u}$ and $\bar{p}$ are calculated via ensemble averaging. The ensemble average is found by taking the mean of an ensemble of all the possible states of a system at a point in time

$$\bar{u}_i = \lim_{N\to\infty} \frac{1}{N} \Sigma_{n=1}^{N} u_i \tag{3.2}$$

where N is the number of members of the ensemble. The number of different states used must be large enough to eliminate the effect of turbulent perturbations.

Substituting these equations back into the original Navier-Stokes equations for incompress-

ible flow (equations 2.8-10) and converting them to Cartesian tensor form gives the continuity equation

$$\frac{\partial \rho}{\partial t} + \frac{\partial}{\partial x_i}(\rho \bar{u_i}) = 0, \tag{3.3}$$

and the momentum equation

$$\rho \frac{D\bar{u}_i}{Dt} = -\frac{\partial \bar{p}}{\partial x_i} + \frac{\partial}{\partial x_j}\left[\mu\left(\frac{\partial \bar{u_i}}{\partial x_j} + \frac{\partial \bar{u_j}}{\partial x_i}\right)\right] + \frac{\partial}{\partial x_j}(-\rho\overline{u_i' u_j'}), \tag{3.4}$$

where $-\overline{u_i' u_j'}$ are the Reynolds Stresses, which relate to the time averaged rate of turbulent momentum transfer and are solved via the turbulence modelling methods below. Using averaged variables reduces the computational effort needed to solve the equations.

3.2.3 One and Two Equations models

The most computationally efficient turbulence modelling methods are one and two equation models. A Reynolds-Averaged Boussinesq approach is used which assumes that the mean velocity gradients which form the Reynolds stress tensor are proportional to the mean strain rate. This can be expressed for incompressible flow as

$$-\rho\overline{u_i' u_j'} = \mu_t\left(\frac{\partial u_i}{\partial x_j} + \frac{\partial u_j}{\partial x_i}\right) - \frac{2}{3}\rho\kappa\delta_{ij}, \tag{3.5}$$

which can be further simplified to

$$\tau_{ij} = 2\,\mu_t\,S_{ij} + \frac{2}{3}\rho k\delta_{ij}, \tag{3.6}$$

where μ_t is the turbulent viscosity which must be solved, τ_{ij} is the Reynolds strain tensor and S_{ij} the strain rate tensor. Equation 3.5 also introduces κ the turbulent kinetic energy defined as $\kappa = \overline{u_i' u_j'}/2$. One and two equation models apply extra transport equations to solve the transport of turbulent energy. While turbulence models have evolved rapidly over the past few years leading to the production of complex mathematical models, the basic transport equations for a given variable θ can be simplified to

$$\underbrace{\rho\frac{D\theta}{Dt}}_{\text{Transient and convected terms}} = \underbrace{\frac{\partial}{\partial x_j}\left(\Gamma_\theta \frac{\partial \theta}{\partial x_j}\right)}_{\text{Diffusion term}} + \underbrace{P_\theta}_{\text{Production of } \theta} + \underbrace{D_\theta}_{\text{Dissipation of } \theta} + \underbrace{S_\theta}_{\text{Other source terms}} \tag{3.7}$$

3.2.3.1 The Spalart-Allmaras Model

The Spalart-Allmaras model is a simple, single equation model which solves a transport equation for kinematic eddy viscosity (μ_t/ρ). The Spalart-Allmaras model requires little computational effort as it adds only one additional equation but is generally applied to coarse meshes to gain a rough measure of turbulence [153].

3.2.3.2 $\kappa - \epsilon$ Models

$\kappa - \epsilon$ models require the solution of only two extra equations making them relatively computationally efficient and more robust than single equation modelling. By solving the transport of turbulent kinetic energy (κ) and turbulent dissipation (ϵ), the velocity and length scale of turbulence can be obtained. As in the Spalart-Allmaras model, a Boussinesq approach is employed using κ and ϵ to determine turbulent viscosity. The equation for transport of turbulent kinetic energy in the standard $\kappa - \epsilon$ model can be written

$$\rho\frac{D\kappa}{Dt} = \frac{\partial}{\partial x_j}\left[\left(\mu + \frac{\mu_t}{\sigma_\kappa}\right)\frac{\partial \kappa}{\partial x_j}\right] + \tau_{ij}\frac{\partial \bar{u}_i}{\partial x_j} - \rho\epsilon, \tag{3.8}$$

and transport of ϵ

$$\rho\frac{D\epsilon}{Dt} = \frac{\partial}{\partial x_j}\left[\left(\mu + \frac{\mu_t}{\sigma_\epsilon}\right)\frac{\partial \epsilon}{\partial x_j}\right] + C_{\epsilon 1}\frac{\epsilon}{\kappa}\tau_{ij}\frac{\partial \bar{u}_i}{\partial x_j} - \left(C_{\epsilon 2} + R\right)\rho\frac{\epsilon^2}{\kappa}, \tag{3.9}$$

For the standard $\kappa - \epsilon$ model, coefficient $R = 0$ and turbulent viscosity is obtained via the relationship

$$\mu_t = \rho C_\mu \frac{k^2}{\epsilon}. \tag{3.10}$$

$\kappa - \epsilon$ models have evolved to produce more accurate forms including the RNG $\kappa - \epsilon$ model [190] which applies an approach termed 'renormalisation group theory' to the standard model which enhances its accuracy for modelling swirling flows. For the RNG $\kappa - \epsilon$ the coefficient R

in equation 3.9 is defined as

$$R = \frac{C_\mu \eta^3 \left(1 - \frac{\eta}{\nu_0}\right)}{1 + \beta\eta^3}, \tag{3.11}$$

where $\nu = (\kappa/\epsilon)\sqrt{2S_{ij}S_{ji}}$, $\nu_0 = 4.38$ and $\beta = 0.012$. At low Reynolds numbers the RNG $\kappa - \epsilon$ model solves the turbulent viscosity through the differential equation

$$d\left(\frac{\rho^2 k}{\sqrt{\epsilon\mu}}\right) = 1.72\frac{\hat{\nu}}{\sqrt{\hat{\nu}^3 - 1 + C_\nu}}d\hat{\nu}, \tag{3.12}$$

where $\hat{\nu} = \mu_{\text{eff}}/\mu$ and $C_\nu \approx 100$. At high Reynolds numbers this gives equation 3.10.

3.2.3.3 $\kappa - \omega$ models

$\kappa - \omega$ models are similar to $\kappa - \epsilon$ models in that they require the solution of two extra transport equations. The kinematic turbulent viscosity (μ_t ρ) is assumed to be a function of turbulent kinetic energy and specific dissipation rate (ω), solutions to which are found using derivations of the Boussinesq approach.

The equation for kinetic energy transport used by the standard $\kappa - \omega$ model is similar to that used in the $\kappa - \epsilon$ model with the ϵ term replaced by a function combining turbulent kinetic energy with the specific dissipation rate $\omega = \epsilon/\kappa$. The model used by Fluent is based on the form derived by Wilcox in 2006 [184].

$$\rho\frac{D\kappa}{Dt} = \frac{\partial}{\partial x_j}\left[\left(\mu + \frac{\mu_t}{\sigma_\kappa}\right)\frac{\partial\kappa}{\partial x_j}\right] + \tau_{ij}\frac{\partial\bar{u}_i}{\partial x_j} - \rho\beta_0^* f_{\beta^*}\kappa\omega. \tag{3.13}$$

The transport equation for ω is defined

$$\rho\frac{D\omega}{Dt} = \frac{\partial}{\partial x_j}\left[\left(\mu + \frac{\mu_t}{\sigma_\omega}\right)\frac{\partial\omega}{\partial x_j}\right] + \alpha\frac{\omega}{\kappa}\tau_{ij}\frac{\partial\bar{u}_i}{\partial x_j} - \rho\beta_0 f_\beta\omega^2, \tag{3.14}$$

where σ_κ and σ_ω are the turbulent Prandtl numbers which give the ratio of viscous diffusion rate to thermal diffusion rate. Modelling the dissipation of κ and ω and the production of ω is complicated by the introduction of coefficients β^*, f_{β^*}, α, β and f_β. where

$$\beta^* = \beta_\infty^*\left(\frac{4/15 + (\text{Re}_t/R_\beta)^4}{1 + (\text{Re}_t/R_\beta)^4}\right), \tag{3.15}$$

$$f_{\beta^*} = \begin{cases} 1 & \chi_k \leq 0, \\ \frac{1+680\chi_k^2}{1+400\chi_k^2} & \chi_k > 0. \end{cases} \tag{3.16}$$

$$\chi_k \equiv \frac{1}{\omega^3}\frac{\partial k}{\partial x_j}\frac{\partial \omega}{\partial x_j}, \tag{3.17}$$

$$\alpha = \frac{\alpha_\infty}{\alpha^*}\left(\frac{\alpha_0 + \mathrm{Re}_t/R_\omega}{1+\mathrm{Re}_t/R_\omega}\right), \tag{3.18}$$

$$\mathrm{Re}_t = \frac{\rho k}{\mu\omega}, \tag{3.19}$$

$$f_\beta = \frac{1+70\chi_\omega}{1+80\chi_\omega}, \tag{3.20}$$

$$\chi_\omega = \left|\frac{\Omega_{ij}\Omega_{jk}S_{ki}}{(\beta^*_\infty\omega)^3}\right|, \Omega_{ij} = \frac{1}{2}\left(\frac{\partial u_i}{\partial x_j} - \frac{\partial u_j}{\partial x_i}\right). \tag{3.21}$$

S_{ki} is the stress tensor. Turbulent viscosity is calculated via

$$\mu_t = \alpha^*\frac{\rho k}{\omega} \tag{3.22}$$

Where α^* is a low-Reynolds-number correction coefficient

$$\alpha^* = \alpha^*_\infty\left(\frac{\alpha^*_0 + \mathrm{Re}_t/R_\omega}{1+\mathrm{Re}_t/R_\omega}\right). \tag{3.23}$$

The values of further constants are given in table 3.3.1.

3.2.3.4 Limitations

The Boussinesq assumption linking Reynolds stress and mean strain rate greatly simplifies the solutions of turbulent flow. It is, however, only valid in certain simple flow regimes and therefore cannot be relied upon to give accurate solutions in complex flows where rotation and curvature effects are present. The complex secondary flows caused by vortex formation and dissipation in AAA disease may render the Boussinesq assumption invalid.

3.2.4 Large Eddy Simulation (LES)

LES models assume that while large turbulent eddies will be affected by the geometry and surrounding flow features, the smaller eddies are isotropic in nature as implied by Kolmogorov. Large eddies are solved numerically and smaller eddies are filtered out and modelled through the use of a sub-gridscale model. Filtering of sub-gridscale turbulence can be achieved implicitly by using the scale of the grid itself or explicitly depending on the sub-gridscale model used. Fluent filters turbulent eddies implicitly as a function of grid element volume.

Once filtered, the variables relating to the resolvable large eddies and fluctuating small eddies can be described in a similar notation to that used in the RANS method

$$\theta_i = \bar{\theta}_i + \theta'_i, \tag{3.24}$$

where $\bar{\theta}_i$ is the resolvable scale and θ'_i the subgrid-scale.

Substituting the resolvable components of these variables into the incompressible Navier-Stokes equations gives the following equation for the solution of large eddies

$$\rho\frac{D\bar{u}_i}{Dt} = -\frac{\partial\bar{p}}{\partial x_i} + \frac{\partial}{\partial x_j}\left[\mu\left(\frac{\partial\bar{u}_i}{\partial x_j} + \frac{\partial\bar{u}_j}{\partial x_i}\right)\right] + \frac{\partial\tau_{ij}}{\partial x_j}, \tag{3.25}$$

where τ_{ij} is the sub gridscale stress tensor defined by

$$\tau_{ij} \equiv \rho\overline{u}_i\overline{u}_j - \rho\overline{u_i u_j}. \tag{3.26}$$

The above equations are analogous to the RANS equation 3.4. As with the RANS equations, the Boussinesq hypothesis can be applied and the sub-gridscale velocity substituted into the filtered Navier-Stokes equation This creates a single equation for which turbulent viscosity must be obtained via a sub-gridscale turbulence model. The Boussinesq hypothesis is theoretically more accurate in this instance as the assumption that turbulent viscosity is isotropic is more realistic at sub-gridscale magnitudes. Fluent offers a range of models for solving sub-gridscale turbulent viscosity (μ_t). For this investigation the Smagorinsky-Lilly model [147] is used which solves turbulent viscosity via

$$\mu_t = \rho L_s^2\sqrt{2\overline{S}_{ij}\overline{S}_{ij}}, \tag{3.27}$$

where L_s is the sub-gridscale mixing length determined via

$$L_s = \min\left(Ky_w, C_s V_e^{1/3}\right), \tag{3.28}$$

where V_e is element volume, y_w is distance to the wall and C_s and K are constants. LES models are more computationally expensive than RANS models, especially at near-wall areas where a fine boundary layer is required, but can theoretically provide true flow characteristics as opposed to the averaged solutions found through RANS methods.

3.2.5 Reynolds Stress Model

Another method for solving the Reynolds stress tensor is to use the Reynolds stress model (RSM) which solves the transport equations for each of the terms in the stress tensor, resulting in seven additional equations to be solved for a three dimensional geometry. Applying the RSM removes the need to apply the Boussinesq assumption as used in the RANS models which can potentially make turbulence modelling more realistic. Due to the need to solve the extra equations, the RANS model is computationally more demanding than the RANS models. Because of this extra computational expense, the RSM has not been implemented in this study.

3.3 Turbulence Investigation

The effectiveness of a variety of turbulence models in predicting flow dynamics in AAA disease were investigated. The 2-equation RNG $\kappa - \epsilon$ and $\kappa - \omega$ models [162] and the more powerful LES model are relevant to the simulation of blood flow in large arteries and have been used in previous studies [105] and so were chosen for comparison in this investigation. The aim of this investigation is firstly to validate each of the turbulence models by comparison with experimental data and secondly to assess differences in haemodynamics between each model and in comparison with laminar modelling. The most effective model in terms of accuracy and efficiency of simulation can then be ascertained. Simulations using each of the turbulence models were compared with the steady flow experiments by Asbury et al [4]. The effects of the turbulence models on pulsatile AAA flow dynamics were then investigated by applying each model to the fully developed AAA model described in Chapter 2. A comparison of LES models featuring different methods of generating inlet turbulent perturbations was studied as part of this investigation to determine the effects of defining turbulence at the inlet on simulation accuracy

Turbulence Model	Coefficients
RNG $\kappa - \epsilon$	$C_{mu} = 0.0845$ $C_{1\epsilon} = 1.42$ $C_{2\epsilon} = 1.68$
$\kappa - \omega$	$\alpha^*_\infty = 1$ $\alpha_\infty = 0.52$ $\alpha_0 = 0.111$ $\beta^*_\infty = 0.09$ $\beta = 0.072$ $R_\beta = 8$ $\sigma_\kappa = 2$ $\sigma_\epsilon = 2$
LES	$C_s = 0.1$ $K = 0.41$

Table 3.1: *Turbulence model coefficients*

and haemodynamics.

3.3.1 Methods

The coefficients of the RNG $\kappa - \epsilon$, $\kappa - \omega$ and LES models used throughout this investigation are given in table 3.3.1.

Mesh density and boundary conditions, unless explicitly stated, were taken as those defined in Chapter 2. Before turbulent models can be applied to numerical simulations the near wall conditions and turbulent boundary conditions must first be defined.

3.3.1.1 Near wall turbulence modelling

Near wall effects are of particular importance when modelling turbulence. Close to a boundary, turbulent flows diverge into three distinct flow regimes. A viscous sublayer of laminar flow is formed immediately adjacent to the wall as velocity fluctuations in the tangential and normal direction are damped [145]. Outside of this laminar layer there is a layer of higher intensity turbulence (figure 3.1). A large velocity gradient in the near wall region caused by the zero velocity no-slip wall boundary condition produces high levels of turbulent kinetic energy. Between the laminar and turbulent regimes there is a buffer layer in which flow is in transition to turbulence [145]. These effects can be accounted for via the inclusion of either a near wall function or enhanced wall treatment approach. Wall functions do not seek to resolve the flow in

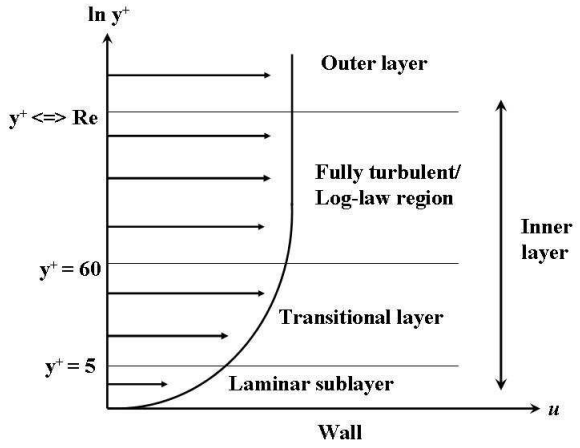

Figure 3.1: *Turbulent boundary layers*

the near wall region directly, but instead apply functions which account for the behaviour of the viscous and buffer layers through a series of assumptions. This allows for a less refined grid to be used in the near wall area, thus promoting computational efficiency. Fluent offers the choice of a standard wall function based on work by Launder and Spalding [79] and a non-equilibrium function proposed by Kim and Choudrey [73] which incorporates pressure gradient effects. Wall functions have been shown to be effective for high Reynolds number flows but less effective at low Reynolds numbers and regions of flow separation [183] as the basic assumptions become less valid.

Enhanced wall treatment uses a two-layer model which solves the laminar and turbulent regions independently with a 'blending' region in the middle to create a complete model of all three layers. In order to accurately model the laminar sublayer, a fine layer of elements adjacent to the wall on the same scale as the sublayer are necessary. The choice of wall treatment depends on the size of this near wall layer and the accuracy of the turbulence model used.

When solving near wall turbulence, the scale of each of the three layers and the scale of the grid required for solving must be determined. As the scaling will vary among different turbulent regimes, the near-wall distances are measured using the wall unit

$$y^+ \equiv \frac{\rho u_\tau y_w}{\mu}, \tag{3.29}$$

where u_τ is frictional velocity and y_w is the distance to the wall. The laminar sublayer resides in the region $0 < y^+ < 5$. For accuracy in solving the enhanced wall treatment, the first grid point from the wall must be in the region $y^+ < 1$. The value of y^+ given by the refined boundary layer in this study is 0.095 for Re=500 and 0.305 for Re=2600. The boundary between laminar and turbulent flow regimes at the wall is defined by the near wall Reynolds number $Re_y = (\rho u^+ y^+)/\mu$ with turbulent , where $u^+ = \overline{u}/u_\tau$ with flow beginning above Re_y=200. Since the near wall boundary layer of elements is sufficiently small, enhanced wall treatment are used with the RNG $\kappa - \epsilon$ and $\kappa - \omega$ models. The near wall boundary layer has a sufficiently fine layer of elements to allow the LES model to obtain WSS values using the laminar stress-strain relationship $u^+ = y^+$.

3.3.1.2 Turbulent boundary conditions

With the introduction of turbulence models we must also introduce turbulent inlet boundary conditions. Turbulence intensity (TI) and hydraulic diameter were used as boundary conditions for all turbulence models in this investigation. TI is defined as

$$TI \equiv \frac{u'}{\bar{u}} \cong 0.16\ Re_{d_h}^{-\frac{1}{8}}, \tag{3.30}$$

based on the hydraulic diameter Reynolds number defined by

$$Re_{d_h} = \frac{\rho u_{in} d}{\mu}, \tag{3.31}$$

where the hydraulic diameter for a cylinder is given as the inlet diameter d.

Defining turbulent fluctuations at the inlet may be vital in describing turbulent conditions throughout the AAA flow. While the two-equation models require only TI and hydraulic diameter, FLUENT provides algorithms for defining inlet velocity fluctuations for the LES model. The simplest method is to assume there are no perturbations at the inlet and any turbulence is created within the AAA geometry itself. Turbulent fluctuations can be added to the inlet by seeding the inlet plane randomly with 'vortex points' which generate 2D vortices normal to the streamwise direction of flow. The vorticity generated at each vortex point is a function of the turbulent kinetic energy (κ), the area of the inlet plane (A) and the number of points (N)

$$\Gamma_v(x,y) = 4\sqrt{\frac{\pi A k(x,y)}{3N[2\ln(3) - 3\ln(2)]}}. \tag{3.32}$$

The degree to which inlet turbulent perturbations affect the overall haemodynamics and accuracy of AAA modelling remains unknown. As part of this investigation, LES models were studied with different methods of inlet perturbation boundary conditions in order to test the accuracy of each method and assess the extent to which applying inlet perturbations affects haemodynamics throughout the AAA simulation. The perturbation methods applied to the LES models are described in sections 3.3.1.3 and 3.3.1.4 for steady and pulsatile flows.

The accuracy of the LES model can be improved through the use of a central-differencing discretisation scheme in solving the momentum equations [107]. Central-differencing schemes differ from the schemes described in section 2.2.4. They use the average values of scalars stored at the centre of elements adjacent to a face and their reconstructed gradients to calculate the face value via

$$\theta_f = \frac{1}{2}\left(\theta_c 0 + \theta_c 1\right) + \frac{1}{2}\left(\nabla\theta_{rec,c0} \cdot \vec{r}_0 + \nabla\theta_{rec,c1} \cdot \vec{r}_1\right) \tag{3.33}$$

where $\theta_c 0$ and $\theta_c 1$ are the elements adjacent to face f, $\nabla\theta_{rec,c0}$ and $\nabla\theta_{rec,c1}$ are the reconstructed gradients in these elements and $\vec{r}$ is the directional vector between the element centre and face f. Solutions using central-differencing schemes can be unstable and so Fluent used a Bounded Central-Difference (BCD) scheme to reduce these instabilities.

3.3.1.3 Steady Flow

To compare the accuracy of the turbulence models in predicting AAA flow dynamics, the study of steady flow experiments in axisymmetric AAA models by Asbury et al [4] were simulated using each of the turbulence models and a laminar flow solver.

Taking the axisymmetric geometry of maximum bulge diameter D=1.88*d* as described in Chapter 2 and scaling it by 0.637 provides a geometry of similar dimensions to that used by Asbury et al. In scaling down the AAA size it was necessary to rescale the physical properties of the blood mimicking fluid used in the experimental model. The fluid properties used were dynamically scaled from those of blood used previously in this investigation. The variables $\rho = 1170\text{kg/m}^3$

and $\mu = 0.00141$kg m^{-1} s^{-1} were used to match the rescaled blood mimicking fluid used in the Asbury study. Steady flow Reynolds numbers of 500 and 2600 were applied to the model, $Re = 500$ representing laminar flow conditions and $Re = 2600$ representing a transition to turbulence. Fully developed parabolic flow profiles were adjusted to the relevant Reynolds number and added to the inlet. TI inlet boundary conditions for the Re=500 and Re=2600 models were calculated using equation 3.30 to be 0.074 and 0.06 respectively with a hydraulic diameter of 1.266cm. LES models with a 'no inlet perturbations' algorithm and a 'vortex perturbation at inlet' algorithm were compared to assess the accuracy of adding turbulent perturbations at the inlet. For the two-equation and laminar models, simulations were run with a steady flow solver until the residuals of velocity and turbulence were less than 1x10^{-6}. Since the LES model involves the solution of transient eddies, a second order unsteady solver was applied with a timestep of $\triangle t = T/200$ (4.6405×10^{-3} seconds) and run for 200 timesteps or until the solution was timestep independent.

3.3.1.4 Pulsatile Flow Models

Pulsatile flow simulations were conducted in the model D=2.1*d*, analagous to a developed AAA, using a patient averaged pulsatile inlet waveform as described in Chapter 2 and simulations were run until the flow became cycle independent.

Unlike steady flow conditions, the TI at the inlet changes with time under a pulsatile flow regime. An average TI of 0.08 based on the mean flow wave velocity was used for the $\kappa - \epsilon$ and $\kappa - \omega$ models with a fixed hydraulic diameter of 1.9cm. While the steady flow simulations recreated experimental conditions in which it can be assumed that turbulent perturbations at the inlet are limited, the pulsatile flow simulations recreate flow conditions present in a physiological AAA and consequently less is known about inlet turbulent conditions. This becomes important when we consider which inlet LES algorithm to apply. It may be that turbulent fluctuations at the inlet are present in sufficient number and intensity to affect flow dynamics downstream. For this reason the LES was run with a 'no inlet perturbations' algorithm and with a 'vortex perturbation at inlet' algorithm, with TI set to the mean value 0f 0.08, to compare the impact of different turbulent perturbation methods on flow. The models described thus far use averaged inlet TI. To investigate the effectiveness of fixed inlet TI a further LES model was included featuring a time-varying inlet TI. Time varying inlet TI was determined by applying a no inlet perturbation LES model to the d/D=1 straight tube model described in Chapter 2. The patient

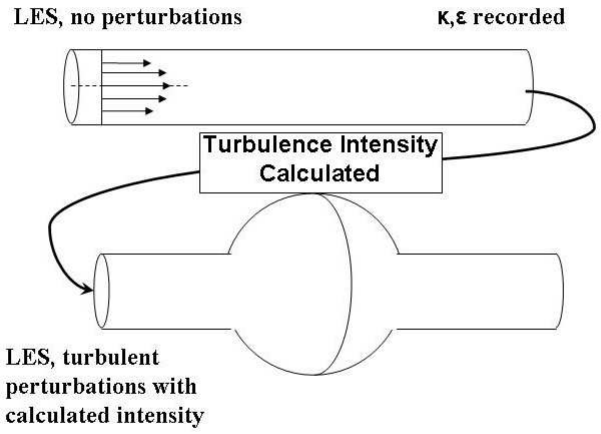

Figure 3.2: *Protocol for creation of LES time varying inlet turbulence model*

averaged inlet flow waveform was applied as described above and on the third cycle measurements of turbulent kinetic energy and turbulent dissipation rate were recorded at the outlet at every time step. By applying a 'no inlet perturbation' condition at the inlet, any turbulence in the system will be generated inside the vessel. The outlet κ and ϵ values were used to calculate TI which was fed back into the d/D=2.1 turbulence model as a LES boundary condition (figure 3.2). Since the degree of TI at each time point will have been generated in a model simulating a healthy section of aorta it will theoretically have a more realistic value than simply applying a mean value throughout the cardiac cycle.

3.3.2 Data Analysis

WSS profiles from AAA simulations using laminar, RNG $\kappa - \epsilon$, $\kappa - \omega$ and LES models with and without inlet perturbations were compared together and with the results of experiments by Asbury et al with steady Reynolds numbers of 500 and 2600. Flow at a Reynolds number of 500 should remain laminar and so the laminar model should adequately account for patterns in WSS and a suitable turbulence model will give similar results as the laminar model. Conversely, Reynolds numbers of 2600 should exhibit a transition to turbulent flow [120] and therefore produce a deviation between laminar and turbulent models. Longitudinal profiles of axial WSS were obtained for each simulation and used as the variable of comparison throughout the investigation. WSS was chosen as it has been shown to become disturbed in turbulent

flows. The study by Asbury et al includes WSS data normalised by scaling the experimental data by the corresponding values of Poiseuille flow in a straight tube. Simulated WSS results for steady flow simulations were normalised using the experimental inlet WSS and simulated inlet WSS

$$WSS_{norm} = WSS_{sim,z}\left(WSS_{exp,in}/WSS_{lam,in}\right), \tag{3.34}$$

where $WSS_{sim,z}$ is simulated WSS at distance from centre z, $WSS_{lam,in}$ is simulated laminar inlet WSS and $WSS_{exp,in}$ is experimental inlet WSS. Normalising WSS values allows a direct comparison with the experimental data. The experimental data provides an opportunity for validating CFD simulations though it should be noted that only eight data points are provided throughout the model which is not enough to describe fine patterns in WSS profiles. While the dimensions of the experimental and simulated models are similar, there will be subtle differences in the curvature of the bulge which may result in differences in flow dynamics. For Reynolds numbers of both 500 and 2600 simulations, all LES models were deemed to be time step independent at $200 \triangle t$ where $\triangle t = 4.6405 \times 10^{-3}$ seconds. At earlier timesteps vortex formation was observed at progressively upstream points.

For pulsatile flows, transition to turbulence has been shown to be confined to the deceleration phase of the cardiac cycle [191] and so results were recorded at points corresponding to the beginning, middle and end of the deceleration phase. Contours of velocity magnitude were obtained at each time point for each turbulence model simulation to show a visual comparison of differences in haemodynamics between models. Axial WSS against distance from cavity centre was also plotted for each model at each time point.

3.3.3 Processing Time

In order to assess the efficiency of a particular turbulence model the accuracy of the simulation must be weighed up against the solution time. Each of the pulsatile flow turbulence model simulation and the laminar flow simulation were run for 2 cycles to provide cycle independence after which the time taken to solve a further 10 timesteps was recorded. A timestep of $\triangle t = T/200$ (4.6405×10^{-3} seconds) was used and the solution at each timestep considered solved after all residuals were below $1x10^{-6}$ or if this limit is not reached then a maximum of 60 iterations. All simulations were carried out with background processes kept to a minimum to standardise the results.

3.4 Results

3.4.1 Steady Flow

Laminar and $\kappa-\omega$ models follow the trends of the normalised Asbury data at Reynolds numbers of 500 and 2600 (figures 3.3(a) and 3.3(b)) with WSS dipping to around 0 throughout the cavity then rising up to the peak WSS at the distal end. The most distal experimental data point appears to be an excellent fit with the $\kappa-\omega$ data, however due to sparse experimental data the exact point of maximum WSS cannot be determined from the Asbury et al data and so an exact match in values at this point may not indicate perfect validation. At Reynolds number 2600, the laminar model under-predicts experimental maximum WSS by around 15% while maximum WSS in the $\kappa-\omega$ model is similar to the experimental maximum. Slight deviations between laminar and $\kappa-\omega$ models are observed towards the proximal end of the cavity at Reynolds number 2600 though experimental data is too sparse to determine which model is more accurate. The RNG $\kappa-\epsilon$ model produces the worst fit with the experimental data. While WSS magnitudes at the proximal end of the aneurysm are similar, maximum WSS is significantly higher than all simulated and experimental data. Vortex formation is situated further upstream than in all other models and so produces significantly different patterns in axial WSS.

At Reynolds numbers of 500 and 2600, WSS profiles for both LES models were similar to the general trends of the experimental data (figures 3.4(a) and 3.4(b)), with the exception of the point of high magnitude retrograde WSS at the distal end of the cavity, which is significantly higher in the LES models. Since the experimental results are limited in terms of data points the actual magnitude of retrograde flow created before the flow reattachment point cannot be validated. WSS profiles in the $Re = 2600$ model show that the LES model with no inlet perturbations predicts similar WSS profiles to the laminar model with the exception of points at the inlet and at the point of peak WSS. At these points there is a difference of around 0.15 Pascals between WSS magnitudes. The inlet perturbation vortex method LES model differs from the no inlet perturbation model with lower WSS magnitudes at the inlet and outlet, higher and more variable peak WSS and evidence of vortex formation slightly proximal to that in the other models. The higher peak WSS present in both LES models is in line with the maximum experimental WSS. Both LES models also contain higher variability around the AAA circumference than the laminar and 2 equation models.

In steady flows the laminar model fits the trends in experimental data but under predicts maxi-

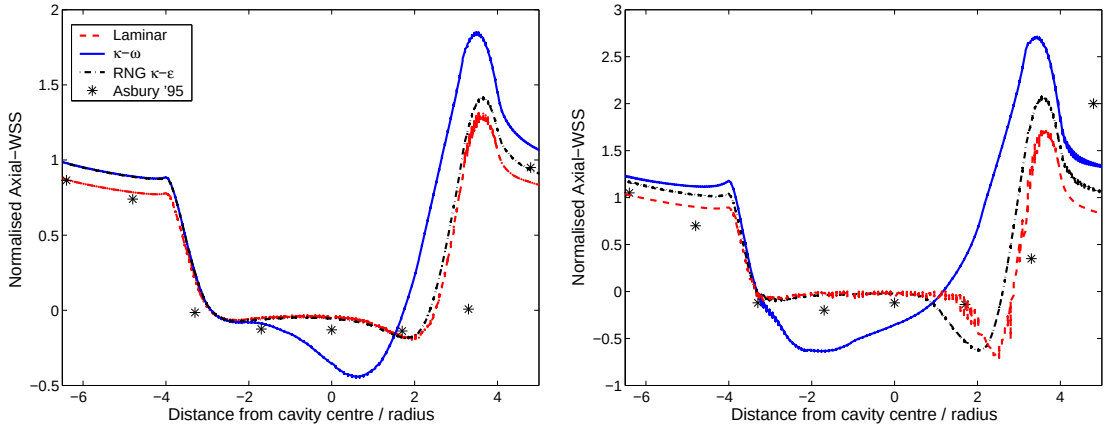

(a) $Re = 500$ (b) $Re = 2600$

Figure 3.3: *Normalised axial WSS profiles for two-equation and laminar models*

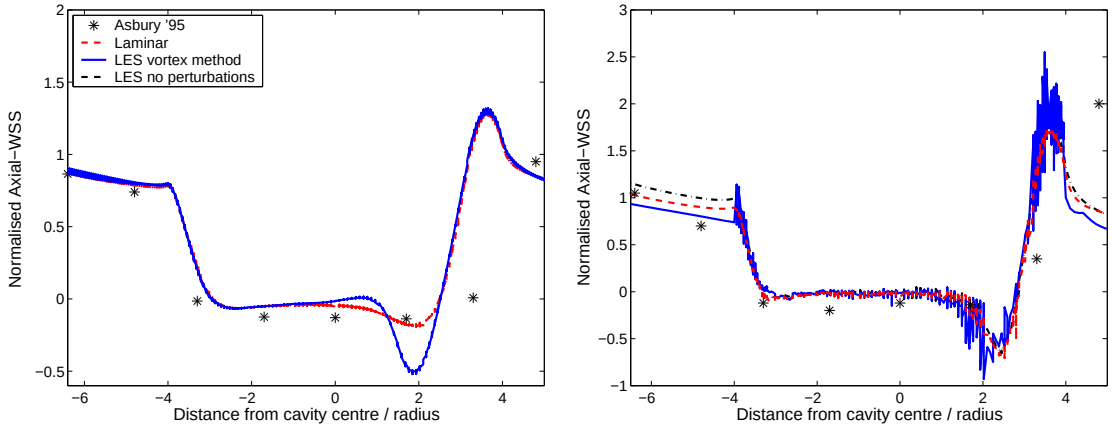

(a) $Re = 500$ (b) $Re = 2600$

Figure 3.4: *Normalised axial WSS profiles for LES and laminar models*

mum WSS at a Reynolds number of 2600 while the $\kappa-\omega$ model was more accurate in predicting WSS values than the RNG $\kappa - \epsilon$ model. The $\kappa - \omega$ appears to give a better prediction of peak WSS in transitional flow than laminar modelling alone though laminar models may be more accurate at lower WSS magnitudes.

3.4.2 Time Varying Turbulence Intensity LES Model

Applying the no inlet perturbation algorithm LES model to the straight tube $D = d$ for a full cardiac cycle produced peak outlet values of κ (figure 3.5(a)) and ϵ (figure 3.5(b)) during mid systole and a smaller peak in both values during the beginning of diastole. These values were

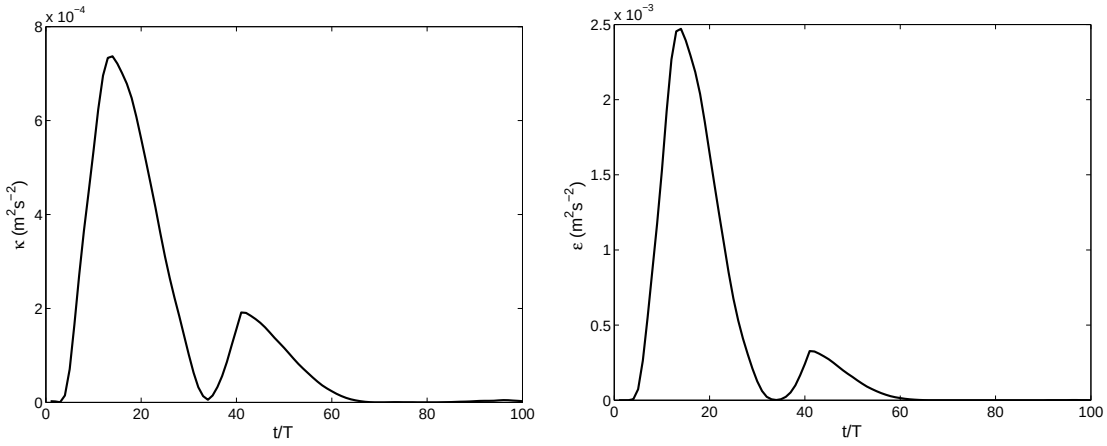

(a) κ (b) ϵ

Figure 3.5: *Profiles of turbulent kinetic energy and dissipation rate throughout cardiac cycle*

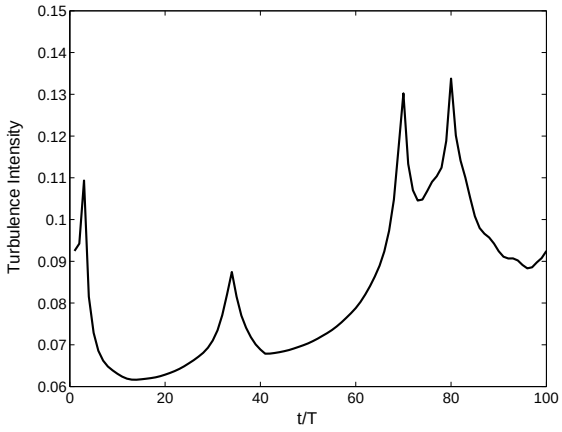

Figure 3.6: *Profile of turbulence intensity throughout cardiac cycle*

used to calculate the magnitude of TI shown in figure 3.6 throughout the cardiac cycle. Of interest in this investigation is the peak in TI during the the acceleration phase (t/T = 0.2 to 0.4) in which transition to turbulence has been observed in previous investigations. Time varying TI was used as a boundary condition in the time varying inlet vortex perturbation LES model.

3.4.3 Pulsatile Flow

Contours of velocity magnitude at mid systolic and decelerating flow time points t/T = 0.2 and 0.3 (figures 3.7 and 3.8) show that the $\kappa - \omega$ model exhibits similar haemodynamics to the laminar solution though the velocity profiles are more blunted. Velocity magnitudes in the no inlet perturbation LES model are closer to the laminar solution than both 2-equation models,

though still slightly blunted, while the fixed and variable TI vortex perturbation LES models show perturbations are present throughout the cavity, especially in the variable TI model. While these perturbations are noticeable, especially towards the distal end, the general characteristics of flow observed in the no perturbation model are preserved. The RNG $\kappa - \epsilon$ model shows a change from blunted velocity profiles similar to the $\kappa - \omega$ model at t/T = 0.2 to internal velocity dynamics which are significantly more simplified than all other models at t/T=0.3. At the end of the deceleration phase (figure 3.9), the RNG $\kappa - \epsilon$ model retains the simplified haemodynamics and does not exhibit the central core of higher velocity flow apparent in the rest of the models. The laminar, $\kappa - \omega$ and no perturbation LES models share similar haemodynamic trends though the $\kappa - \omega$ model produces more blunted velocity profiles than the LES model which are in turn more blunted than the laminar model. The fixed and variable inlet perturbation LES models, while retaining the central slug of velocity present in other models, are dominated by large amounts of perturbations throughout the cavity which change the overall haemodynamics.

Both of the LES method models with vortices applied at the inlet cause a breakdown in the symmetry of flow. Symmetry is preserved in all other turbulent model methods including the no inlet perturbation LES model.

The trends in velocity contours are reflected in the WSS plots for each turbulence model (figures 3.10 and 3.11). The $\kappa - \omega$ and no perturbation LES model simulations have similar WSS profiles to the laminar model, though the $\kappa - \omega$ model has a lower peak in minimum WSS during mid deceleration and vortex detachment and reattachment points are located further upstream at t/T=0.4. The simplified haemodynamics of the RNG $\kappa - \epsilon$ model translate into the under prediction of peak WSS during mid deceleration when compared to other models, and a comparative lack of complexity in the WSS profile observed at t/T = 0.4. The fixed and time varying TI inlet vortex perturbation LES models, while exhibiting a higher degree of WSS variation than other models, show similar trends in WSS profiles to the laminar and no perturbation models during t/T = 0.2 to 0.3 though a significant departure is observed at the end of the deceleration phase. At t/T = 0.4, WSS values at the proximal and distal ends of the cavity are significantly less negative in the inlet perturbation LES models than the no perturbation and laminar models.

This sudden and significant shift in WSS magnitudes is analysed in more detail in the WSS plots in figure 3.12 which shows the difference in WSS values becoming greater in all areas outside of the cavity centre between the middle and end of the deceleration phase.

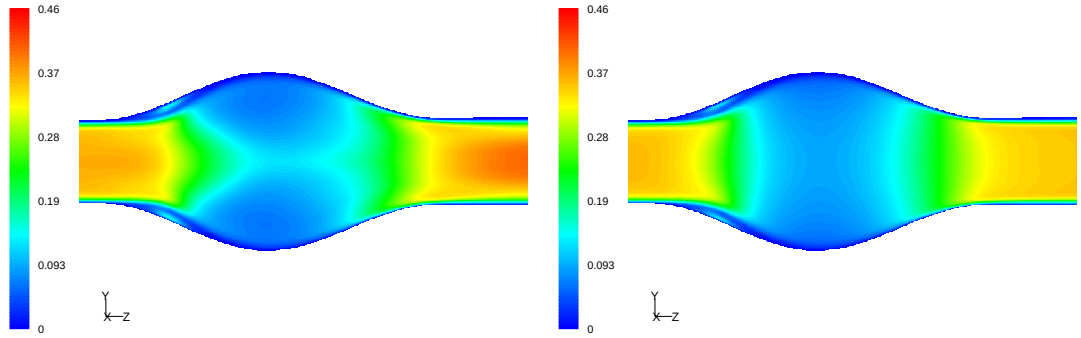

(a) laminar

(b) RNG $\kappa - \epsilon$

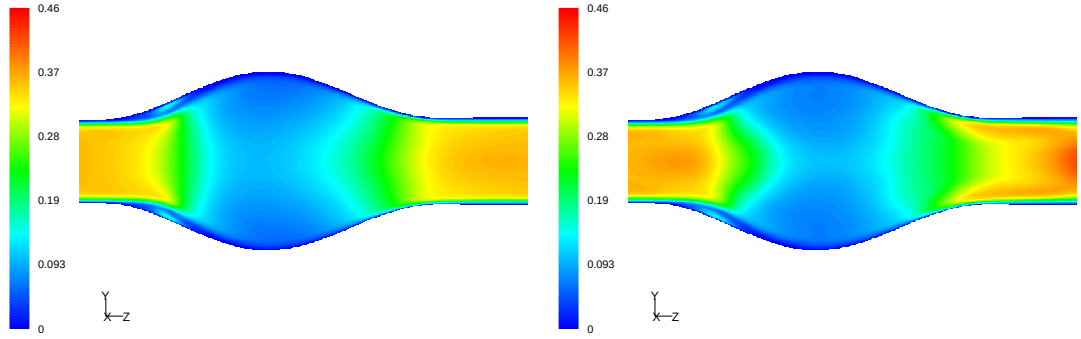

(c) $\kappa - \omega$

(d) LES with no perturbations

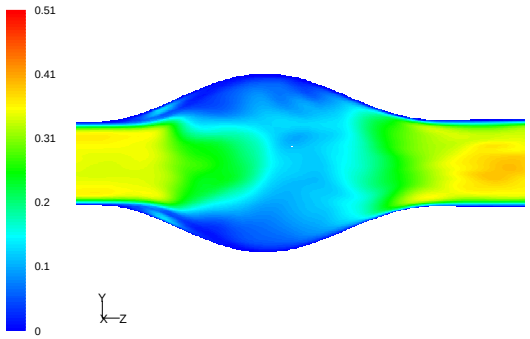

(e) LES with vortex method and fixed inlet turbulence intensity

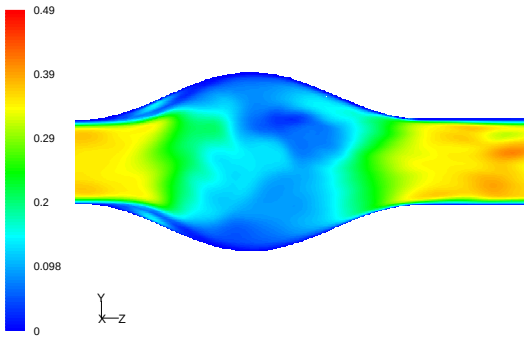

(f) LES with vortex method and time varying inlet turbulence intensity from pipe flow

Figure 3.7: *Contours of velocity magnitude (m/s) at t/T = 0.2*

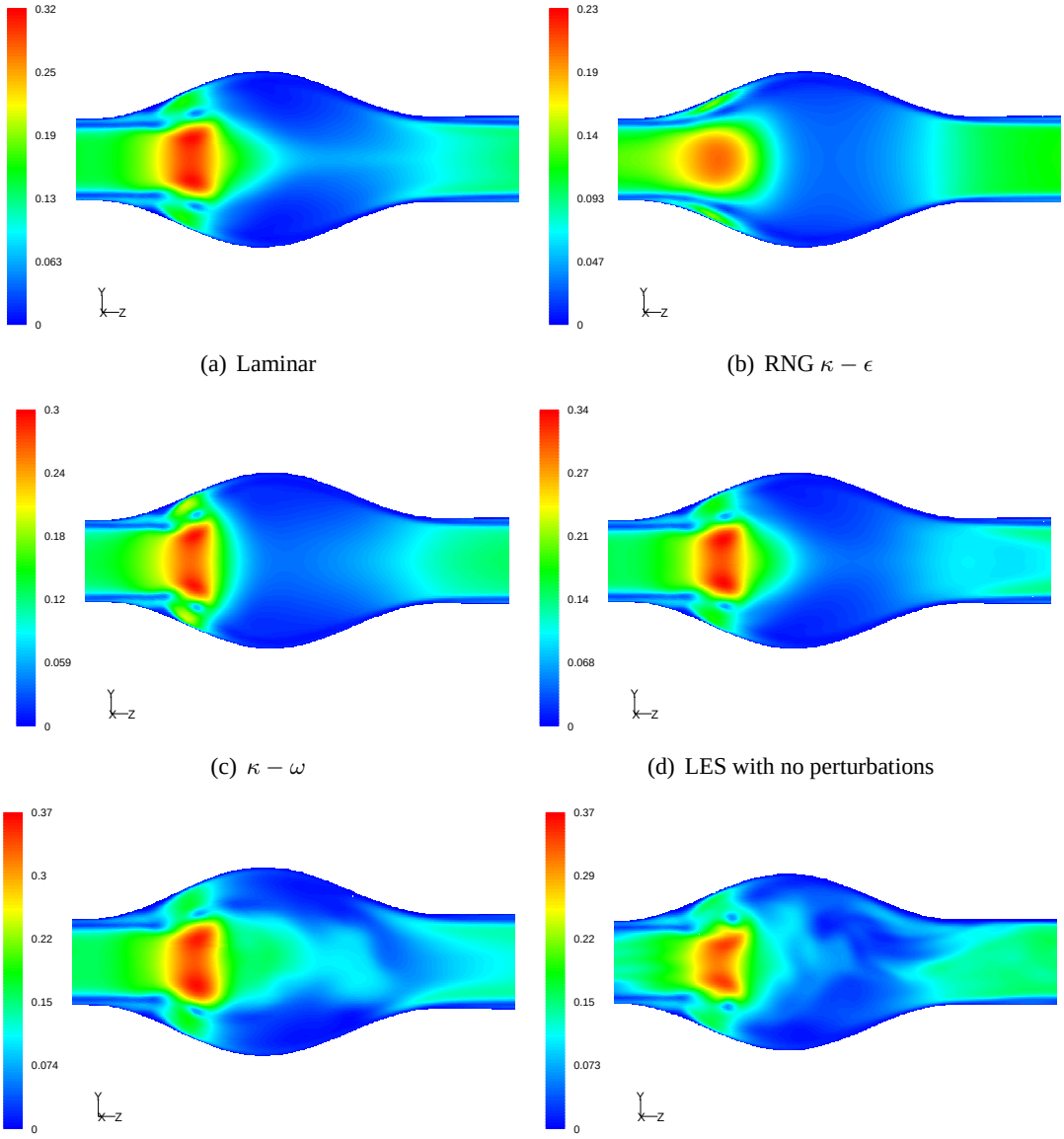

(a) Laminar

(b) RNG $\kappa - \epsilon$

(c) $\kappa - \omega$

(d) LES with no perturbations

(e) LES with vortex method and fixed inlet turbulence intensity

(f) LES with vortex method and time varying inlet turbulence intensity from pipe flow

Figure 3.8: *Contours of velocity magnitude (m/s) at t/T = 0.3*

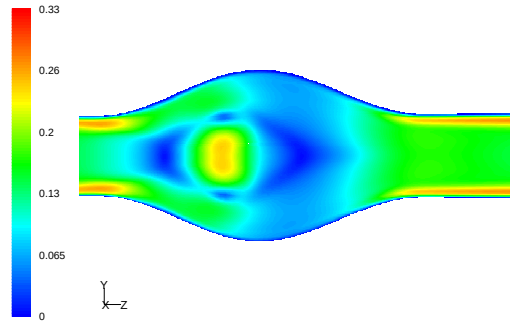

(a) Laminar

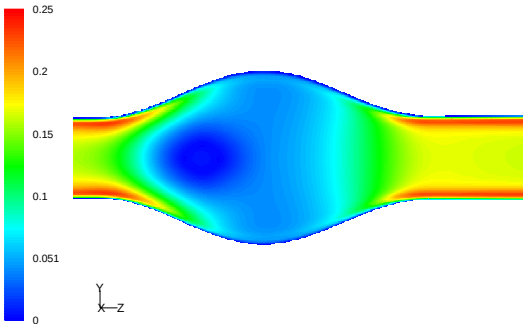

(b) RNG $\kappa - \epsilon$

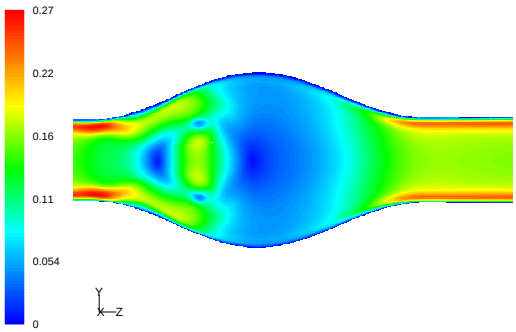

(c) $\kappa - \omega$

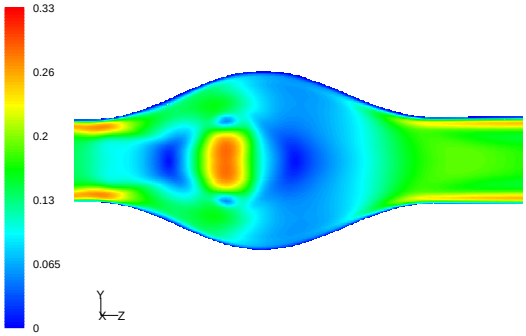

(d) LES with no perturbations

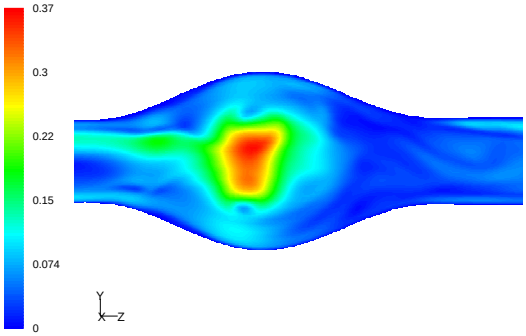

(e) LES with vortex method and fixed inlet turbulence intensity

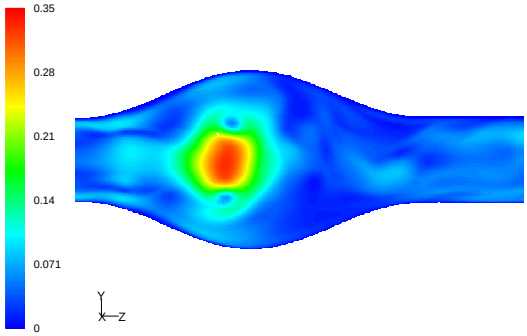

(f) LES with vortex method and time varying inlet turbulence intensity from pipe flow

Figure 3.9: *Contours of velocity magnitude (m/s) at t/T = 0.4*

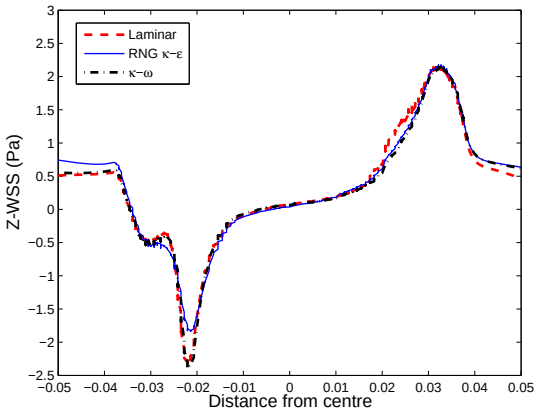

(a) t/T=0.2

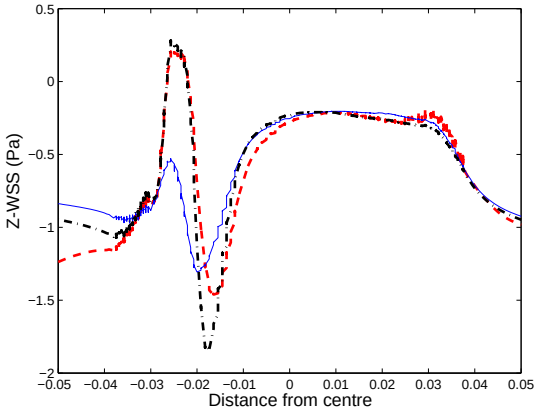

(b) t/T=0.3

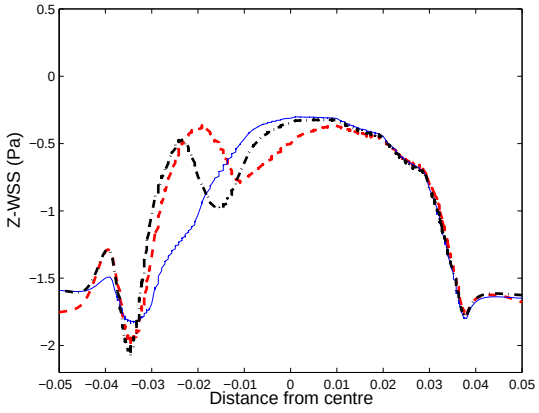

(c) t/T=0.4

Figure 3.10: *Longitudinal profiles of Z-WSS for two-equation turbulence models*

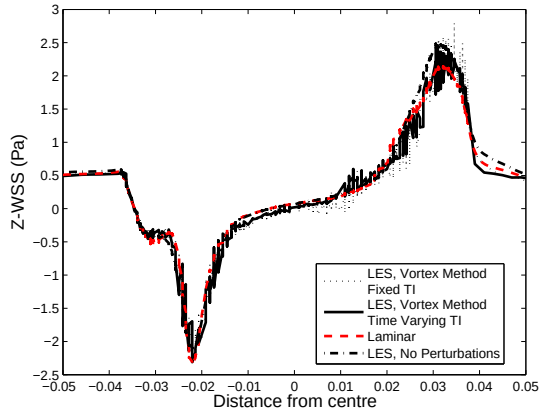

(a) t/T=0.2

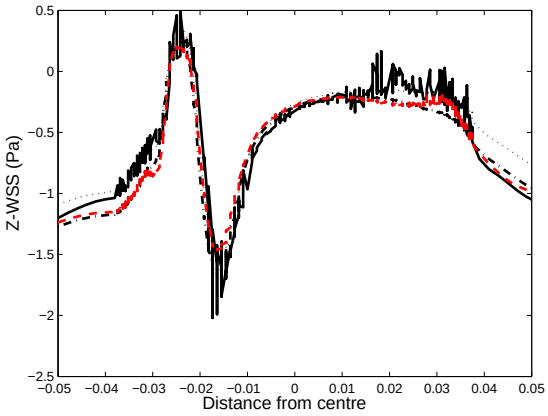

(b) t/T=0.3

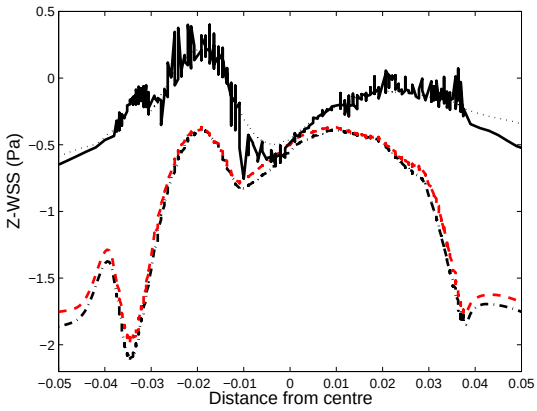

(c) t/T=0.4

Figure 3.11: *Longitudinal profiles of Z-WSS for LES turbulence models*

Model	Solution Time for 10 Timesteps
Laminar	2h 18 mins
RNG $\kappa - \epsilon$	2h 10 mins
$\kappa - \omega$	2h 8 mins
LES, no perturbations	2h 15 mins
LES inlet vortex method	2h 18 mins

Table 3.2: *Processing time*

The RNG $\kappa - \epsilon$ turbulence model oversimplifies haemodynamics when compared to other models leading to a lack of complexity in WSS profiles and significant underestimation of peak WSS. The $\kappa - \omega$ and no inlet perturbation LES model follow the haemodynamic trends of the laminar simulation through the deceleration phase, however both produce more blunted velocity profiles. WSS trends follow laminar trends for both models though the haemodynamic differences present in the $\kappa - \omega$ model lead to minor differences in WSS profiles during the deceleration phase. Perturbations applied to the LES model at the inlet pervade throughout the cavity. WSS profiles remain unchanged until the latter half of the deceleration phase at which point perturbations significantly change the haemodynamics and WSS profiles, especially away from the cavity centre. There is no significant difference in WSS between time varying and fixed perturbation boundary conditions in LES models.

3.5 Processing Time

The processing times for each model are given in table 3.5.

While effort was taken to eliminate background computational processes while the simulations were running, there may be slight differences in CPU uses between simulations and as such the solutions times should be used as a general guide to computational effort.

3.6 Discussion

Pulsatile flow in AAAs involves a burst of higher Reynolds number flow during systole while the bulk of the cycle remains at a lower Reynolds number. When choosing a turbulence model it is therefore important to ensure that it remains accurate over the entire range of Reynolds numbers and that it will account for the formation and dissipation of vortices which are a key feature of AAA haemodynamics. Due to the reduction in modelling assumptions, LES models

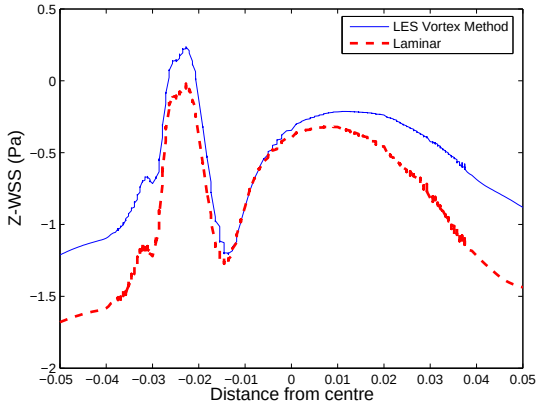

(a) t/T=0.325

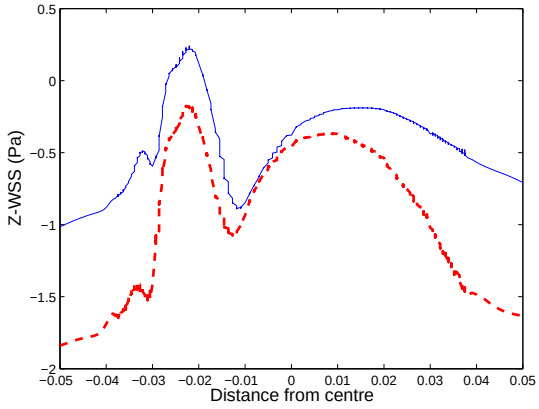

(b) t/T=0.35

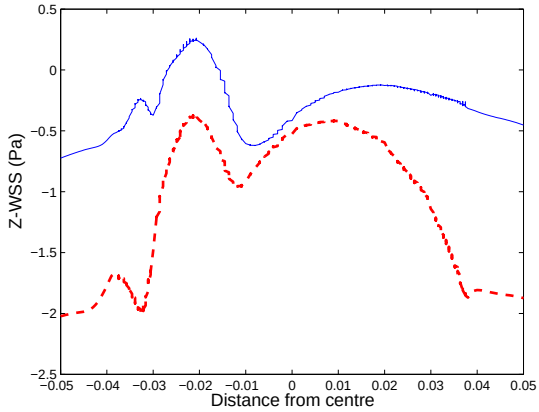

(c) t/T=0.375

Figure 3.12: *Longitudinal profiles of Z-WSS for LES turbulence models*

would be expected to provide more accurate turbulence modelling than 2-equation models but consume more processing time.

The results show that the RNG $\kappa-\epsilon$ model produces inaccuracies in vortex modelling in steady flow and over simplifies vortex behaviour in pulsatile flow resulting in a loss of complexity and significant damping of peak WSS. Since vortex behaviour is integral to AAA haemodynamics, the results of this study suggest that the RNG $\kappa-\epsilon$ model should be avoided for AAA modelling. This finding corroborates results of an investigation by Varghese and Frankel [172] of physiological flow in stenosed arteries which found the RNG $\kappa-\epsilon$ model to be less accurate than the $\kappa-\omega$ model. The RNG $\kappa-\epsilon$ model also faired the worst in terms of solution time which is surprising given the simple nature of the model when compared with LES.

The $\kappa-\omega$ and LES model simulations are consistent with the experimental data and produce maximum WSS values closer to the experimental values than laminar simulation in steady, transitional flow. The limited data points provided by the experimental results and possible differences in curvature between simulated and experimental AAA models places limitations on the ability for detailed quantitative analysis. In pulsatile flow, the LES model with no turbulent perturbations at the inlet produced haemodynamics similar to laminar simulation while the $\kappa-\omega$ model produced noticeably blunted velocity profiles but retained the haemodynamic trends of the laminar and no inlet perturbation LES model. The $\kappa-\omega$ model exhibited the shortest solution time making it the most computationally efficient model. The no perturbation LES model took 5.47% longer to solve which would still make the LES model viable if it is deemed to add further accuracy to the simulation. The results show that the $\kappa-\omega$ and no perturbation LES models produce simulations with similar haemodynamic trends, making them both candidates for simulating general AAA haemodynamics. When higher levels of accuracy are required, such as when modelling near wall cell interactions, the differences in velocity profiles and WSS magnitude may become more important. Both models have a similar level of accuracy in steady flow, but this investigation does not show which of these 2 models is more accurate in pulsatile flow. Further investigation is therefore required to compare both models with experimental data.

Since there are no extra viscous terms added, the laminar model was expected to have the fastest solution time. In practice it took the same length of processing time as the vortex method LES model which is longer than the time taken using the $\kappa-\omega$ model. This finding is important since turbulence models may be neglected when modelling due to the extra processing time added.

While this may still be true in simple models, these results suggest that there is no significant additional processing time incurred through the use of the $\kappa - \omega$ or LES models.

The lack of significant differences in processing time between laminar, $\kappa - \omega$ and LES models may be due to the increase in processing created by the inclusion of the fine boundary layer and the use of second order accuracy. These may dilute the differences in processing time created by the inclusion of more complex turbulence models. While the LES models require the fine boundary layer of elements used in this investigation, the $\kappa - \omega$ model is designed to be applicable to coarser meshes as well and so efficiency could be increased if the near wall boundary layer is removed.

The similarities in processing time indicate that the extra computational effort required to apply the RSM turbulence model may not significantly effect the overall processing time. The RSM does not require the application of the Boussinesq approximation and so may provide more accurate turbulent modelling. This study can be extended to include the RSM as a viable turbulence model in AAA simulation.

Under pulsatile flow conditions the influence of inlet boundary conditions becomes more apparent. Applying zero perturbations at the inlet produces a model with similar flow dynamics and WSS profiles to the laminar model whereas the addition of vortex perturbations at the inlet creates noticeable instabilities in the flow throughout the aneurysm. These instabilities are reflected in the lowering of WSS profiles towards the end of the deceleration phase. This would suggest that when numerically modelling AAAs the turbulent perturbations entering the flow at the inlet have a much greater effect on flow dynamics and WSS than perturbations created within the model. If this is the case, it is necessary to quantify the intensity of perturbations at the inlet. It should be noted that any divergence between LES models was shown to occur around the middle of the deceleration phase. At other time points measured, all models show similar trends in WSS distribution.

The comparison of LES models with time varying and fixed turbulence intensity inlet perturbation boundary conditions reveals that both models have similar trends in WSS towards the end of the deceleration phase. Specifying the intensity of inlet perturbations changes the WSS profiles relatively little when compared to zero inlet-perturbation models, this suggests that it is the spatial distribution of turbulence which is critical. In this investigation a fixed number of perturbations were seeded at the inlet and so a study varying the number of inlet vortices

would clarify the effects of spatial distribution. The turbulence intensity boundary conditions derived from the straight tube model are limited as a result of the lack of spatial distribution of turbulence. A further investigation in which the vorticity and radial velocity vectors are measured at the outlet of the tube at each timestep and then fed back into the dilated AAA model would provide temporally and spatially varying turbulence inlet boundary conditions. Comparing the results of the investigation with results using a spectral synthesiser turbulent inlet boundary condition method, which generates perturbations through summation of inlet Fourier harmonics, may also be useful.

Applying perturbations at the inlet of the LES models produced a breakdown in flow symmetry. Simple AAA models are often assumed to be axi-symmetric. This study shows that the assumption of axi-symmetry may be inappropriate when turbulent perturbations are applied at the inlet and suggests that the local dynamics of flow in an AAA may be dictated by upstream turbulent perturbations even in symmetrical vessels.

The effect of turbulent perturbations at the inlet on flow dynamics and WSS profiles observed in this study has implications in modelling AAAs using both generalised and patient specific models. Currently, CFD models of AAA tend to assume laminar inlet boundary conditions [37, 86, 144]. There is no input of radial velocity components and so inlet turbulence information is lost. Given the high degree of secondary flow features present in the blood as it passes the aortic arch [92], it is likely that these features will continue to be present when the flow reaches the abdominal aorta and so cause deviations from laminar flow and possibly an increased likelihood of turbulent perturbations. As the distribution of these perturbations has been shown to have a significant effect on flow dynamics and WSS, the inclusion of spatial velocity data normal to the z-directional flow may be necessary when modelling AAA disease. The inclusion of radial velocity information in patient specific AAA is the subject of Chapters 5 and 6.

3.7 Conclusions

During steady flow regimes, the $\kappa-\omega$ and LES models predicted peak WSS with more accuracy than the laminar model alone whereas the RNG $\kappa-\epsilon$ model failed to accurately simulate vortex behaviour.

Applying a LES model with no inlet perturbations and a $\kappa-\omega$ model to AAAs with pulsatile flow regimes lead to similar trends in haemodynamics to the laminar model, with differences

occurring in WSS profiles towards the end of the deceleration phase. While applying the $\kappa - \omega$ and no inlet perturbation LES models did not significantly alter the flow haemodynamics for much of the cardiac cycle, the use of turbulence models throughout the whole cycle is justified since adding turbulence models did not significantly affect the solving time of the models investigated. The $\kappa - \omega$ model was the most computationally efficient model, producing the fastest solution while retaining the characteristics of the flow.

Applying turbulent perturbations at the AAA inlet had a significant effect on velocity and WSS profiles during the deceleration phase. The difference between fixed and time varying perturbation intensity was less significant. The effects of secondary flow and perturbations at the inlet are therefore an important factor to consider when analysing turbulent flow in AAAs and an assumption of linear flow at the inlet may lead to errors in a numerical solution.

The LES turbulence model with no inlet perturbations has been used throughout the rest of this study. This chapter reveals that either the LES or the $\kappa - \omega$ model would be sufficient for determining AAA haemodynamics. The LES model was chosen as the modelling of particle motion in flow requires the highest precision of modelling feasible. The differences in haemodynamics between each model are not significant and only occur during the end of systole but may have a greater effect on particle motion in flow. LES models are formulated to provide greater accurate than two equation models at the cost of larger processing times and since the difference in processing time between the two models has not been shown to be significant in this study, the LES model was used. The quantity and distribution of inlet turbulence is not known for generic AAA models and so the no perturbation methodology is applied in Chapter 4. In Chapters 5 to 7 inlet velocity is quantified spatially over the inlet plane in most cases, negating the need for inlet turbulence assumptions and so the no perturbation methodology is also applied here.

Chapter 4
Monocyte Tracking in Generic AAAs

4.1 Introduction

In order to elucidate the behaviour of inflammatory cells within AAA disease and the haemodynamics which drive this behaviour, blood flow and its effect on monocytes is simulated in generalised, axi-symmetric AAA geometries with physiologically realistic dimensions. The distribution of monocyte adhesion is clinically relevant as areas of concentrated monocyte adhesion may be associated with higher levels of inflammatory wall degradation when compared to areas exposed to little or no adhesion [53]. By modelling various sizes of AAA, as described in Chapter 2, patterns in haemodynamics and cell deposition with AAA progression can be observed.

Haemodynamics and WSS in simplified AAA geometries similar to those used in this study have been investigated previously. Studies of experimental AAAs under physiological pulsatile flow by Egelhoff et al [37] and Salsac et al [144] focus on AAAs with diameters up to the critical 5.5 cm surgical intervention point while a numerical study by Fraser [46] models aneurysms with diameters of 4 to 7 cm. All studies show vortex formation is present in even the smallest diameter aneurysms. As aneurysm diameter increases, the scale of the vortices and their effects on haemodynamics increases. Previous studies use different inlet waveforms but the general trends in haemodynamics and WSS can be used as a qualitative comparison with those simulated in this study.

While this study is the first to numerically model monocyte behaviour in AAAs, numerical modelling of blood cells, including monocytes, has been achieved previously. Longest et al [95] and Buchanan et al [14] modelled monocytes as discrete particles interacting with the background blood flow. Longest et al confirmed the validity of their model against the Karino and Goldsmith [66] experimental investigation of red blood cell motion in flow through an annular expansion. Cell adhesion to the lumen was quantified by Buchanan et al using a probabilistic method based on local cell residence times. This was extended by Longest et al [95] to incorporate the distance of the cell from the wall and a critical value of WSS over which no

adhesion could occur. The Longest et al near wall particle residence time (NWPRT) approach is used in this study as it has been used previously to simulate the probability of monocyte adhesion in large arteries.

WSS has been shown to affect the adhesion of cells to the lumen [80, 189]. Previous studies [96] have built a WSS limiting factor into the cell residence time models which provide a critical WSS value over which cell adhesion does not occur. The effects of WSS on inflammatory adhesion have been shown by experimental studies to vary depending on the strength of WSS. At high WSS, no adhesion is possible [80, 189] and as WSS decreases the probability of adhesion increases gradually. Despite evidence for a gradual change in adhesion probability, previous models have used a fixed critical WSS value based on the magnitude of inlet flow. In this study, a more physiologically accurate variable WSS limiter is created based on *in vitro* experimental data and attached to the NWPRT model. This novel WSS limiter will account for the effects of variable WSS on the probability of cell adhesion in the AAA. By comparing NWPRT data from models with and without the WSS limiter, the effects of WSS on monocyte adhesion can be observed.

4.2 Discrete Phase Modelling (DPM) Theory

Using DPM allows the motion of individual particles to be modelled within the flow field. Solving the trajectories of each particle at every timestep can become computationally demanding therefore, depending on the processing power available, there is currently an upper limit on the number of cells which can be simulated at any one time. When particles are sufficiently sparse within a flow, their motion can be simulated using one-way modelling whereby particle motion is assumed to have a negligible effect on the bulk continuum flow field. When particles are present in a large concentration, such as red blood cells, a two-way coupled model must be incorporated in which particle motion changes the dynamics of the background flow, requiring the solution of an extra level of particle-flow equations. Monocytes are present in the blood in sufficiently low concentrations ($3 \times 10^{-5}/ml$) to be within the bounds of DPM and have previously been modelled using one-way DPM [95, 96].

To model particle trajectories using DPM, the Navier-Stokes equations of the background flow must first be solved to obtain the momentum and direction of the flow field which is in turn used to calculate particle motion. The effects of the flow field on particle trajectories are a function

of the lift and drag forces peculiar to a given particle as well as certain body force terms which may be included, depending on the attributes of the particle and the flow system it resides in. Following Newton's second law of motion, the acceleration of a particle in the x,y and z planes at each timestep of the simulation must equal the forces acting on it per unit particle mass. In the x direction, the sum of forces relevant to this investigation can be generalised by

$$m\frac{du_p}{dt} = F_D + F_L + F_P + F_\tau + F_{NW} \tag{4.1}$$

where u_p is the x-directional velocity of the particle, F_D is drag force, F_L is lift force, F_P is pressure gradient force, F_τ is shear stress force and F_{NW} is a general term for specific lift and drag terms which come into effect in the near wall region.

The specific force equations and coefficients required to simulate monocyte motion must be determined for cells within the bulk flow and at the near wall regions where many of the standard equations of particle motion break down. Each of the relevant forces are described in more detail below.

4.2.1 Drag coefficient

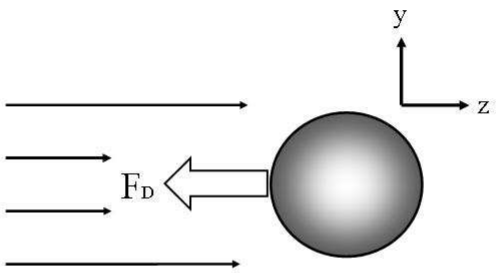

Figure 4.1: *Drag force*

Drag force (figure 4.1) acting on a particle in a steady-state system is a function of the difference in velocities between the particle and the fluid medium, the density of the surrounding fluid and the cross-sectional area of the particle. Drag force can therefore be described as

$$F_D = C_d\frac{\rho_f u_{pf}^2}{2}A, \tag{4.2}$$

where A is the cross sectional area ($\pi d_p^2/4$ in the case of a sphere), ρ_f is the fluid density, u_{pf} is the velocity difference between particle p and the surrounding fluid and C_d is the drag coefficient. The formulation of C_d depends on the relative Reynold's number of the flow, defined as

$$\mathrm{Re_r} \equiv \frac{\rho_p d_p \left| u_{pf} \right|}{\mu_p} \tag{4.3}$$

It is useful when understanding the drag coefficient used to observe the relationship between the steady-state drag force and the relative Reynolds number. Rearranging equation 4.2 for a sphere gives

$$F_D = C_d \rho_f u_{pf}^2 \frac{\pi d_p^2}{8} \tag{4.4}$$

A number of methods for formulating the drag coefficient in different flow regimes exist but since blood cells operate at $Re_r << 1$ the Stokes drag force is the most appropriate. Stokes drag force, derived from the Navier-Stokes equations, defines the drag coefficient as

$$F_D = 3\pi \mu_p d_p u_{pf} \tag{4.5}$$

and so rearranging equation 4.4 gives

$$C_d = \frac{24}{Re_r} \tag{4.6}$$

This can be used to calculate the time taken by a particle to respond to a change in the velocity of the carrier fluid, the particle momentum response time

$$\tau_p = \frac{\rho_p d_p^2}{18\mu} \tag{4.7}$$

Since monocytes are relatively spherical in shape with a rigid shell when in flow, they fit well with the assumptions of small, rigid, spherical particles used in defining drag forces and require no caveats to account for irregular shape or morphing of particles. The structure of leukocytes becomes more fluid upon contact with the endothelium, but while in vascular flow the structural rigidity of monocytes preserves the shape of the cell and prevents disintegration or erosion. Morsi and Alexander [112] calculated and tested experimentally a more generalised version of C_d in the form of the second order polynomial

$$C_d = a_1 + \frac{a_2}{Re_r} + \frac{a_3}{Re_r^2}, \tag{4.8}$$

where a_1, a_2 and a_3 are constants which vary with the range of Re_r from $<< 1$ to 5x10^4 . At $R_r < 0.1$, $a_1 = a_3 = 0$ and $a_2 = 24$, thus reducing the drag coefficient to the Stokes drag term.

4.2.2 Basset-Boussinesq-Oseen Equation

The motion of a small, rigid sphere in three-dimensional non-uniform Stokes flow was studied by Maxey and Riley [102] who identified further forces created either by the particle or the surrounding fluid. The pressure gradient (figure 4.2) and shear stress forces can be written

$$F_P = (- \bigtriangledown \cdot p)\, V_p \ , \ F_\tau = (\bigtriangledown \cdot \tau)\, V_p, \tag{4.9}$$

where V_p is the volume of the particle. The 'virtual mass' force, created by the acceleration

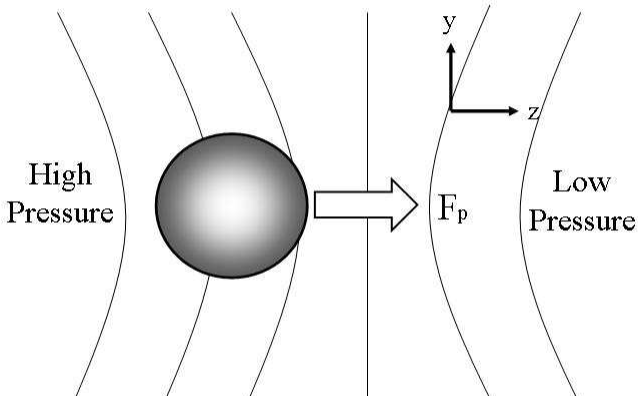

Figure 4.2: *Pressure gradient force*

of fluid around the particle is calculated by multiplying particle mass by the differential of the relative velocity

$$F_{vm} = \frac{\rho_f V_p}{2} \left(\frac{Du_p}{Dt} - \frac{Du_f}{dt} \right). \tag{4.10}$$

Where D/dt is the substantive derivative as described in equation 2.11. The delay between relative velocity change and the viscous effects on the particle means that the initial particle and fluid velocities affect the force balance on the particle further along its trajectory as described

by the Basset history integral term

$$F_{Basset} = \frac{3}{2}\sqrt{\pi\rho\mu}\left[\int_0^t \frac{\frac{Du_p}{Dt'} - \frac{du_f}{dt'}}{\sqrt{t-t'}}dt'\right], \tag{4.11}$$

where the term in parenthesis accounts for the effects of the initial velocity.

By including the non-uniform flow corrections to each of the above forces derived by Faxen [39] and the gravitational body force mg, the Basset-Boussinesq-Oseen (BBO) equation of motion of a small, rigid, spherical particle in a low Re_r, flow field can be written

$$m\frac{du_p}{dt} = F_D + F_P + F_\tau + F_{vm} + F_{Basset} + mg. \tag{4.12}$$

For the simulation of blood cells in a large artery this equation can be simplified. Numerical analysis by Jung et al [65] found the virtual mass to be relatively small when compared to the drag force and was assumed to be negligible in large artery simulation. Longest [94] states that since the particle response time, τ_p of cells in blood is small (on the order of 10^{-6} seconds) when compared to the overall pulse period (usually around 1 second), the effects of including the Basset history term will be negligible and so is not included in this study. The equation of particle motion can therefore be simplified to

$$m\frac{du_p}{dt} = F_D + F_P + F_\tau. \tag{4.13}$$

It should be noted that the BBO equation does not account for the effects of particle rotation on relative particle motion.

4.2.3 Lift Force

The rotation of spherical particles in flow can create a lift force acting on the particle (figure 4.3. Particle rotation can be caused either by velocity gradients in the fluid or due to contact with a boundary such as the lumen in arteries. The Saffman lift force [142] for small Re_r is a function of particle size, fluid viscosity, relative velocity and the square root of the shear Reynolds number

$$F_{Saff} = 1.61\mu d|u_{pf}|\sqrt{Re_{ss}} \tag{4.14}$$

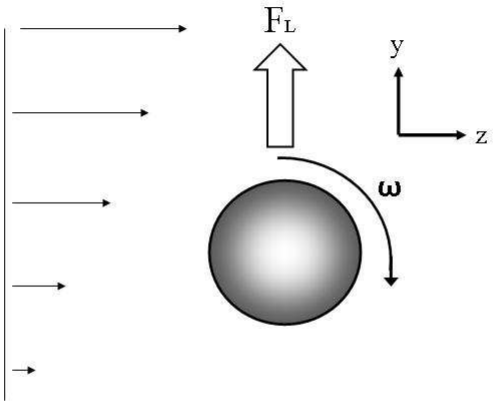

Figure 4.3: *Lift force*

where shear Reynolds number is defined as

$$Re_{ss} = \frac{\rho_f D^2}{\mu} \cdot \frac{du_f}{dy} \tag{4.15}$$

The Saffman lift force, as well as more recent derivations such as those by Wang and Squires [181], assume that the particle Reynolds number is small compared to the shear gradient Reynolds number which is in turn much smaller than unity so $Re_r << Re_g << 1$. Mclaughlin [103] expanded the Saffman lift force to account for larger Reynolds numbers.

The Saffman force assumes that particle rotation is solely attributed to fluid gradient effects. Any deviation in rotation caused by external forces, such as particle-boundary collisions is therefore not accounted for by the Saffman lift force. The change in lift force created by the difference in rotation is described by the Magnus force which for low Reynolds number flows [141] can be written

$$F_{Mag} = \frac{\pi}{8} d_p^3 \rho_f \left(u_{pf} \times \omega_{pf}\right), \tag{4.16}$$

where ω_{pf} is the difference between fluid and particle spin velocity. To calculate Magnus lift force, the particle rotation rate must be known at all times. In the vasculature this becomes difficult due to collisions between cells within the flow and the various binding behaviours of leukocytes when contact is made with the lumen. For these reasons, the Magnus force is generally neglected when modelling blood flow.

For small, spherical particles such as leukocytes, neither of the above lift forces have a sig-

nificant effect on the drag forces affecting the particle [28]. Because of the negligible effects of lift forces on particles in flow away from a boundary, F_L from equation 4.1 can be set to zero throughout the bulk of the model. Lift force becomes more significant when a particle approaches a wall at which point it must be accounted for with a near wall lift force term as described below.

4.2.4 Near Wall lift and drag forces

Stokes drag term is sufficient when modelling blood-cell sized particles in unbounded flows though the term breaks down when the particles approach a boundary with a no-slip condition. In order to observe the probability of particle-wall adhesion, accurately simulating the behaviour of the particle in the near-wall region becomes important and the need for accuracy of lift and drag forces is non-trivial. A particle is in the near wall region when the distance from the centre of the particle to the wall is on the same order of magnitude as the particle diameter. Upon entering the near wall region, the modified shear gradient created by the presence of a boundary causes the Stokes drag term to fail and generates an increase in particle rotation which in turn creates an increase in lift force magnitude.

Goldman, Cox and Brenner [52] define the drag on a sphere moving normal to a boundary as

$$F_n = (-m_p \frac{1}{\tau_p} u_{pfn}) f_{norm} \tag{4.17}$$

where f_{norm} is a coefficient dependent on both particle radius and the distance of the particle from the wall.

Goldman et al [52] give a similar equation for the drag on a sphere moving tangentially to the boundary

$$F_t = (-m_p \frac{1}{\tau_p} u_{pft}) f_{tang} \tag{4.18}$$

where the coefficient f_{tang} is a function of angular velocity, shear rate and the ratio of particle-wall distance to particle diameter.

Young and Hanratty [192] proposed analytical solutions to the near wall drag forces and found them to be consistent with experimental results. Loth [97] provides simple approximations of the Young and Hanratty drag coefficients which are stated to be within 2% accuracy of the

originals and can be expressed with reference to equations 4.17 and 4.18 as

$$f_{tang} = 1 + 0.7(d_p/h_p)\ ,\ f_{norm} = 1 + 1.1(h_p/d_p - 1)^{-1}. \tag{4.19}$$

The Saffman lift force also fails in the near-wall region. Since its initial conception, the lift force has evolved from the original model proposed by Saffman into a model which encompasses a wider range of flow regimes, including conditions in the near-wall region.

Vasseur and Cox [175] modelled particle forces between parallel walls and defined a lift force due to the presence of a boundary which holds even at distances outside of the near wall region and Cox and Hsu [26] derived an analytical solution for inertial migration velocity of a small sphere in a vertical linear shear flow.

While these models were shown to be in good agreement with experimental data, they still did not account for the lift and drag forces on particles in the critical near-wall region wherein the distance between the particle and the wall is the same order of magnitude as the particle radius. Cherukat and McLaughlin [21] modified the existing lift force models to create a new model which was shown to agree with experimental observations of particles in the near-wall region. As with the near-wall drag forces, the lift force proposed by Cherukat and McLaughlin is based on shear rate, particle radius and the ratio of particle-wall distance to particle radius and can be written

$$F_{lift} = \rho_f d_p^2 u_s^2 \cdot I\left[\frac{h_p}{d_p}, \frac{\dot{\gamma} d_p}{u_s}\right] \tag{4.20}$$

where $\dot{\gamma}$ is shear rate and u_s is the wall-tangent particle slip velocity $u_s = (u_{pt} - u_{ft})$

By integrating their experimentally-validated model, Cherukat and McLaughlin showed that the function I can be approximated by

$$\begin{aligned} I = &\left[1.7631 + 0.3561\lambda - 1.1837\lambda^2 + 0.845163\lambda^3\right] \\ &- \left[3.24139\lambda^{-1} + 2.676 - 0.8248\lambda - 0.4616\lambda^2\right]\Gamma \\ &+ \left[1.8081 + 0.8796\lambda - 1.9009\lambda^2 + 0.98149\lambda^3\right]\Gamma^2, \end{aligned} \tag{4.21}$$

where $\lambda = h_p/d_p$ and $\Gamma = \dot{\gamma} a_p/u_s$ This approximation was found to result in a force much

smaller than that predicted by Saffman.

4.2.5 Cell Dispersion

In this study, monocytes are modelled as sparsely concentrated discrete particles moving within a fluid phase. Whole blood is, however, composed of a high concentration of red blood cells and so, as the blood moves through the vessel, monocytes will collide with red blood cells and other leukocytes, potentially displacing them in a way which cannot be accounted for by fluid mechanics alone. Longest et al [95] added a dispersion function to their model of cell motion to account for red blood cell collisions. The function assumes that collision intensity fits a Gaussian distribution and the resulting displacements are generated via a Monte Carlo statistical approach controlled by a dispersion coefficient. Leaving out a dispersion factor reduces some of the random mixing present in blood flow, but the model used by Longest et al contains a number of assumptions about cell behaviour with no physiological data to back them up. Their study reveals a relatively small (less than 5%) difference between residence time results with and without a dispersion function. For these reasons a dispersion factor was not included in this study.

4.2.6 Near Wall Particle Residence Time Model Theory

As discussed in Chapter 1, the process of leukocyte adhesion and transmigration is complex, involving cells rolling on the endothelium as weak selectin bonds are formed and broken then finally adhering to integrins before entering the wall. To model these biochemical interactions for the concentration of monocytes found in the aorta on a macroscopic scale would be hugely computationally demanding. Previous studies have used probablistic methods to determine cell adhesion and to circumvent the need for nanoscale simulation. Longest et al. [95] propose a non-dimensional Near Wall Particle Residence Time Model (NWPRT) parameter based on particle-wall distance and particle velocity magnitude.

Longest et al validated their NWPRT parameter through simulations which achieved significant positive correlation with *in vitro* cell deposition studies of both monocytes (Hinds et al [59]) and platelets (Affeld et al [2]) in axisymmetric geometries. Significant correlation was found to occur only when the NWPRT was used in tandem with the near-wall lift and drag terms.

Kim et al [72] propose an extension to the Longest NWPRT model accounting for particle

trajectory and inward normal flow velocity to create a more flexible model, accounting for particle rolling, to use for a variety of cell species. The model was applied to monocytes and platelets in a stenotic tube geometry. Since the variables in the Kim et al model tend towards the same values as the Longest model when observing monocyte behaviour it seems efficient to use the simpler, validated Longest et al NWPRT parameter.

4.2.7 WSS Limiter

Experimental investigations [80, 189] have shown that high WSS retards leukocyte adhesion. The NWPRT model is limited by the cell-wall distance and residence time of cells in each volume (thus is also limited by cell velocity) but is not limited by WSS. To create a more physiologically accurate model, the addition of a WSS-limiter to the NWPRT model is required whereby the original NWPRT model is multiplied by a scaling factor depending on leukocyte adhesion efficiency at a given WSS. This weakness has previously been noted by Longest et al in the implementation of their NWPRT parameter. Their solution was to incorporate an absolute-value WSS limiter whereby no cells adhere above a given WSS value. In the absence of physiological adherence data, this cut-off point was chosen arbitrarily to be one half of the time averaged WSS of the vessel observed.

In vitro studies by by Worthen et al. [189], Lawrence et al. [80, 81] show that the adhesion probability of free flowing leukocytes to a surface decreases as WSS increases. The evidence for probability of adhesion decreasing as a function of WSS means that the fixed critical WSS value used by Longest et al is physiologically unrealistic. A more realistic WSS limiter is defined below using data from the *in vitro* studies to create a function of adhesion probability based on WSS magnitude.

4.3 Methods

4.3.1 Numerical modelling of flow

The axisymmetric geometries with maximum bulge diameters of $D = d$, $D = 1.3d$, $D = 1.5d$, $D = 1.8d$ and $D = 2.1d$ where inlet diameter $d = 1.9$cm, as described in Chapter 2, have been used throughout this chapter. The techniques for meshing the geometries and near-wall boundary layer as well as details of the patient averaged flow waveform attached at the inlet are

also described in Chapter 2.

Chapter 3 shows that blood flow in both simple and patient-specific AAA models feature vortex formation and flow in transition to turbulence, particularly during the deceleration phase of systole. A LES turbulence model was applied to the numerical solver to provide accurate modelling of viscous mixing on the scale required. The model was included with no perturbations set at the inlet, and so turbulent eddies are created by flow downstream of the inlet. As the LES turbulence model is incorporated, the pressure coupling used is the Bounded Central Difference (BCD) method, otherwise all solver variables are as described in Chapter 2.

4.3.2 Particle Modelling

4.3.2.1 Monocyte Variables

The diameter, density and average concentration in whole blood of monocytes were taken as averaged values from literature. These variables are shown in table 1.1 Particles were injected at evenly spaced intervals on a cross-sectional plane at each timestep. The inlet velocity wave used features a period of backwards flow during late systole and so the injection plane was situated 1.5 cm downstream from the inlet to limit the number of particles escaping through the inlet. As the average flow velocity over one wave cycle is 3.44 cm/s, an injection of 12700 monocytes at each timestep will yield an average of 3×10^{-5} monocytes/ml of blood after one cycle, in agreement with the average physiological concentration.

4.3.2.2 Forces Acting on Particles

Particles were modelled using a one-way Lagrangian method. Particle trajectories were modelled as functions of Stokes drag force, pressure gradient and near-wall lift and drag forces. The equations of particle motion can be expressed by

$$m\frac{du_p}{dt} = F_D + F_P + F_{NWlift} + F_{NWdrag} \tag{4.22}$$

4.3.2.3 Near-Wall Lift and Drag Forces

The standard particle lift and drag force models which hold throughout the fluid continuum break down when a particle enters a near-wall region where the particle-wall distance is on the same order of magnitude as the particle radius. The near-wall lift and drag forces proposed by Cherukat and McLaughlin [21] and previously used to model monocyte and platelet dynamics by Longest et al [95] were used.

Near wall drag force, can be expressed as a combination of equations 4.17 and 4.18 with added variables to describe the dependence on particle direction

$$F_{NWdrag} = \frac{1}{\tau_p}\left[sgn_n|u_{pfn}|f_{norm} + sgn_t|u_{pft}f_{tang}\right] \tag{4.23}$$

where u_{pft} and u_{pfn} are the differences in velocity between the particle and the surrounding fluid in the tangential and normal directions respectively and f_{tang} and f_{norm} are the analytical solutions in the tangential and normal directions as described in equation 4.19. For the normal component of the equation, the directional variable is

$$sgn_n = \begin{cases} +1 & \text{if } u_f < 0, \\ -1 & \text{if } u_f > 0 \end{cases} \tag{4.24}$$

and for the tangential component

$$sgn_t = \begin{cases} +1 & \text{if } u_t < 0, \\ -1 & \text{if } u_t > 0 \end{cases} \tag{4.25}$$

Near wall lift force is given in equation 4.20 in which I is taken to be the numerical approximation given in equation 4.21

User defined functions accounting for near-wall forces were written in C code and compiled in Fluent.

4.3.3 Near Wall Particle Residence Time Model

The NWPRT model described by Longest et al [95] was used in this investigation. The structure of the model is based on equation 1.3 with s = 1 and can be written

$$NWPRT = \frac{Q}{n_{tot} V_{nw}} \sum_{i=1}^{n} \int_{path,i} \left(\frac{a_p}{h_p} \right) \frac{1}{|v_i|} dr \tag{4.26}$$

The average flow rate Q, the total number of cells n_0 and the near wall volume V_{nw} are used to normalise the equation as a non-dimensional parameter. V_{nw} is calculated by multiplying the surface area by the height of the near wall region. The ratio of cell radius to the distance from the cell centre to the wall, a_p/h_p, provides a statistical parameter governing the likelihood of cell attachment when divided by particle velocity magnitude v_i. Longest et al apply a correction factor s to the model which is assigned a value depending on the species of cell being tracked.

The height of the active near-wall region must be on the same scale as the particle observed. In this study the height was taken to be $50\mu m$, to scale with the monocyte diameter of $16\mu m$ and the first near-wall volume height of $30\mu m$.

The NWPRT model was coded in C and attached to Fluent as a user defined function.

4.3.4 Creation of a WSS Limiting Factor

To create a physiologically realistic WSS-limiting factor, data from previous *in vitro* leukocyte adhesion studies was analysed. When choosing studies for analysis, the methodology is important. Studies in which leukocytes are initially attached to the wall before exposure to shear stresses show that they stay bound even at fairly high WSS of around 3.6 Pa [82], possibly due to strong integrin bonding. Since in this study the monocytes are not pre-fixed, experiments using free-flowing leukocytes were analysed. Results from studies by Worthen et al. [189] and Lawrence et al. [80, 81] were used. The three studies share a similar methodology whereby leukocytes were placed in suspension by an active surface and exposed to varying amounts of WSS. Lawrence and Springer used neutrophils on an artificial bilayer containing selectins. Worthen used neutrophils on a layer of cultured endothelium and Eskin used Polymorphonuclear Leukocytes (PMNL) on Human Umbilical Vein Endothelial Cells (HUVECs). It should be noted that while these studies use neutrophils, it is assumed that monocytes will behave in a

similar manner as the mechanisms for adhesion are similar.

Each study shows the number of leukocytes adhering to the surface at varying WSS magnitudes. To convert the occurance of adhesion into adhesion efficiency, the data was normalised by dividing the number of attached cells by the total number of cells released in the near surface region giving a factor of adhesion efficiency between 0 and 1. At efficiency of 1, all cells will attach, at efficiency 0, no cells attach.

All studies show no adhesion occurs above a WSS of 0.36 Pa. The Lawrence and Springer and Eskin et al studies show adhesion efficiency decreases linearly between WSS of 0.075 and 0.36 Pa. Out of the studies analysed, only Worthen et al provided data below a WSS of 0.075 Pa. As the WSS tends to zero, the adhesion efficiency increases exponentially.

The variable WSS limiting value was created by fitting a curve to the combined adhesion efficiency against WSS magnitude data of all three *in vitro* studies. The equation of this curve was then applied to the NWPRT model so that $NWPRT_{shearlimited} = NWPRT \times ShearLimit$ A curve with equation

$$ShearLimit = \frac{(\tau_w - 0.4)^2}{(2.4\tau_w) + 0.16} \tag{4.27}$$

was shown to fit the experimental data well. Figures 4.4(a), 4.4(b) and 4.4(c) show the WSS-limiting curve plotted against normalised results of the Eskin, Lawrence and Springer and Worthen data respectively.

4.3.5 Monocyte Modelling Protocol

Monocytes were released from the beginning of the third pulsatile cycle to ensure cycle independence in the background flow. Cells were injected at each t=T/200 (4.6406×10^{-3} second) time step over one full wave cycle. The user defined function for NWPRT was attached at the start of the fourth cycle so the cells injected on the previous cycle will already be dispersed throughout the geometry. Cells were then tracked and NWPRT obtained for a further 6 cycles.

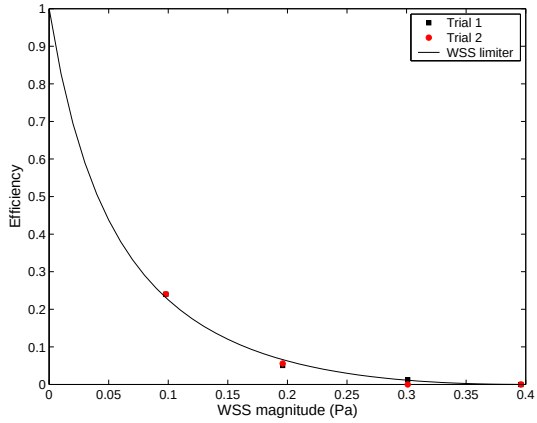

(a) Lawrence et al, '87

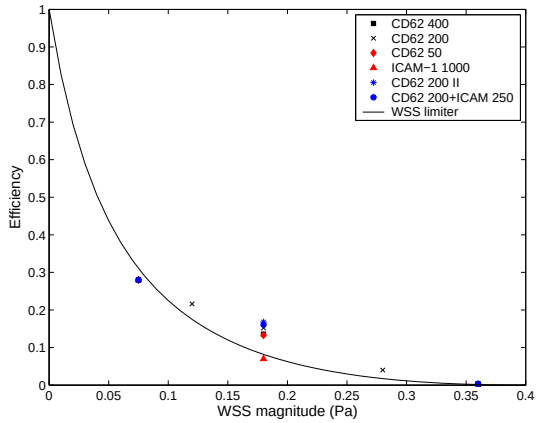

(b) Lawrence et al, '95

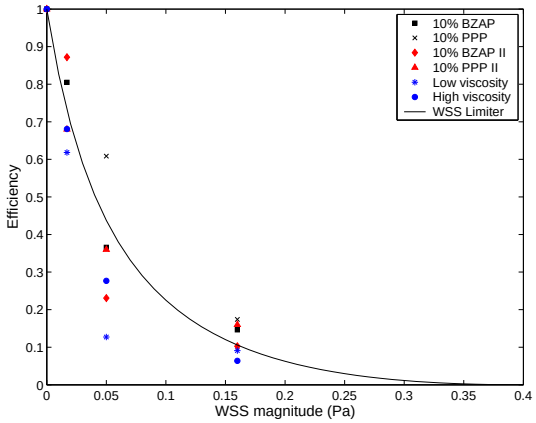

(c) Worthen et al

Figure 4.4: *WSS limiting function plotted against normalised leukocyte adhesion efficiency from in vitro experimental data;(a)Lawrence et al, '87 (b)Lawrence et al '95 trials on a membrane containing the selectin CD62 and ICAM-1 in the densities shown (sites per μm^2) (c) Worthen et al trials using high and low viscosity fluid and different blood plasma types. BZAP = bovine zymosan-activated plasma, PPP = platelet poor plasma*

Fluid Properties		Particle Properties		Transient Properties	
Viscosity (μ_f)	Density (ρ_f)	Radius	Density (ρ_p)	Re_{mean}	α
0.001 Pa	1000 kg/m^3	$3.75\mu m$	1130 kg/m^3	23.2	0.23

Table 4.1: *Properties used in Karino and Goldsmith's model of cell motion in an annular expansion [66]*

4.3.6 Motion of a Red Blood Cell in an Annular Expansion

To validate the choice of lift and drag forces acting on the simulated particles, the experimental investigation tracking the motion of a hardened red blood cell in water through an annular expansion subject to pulsatile flow conducted by Karino and Goldsmith [66] was reproduced. The Karino and Goldsmith experiment has previously been used as validation for numerical models by Longest et al [95]. The expansion geometry used was a straight tube of diameter 1.51×10^{-4}m flowing into a larger tube of diameter 5.04×10^{-4}m. In order to calibrate the numerical flow dynamics with those in the experimental investigation a steady flow simulation was replicated with an inlet Reynolds number of 37.8 using a solution of water mixed with aqueous $Cd(NO_3)_2$. The attachment point found in the numerical model after 2500 iterations was found to be 7×10^{-4}m compared to 7.15×10^{-4}m in the experimental model. The physical properties of the cells and fluid used in the pulsatile flow experiment are given in table 4.3.6.

A sinusoidal inlet flow waveform was applied at the inlet with an average Reynolds number of 23.2 conforming to the Womersley parameter $\alpha = 0.23$

For numerical modelling, the annular expansion was simplified to a two-dimensional axisymmetric backwards facing step meshed with 50212 square grid elements. For the purposes of numerical modelling, the red blood cells have been assumed as spherical despite their physiological biconcave nature. This assumption has been used previously by Longest et al [95] and others [72] to validate numerical models against the Karino and Goldsmith experiment.

It should be noted that for the annular expansion experiment, the cell does not reach a point sufficiently near the wall to encounter the near wall lift and drag forces and so they are not specifically validated via this experiment. The near-wall forces used have been previously validated by Cherukat and McLaughlin [21].

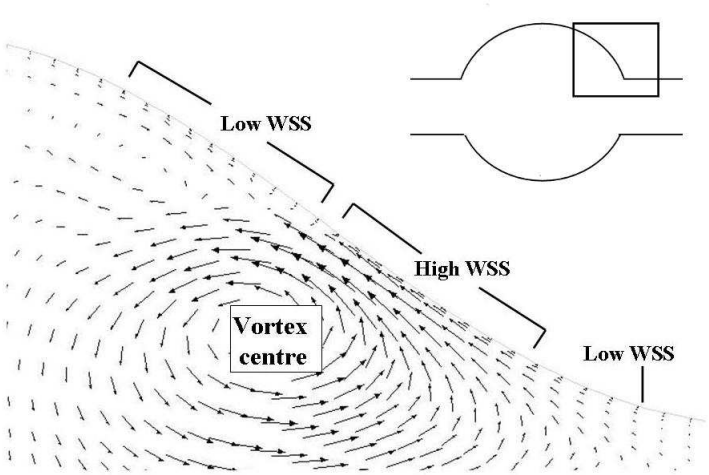

Figure 4.5: *Regions of high and low WSS magnitude around dissipating vortex*

4.3.7 Analysis of Haemodynamic and NWPRT Data

Cross sectional contour plots of velocity magnitude overlaid with vectors of axial velocity were used to show overall haemodynamics including areas of secondary flow and regions of vortex formation. Contours of WSS magnitude allow the distribution of WSS intensity to be observed throughout a full cardiac cycle. The cumulative NWPRT over 5 cycles is displayed as histograms of NWPRT against distance from the centre of the cavity to show the spatial distribution of monocyte adhesion probability.

Previous investigations have shown AAAs to be dominated by vortex formation [4, 15, 37] and dissipation. Vortex behaviour is therefore likely to control the motion of monocytes transported in the flow. To investigate any correlation between monocyte adhesion probability and vortex behaviour, a variable is required which shows the relative position of vortices throughout the cardiac cycle. This can then be compared with the spatial aggregation of NWPRT. The region of the wall proximal to the centre of the vortex will experience high velocity reverse flow in the near wall region. This will create a region of high magnitude negative WSS surrounded by regions of low to zero WSS at the points of flow detachment and attachment (figure 4.5).

Discrete regions of high magnitude negative WSS in longitudinal axial WSS profiles indicate the presence of a vortex proximal to the wall as seen in the steady flow WSS plots in Chapter 2. Time averaged axial WSS values can be used as a proxy variable to indicate the regions in

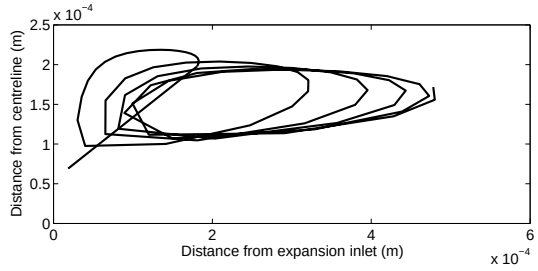

(a) T/t=0 - T/t=0.5

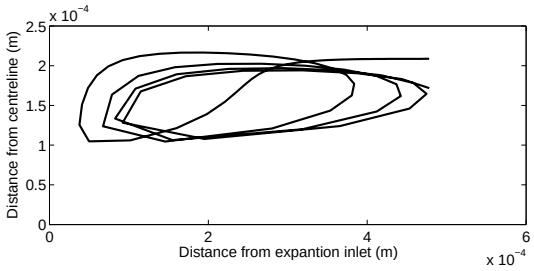

(b) T/t=0.5 - T/t=1

Figure 4.6: *Path of hardened red blood cell in an annular expansion during one pulsatile cycle*

the AAA in which vortices reside and the relative intensity of a vortex.

Plots of time averaged WSS against distance from cavity centre were created using the variable

$$WSS_{mean} = \frac{1}{T}\int_0^T WSS\, dt. \tag{4.28}$$

The vortex behaviour defined by WSS plots were compared with regions of peak NWPRT.

4.4 Results

4.4.1 Motion of a Red Blood Cell in an Annular Expansion

The particle enters the region of recirculating fluid in the expansion, travels 10 circuits and then exits the region in a path parallel to the wall (Figure 4.6) all in less than one pulsatile cycle ($T = -\pi/3 - 3\pi/2$). This result fits with the experimental observations of Karino and Goldsmith [66]. The time of injection in the simulated model was $t_{inj} = 1.05$ seconds.

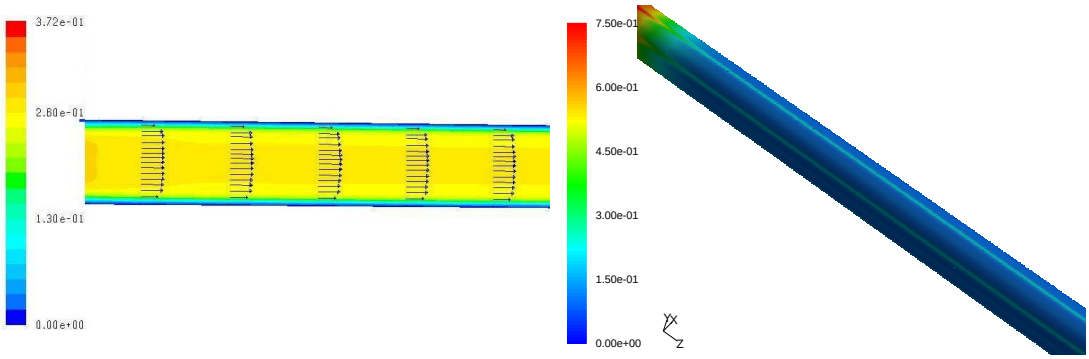

(a) T/t=0.25

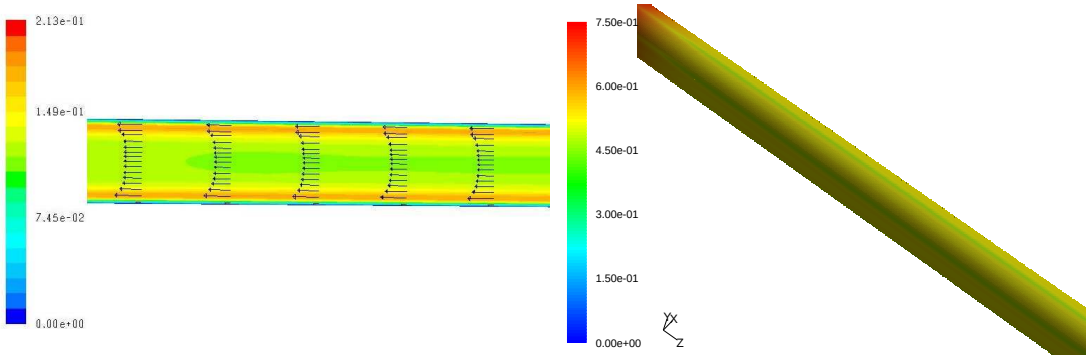

(b) T/t=0.5

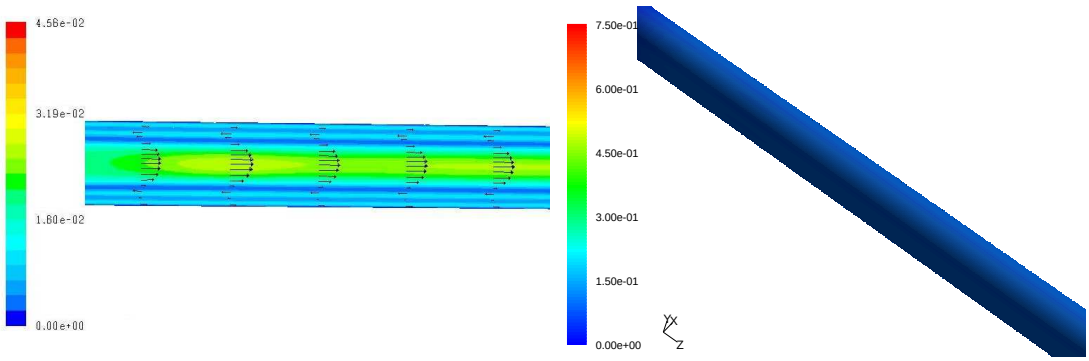

(c) T/t=0.75

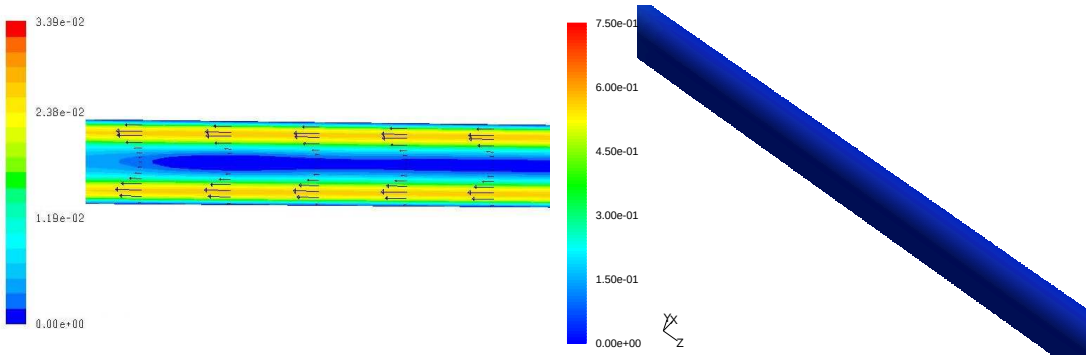

(d) T/t=1

Figure 4.7: *Contours and vectors of velocity magnitude (m/s) and (Right) contours of WSS (Pa) for* $D = d$

4.4.2 Haemodynamics and NWPRT

Contours and vectors of velocity magnitude show that the presence of an aneurysm cavity causes vortex formation and dissipation. Velocity profiles in the straight tube (Figure 4.7), analogous to a healthy aorta, show no presence of vortex formation. The profiles remain parabolic, in keeping with the theory of flow in a straight tube which leads to generally homogeneous WSS distribution at each time point.

In model $D = 1.3d$ a small, annular vortex forms and dissipates at the proximal end of the cavity (figure 4.8) with peak WSS aligned with the centre of the dissipating vortex. A second, longer and thinner, vortex is also formed briefly along the cavity centre during diastole but does not attach to the wall.

As AAA diameter increases from $D = 1.3d$ to $D = 1.8d$, the intensity of the vortex produced also increases and the vortex translates further downstream before dissipating (figures 4.8, 4.9 and 4.10). At $D = 1.8d$ the vortex dissipates at the distal end of the cavity. The band of high WSS follows the path of the vortex with peak WSS during vortex formation at the proximal end of the cavity and a lower, but significantly above average band around the point of vortex dissipation. In all AAA models, regions of high WSS form discrete bands, generally related to vortex behaviour. Outside of these bands WSS and near wall velocity is much lower, with regions of stagnation forming at the cavity centres. At $D = 1.8d$, the force of the dissipating vortex creates a smaller, secondary vortex proximal to the original, producing a smaller band of WSS around 0.5 Pa.

The region of vortex dissipation remains at the distal end of the cavity in the $D = 2.1d$ model (figure 4.11). The dissipating vortex is more intense than in the $D = 1.8d$ model and so the secondary, proximal vortex becomes larger. WSS distribution is similar to that observed in $D = 1.8d$, but higher in magnitude (maximum WSS is 2.77 Pa in $D = 1.8d$ and 3.02 Pa in $D = 2.1d$). In the largest AAA, $D = 2.9d$, a third vortex is present towards the proximal end of the cavity during diastole (figure 4.12).

NWPRT is concentrated at the inlet of geometry $D = d$ (figure 4.13(a). The significant peak in inlet residence time may be an artefact caused by cells injected into the near wall region which migrate prematurely towards the wall and skew the residence times. The high NWPRT in this region of a straight tube with laminar flow suggests that similar patterns occurring in the AAA models may also be physiologically unrealistic.

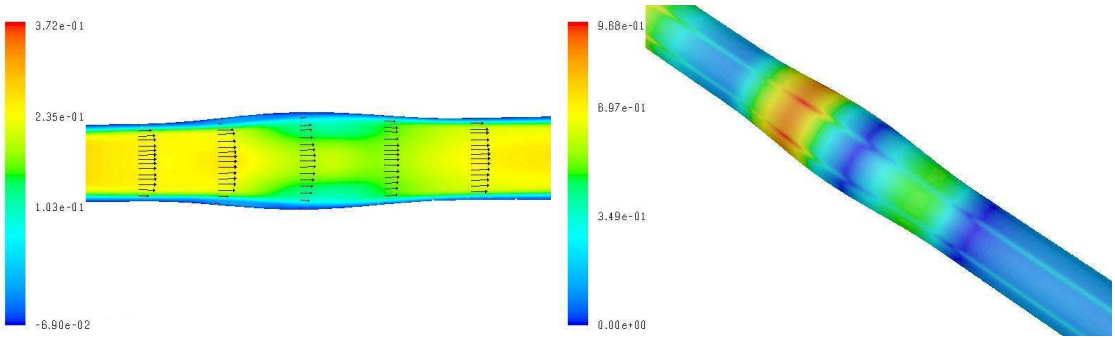

(a) T/t=0.25

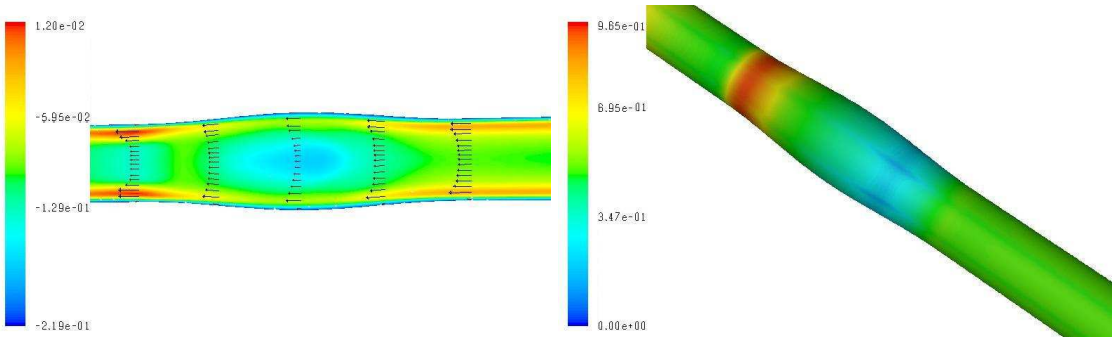

(b) T/t=0.5

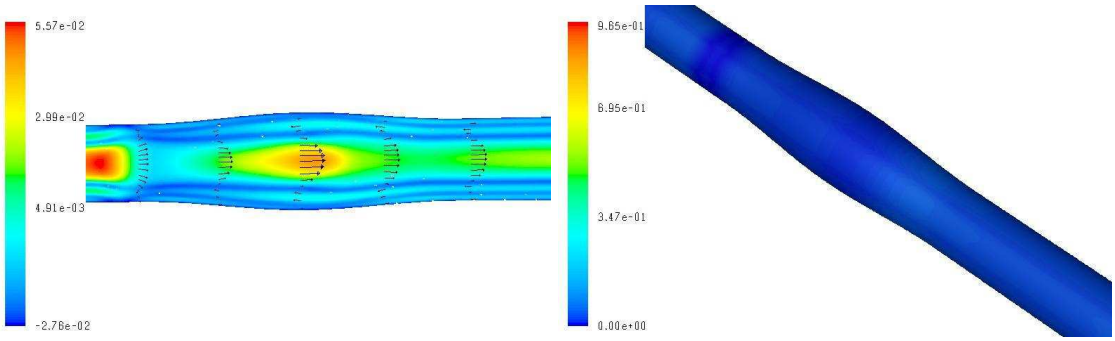

(c) T/t=0.75

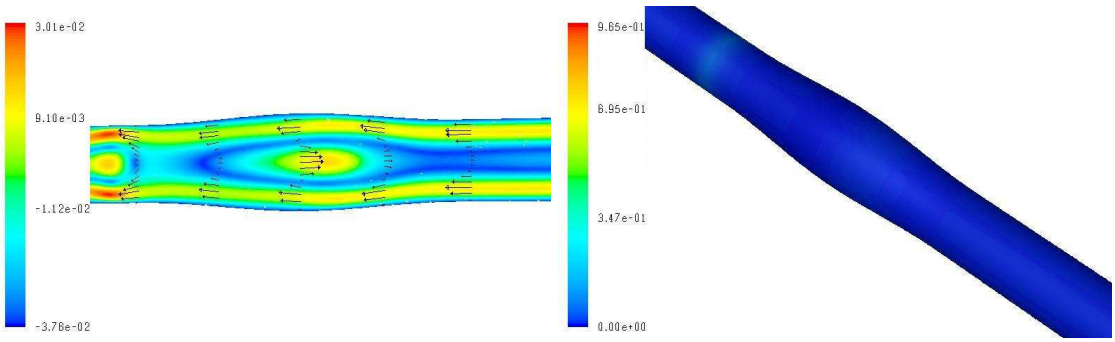

(d) T/t=1

Figure 4.8: *Contours and vectors of velocity magnitude (m/s) and (Right) contours of WSS (Pa) for* $D = 1.3d$

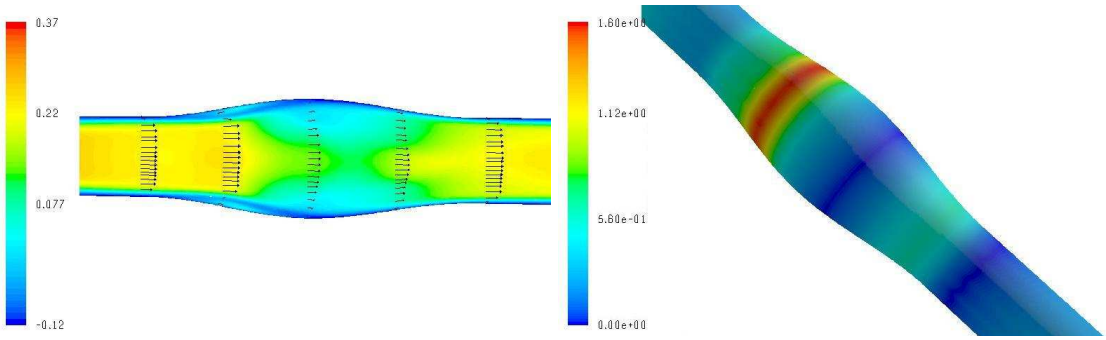

(a) T/t=0.25

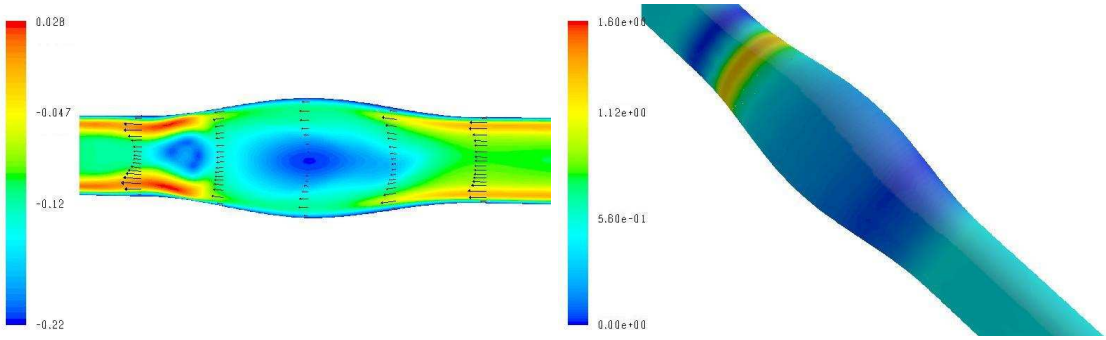

(b) T/t=0.5

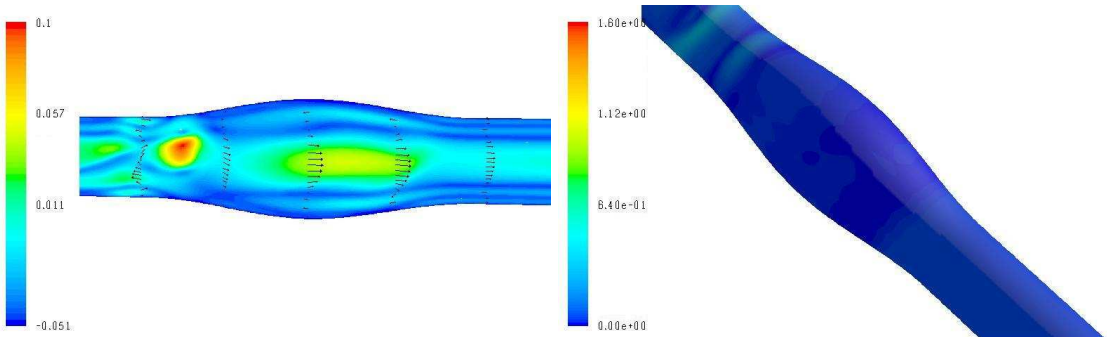

(c) T/t=0.75

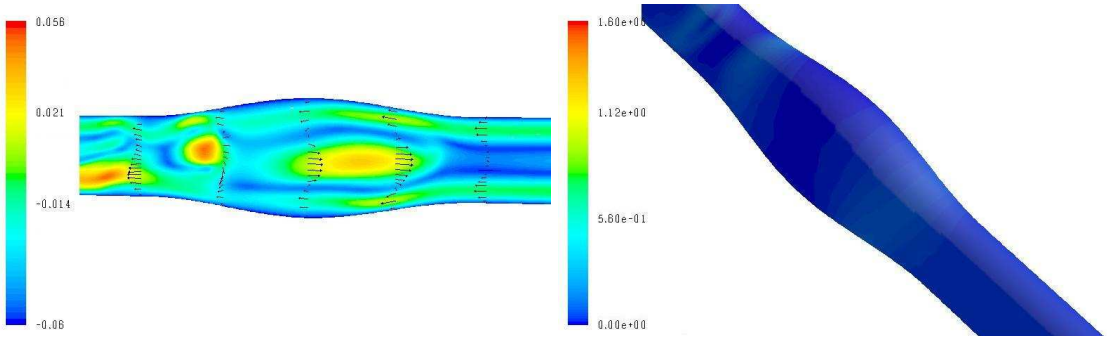

(d) T/t=1

Figure 4.9: *Contours and vectors of velocity magnitude (m/s) and (Right) contours of WSS (Pa) for* $D = 1.5d$

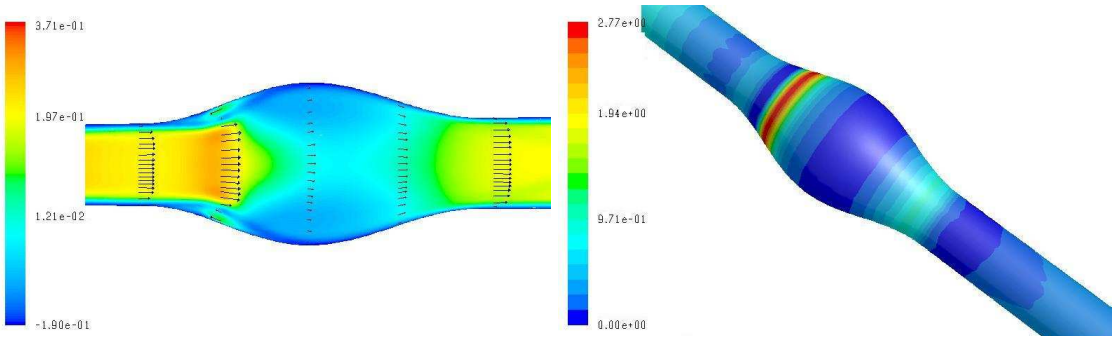

(a) T/t=0.25

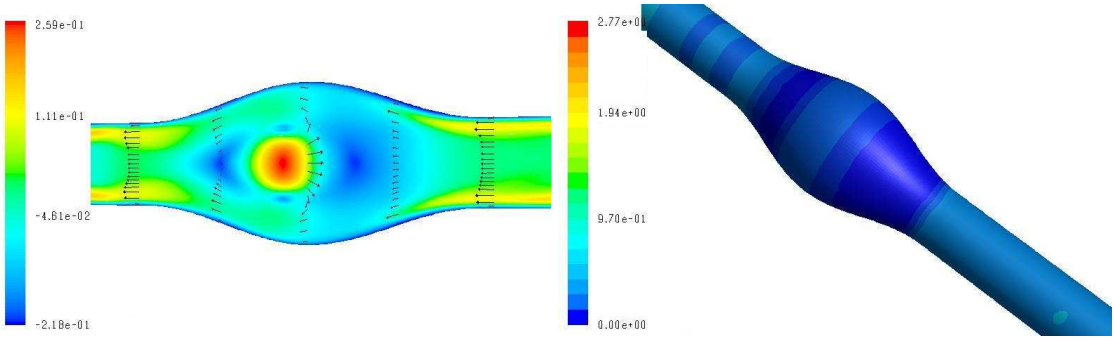

(b) T/t=0.5

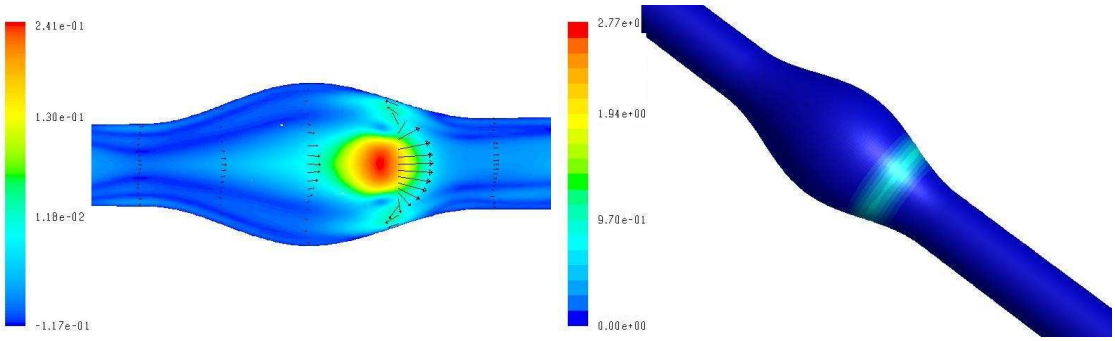

(c) T/t=0.75

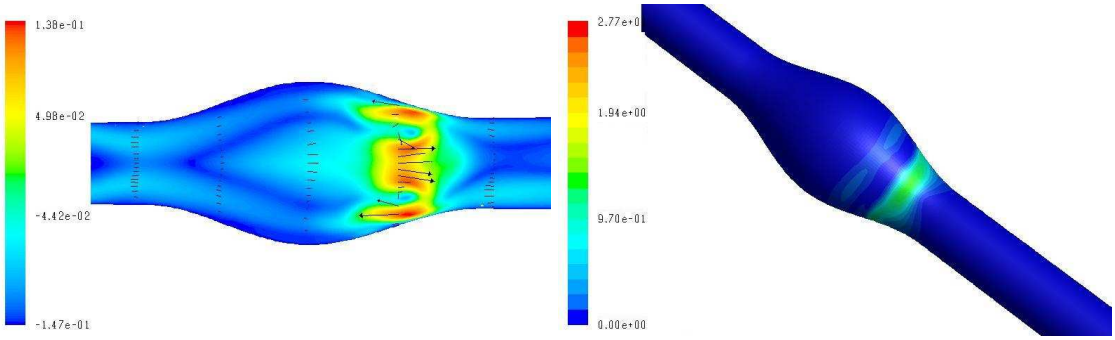

(d) T/t=0.25

Figure 4.10: *Contours and vectors of velocity magnitude (m/s) and (Right) contours of WSS (Pa) for* $D = 1.8d$

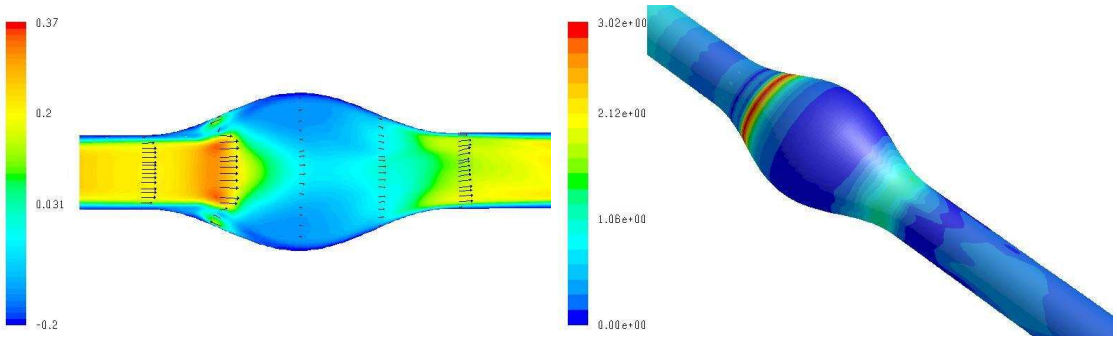

(a) T/t=0.25

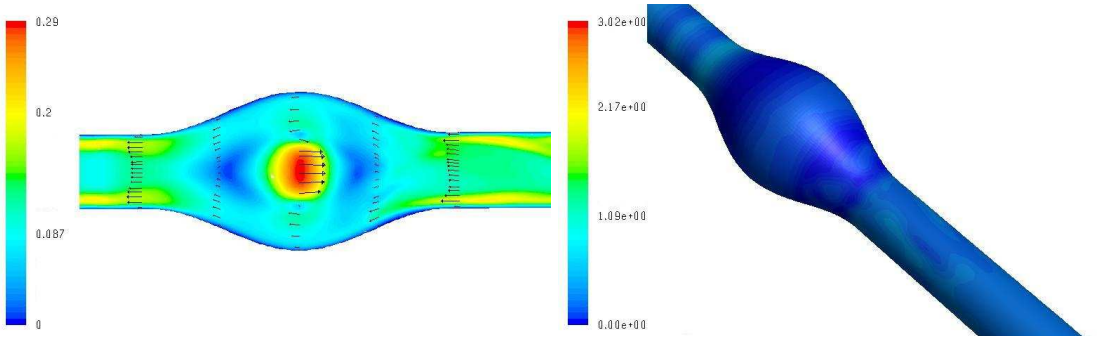

(b) T/t=0.5

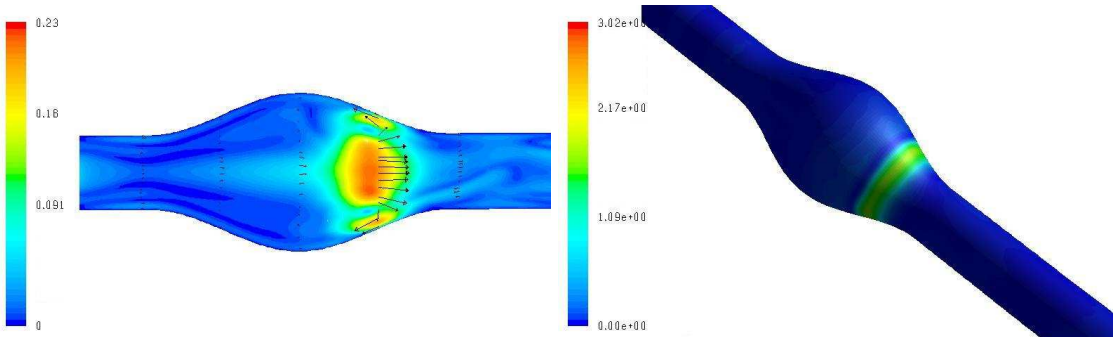

(c) T/t=0.75

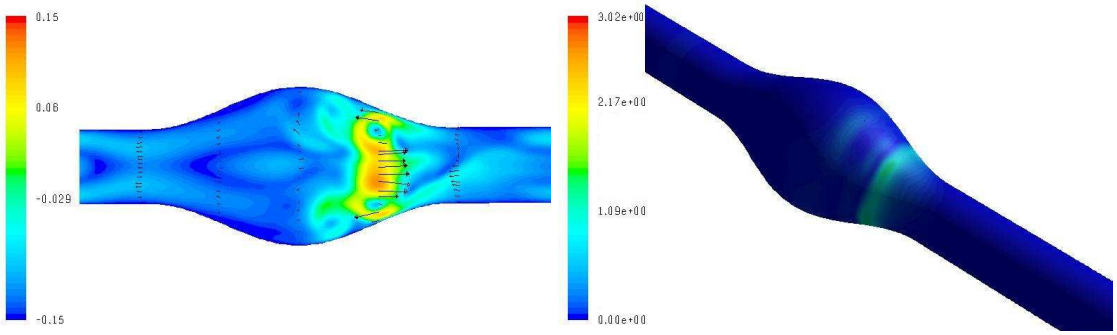

(d) T/t=1

Figure 4.11: *Contours and vectors of velocity magnitude (m/s) and (Right) contours of WSS (Pa) for* $D = 2.1$

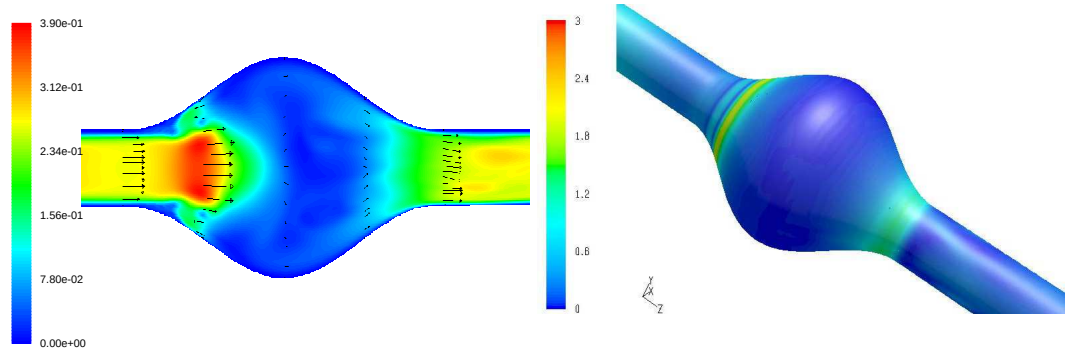

(a) T/t=0.25

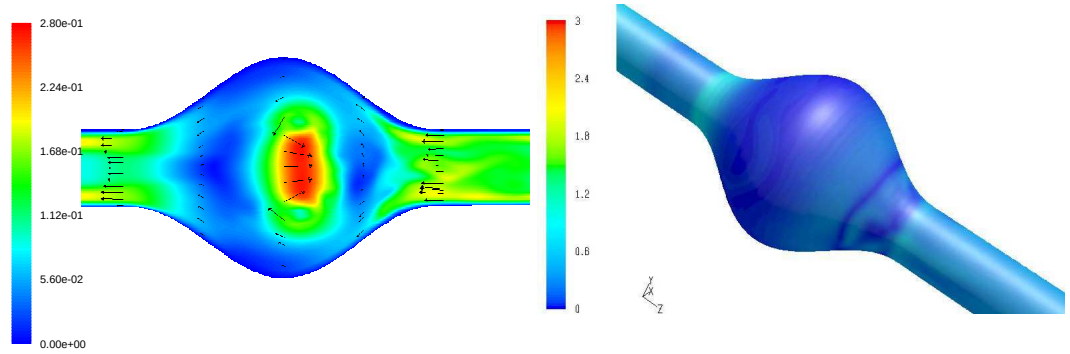

(b) T/t=0.5

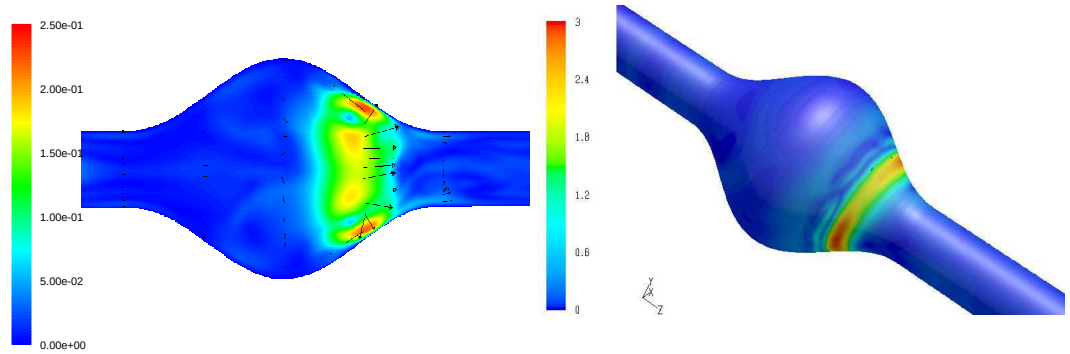

(c) T/t=0.75

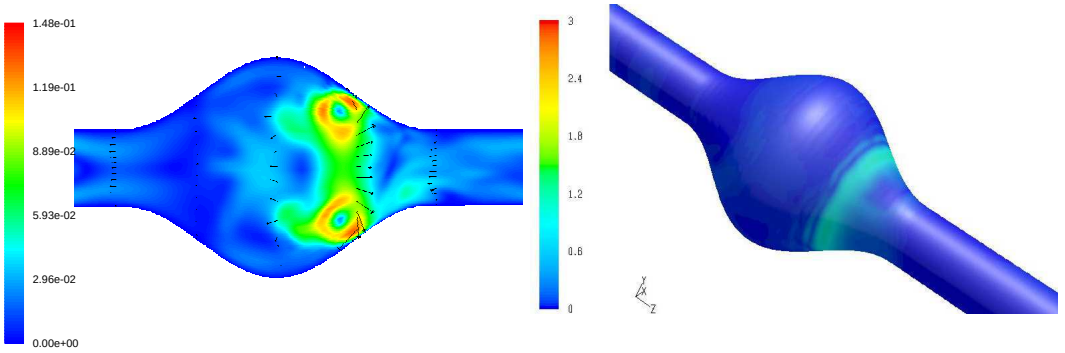

(d) T/t=1

Figure 4.12: *(Left) Contours and vectors of velocity magnitude (m/s) and (Right) contours of WSS (Pa) for* $D = 2.9$

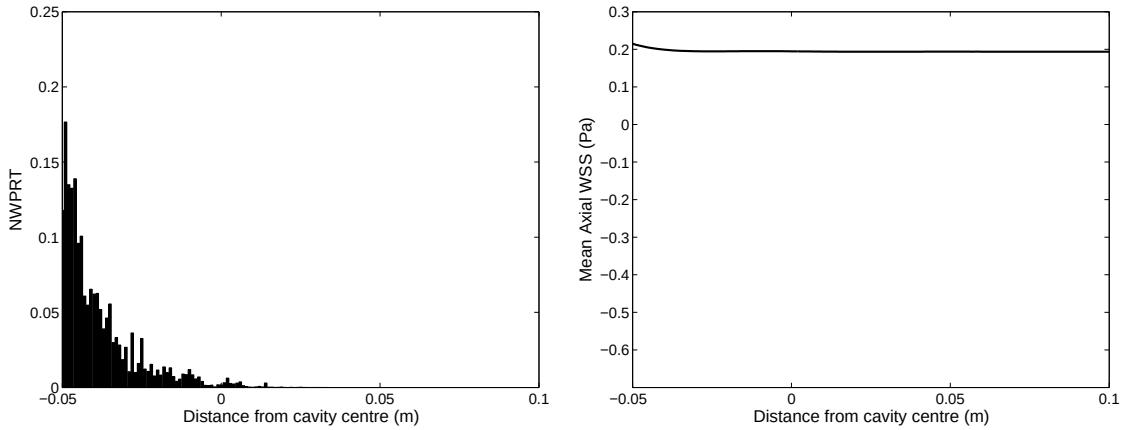

(a) (b)

Figure 4.13: *(a) Histogram of WSS-limited NWPRT against distance from cavity centre and (b) time averaged axial WSS against distance from cavity centre for $D = d$.*

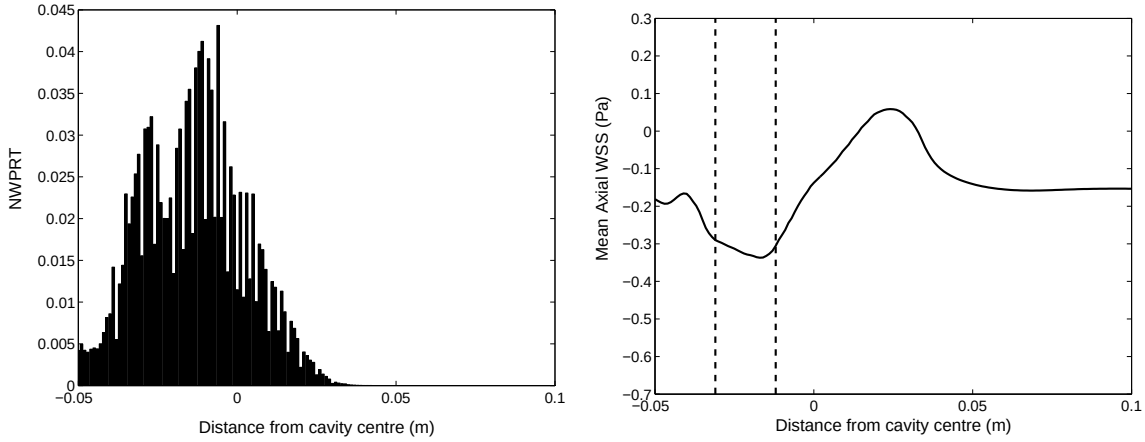

(a) (b)

Figure 4.14: *(a) Histogram of WSS-limited NWPRT against distance from cavity centre and (b) time averaged axial WSS against distance from cavity centre for $D = 1.3d$. Dashed lines align with regions of peak NWPRT.*

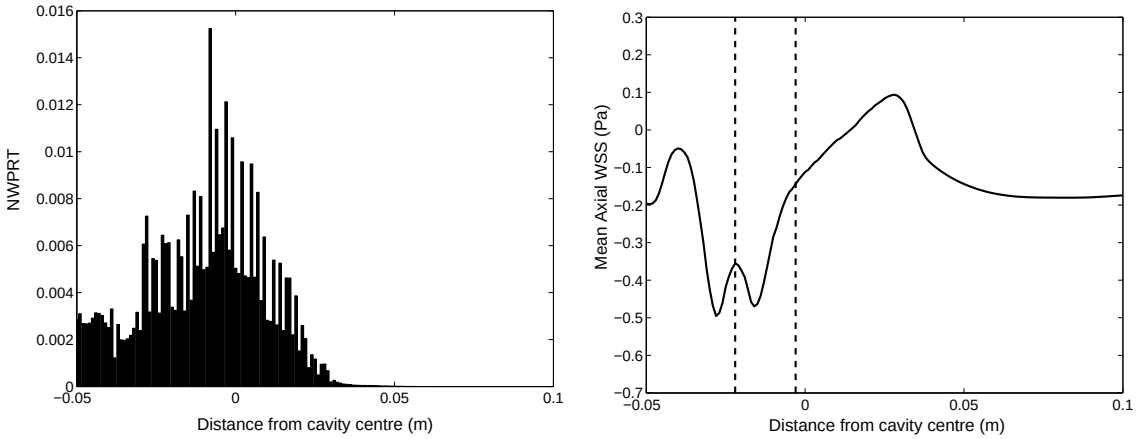

(a) (b)

Figure 4.15: *(a) Histogram of WSS-limited NWPRT against distance from cavity centre and (b) time averaged axial WSS against distance from cavity centre for $D = 1.5d$. Dashed lines align with regions of peak NWPRT.*

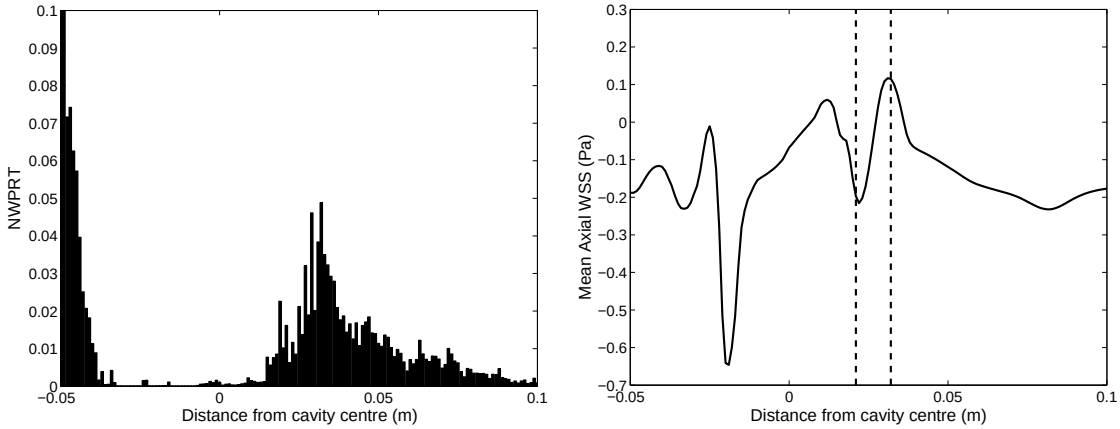

(a) (b)

Figure 4.16: *(a) Histogram of WSS-limited NWPRT against distance from cavity centre and (b) time averaged axial WSS against distance from cavity centre for $D = 1.8d$. Dashed lines align with regions of peak NWPRT.*

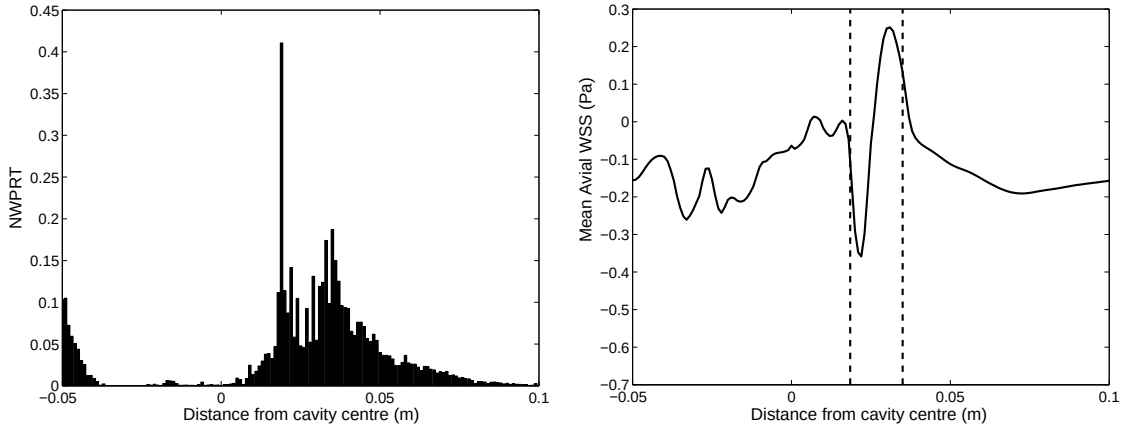

(a) (b)

Figure 4.17: *(a) Histogram of WSS-limited NWPRT against distance from cavity centre and (b) time averaged axial WSS against distance from cavity centre for $D = 2.1d$. Dashed lines align with regions of peak NWPRT.*

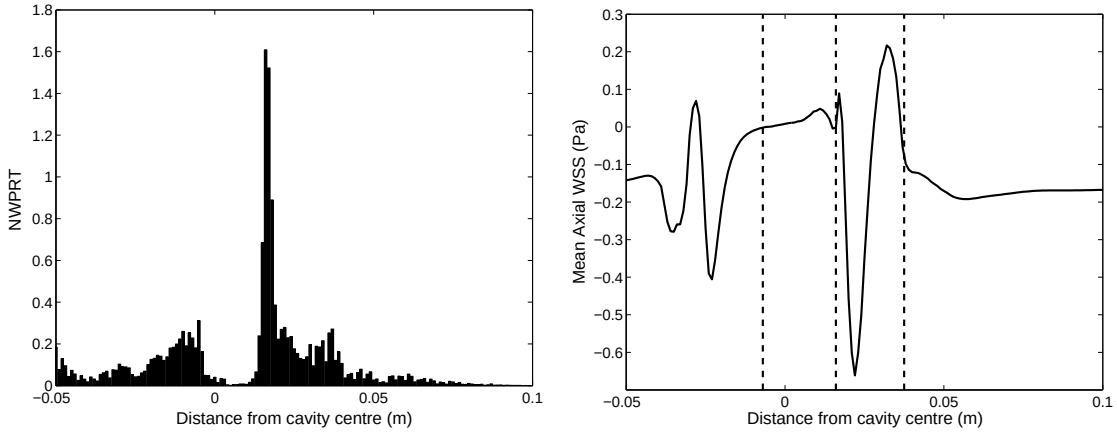

(a) (b)

Figure 4.18: *(a) Histogram of WSS-limited NWPRT against distance from cavity centre and (b) time averaged axial WSS against distance from cavity centre for $D = 2.9d$. Dashed lines align with regions of peak NWPRT.*

In $D = 1.3D$, two peaks of NWPRT are produced in the proximal half of the cavity, reducing to zero at the distal end (figure 4.14(a)). Peak NWPRT then moves distally with increasing AAA diameter. At $D = 1.5d$, figure 4.15(a) shows that maximum peak NWPRT is situated around the centre of the cavity, with a smaller peak 2.5 cm upstream. Unlike previous models there is very little residence time on the proximal side of the $D = 1.8d$ cavity (figure 4.16(a)). Two peaks of NWPRT occur towards the distal end, a thin peak of high magnitude NWPRT at a distance of 2.5 cm downstream of the centre and a second, wider but lower magnitude peak at the outlet. Model $D = 2.1$ departs from the previous trend of NWPRT distributions moving distally with increasing AAA diameter (figure 4.17(a)). Peaks in NWPRT are observed centred approximately 2 and 3 cm downstream of the cavity centre. A gradual decrease in residence time is seen downstream of the distal peak. $D = 2.1d$ also deviates from the trend of maximum NWPRT magnitudes which decrease in size between $D = 1.3d$ and $D = 1.8d$ and increases by a factor of 100 between $D = 1.8d$ and $D = 2.1d$. NWPRT in $D = 2.9d$ produces a distribution with 3 peaks and a higher magnitude than the $D = 2.1d$ model (figure 4.18(a)).

In models $D = 1.8d$ to $D = 2.9d$, mean WSS plots (figures 4.16(b), 4.17(b) and 4.18(b)) show spikes of high negative WSS at the proximal and distal ends of the aneurysm cavity, caused by the formation and dissipation of vortices as observed in figures 4.10 and 4.11. As the cavity becomes larger, the proximal spike diminishes in size while the distal spike increases. The increase in the distal spike is due to the dissipating vortex residing longer and releasing more energy at the distal wall, as seen in figures 4.8 to 4.12. In each of these three larger geometries, the upstream peak in NWPRT is aligned with the base of the distal WSS spike, the point at which flow detaches from the dissipating vortex. The downstream peak in NWPRT is aligned at a point distal to the spike of positive WSS, which is the region downstream of the flow reattachment point where flow from the dissipating vortex is forced towards the wall.

In the two smaller AAA geometries, mean WSS plots (figures 4.14(b) and 4.15(b)) show that the regions of vortex creation and dissipation are not discrete as the vortex does not travel into the distal half of the cavity before dissipating. NWPRT still follows the trends of the larger aneurysms with peak NWPRT distributed on either side of the point of vortex dissipation.

Histograms of NWPRT for simulations without the inclusion of the WSS limiter are found in Appendix B. Applying the variable WSS limiter to the NWPRT model reduces the relative magnitude of the proximal residence time peak in all models, sometimes significantly, and divides the $D = 2.1d$ result from one elongated peak into 2 peaks.

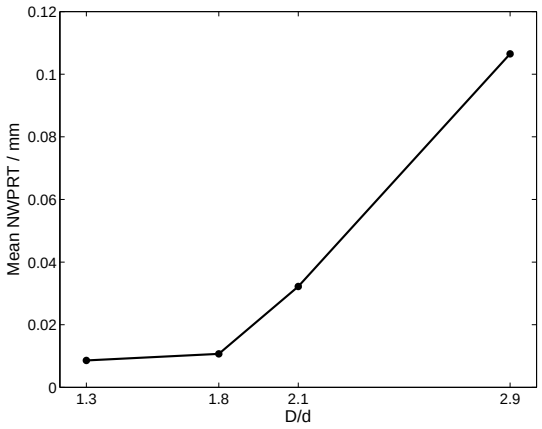

Figure 4.19: *Mean NWPRT per millimeter for all AAA model sizes*

As AAA diameter increases, the region of vortex dissipation progresses distally between $D = 1.3d$ and D=$1.8d$, at which point the primary vortex dissipates at the distal end while a secondary vortex is formed immediately upstream. Further increases in diameter retain these general characteristics of haemodynamics though the intensity of the vortex increases. Bands of maximum WSS magnitude appear to co-locate with vortex regions and regions outside of these bands generally have significantly lower WSS and near wall velocities. NWPRT in all AAA geometries have two or three peaks in NWPRT, depending on the number of vortices present, these move distally between $D = 1.3d$ and $D = 1.8d$ then move proximally in larger geometries. The magnitude of peak NWPRT decreases between $D = 1.3d$ and $D = 1.8d$ then increases significantly in aneurysms larger than $D = 1.8d$.

Figure 4.4.2 shows that the average NWPRT per millimeter remains similar between $D = 1.3d$ and $D = 1.8d$ then rises rapidly as as the aneurysm increases in size.

4.5 Discussion

Haemodynamics within the simplified AAA geometries were very much driven by the formation and dissipation of annular vortices within the cavities. The formation, translation and dissipation of vortices seen in the simulations have been observed in previous simulations such as those by Finol and Amon [41]. Finol and Amon noted that multiple, counter-rotating vortices occur in the cavity of larger AAAs at high Reynolds numbers, a similar effect to the vortices found in the two largest models investigated here. Ehelhoff [37] investigated flow dynamics in AAA models with a range of bulge sizes and found that the flow regimes found could be

divided into three groups; small AAAs with low Reynolds numbers in which flow stays attached throughout the pulsatile cycle, medium AAAs in which vortex formation and translation begins even at lower Reynolds numbers and large AAAs which contain fully formed vortices and a transition to turbulence. These regimes fit well with the haemodynamics described in the AAAs investigated in this study.

WSS magnitude and direction is controlled by the dynamics and intensity of vortices within the AAA. In smaller aneurysms the region of high magnitude negative WSS associated with vortex dissipation moves downstream as the aneurysm increases in size. This trend is seen in the experimental investigation of small aneurysms by Salsac et al. In larger aneurysms, the region of vortex dissipation remains static and attached to the distal wall, while the time averaged peak negative WSS increases in magnitude indicating higher vortex intensity. Time averaged WSS plots of larger AAAs in the investigation by Fraser [46] are similar to those in this study and show the spatial trends continuing for AAAs of greater than 5.5 cm diameter, while the peak negative WSS magnitude stops increasing at a diameter of 5cm.

Longest et al included a fixed critical WSS limit, assumed to be half of the time averaged WSS for the artery investigated, above which NWPRT is no longer recorded. This assumption was arbitrary, and so a more physiologically realistic WSS-limiter was created for this study based on a meta-analysis of *in vitro* investigations of leukocytes rolling on endothelial cells under various shear stresses. The WSS-limited NWPRT model produced significant differences in residence times around the proximal peak in NWPRT, reducing its magnitude relative to the distal peak. This indicates that the proximal peak is formed in a region exposed to higher WSS. The differences observed suggest that a WSS limiter is necessary to produce accurate results when modelling the probability of monocyte adhesion in AAAs.

As each vortex dissipates, the monocytes which were initially pulled into the rotating flow are released against the lumen where they can become trapped in low velocity near wall flows increasing the NWPRT and the probability of cell attachment. In smaller AAAs, the magnitude of points of peak NWPRT decreases and moves distally as the maximum bulge diameter increases. This study shows that at a critical AAA diameter the primary vortex creates smaller vortices upstream and peak NWPRT increases in magnitude while the distribution moves back upstream. In physiological terms, this means that as the AAA is initiated and begins to grow, there is a higher probability that monocytes will infiltrate the proximal end of the aneurysm and as the AAA grows the area most likely to be infiltrated by monocytes moves downstream until

the AAA. Once the aneurysm has developed is reaches the critical diameter above which the regions of high probablity of inflamation move upstream. Conversely, an increase in ILT may keep the cavity below the critical diameter and lead to monocyte infiltration moving upstream. The results suggest that when the aneurysm cavity exceeds the critical diameter the probability of monocyte adhesion increases exponentially. Physiologically this would create a positive feedback effect resulting in further expansion of the aneurysm. Formation of thrombus in the cavity may prevent the aneurysm from reaching this critical stage, and so play a protective role in AAA pathology. This study shows the critical AAA size at which haemodynamics change to be around $D = 1.8d$, giving a maximum diameter of 3.42 cm with the dimensions used here which is well below the 5.5 cm AAA size at which surgery is considered.

The simulations show that, in simple geometries at least, monocyte adhesion is likely to occur in distinct areas, or hotspots, within the AAA cavity. The largest of these hotspots are aligned with regions of vortex dissipation. Outside of these areas, the probability of adhesion is generally much lower or negligible. If these hotspots of monocyte adhesion correlate with regions of wall which are high in macrophage content then it can be assumed that higher levels of wall degradation occur in these areas due to the degredation of the ECM via macrophage-linked substrates. Conversely, the areas with limited or no monocyte activity would be expected to contain less intra-wall macrophages and so receive limited degradation. If, however, imaging or histology of the wall were to show no correlation between areas of peak monocyte residence time and macrophage accumulation then this study suggests that monocytes enter the wall, or are transported through the wall via a radically different method than the standard model of transmigration.

By applying the techniques used in this chapter to patient specific AAA geometries and performing validation studies to ensure a correlation between high monocyte NWPRT and cell infiltration, this technique could be used to identify hotspots of monocyte infiltration and thus structural dynamics in patients. Further clarification of the role of monocyte adhesion in inflammation and subsequent aneurysm rupture would require clinical studies, possibly involving the use of PET-FDG imaging to assess infmallation, and longitudinal studies to follow patients to rupture.

4.6 Conclusions

By studying haemodynamics in simplified AAA geometries with a variety of physiologically realistic diameters it is clear that the formation and dissipation of vortices are the defining characteristics of flow in AAA. It is this vortex behaviour which appears to control the motion and residence times of monocytes seeded into the flow. Cells are pulled into the vortex as it grows and then released towards the wall at the point of flow detachment and reattachment. In accordance with vortex progression, peak monocyte residence times are located towards the proximal end of the AAA cavity in smaller aneurysms, moving downstream as the aneurysm gets progressively larger until a critical AAA size. Above this size, the peak particle residence times increases significantly and become concentrated further upstream as the AAA enlarges. Since only the lumen is observed in this study, the results could also describe monocyte patterns in monocyte adhesion as thrombus builds up inside the cavity of a larger AAA. In each model the probability of monocyte adhesion calculated through NWPRT was distributed in hotspots of high adhesion probability with large areas of little or no cell residence time where adhesion is unlikely. Having elucidated the discrete regions of high and low monocyte residence time within the cavities of simple aneurysms, the techniques can now be applied to patient specific geometries and waveforms to determine if these hotspots are manifested in patient AAAs.

Chapter 5
Patient Specific Investigation

5.1 Introduction

So far flow has been simulated in models of generalised AAA geometries using an averaged patient flow wave form. In this chapter, these models are extended to patient-specific geometries and the effects of applying inlet boundary conditions of increasing complexity are investigated.

As computational processing power has increased and imaging techniques have improved in resolution and efficiency, the CFD modelling of haemodynamics in patient specific geometries with physiological inlet flow conditions has become possible. Patient-specific CFD simulations have the potential to be an invaluable clinical tool in assessing haemodynamics and stresses in large arteries [61, 156, 166]. In order to reach the stage of clinical usage the relative haemodynamic errors which arise through the use of different inlet boundary condition methods must be quantified in order to build an effective protocol for future modelling. Inlet boundary condition methods vary in complexity and, in theory, the more information that is required to create the boundary condition, the more similar it will be to *in vivo* conditions. When defining boundary conditions, aquiring the velocity information requires effort in terms of aquisition time and computational effort and so an investigation of boundary conditions must weigh up the relative errors involved against the efficiency of modelling.

Inlet boundary conditions of varying complexity are used in CFD simulations depending on the flow information available and the accuracy required. Pressure waveforms [180] or 1 dimensional circulation models [19] are generally required when wall motion is observed though on their own they include non of the spatial dynamics of the flow required for solving the 3 dimensional N-S equations of flow.

In rigid walled models, velocity inlet boundary conditions are generally used. If the spatial variation of inlet velocity is not available, the inlet velocity can be modelled either by a plug flow where a single velocity is applied over the entire inlet plane or by assuming flow is fully developed and converting the velocities to a series of profiles which agree with the Womersley number. Marzo et al [101] investigated the use of plug and Womersley flow profiles in

intracranial aneurysms and found that there is little difference in aneurysm cavity dynamics when applying either boundary condition though Womesley inlet flow is still commonly used for modelling patient specific aneurysms [46, 86].

While providing a theoretical solution for fully developed axial flow, Womersley flow profiles do not account for the spatial heterogeneity of axial flow and lack radial velocity information and so can only simulate bulk-flow dynamics and not secondary flow at the inlet.

As blood flows over the aortic arch secondary, helical, flows are formed [62]. While these helical flows are damped as blood travels down the relatively straight descending aorta, some of this secondary flow is still present below the renal arteries at the inlet of AAAs [48]. Limiting the velocity information used to create the inlet boundary conditions may remove some, or all, of the complexity of the upstream flow which may affect the accuracy of the downstream simulation. This effect has already been observed in Chapter 3 in which the application of turbulent perturbations at the inlet when using the LES model produces significantly different WSS profiles during late systole than when turbulence forms in the AAA geometry alone.

PC-MRI data can be used to obtain spatial velocty variability. This can be the velocity component in the direction of highest velocity magnitude, the 'head to foot' component in the case of the aorta, or the x, y and z components of flow velocity giving fully three dimensional inlet velocities. Of all the inlet boundary condition methods it is only tri-directional velocity which accounts for the complex secondary flows at the inlet and the angle of the aorta at the AAA neck however obtaining 3 directions of velocity requires increased imaging and computational effort. Despite this, there have been relatively few studies which utilise the spatial distribution of PC-MRI data. Long et al [93] compared simulations of flow using through-plane PC-MRI velocities at the inlet in the healthy aorta while Kose et al [74] and Fraser [46] did similar in AAA. Kose et al found 2D PC-MRI data to be significantly more accurate than plug-flow alone.

The studies mentioned above apply only axial velocities and there have been no previous studies to determine whether a lack of spatially varying or radial velocity data at the AAA inlet will affect the dynamics of flow and WSS inside the aneurysm cavity. A comparison of boundary condition types with *in vivo* flow data is required to assess the validity of previous published simulations and to identify the amount of detail required when selecting boundary conditions. In this study, PC-MRI was used to obtain patient specific blood flow velocities in the axial and radial directions and create velocity inlet boundary conditions of axial velocity, axial and radial

velocity and fully developed Womersley flow profiles.

Fluid dynamics and WSS are simulated in three patient specific AAA geometries segmented from CT scans. Using PC-MRI velocity data, three different types of velocity inlet boundary conditions are compared; three-components of velocity, one-component of velocity (head to foot) and parabolic velocity profiles based on centreline velocity at each timestep.

5.2 Method

The inlet boundary condition investigation used patient specific geometries and physiological flow waveforms created taken from 3 patients. Ethics permission was obtained and informed consent given by each patient. Geometry data was obtained from CT imaging, and inlet velocity data was obtained using PC-MRI.

To reduce error in simulations it is crucial to accurately determine the outline of the vessel lumen in each slice and to obtain a sufficient number of slices to ensure that interpolation between slices is kept to a minimum. The accuracy in ascertaining the lumen depends very much on the resolution of the scan and the contrast in image intensity between blood and lumen. Since the vessel wall is in motion throughout the cardiac cycle, defining the position of the lumen becomes a temporal as well as a spatial problem. Previous experience in acquiring geometry data using 1.5T MRI has met with problems of movement artefact obscuring the lumen walls, and preventing accurate segmented AAA geometry being obtained. Our experience with CT data [46] is that the AAA datasets are of low noise free from artefact and with good contrast between lumen and thrombus/wall, from which high quality segmented geometries can be obtained. As the geometry is acquired from CT and the inlet velocity from PC-MR it is important that the time taken between scans is minimal. The AAA is constantly evolving and so if too long a duration is left between scans the geometry may have changed which may in turn affect the velocity and haemodynamics of the AAA. For each patient the 2 sets of scans were conducted within a week of each other.

5.2.1 Phase-Contrast MRI

For all patients, gated PC-MRI measurements were taken at a cross-section immediately below the renal arteries at the neck of the AAA to provide inlet boundary conditions. At each cross-

Parameter	Value
Repetition time	5.215×10^{-2}seconds
Echo time	2.41×10^{-3}seconds
Flip angle	30°
Acquisition matrix	192x132
Pixel bandwidth	555 kHz
Velocity encoding	1.5m/s

Table 5.1: *PC-MR imaging parameters*

section, phase data and image intensity data was collected in through-plane, right to left and anterior to posterior directions at 20 equally spaced time points throughout the cardiac cycle using a 1.5 Tesla scanner. Blood velocity was obtained from the phase data and intensity images are used to define the lumen boundary at the inlet. The cardiac cycle duration was different for each patient and so the spacing of time points was also different. For patient 1 data was taken at 5.75×10^{-3} second intervals, for patient 2 data was taken at 3.36×10^{-3} second intervals and for patient 3 data was taken at 5.67×10^{-3} second intervals. The imaging parameters used to acquire PC-MR data are shown in table 5.1.

5.2.2 Generating Velocity Boundary Conditions

Due to lack of contrast between the blood and the wall in the phase data images, PC-MR intensity data was used to define the boundary of the lumen on the inlet plane. The flow intensity images during systolic flow have the largest contrast between the blood and lumen and so provide more accuracy when applying contours than during diastolic flow (figure 5.1(a)). For each direction of velocity in each patient, three intensity images at systolic time points were chosen to segment the inlet. 12 points at which the intensity drops (signalling the edge of the lumen) were marked manually on each image using Matlab (The MathWorks Inc.,Natick, Massachusetts). Using a pixel-intensity based interpolation method these 12 points were joined to form a contour of the vessel lumen. As this is essentially a manual method, there are slight variations in the contour shape for each image so the contours were split into 20 equally spaced points and the locations of each point were averaged over all of the contours to create a new, averaged, contour (figure 5.1(b))

Once the perimeter of the lumen was defined, a mask was created from the averaged contour and applied to each of the phase contrast data sets at every time point (figure 5.1(c)). All pixels lying outside of the contour were given zero velocity magnitude. MRI signal phase is

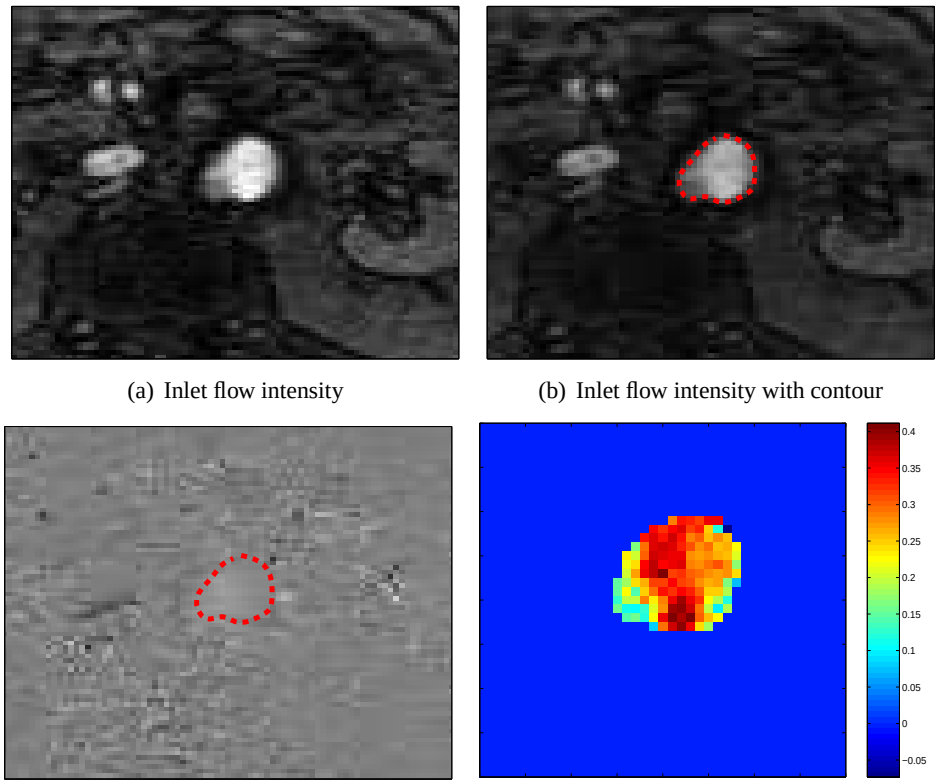

(a) Inlet flow intensity

(b) Inlet flow intensity with contour

(c) Applying contour to phase data

(d) Axial inlet velocity (m/s)

Figure 5.1: *Generation of inlet velocity*

measured as an angle between $-\pi$ and π. To convert the phase angle to velocity information a velocity encoding protocol is used. Pixel intensity lying within the lumen contour was rescaled by multiplying it by a rescale slope and adding a rescale intercept. For all patients the rescale slope was 2 and the rescale intercept -4096. The PC-MRI data used was velocity encoded with a sensitivity of 1.5 m/s equating to a pixel value of 4096 and so each pixel must be rescaled. The conversion of raw data to scaled velocity data can be described

$$v = \frac{(2M - 4096)\,1.5}{4096}, \tag{5.1}$$

where M is the unscaled PC-MR data.

As an averaged contour was used, the mask does not filter out all areas of the vessel lumen, leading to a scattering of significantly higher magnitude of velocities at the near-wall areas. A filter was applied to remove these artefacts by zeroing any velocities above 2.5 standard deviations from the mean velocity magnitude. As previous publications have noted [64] the PC-MRI data appears to have a high level of noise throughout, becoming more prominent in regions of low velocity (figure 6.7). For patients 1 and 3 all PC-MRI planes were aligned in the same plane for right to left, anterior to posterior and through-plane flow data sets. Patient 2 exhibited slight movement of position between the through-plane and the 2 radial velocity scans at the inlet. By comparing the maximum kidney widths for the MR images with CT slices there was found to be a 17 to 19 degree difference between the two slices. The left to right inlet data was adjusted accordingly to account for this difference.

Velocity data was obtained at 20 equally spaced time points. The timestep size convergence study on a simplified geometry conducted in Chapter 2 suggests simulations require a timestep size of T/200 seconds. It is therefore necessary to interpolate inlet velocities between the 20 data time points to create a smooth transition. For each inlet velocity data set a spline was used to interpolate velocities for each pixel over all timesteps and create a set of 200 interpolated velocity slices.

User defined functions were required to convert the velocity data into inlet boundary profiles for input into Fluent. Boundary condition methods used were;

i) All axial and radial (head to foot, anterior to posterior and left to right) components of velocity applied at each node on the inlet plane,

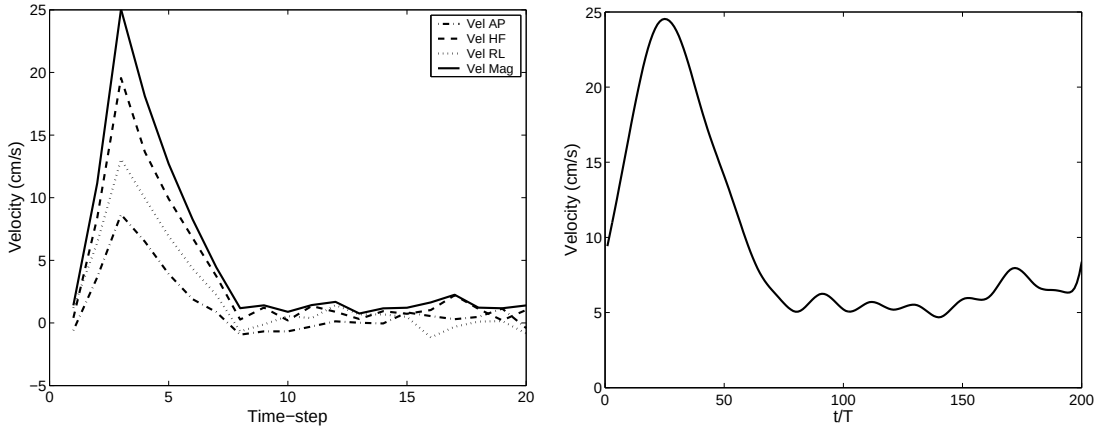

(a) Mean Inlet Velocity (b) Centreline Velocity

Figure 5.2: *Patient 1*

ii) The axial (head to foot only) velocity applied at each node on the inlet plane,

iii) Womersley flow inlet velocity profiles based on the inlet centreline velocity applied over the inlet plane.

Centreline velocity refers to the velocity at the point of maximum systolic flow. For each patient, the PC-MRI data describing the time point with the highest average velocity magnitude was taken to be the point of maximum systole. At maximum systole the pixel on the inlet plane with maximum velocity magnitude was nominated as the centreline value. The velocity at the point of centreline value was acquired at each timestep. The centreline velocity was converted into a two dimensional velocity profile satisfying the Womersley parameter as in Chapter 2. A user defined function was needed to convert the 2-D profile into a 3-D Womersley profile inlet boundary condition to be used in Fluent.

The axial and radial inlet velocity profiles, as well as the inlet velocity magnitude and the centreline velocities used to create the Womersley inlet flow boundary conditions are shown in figures 5.2, 5.3 and 5.4.

5.2.3 Patient AAA Surface Imaging

CT slices were obtained at 1mm intervals between the renal arteries and the femoral artery bifurcations for all three patients. The slices were segmenting using a Matlab based semi-automated threshold method. A rectangle was marked inside the lumen of the vessel (or vessels

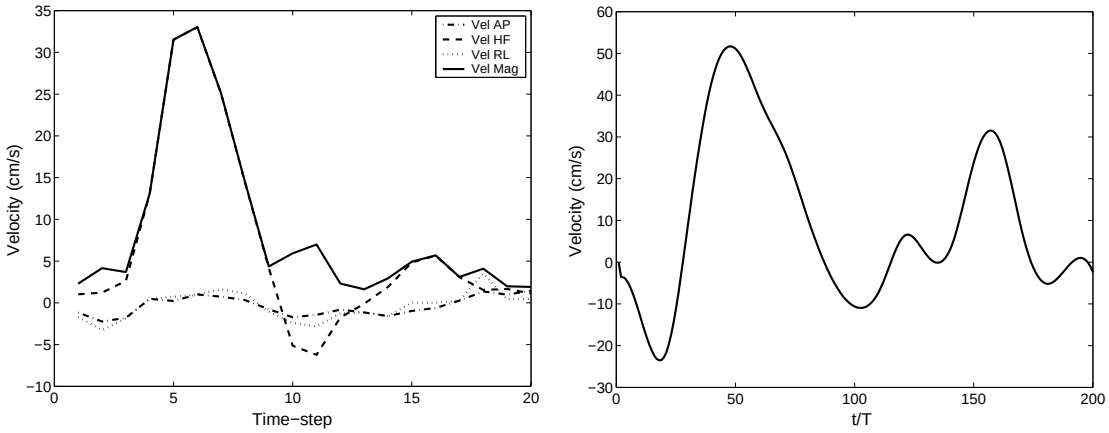

(a) Mean Inlet Velocity (b) Centreline Velocity

Figure 5.3: *Patient 2*

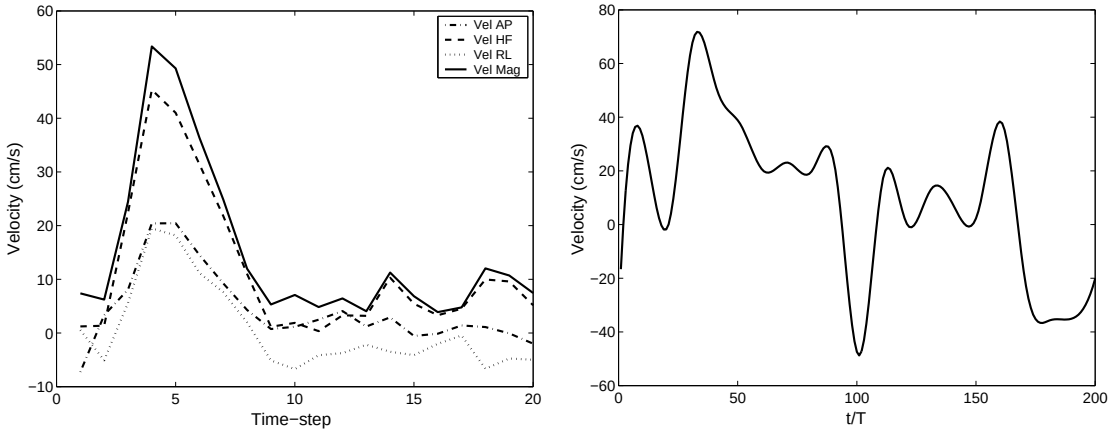

(a) Mean Inlet Velocity (b) Centreline Velocity

Figure 5.4: *Patient 3*

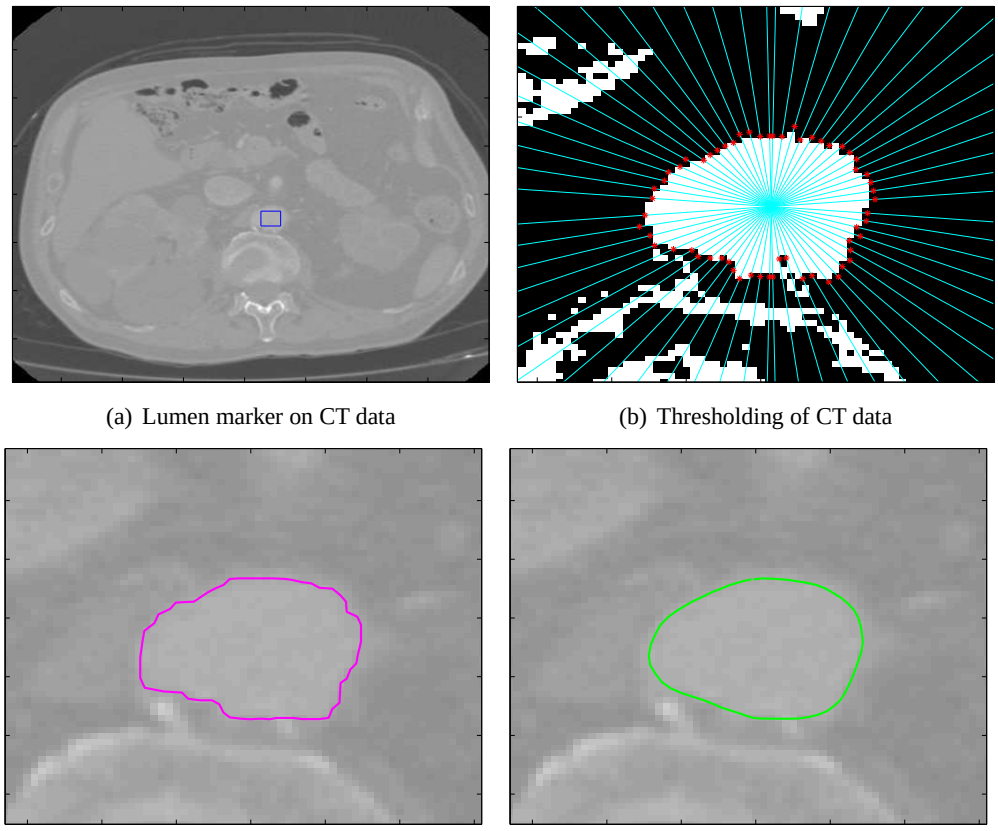

(a) Lumen marker on CT data

(b) Thresholding of CT data

(c) Applying median filtered contour

(d) Applying mean filtered contour

Figure 5.5: *Segmentation of lumen surface from CT slice*

in the case of slices distal to the bifurcation point) of each slice (figure 5.5(a)). An automated process of image thresholding and contouring was then implemented on each slice. Thresholding was based on the pixel intensity values within each rectangle. To obtain lumen contours, lines radiating from the central point of each rectangle were applied at each slice. The point along each line at which the pixel intensity dropped was used to mark the lumen (figure 5.5(b)). Sixty of these lines were applied to each rectangle, and all points interpolated to form a contour. In order to remove outliers and smooth the contour, a median filter (figure 5.5(c)), then a mean filter (figure 5.5(d)) were applied to all x, y coordinates on a slice.

5.2.4 Geometry Reconstruction

The lumen contours were exported to Rhinoceros v 3.0 (Robert McNeel and Associates, Seattle, USA) for stitching. The contours of the AAA and each of the iliac arteries were individually lofted to create three discrete surfaces. Joining these surfaces at the bifurcation point however

is a non-trivial task. Despite the high resolution of z-directional CT slices, the exact shape of the bifurcation point must be interpolated from the shape of the contours at the base of the AAA and the start of the iliac arteries. Direct interpolation may yield a very defined, sharp bifurcation point which is rarely seen *in vivo* and so the join must be smoothed. It is important to strive for physiological accuracy when modelling the bifurcation point as high WSS may be located at or slightly downstream of it [93] and so small errors in bifurcation reconstruction may produce amplified errors in WSS observations. The iliac arteries were joined to the base of the AAA in Rhinoceros using interpolated curves. These curves were then converted to surfaces creating the defined bifurcation point. The bifurcation was then smoothed and the shape compared visually with sagittal CT slices to assess whether the amount of smoothing is sufficient. In order to prevent outlet flow conditions from affecting the haemodynamics of the AAA sac, outlet lengths were added. To ensure a smooth transition of flow the direction of the outlet lengths were aligned with the end of the iliac arteries by extrapolating the line between the centre points of the last 2 contours to a length $11d$, where d is the average diameter of the final iliac contour, as defined for simple AAA geometries in Chapter 2. This final contour was copied to the endpoint of the extrapolated line and lofted to the iliac artery. The AAA inlet and iliac outlets were capped with a surface to create a self-contained shell. All surfaces were converted to meshes in Rhino and exported as an STL file. Magics (Materialise, Leuven, Belgium) software was used to fix any holes and overlapping or highly skewed triangles in the surface mesh, 'cut' the ends of the outlet to provide a flush outlet plane and if necessary re-mesh the geometry with a finer mesh to provide a suitable medium for finite volume meshing.

Patient geometries are shown in figures 5.6, 5.7 and 5.8.

5.2.5 CT-MR Registration

All PC-MR and MR inlet slices were obtained between the base of the renal arteries and the neck of the AAA while CT scans began above the renal artery and continued until the femoral artery. The two different modalities were registered together to ensure that the inlet plane was correctly aligned. The averaged MRI lumen contour for each patient was transposed against each of the CT slices in the renal-AAA neck region to ascertain the best match and thus register the two images.

Mid-plane PC-MRI validation slices were registered by comparing the position information stored in the Dicom file with that of the inlet slices. Once the inlet CT and MR images were

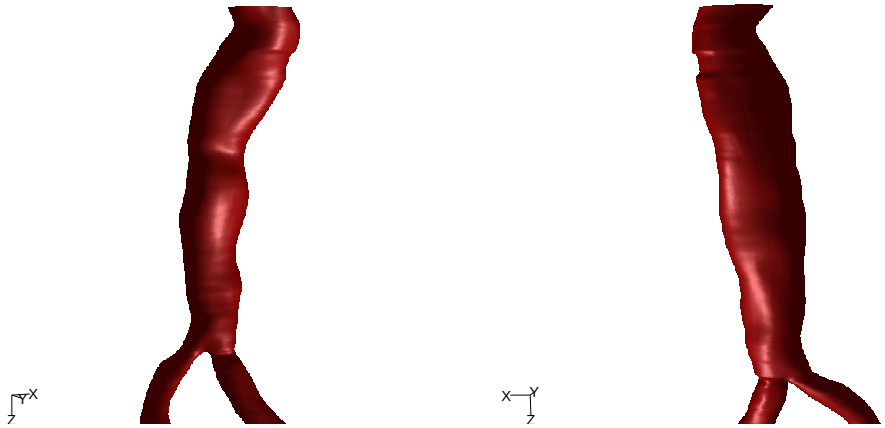

(a) Anterior View (b) Posterior view

Figure 5.6: *Patient 1 Geometry*

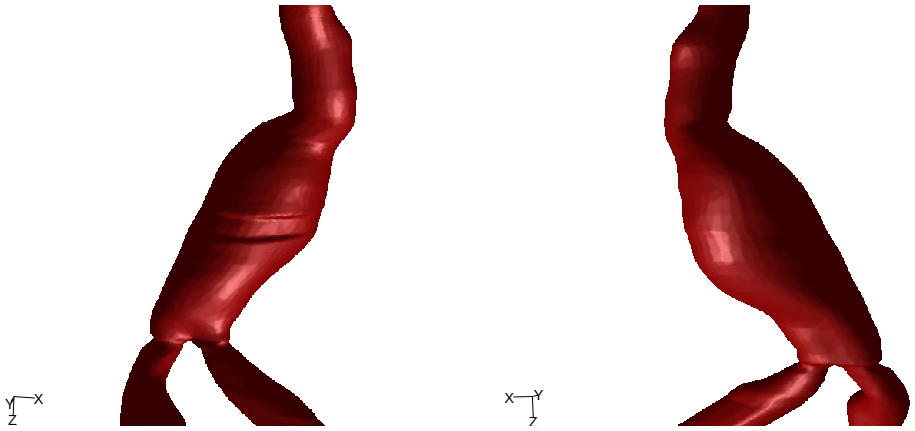

(a) Anterior View (b) Posterior View

Figure 5.7: *Patient 2 Geometry*

(a) Anterior View (b) Posterior View

Figure 5.8: *Patient 3 Geometry*

First layer height	30μm
Growth Factor	2
Number of Rows	8
Total Depth	765μm

Table 5.2: *Boundary Layer Properties*

Patient	Volumes	Faces	Nodes
1	1901961	4210929	578082
2	2158488	4999407	803533
3	757945	1735179	267370

Table 5.3: *Mesh sizes*

aligned the mid-plane slices could then be registered against the CT contours.

5.2.6 Volume Meshing

Surface meshes were exported to Gambit (Fluent Inc., Lebanon, New Hampshire, USA) to add volume meshes. The protocol for volume meshing the generic models used in Chapter 2 was used to mesh the patient specific models where feasible. Any hard surfaces and small faces were collapsed using the clean-up module in Gambit to leave a smooth surface mesh. The edge of the inlet plane was meshed with 100 points and the left and right outlet planes with 50 points each. Since the patient-specific models will be used to observe WSS and track near-wall cell behaviour, a finely meshed boundary layer is required. The boundary layer used was similar to that of the generic model with a slightly larger scaling due to the radius of the inlet (see table 5.2.6) The inlet and outlet faces were meshed using a paved quad-element scheme.

The AAA volumes were meshed using a tetrahedral scheme. Details of mesh size for each of the 3 patients are given in table 5.2.6.

Examples of the volume meshing regime and boundary volume layer are shown in figure 5.9. With the inlet and outlet boundaries set, the patient-specific meshes were exported to Fluent for solving.

5.2.7 Solver Variables

All patient specific models and boundary condition simulations were solved with the same variables. A second-order unsteady flow solver was applied in Fluent. As in previous simulations,

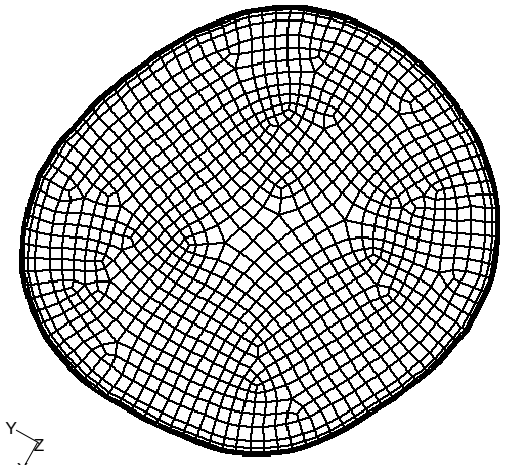

(a) Inlet Mesh

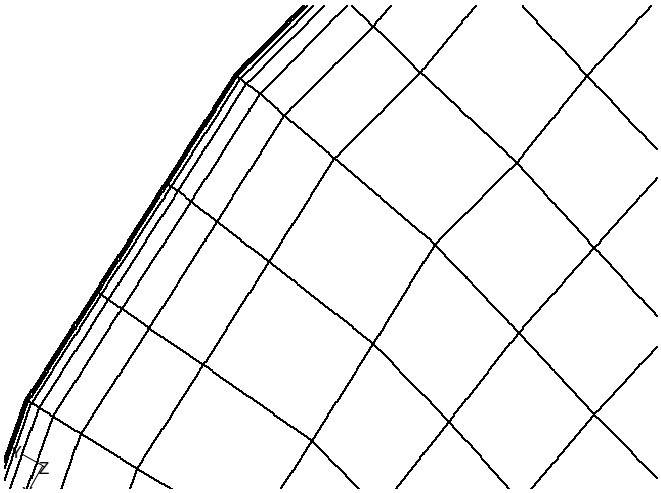

(b) Close-up of boundary layer

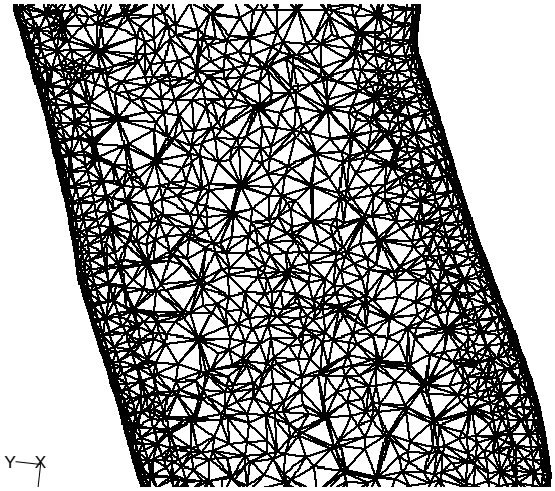

(c) Mesh through neck of AAA, patient 2

Figure 5.9: *Examples of finite volume mesh*

Patient	Timestep Size	Cycle Length
1	5.755×10^{-3} seconds	1.151 seconds
2	3.355×10^{-3} seconds	0.671 seconds
3	5.67×10^{-3} seconds	1.134 seconds

Table 5.4: *Temporal variables*

the material properties of blood were taken to be; viscosity = 0.0035 kg/ms and density = 1056 kg/m^3 A LES viscosity model was applied (see Chapter 3) with no inlet perturbations and SIMPLE pressure-velocity coupling. The convergence criteria were set to; continuity $= 1 \times 10^{-3}$ and x, y and z-velocity $= 1 \times 10^{-5}$. The x and y velocities are relatively small and so a low convergence criteria is required. Due to the complexity of the secondary flow the solution rarely completely converged, though the residuals of velocity and continuity were shown to plateaux at the orders of magnitude used here.

5.2.8 Boundary Conditions

Three simulations were required in each of the three patient models to compare the three different inlet boundary condition types. The three directional velocity (3DV) boundary condition required user defined functions of x, y and z-components of inlet velocity at each timestep. For the axial-velocity only (1DV) simulations, the x and y components of inlet velocity were set to zero and only the z-component user defined function was used. The Womersley inlet flow wave was attached via a user defined function to the AAA geometries with extended inlet lengths.

5.2.9 Timestep size and cycle independence

The wavelength of the cardiac cycle and the size of the timesteps were determined from the PC-MRI Dicom file information. Table 5.2.9 shows the cycle lengths and timestep sizes for each of the three patients.

A limit of 70 iterations per timestep was shown to be sufficient as residuals were shown to reach a plateaux before this point.

5.2.10 Data Collection

Each simulation was run for 3 cardiac cycles. Throughout the third cycle measurements of WSS, selected lines of fluid tangent to the instantaneous velocity vector, velocity magnitude, vorticity and x, y and z components of velocity over the mid-plane were taken every tenth of a cycle.

5.2.11 Image and Statistical Analysis

Qualitative trends and differences in haemodynamics and WSS in the different boundary condition simulations were assessed by visual comparison of the data. To objectively compare the differences in haemodynamics between different inlet boundary condition methods, quantitative measures of haemodynamics and WSS variables were used.

5.2.11.1 Flow Structure and Haemodynamics

Plots of fluid flow lines tangent to the instantaneous velocity vector during systole and diastole coloured by velocity magnitude show the evolution of general haemodynamics during the cardiac cycle. Contours of velocity magnitude were obtained on a cross-sectional plane at the cavity mid-point of all 3 geometries during mid systole and mid diastole. Vectors of radial velocity were superimposed onto these contour plots to give a qualitative description of the magnitude and complexity of flow throughout the cardiac cycle.

The properties of secondary flow within the bulk of the vessel blood flow can be quantified by measuring the value of helicity. The helicity of a flow field is the extent to which a fluid flow describes a spiral helical flow through time. Spiral flow is thought to induce more stable flow, reducing turbulence and potentially preserving endothelial function [159]. Helicity of a fluid is a relation between the velocity and vorticity of flow and kinetic helicity density per unit volume H_k can be defined as [111]

$$H_k = V \cdot (\nabla \times V) \tag{5.2}$$

where $(\nabla \times V)$ is vorticity.

Grigioni et al [56] extend this to create a dimensionless factor Ψ of local normalised helicity

$$\Psi = \frac{H_k}{|V||\nabla \times V|}, \; -1 \leq \Psi \leq 1 \tag{5.3}$$

which gives the local values of the cosine of the angle between velocity and vorticity vectors. A value of $\Psi = 0$ occurs in steady, Poiseuille flow in which the vectors of velocity and vorticity are orthogonal, whereas values of $|\Psi| = 1$ occur when flow is purely helical. The sign of Ψ indicates whether the overall direction of helicity is clockwise or counterclockwise.

To obtain a representative sample of helicity throughout a cardiac cycle in AAAs, a helical flow index (HFI) along fluid pathline trajectories was used based on indices created by Grigioni et al [56] and Morbiducci et al [111]. 80 fluid pathlines were defined at each T/10 time point, originating from a point 0.5 cm downstream of the inlet. For each pathline, the mean helical flow index (HFI_p) was determined over the fluid particle trajectory

$$HFI_p = \frac{1}{N_j} \sum_{i}^{N_j} \Psi_i, \tag{5.4}$$

where N_j is the number of 1 cm steps, $i = 1, ..., N_j$, along the trajectory of fluid particle pathline j. At each time point the average HFI_p over all pathlines (HFI_t) is defined as

$$HFI_t = \frac{1}{N_p} \sum_{j}^{N_p} HFI_{p,j}, \tag{5.5}$$

where N_p is the number of pathlines $j = 1, ..., N_p$, at each time point. For simulations with Womersley inlet flow, particle pathline trajectories were truncated if the pathline entered the inlet length. HFI_t gives an analysis of the directional helicity at each timepoint. A value of time averaged mean helical flow magnitude was also obtained via the index

$$\overline{HFI_{mag}} = \frac{1}{N_t} \sum_{k}^{N_t} \frac{1}{N_p} \sum_{j}^{N_p} |HFI_{p,j}| \tag{5.6}$$

where N_t is the number of timesteps $k = 1, ..., N_t$.

5.2.11.2 WSS

Contours of time averaged WSS values indicate regions of disturbed flow and endothelial dysfunction. Time averaged WSS was calculated via

$$|\overline{WSS}| = \frac{1}{T}\int_0^T |WSS|dt \tag{5.7}$$

In pulsatile flows, the effect of oscillating shear stresses throughout the cardiac cycle have been shown to affect the behaviour of endothelial cells and vessel wall thickness [11, 123, 165]. Oscillatory flow has been shown to up-regulate adhesion molecules which may aid monocyte binding to the endothelium [63]. The temporal variation in WSS direction can be expressed in terms of the oscillatory shear index (OSI)[77]

$$OSI = \frac{1}{2}\left(1 - \frac{|\int_0^T WSS_z dt|}{\int_0^T |WSS_z|dt}\right). \tag{5.8}$$

An OSI value of zero indicates that flow is uni-directional at that location throughout the pulsatile cycle whereas a value of 0.5 indicates that the sum of the axial WSS is zero and therefore flow oscillates forward and backwards for the same periods of time during the cardiac cycle.

Quantitative comparisons of near wall parameters in AAA geometries were enabled through the use of the 'patching' method proposed by Thomas et al [167]. Each geometry is split into discrete but contiguous sections and the average values of the required parameter for all nodes within a given patch is calculated. This method allows the comparison of identical patches on simulations with differing inlet boundary conditions. All patches were 3mm in length in the axial direction, beginning 1 cm downstream from the inlet and ending 2 cm downstream of the iliac bifurcation. Above the bifurcation point, the centre point of each 3mm segment was found and divided again at 90° intervals to create 4 patches termed left-anterior (L-A), left-posterior (L-P), right-anterior (R-A) and right-anterior (R-A). Below the bifurcation point, the iliac artery segments were divided into anterior (left/right iliac A) and posterior (left/right iliac P) patches. Mean values of time averaged WSS and OSI were calculated over each patch for comparison between inlet boundary condition methods.

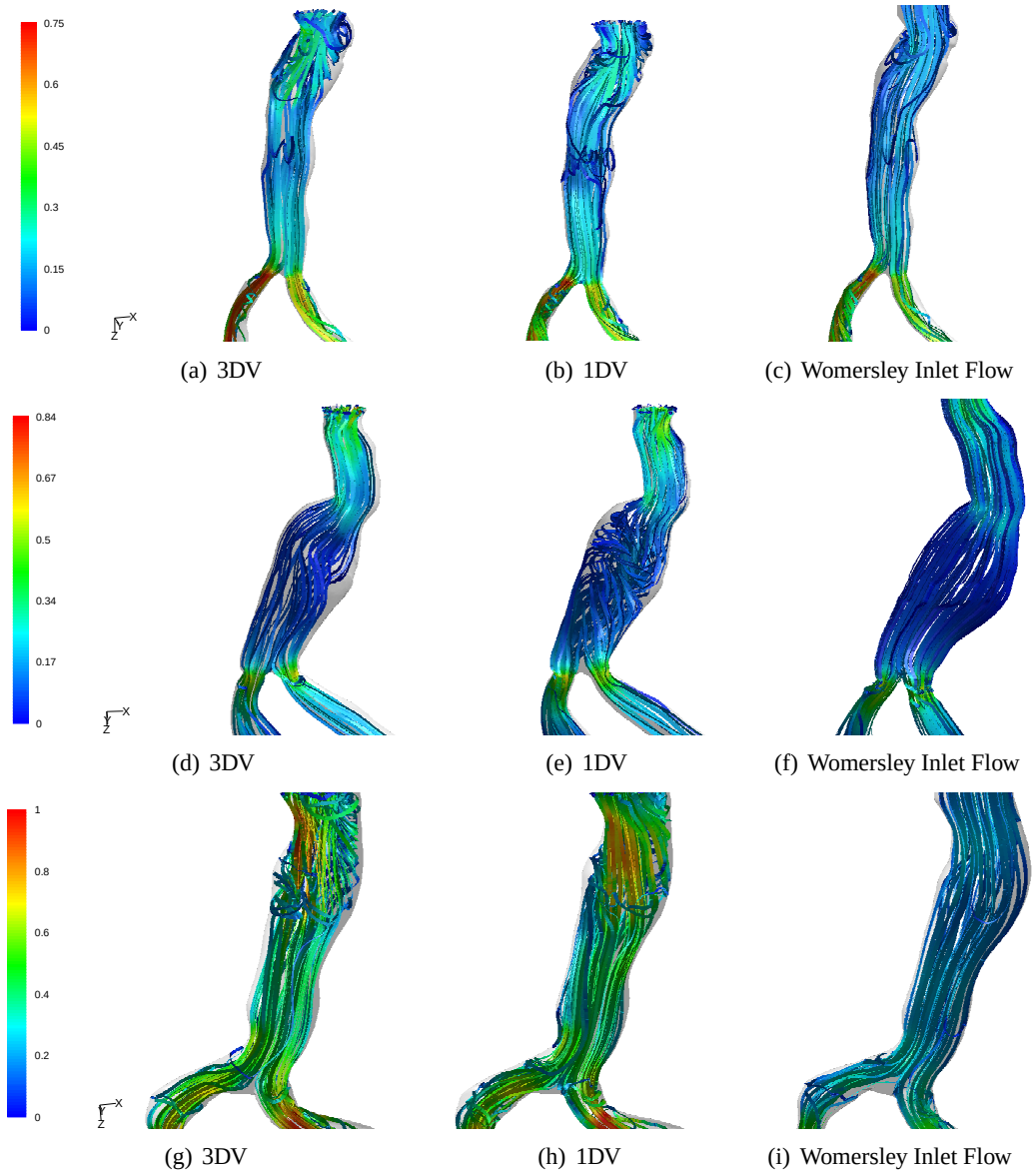

(a) 3DV (b) 1DV (c) Womersley Inlet Flow

(d) 3DV (e) 1DV (f) Womersley Inlet Flow

(g) 3DV (h) 1DV (i) Womersley Inlet Flow

Figure 5.10: *Lines of flow tangent to the instantaneous velocity vector coloured by velocity magnitude (m/s) during mid systole (T/t = 0.2)*

Patient	RMS Difference			
	$\|WSS\|_{TA}$		OSI	
	Axial Inlet Velocity	Womersley Inlet Flow	Axial Inlet Velocity	Womersley Inlet Flow
1	0.051 (8.5%)	0.232 (38.7%)	0.039 (4%)	0.462 (4.7%)
2	0.064 (39.9%)	0.157 (98.6%)	0.211 (28.1%)	0.3118 (41.5%)
3	0.094 (24.6%)	3.499 (76.8%)	0.247 (37%)	0.537 (80.4%)

Table 5.5: *RMS shear stress results*

Patient	$\overline{HFI_{mag}}$ (Percentage difference from axial and radial inlet velocity)		
	Axial and Radial Inlet Velocity	Axial Inlet Velocity	Womersley Inlet Flow
1	0.391	0.409 (4.4%)	0.301 (23.1%)
2	0.283	0.326 (15.2%)	0.191 (32.7%)
3	0.286	0.306 (7.2%)	0.203 (28.9%)

Table 5.6: *Helicity results*

5.3 Results

Lines of flow tangent to the instantaneous velocity vector show that during systole (figure 5.10) regions of secondary flow form, generally around the neck or proximal end of the AAA cavity, in the 3DV and 1DV inlet boundary condition models. Secondary flow appears to form axially orientated vortices in the 3DV inlet models and radial, helical vortices in the 1DV inlet simulations. By diastole (figure 5.11), disturbed flow pervades the entire cavity. In patient 2, the directionality of vortices observed in systole is retained while patients 1 and 3 show more random variations in perturbation alignment during diastole. Much less disturbed flow is found in the Womersley inlet flow simulations with much of the flow apparently laminar in nature throughout the cardiac cycle in patients 2 and 3. Flow velocity is generally highest at the neck and iliac bifurcation points of the aneurysm where the vessel diameter is smallest. With the exception of the low velocities in the patient 3 Womersley inlet flow model (figure 5.10(i)), all inlet boundary condition methods show similar trends in velocity magnitude during systole. During diastole, the Womersley inlet flow simulations give generally higher velocity magnitudes in all 3 patients.

During systolic flow, patients 1 and 3 show similar trends in axial velocities and radial velocity vectors over cross sections of the AAA mid-point (figure 5.12) for all inlet boundary condition methods. The maximum velocity of the patient 3 Womersley inlet flow simulation is around

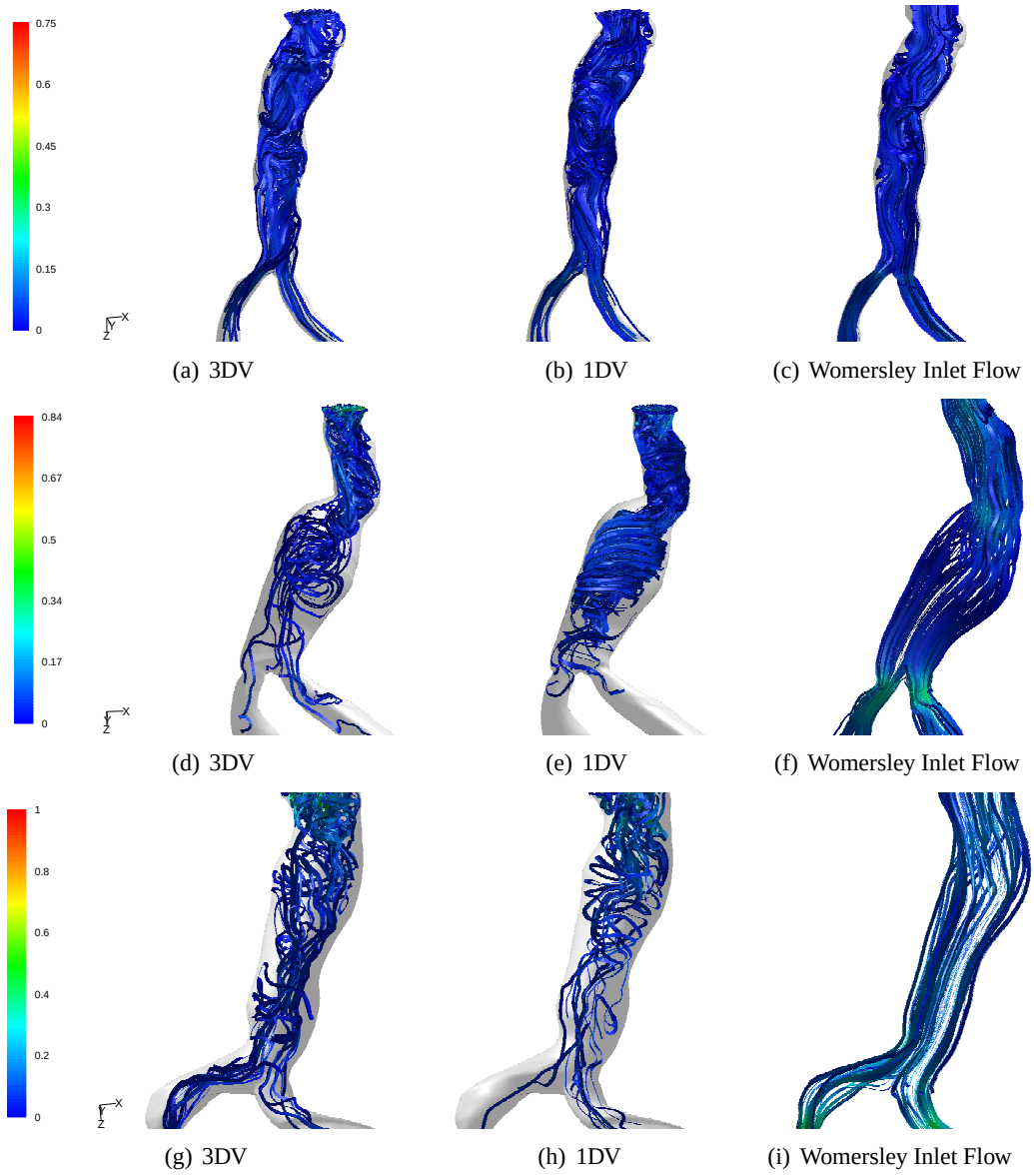

(a) 3DV (b) 1DV (c) Womersley Inlet Flow

(d) 3DV (e) 1DV (f) Womersley Inlet Flow

(g) 3DV (h) 1DV (i) Womersley Inlet Flow

Figure 5.11: *Lines of flow tangent to the instantaneous velocity vector coloured by velocity magnitude (m/s) during diastole (T/t = 0.8)*

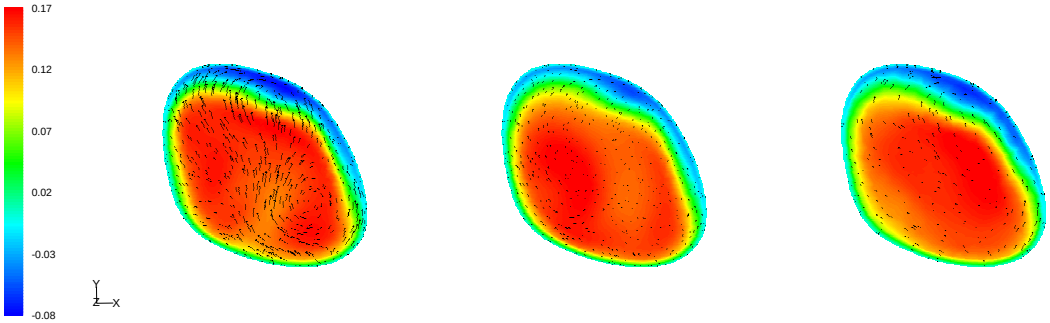

(a) Patient 1, 3DV (b) Patient 1, 1DV (c) Patient 1, Womersley Inlet Flow

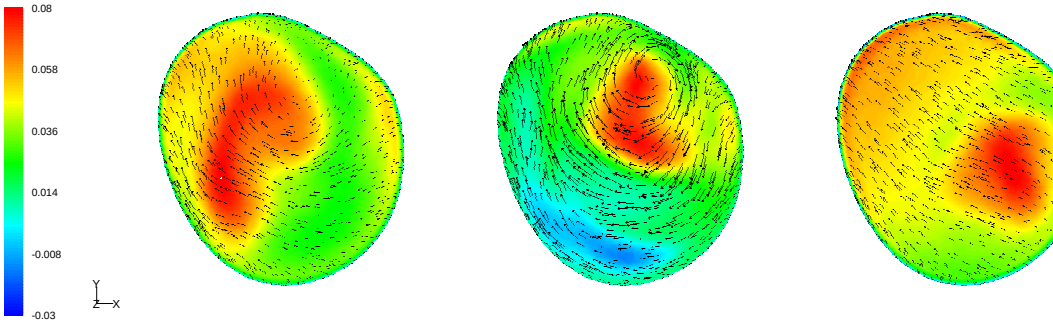

(d) Patient 2, 3DV (e) Patient 2, 1DV (f) Patient 2, Womersley Inlet Flow

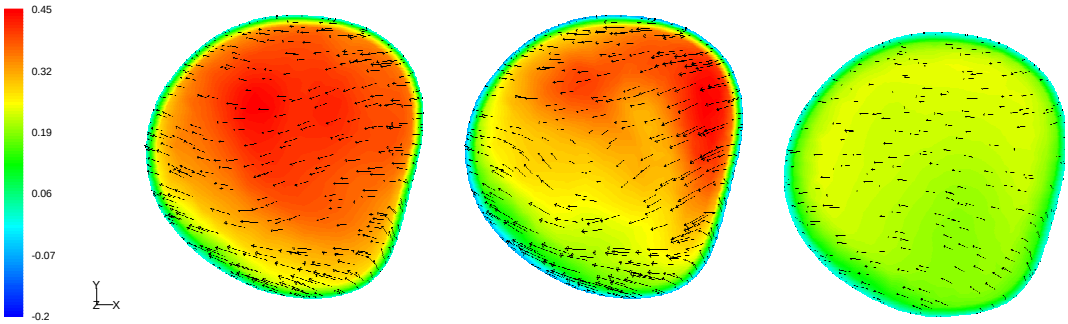

(g) Patient 3, 3DV (h) Patient 3, 1DV (i) Patient 3, Womersley Inlet Flow

Figure 5.12: *Contours of axial velocity (m/s) at midsection of AAA with scaled vectors of radial velocity superimposed. T/t=0.2*

half the magnitude of the 3DV and 1DV simulations and its radial velocity vectors show less disturbed flow. Patient 2 shows more noticeable differences in axial velocity contours between boundary condition methods though it should be noted that the magnitude of velocity is significantly lower than in the other patients and therefore differences may not be as significant. In patient 2, radial velocity vectors of the 1DV model (figure 5.12(e)) show a strong spiral flow dominating. This is still present, but not as defined in the 3DV model and not present at all in the Womersley inlet flow simulation.

In diastolic flow (figure 5.13), all axial flow distributions are different between each boundary condition method, with the exception of the 3DV (figure 5.13(a)) and 1DV (figure 5.13(a)) inlet boundary conditions in patient 1 which are relatively similar. Velocity magnitudes are generally much lower here than during mid systolic flow and so the physiological effects of these differences may also be lower. Differences in radial velocity vectors become more apparent during diastole. 1DV inlet boundary condition simulations show well defined secondary flow, either in a unidirectional spiral (figure 5.13(e)) or counter rotating spirals (figures 5.13(e) and 5.13(h)) while 3DV boundary conditions have more complex radial flow, and so show less well defined spiral flow. Womersley inlet flow simulations tend to reduce the complexity and magnitude of radial secondary flow, although patient 1 still retains simplified counter rotating spirals.

Secondary flow at the iliac bifurcation is generally preserved between boundary condition methods (results not shown).

The large differences in diastolic axial flow velocities between Womersley inlet flow and spatial inlet velocity simulations observed in patients 2 and 3 are due to the fluctuations in inlet velocity which arise due to flaws in the assumptions used when creating Womersley flow profiles from centreline velocity. Centreline velocity is based on a limited sample of velocity data over the inlet plane. It assumes that the centreline will be the region of highest velocity magnitude throughout the cycle (it is known to be the highest during peak systole) and that it is a primary, central peak at each timestep. If the centreline falls on an isolated region of high or low velocity flow then the Womersley flow profile at that timestep may result in a mean inlet velocity significantly higher, or lower, than the actual mean. The high velocity flows experienced during mid-systole make it less likely that this type of spatial heterogeneity will exist and inlet velocity plots show flow tends towards the simple parabolic profiles predicted by Womersley flow. Later in the cycle, secondary flow characteristics become more prevalent and inlet velocity profiles deviate from a simple parabolic profile. In 2 of the 3 patients there is a sharp rise in mean inlet

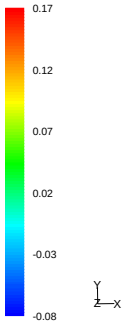

(a) Patient 1, 3DV

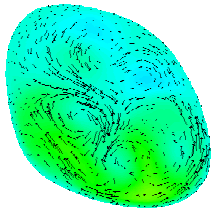

(b) Patient 1, 1DV

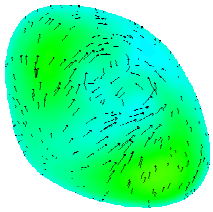

(c) Patient 1, Womersley Inlet Flow

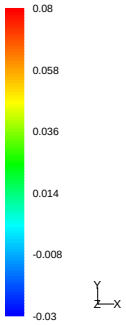

(d) Patient 2, 3DV

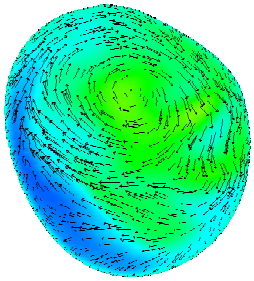

(e) Patient 2, 1DV

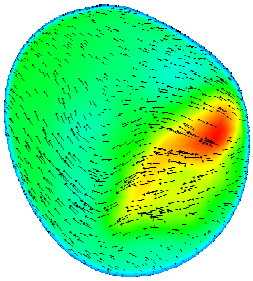

(f) Patient 2, Womersley Inlet Flow

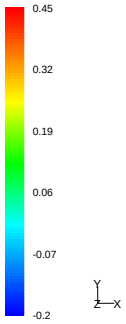

(g) Patient 3, 3DV

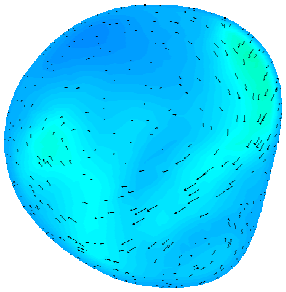

(h) Patient 3, 1DV

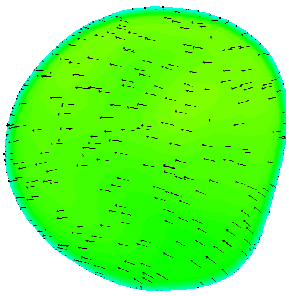

(i) Patient 3, Womersley Inlet Flow

Figure 5.13: *Contours of axial velocity (m/s) featuring scaled vectors of radial velocity at mid-section of patient 1 at T/t=0.8*

velocities during diastole in the Womersley inlet flow model which are not present in other models that take into account spatial velocity variability.

In general, the mean directional value of helicity appears closer to zero for the 3DV than the 1DV inlet boundary condition method (figures 5.14) throughout the cardiac cycle, especially in patients 1 and 3. The root mean squared (RMS) values of helicity magnitude (table 5.3) show that the differences in helical magnitude are indeed lower in the 3DV model (an average difference of 8.9% lower), but not as significantly different as would be predicted from the results of figure 5.14. This could be due to the increased complexity of the 3DV method creating a greater diversity of clockwise and anti-clockwise helicity as seen in the vector plots of figures 5.12 and 5.13 which bring the sum of directional helicity closer to zero. Womersley inlet flow gives more diverse values of mean directional helicity throughout the cardiac cycle though it is generally between the magnitudes given by 3DV and 1 DV simulations. Table 5.3 shows that the RMS of time averaged helicity magnitude for Womersley inlet flow is significantly less than those of the other inlet boundary condition methods in all three patients (the average difference between 3DV and Womersley inlet profile helicity is 28.2%). The low helicity magnitude and higher values of directional helicity in the Womersley inlet flow simulations indicate that the simplified secondary flow tends to be unidirectional.

The regions of highest time averaged WSS occur at the iliac bifurcation point and, for patients 2 and 3, near the inlet and neck of the aneurysm (figure 5.15). There is little difference in the distribution of WSS between the 3DV and 1DV inlet boundary condition methods though table 5.3 shows that differences in the RMS WSS magnitude are significant (an average difference of 24.3%). Womersley inlet flow simulations have generally higher WSS magnitudes and, in patients 2 and 3, there are shifts in the regions of high WSS. The RMS WSS magnitudes show significant differences between WSS in the Womersley flow model when compared to the 3DV and 1DV simulations (an average of 68% difference between Womersley inlet flow and 3DV methods).

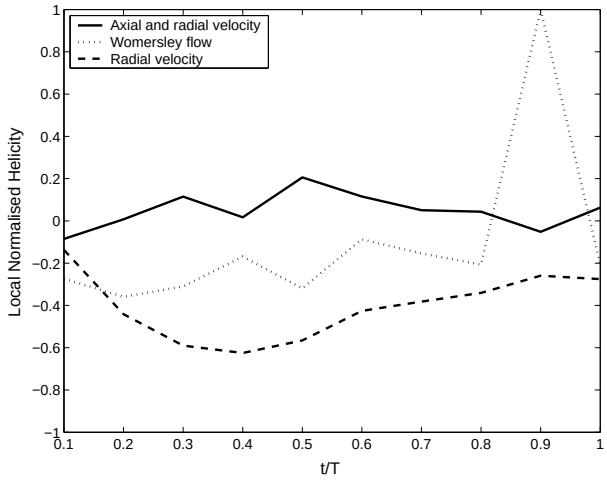

(a) Patient 1

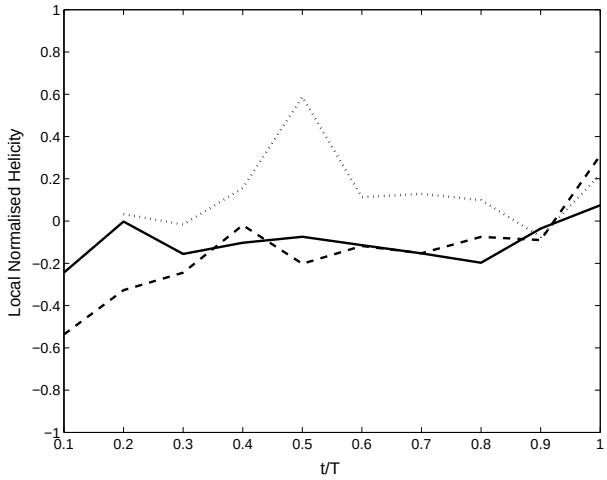

(b) Patient 2

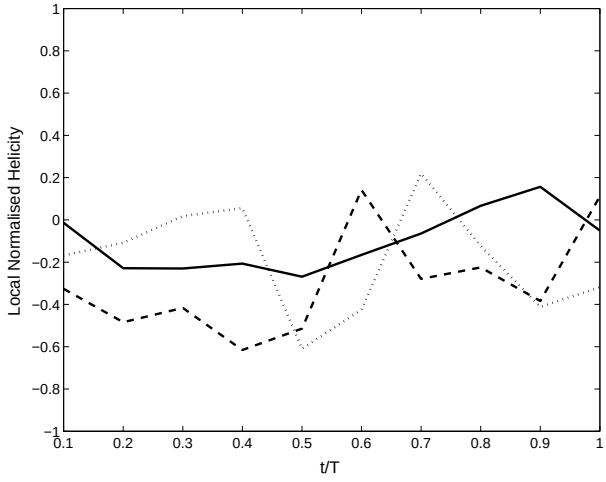

(c) Patient 3

Figure 5.14: *Plots of mean directional helicity*

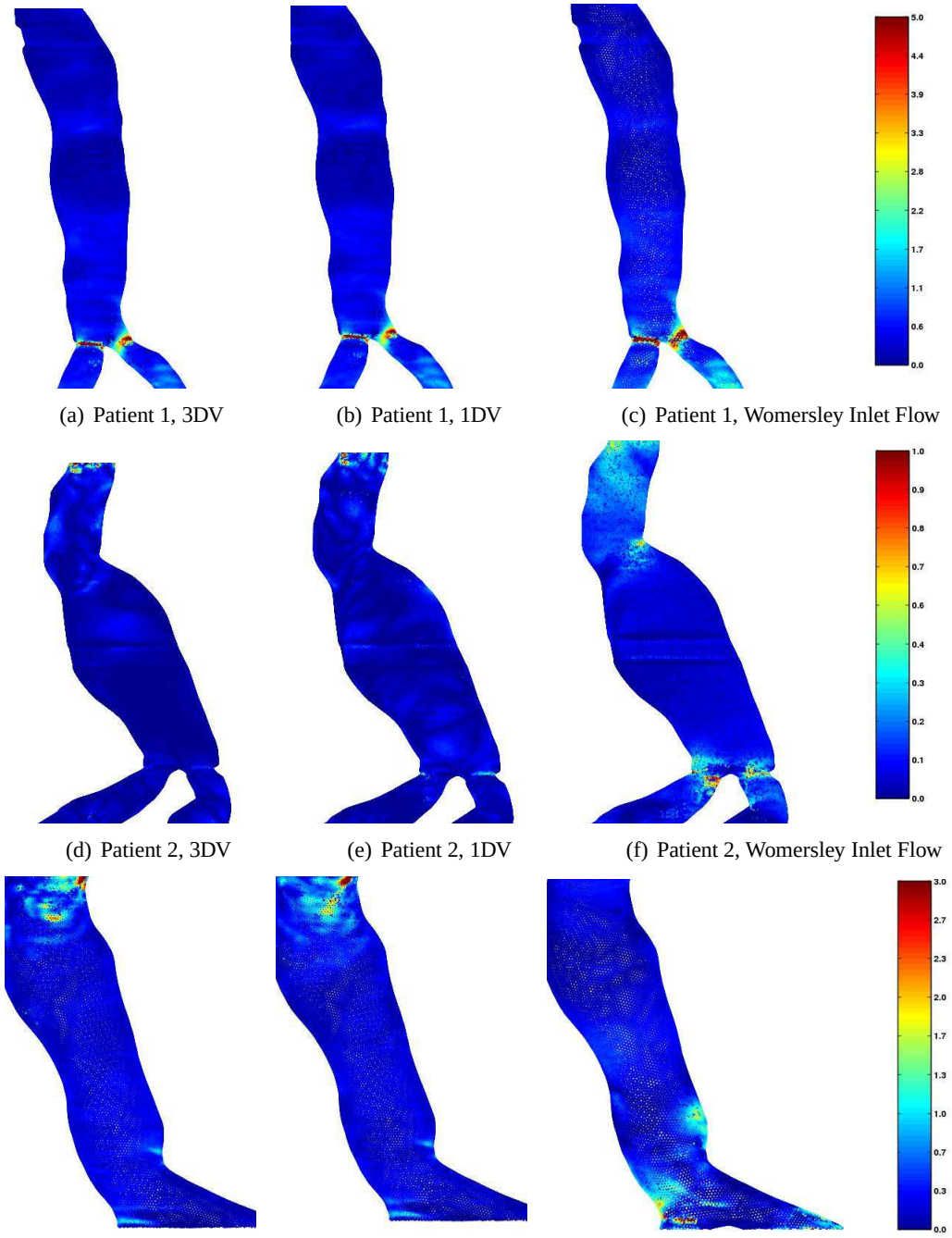

(a) Patient 1, 3DV (b) Patient 1, 1DV (c) Patient 1, Womersley Inlet Flow

(d) Patient 2, 3DV (e) Patient 2, 1DV (f) Patient 2, Womersley Inlet Flow

(g) Patient 3, 3DV (h) Patient 3, 1DV (i) Patient 3, Womersley Inlet Flow

Figure 5.15: *Contours of time averaged WSS magnitude (Pa)*

There is no significant difference in the distribution (figures 5.16(a) 5.16(b) and 5.16(c)) and RMS magnitude (table 5.3) of OSI for all inlet boundary condition methods in patient 1. Patients 2 and 3 however show significant differences in RMS magnitude and distribution of OSI between 3DV and 1DV methods and an even greater difference when compared to Womersley inlet flow simulations which result in generally more unidirectional shear stress (figures 5.16(d) to 5.16(i)).

Applying 3DV and 1DV inlet boundary condition methods creates regions of secondary flow within patient specific AAA models. 3DV inlet flow appears to create axially orientated perturbations while 1DV inlet flow creates more radial, spiralling flow. 3DV secondary flow is also more complex than in 1DV inlet simulations and, while there is an 8.9% increase in the magnitude of helicity in 1DV models, the complexity of the 3DV secondary flow creates counter rotating regions which reduce the directional helicity. These differences in secondary flow are most prevalent during diastolic flow and do not have a significant effect on WSS distribution but create a 24.3% differences in the WSS magnitude and a difference in distribution and magnitude of OSI, especially in patients 2 and 3. Applying the Womersley inlet flow boundary condition significantly reduces secondary flow which leads to less helical flow. The remaining secondary flow is unidirectional in nature. The Womersley inlet flow method also significantly increases WSS magnitude and can affect WSS distribution. OSI shows that Womersley inlet flow gives more unidirectional and simplified shear stresses.

5.3.1 Discussion

Inlet boundary conditions with 3 components of velocity, 1 component of velocity and parabolic Womersley velocity profiles based on patient PC-MR velocity data were applied to patient specific AAA geometries and compared to assess the differences in flow dynamics and near wall shear stress variables.

The method of using centreline velocities to define Womersley flow profiles at each timestep includes assumptions about the maximum flow velocity which can lead to significant errors in inlet velocity magnitudes. These errors are most likely to occur during diastole when flow velocity is lower and more disturbed. The centreline velocity approach has been used previously by Fraser [46]. This study shows that a change in methodology is required to increase accuracy when using Womersley flow profiles. An alternative approach is to estimate the maximum velocity as a function based on the mean, or integrated, inlet velocity at a given timestep.

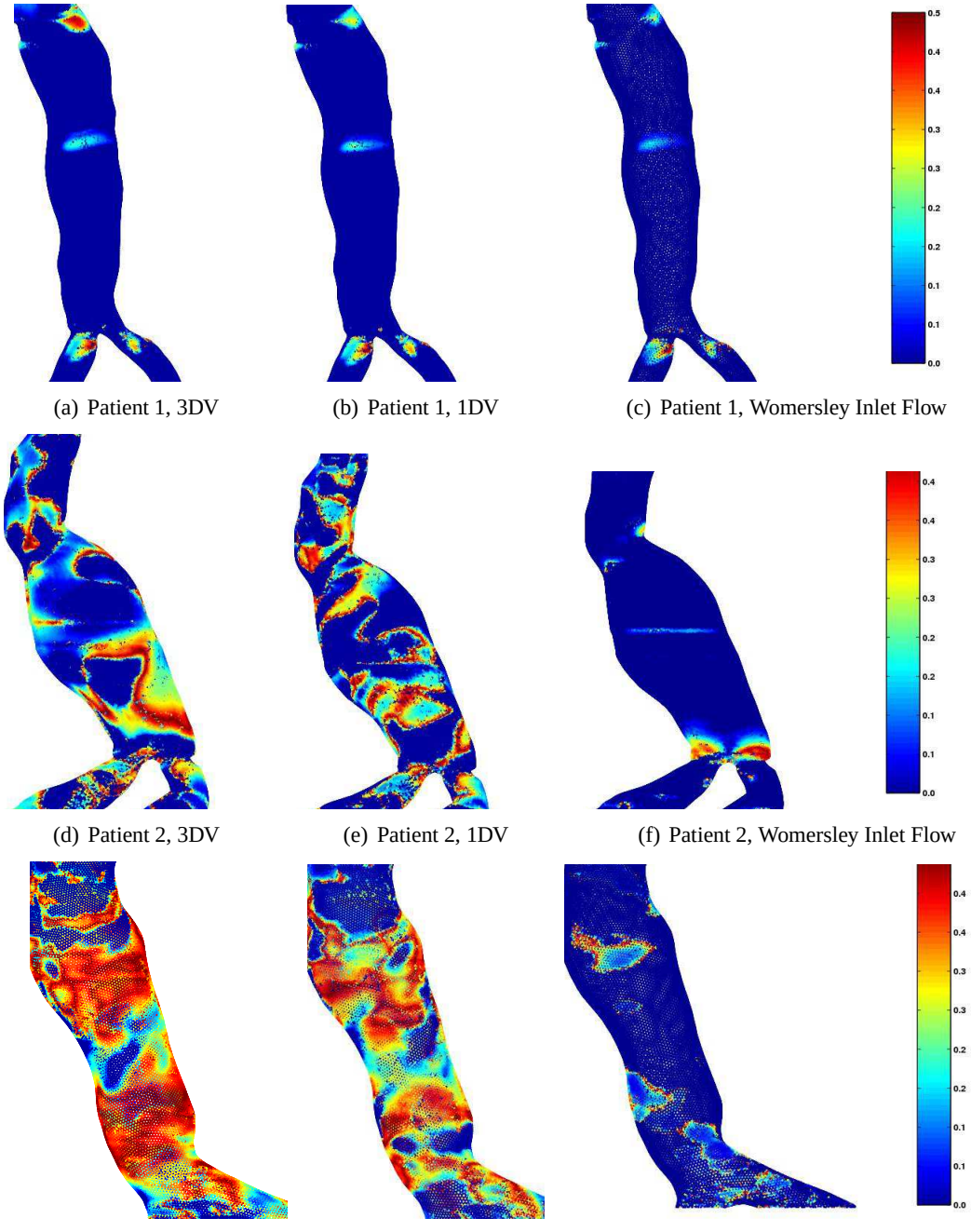

(a) Patient 1, 3DV (b) Patient 1, 1DV (c) Patient 1, Womersley Inlet Flow

(d) Patient 2, 3DV (e) Patient 2, 1DV (f) Patient 2, Womersley Inlet Flow

(g) Patient 3, 3DV (h) Patient 3, 1DV (i) Patient 3, Womersley Inlet Flow

Figure 5.16: *Contours of OSI*

Examples of studies which use this method are suggested in a review by Steinman et al [156]. This method is not ideal as it involves further assumptions of the maximum velocity which may be too conservative. A trade off between the two methods can be sought by sampling a larger area around the chosen centreline to reduce the sampling error.

Recent investigations rely on Womersley flow when modelling CFD in AAAs [86]. This study shows that using parabolic inlet flow profiles provides the general trends in axial velocity and WSS magnitude but there is a significant loss of secondary flow and a simplification of oscillatory flow when compared to inlet profiles featuring spatial velocity information. It may be that a CFD simulation is required to assess areas of maximum WSS and velocity, in which case the use of Womersley profiles may suffice. Creating Womersley profiles requires the least velocity information of all the methods investigated in this study and so time and effort in terms of computational processing and scanning time can be saved if the required information can be simulated using these simplified boundary conditions. However, any study which requires an understanding of secondary flow, including the modelling of the behaviour of transported species should avoid the over-simplified flow structures created through the use of Womersley inlet flow boundary conditions.

Differences in haemodynamics between using 1 and 3 components of inlet velocity are more subtle. In terms of general flow dynamics, trends in both axial velocity and distribution of WSS are similar throughout. WSS is a sensitive variable and there are significant differences in the magnitude of WSS and OSI between 1DV and 3DV methods. The significance of these differences depends on the patient AAA geometry, but the average differences in WSS and OSI magnitudes of 24.3% and 23% respectively are sufficiently large to conclude that the choice of inlet boundary condition method is an important factor when investigating WSS in AAAs using numerical simulation. While both boundary condition methods exhibit spiral flow, they differ, sometimes significantly, in the structure of secondary flow. Differences in secondary flow will have a limited effect on the regions of maximum velocity and WSS but may be critical in particle transfer and adhesion, especially in regions near the wall. To assess which model is the most adequate for modelling particle behaviour we must deduce which boundary condition method provides the most physiologically accurate simulation. The inclusion of radial inlet velocity vectors should provide more realistic secondary flow features though this relies on limiting the errors involved in obtaining and implementing the low magnitude radial velocities. In Chapter 6, the simulated velocities are compared with patient PC-MRI data.

Despite differences in secondary flow throughout the cavity, both 3DV and 1DV models give similar flow dynamics as the blood enters the iliac arteries. This may mean that differences in haemodynamics created in or upstream of the aneurysm cavity do not progress further downstream.

Both 3DV and 1DV boundary condition methods show evidence of helical flow within the AAA cavity, especially during diastolic flow. Helical flow is significantly reduced in the Womersley inlet flow simulations. The presence of spiral flow is thought to be an important factor in vascular mechanics, especially in diseased vessels. An *in vitro* study by Stonebridge et al [158] showed that, while spiral flow makes little difference in a healthy vessel, in stenosed vessels it stabalises flow and significantly reduces near wall turbulence as well as lowering forces acting on the vessel wall. The stabilising effects of spiral flow and the associated stablising of WSS are likely to have an effect on endothelial cell behaviour and disease progression, Houston et al [62] found that carotid atheromatous disease was associated with a lack of spiral flow in the aortic arch.

In this study, radial flow was found to be more complex in the 3DV models, with perturbations reducing its helical nature. As elements of helical flow are present using both 1DV and 3DV methods it seems likely from the results of this study that spiral flow is present, at least to some degree, in AAAs *in vivo*. The results of models with both inlet boundary conditions must be validated to determine which is the most physiologically likely scenario. If the 3DV model is found to provide the more physiologically realistic method it may be that applying radial velocities to CFD models inhibits the helical nature of flow. Obtaining 3 components of velocity using PC-MR scanning involves conducting 3 times as many velocity scans as unidirectional velocity data. Longer scanning times, as well as the extra breath holds required when scanning the abdominal region mean that any loss of accuracy incurred by using only the axial component of flow must be weighed up against the effort required to gain the extra radial velocity vectors.

5.3.2 Conclusions

Womersley inlet flow profiles contain the least velocity information and produced simulations with more linear and generally lower axial velocity flows than simulations which used spatial velocity information. Information on the spiral nature of flow is also lost. At some time points in the cardiac cycle, assumptions in centreline inlet velocity led to significant under or over compensation of inlet velocity when creating Womersley flow profiles. Because of the

associated simplification of haemodynamics, the use of Womersley inlet flow boundary conditions is not advised for analysis of flow characteristics. If used to obtain more general flow dynamics care must be taken to ensure velocities are not skewed by spatially heterogeneous inlet velocities.

Simulations in which 1 and 3 components of spatially varying inlet velocity boundary conditions were applied produced similar axial velocities and WSS distributions though differ in the structure of secondary flow, especially during the latter stages of the cardiac cycle. Differences in flow dynamics between methods cause differences in WSS and OSI magnitude. These differences may be significant depending on the patient geometry. The 3DV models contained more complex radial velocity and a higher degree of axial recirculation than the 1DV models. This additional complexity reduces the defined helical flow throughout the cavity observed in the 1DV model. Despite the differences in secondary flow, flow dynamics in the iliac vessels are generally similar between the 3DV and 1DV models. Both methods would be sufficient to model general flow dynamics though for more detailed simulations, such as particle modelling which involve accurate simulation of secondary flow and WSS, it may be necessary to choose the more physiologically accurate model. In order to assess which model is closer to *in vivo* dynamics the next chapter involves a comparison of simulated results with PC-MR data.

Chapter 6
Comparison of CFD and PC-MRI

6.1 Introduction

In the previous chapter the effects of varying inlet boundary conditions on the haemodynamics and WSS of patient specific AAA were compared. An important, and often overlooked, stage in medical CFD is validation of flow by comparison with *in vivo* measurements and so this chapter compares simulated AAA haemodynamics for the three-directional, one-directional and parabolic inlet velocity boundary conditions described in Chapter 5 against *in vivo* measurements obtained using PC-MR imaging.

Previous investigations have used a variety of techniques to provide boundary conditions for patient-specific AAA CFD simulations. Often the results of these simulations are not validated against *in vivo* data. Kose et al [74] and Long et al [93] found general agreement between simulated and PC-MRI data though there were areas of quantitative disagreement, especially in regions of low velocity and complex flow. Fraser found less correlation citing image artifacts and lack of radial inlet flow data as reasons.

These studies used only the head to foot component of velocity and there exists no comprehensive comparison of the magnitude of errors resulting from the use of different boundary conditions in AAAs which includes radial velocities. The type and quality of boundary conditions often depend upon the precision of *in vivo* acquisition techniques and so authors are often forced to compromise on spatial and temporal accuracy in simulations. A comparison of simulated AAA haemodynamics with *in vivo* measurements will assess the extent to which simulated blood flow deviates from physiological behaviour when using different methods of inlet velocity boundary conditions. A significant difference between *in vivo* data and simulations when using simplified inlet velocity boundary conditions will mean more complex conditions are necessary for future investigations. Conversely, if each boundary condition type results in similar magnitudes of error then the use of simplified boundary conditions can be justified saving both imaging and computational effort. In the Chapter 7, patient-specific AAA blood flow is seeded with monocyte particles and so validation of patient specific haemodynamics provides

Patient	Distance
1	6.6 cm
2	7.46 cm
3	6.16 cm

Table 6.1: *Distance of mid-plane from inlet*

a means of quantifying errors in the underlying flow which controls particle motion, allowing a greater degree of confidence in the results of simulations of monocyte behaviour.

Patient-specific AAA simulations with varying levels of velocity boundary condition complexity are validated against three-component PC-MRI velocity data at a transverse cross-section around the midpoint of the AAA cavity. Flow dynamics between boundary condition methods are compared to assess whether the differences between methods are significant.

6.2 Method

Velocity encoded PC-MR images were obtained over a transverse cross-section around the centre of the AAA cavity for each of the three patient specific models described in Chapter 5. The z-coordinates of these planes in relation to the inlet are given in table 6.1

Mid-aneurysm PC-MR scans were taken in the same scanning session as the inlet scans using an identical protocol, as described in Chapter 5. Velocity data was obtained from the PC-MRI scans in the head to foot, left to right and anterior to posterior directions at 20 equally spaced timepoints throughout a cardiac cycle. Velocity encoded PC-MRI data was segmented using the corresponding intensity images and converted into velocity data as described in Chapter 5. By including mid-section transverse slices in the CFD simulations of each of the three patient specific geometries, the simulated mid-section velocities can be directly compared with the PC-MRI data. A qualitative comparison of velocity vectors can be observed by applying a colour map to velocity magnitudes throughout the plane. The aim of this chapter is to assess which boundary condition method is more accurate by quantifying the difference between simulations and imaging data and so a more rigorous statistical analysis is required. When seeking to validate simulated data it is important to remember that there is an intrinsic error in PC-MRI measurements caused by limitations in resolution, noise present in the image and other artefacts and so there will be intrinsic differences between PC-MRI velocities and the actual velocities encountered *in vivo*. Analysis of data should therefore be conducted as a comparison

of methods and not a comparison with physiological flow.

6.2.1 Image and Statistical Analysis

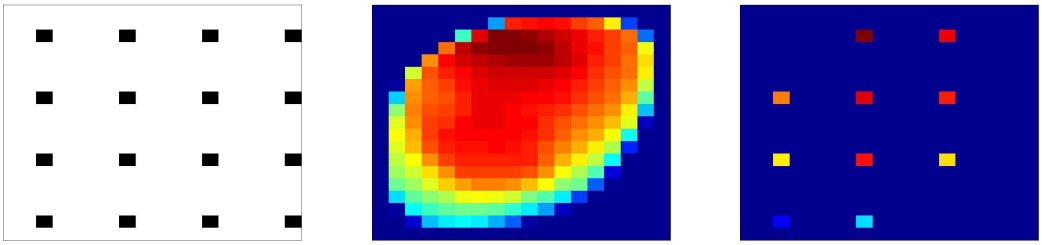

(a) Sample grid (b) Mid-plane velocity data (c) Selected data points

Figure 6.1: *Example of grid-based pixel selection*

All CFD mid-plane velocity data was averaged to create a grid with the same resolution as the PC-MRI data, allowing a direct comparison. Data points for analysis on each plane were selected using Matlab to overlay a grid of equally-spaced pixels on all data sets at each time point and selecting the pixels which fell within the lumen boundary (see figure 6.1). Pixels from systolic and diastolic flow timesteps were grouped seperately to compare possible differences in accuracy between each flow regime. In order to observe the correlation between simulated and MRI derived velocities, linear regression analysis was applied to scatter plots of each inlet velocity boundary condition method against PC-MRI data for all three directions of velocity. Spearman's Rank correlation coefficients were then obtained for each. Regression analysis and correlation coefficients are a useful method of determining a correlation, or lack of, between data sets though apparent strong correlations may be misleading when comparing CFD with imaging methods since we can assume that a significant relation between the CFD and PC-MRI data sets is likely. Bland and Altman [7] review the limitations of using correlation coefficients alone when comparing methods and suggest the use of Bland-Altman plots to offer a more meaningful comparison. For each data point in a Bland-Altman plot, the average of the CFD and MR velocities is plotted against the velocity difference (MRI-CFD). It is assumed that neither the CFD nor the MRI data provides the exact velocity and so the average of the 2 serves as an estimate of the physiological value. The Bland-Altman plot can then be used to observe variance in the difference between methods over a range of flow velocities. Lines of mean difference and mean difference $\pm$ 2 standard deviations were also plotted from which we can work out the standard error in difference between velocities derived through CFD and MRI

for each of the CFD boundary condition methods. The mid-section velocities of simulations with three-directional, one-directional and parabolic inlet velocity profiles were compared with PC-MRI data for all three patients.

6.3 Results

In general, the CFD simulations underestimate average mid-section PC-MRI velocity at higher velocity magnitudes and overestimate average mid-section PC-MRI velocity at low velocity magnitudes in the 3DV and 1 DV models (figure 6.2) and in the Womersley inlet flow model with the exception of systolic flow during systole in patient 3.

Plots of PC-MRI velocity data against CFD in the head to foot direction of patient 1 (figure 6.3) show a slight positive correlation for all three boundary condition methods, the most prominent being the 1DV model. Perhaps more noticeable is the difference in distribution of data points between diastolic and systolic samples. Bland-Altman plots of head to foot velocity (figure 6.4) show less variation in difference between MR and CFD data during systole than diastole, especially in the 1DV and Womersley flow models. The increase in data variability during diastole suggests a higher degree of noise is present during the slower diastolic flow. This dichotomy between systolic and diastolic data is not present in the plots of PC-MRI data against CFD data in the right to left direction (figure 6.5) in which few CFD data points are greater than 0.06 m/s. Bland-Altman plots (figure 6.6) show error to be proportional to average velocity. Velocity data in the anterior to posterior direction, shown in Appendix C, is similar in trends to that of the anterior-posterior direction. Together, these plots suggest that a higher degree of error is present in low velocity flows associated with diastole and with radial velocities throughout the cardiac cycle than the high velocity flows observed during mid-systole. Visualisations of in-plane velocities from diastolic CFD and PC-MRI data (figure 6.7) show that a high degree of noise is present in the PC-MRI data at low velocities. The decrease in signal to noise ratio (SNR) in PC-MRI data at low velocity flows has been observed previously [64, 124] For the greatest accuracy in attaining velocity, the velocity encoding of PC-MRI data must be as close to the observed velocity as possible. The PC-MRI data provided for this study used a fixed velocity encoding sensitivity of 1.5 m/s for all components of velocity. While this sensitivity has been used previously for spatial velocity analysis in the aorta [111] it is a conservative value allowing large amounts of noise to be prevalent in the low velocities observed during diastolic flow and flow in the radial directions. Further evidence of this increase in MR noise at lower

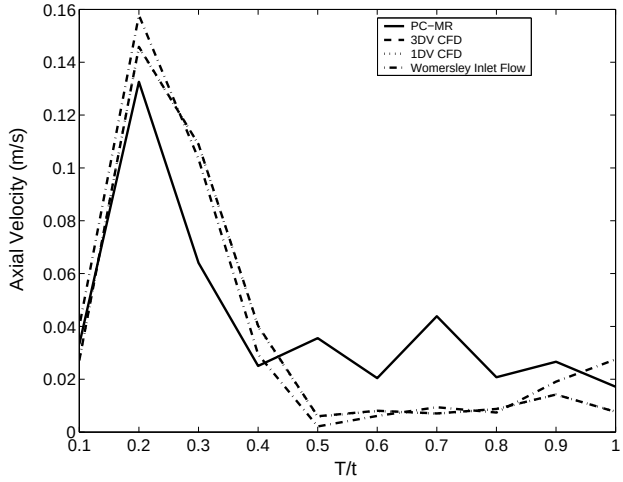

(a) Patient 1

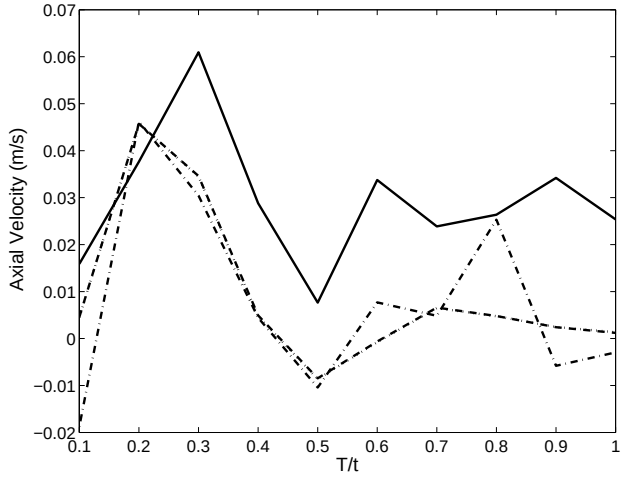

(b) Patient 2

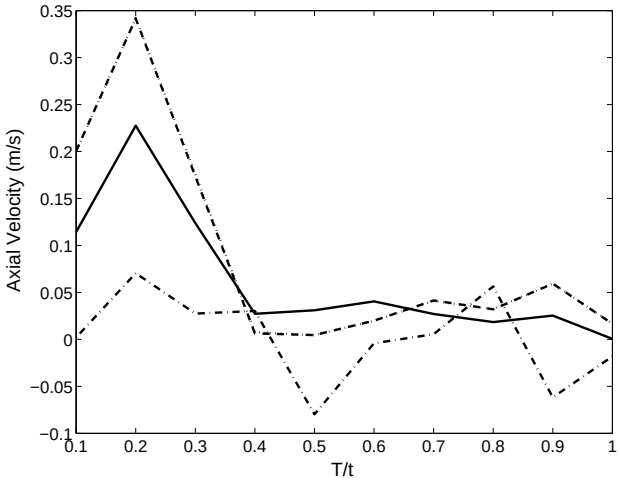

(c) Patient 3

Figure 6.2: *Average mid-plane head to foot velocity*

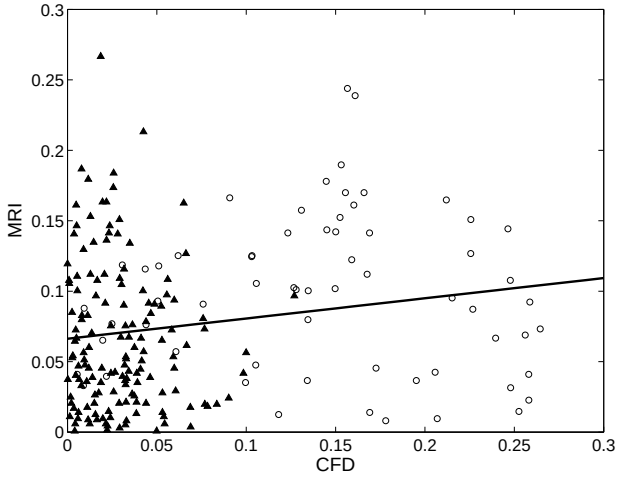

(a) 3DV

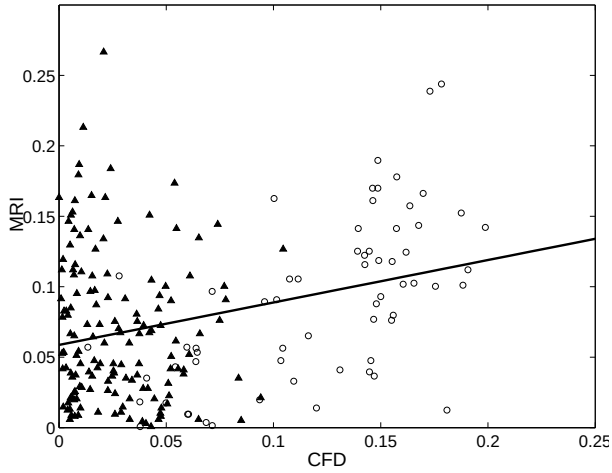

(b) 1DV

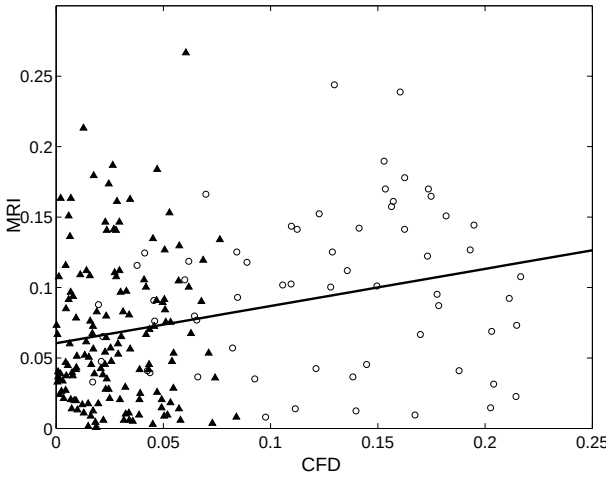

(c) Womersley inlet flow

Figure 6.3: *Scatterplots of CFD against MRI midplane velocity data in heat-foot direction of patient 1. Systolic data is represented by circles, diastolic by black triangles*

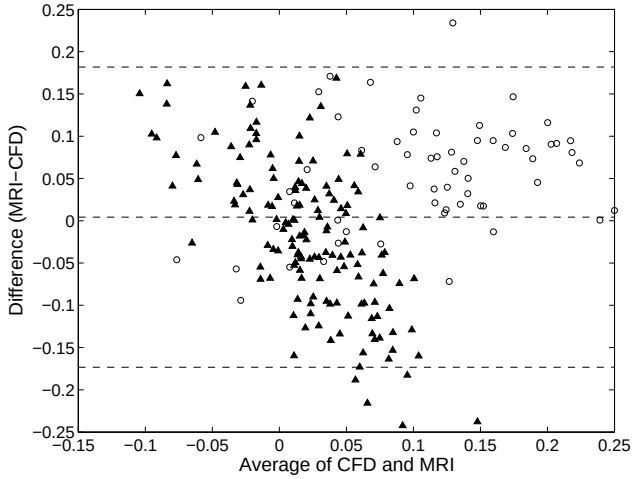

(a) 3DV

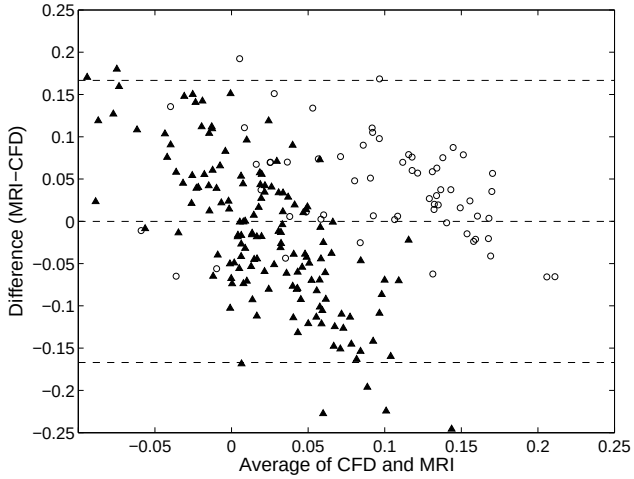

(b) 1DV

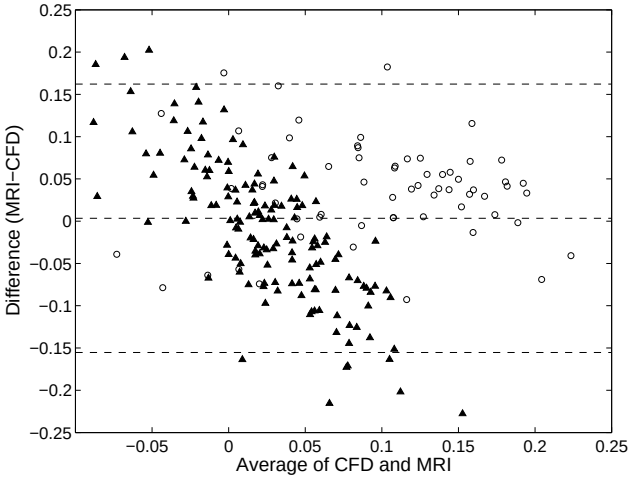

(c) Womersley inlet flow

Figure 6.4: *Bland-Altman plots of CFD against MRI midplane velocity data in head-foot direction of patient 1. Systolic data is represented by circles, diastolic by black triangles*

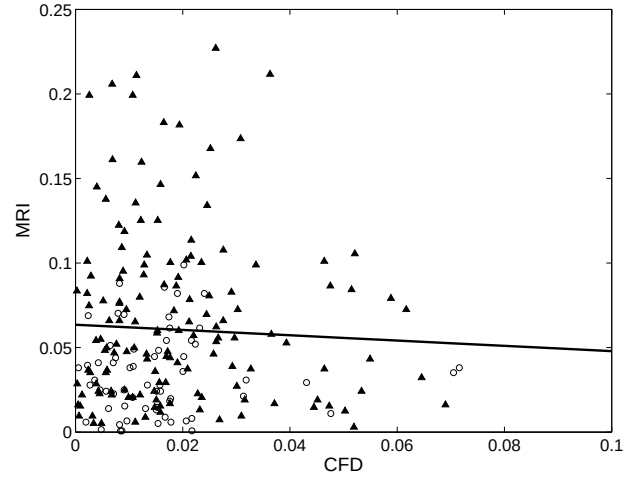

(a) 3DV

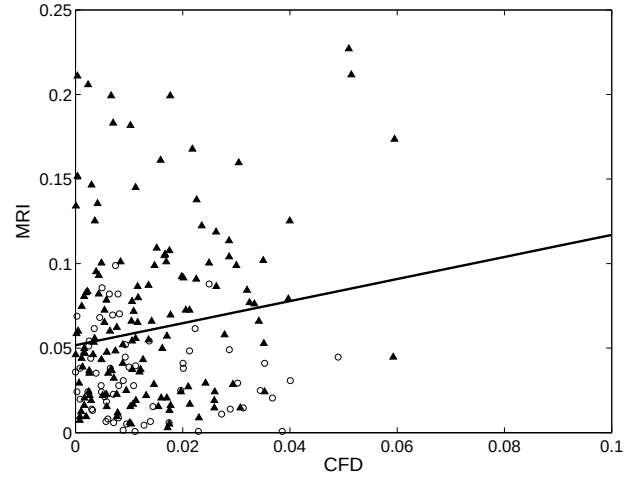

(b) 1DV

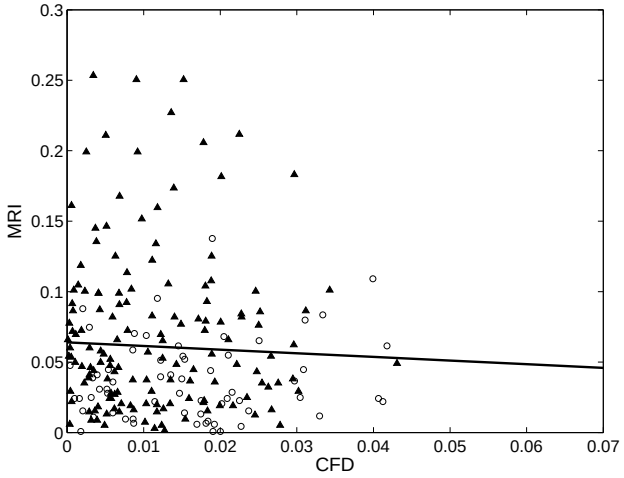

(c) Womersley inlet flow

Figure 6.5: *Scatterplots of CFD against MRI midplane velocity data in right-left direction of patient 1. Systolic data is represented by circles, diastolic by black triangles*

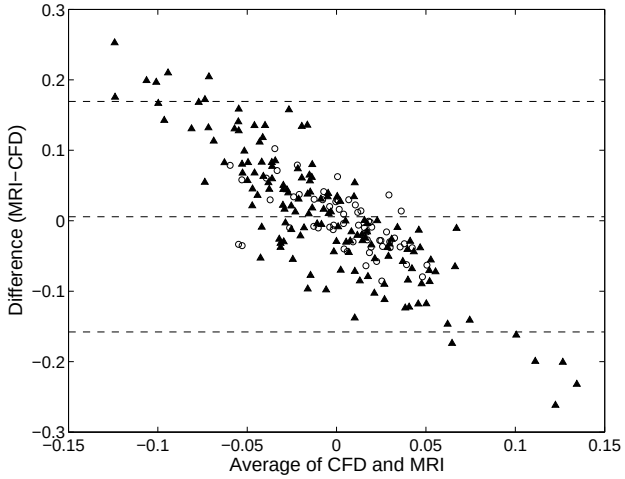

(a) 3DV

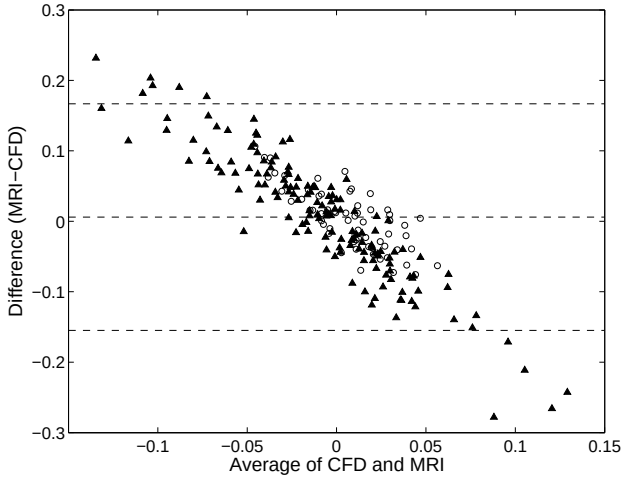

(b) 1DV

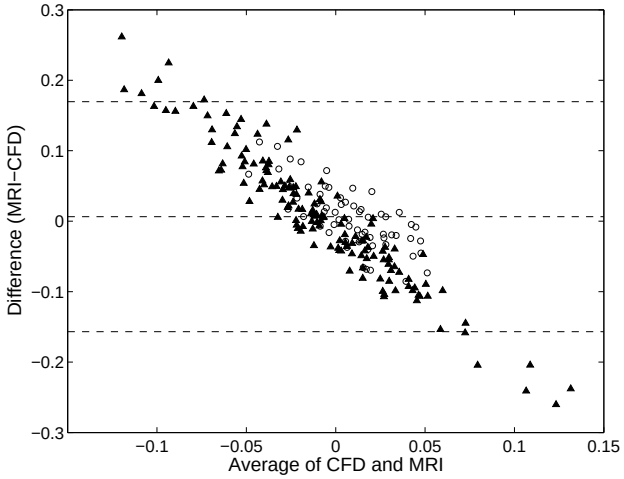

(c) Womersley inlet flow

Figure 6.6: *Bland-Altman plots of CFD against MRI midplane velocity data in right-left direction of patient 1. Systolic data is represented by circles, diastolic by black triangles*

	Axial and radial Inlet Velocity	Axial Inlet Velocity	Womersley Inlet Flow
SRCC	0.584	0.448	0.162
t-value	8.57	7.042	1.715
N	144	200	111
Linear Regression	$0.628x + (6 \times 10^{-3})$	$0.563 + (1.76 \times 10^{-2})$	$0.1086x + (1.07 \times 10^{-1})$
2-tail p-value	1.6×10^{-14}	3×10^{-11}	8.9×10^{-2}

Table 6.2: *Spearman's Rank Correlation Coefficient (SRCC) and t and p values for all samples in which CFD velocity is greater than 0.06m/s*

velocities is found in patient 3 in the 3DV and 1DV boundary condition methods, though not in the Womersley inlet flow model. Unlike patient 1, higher radial velocities mean that the radial flow during systole is also generally more consistent than during diastole (see Bland-Altman plots in Appendix C), The larger cavity diameter present in patient 2 contains generally lower velocity mid aneurysm flow than the other patients and so the distinction between systolic and diastolic velocities is not as well defined. Despite this, velocity differences between MRI and CFD are generally more consistent in systolic flow as shown in Bland-Altman plots in Appendix C.

The level of noise present in the low velocity PC-MRI data prevents useful comparison with CFD derived velocities and so data points in which CFD velocity is below 0.06 m/s were removed from the data sets. Scatter plots and Bland-Altman plots of the remaining data were created, combining data from all three patients in order to compare the simulated data from the three boundary condition method models with the PC-MRI data. Due to the low velocity flow present in patient 2, less than 2% of the data was above the critical 0.06 m/s and so the combined results with lower CFD velocity samples removed is comprised mainly of data from patients 1 and 3.

Linear regression analysis of combined MRI against CFD data (figure 6.8) shows that both the 3DV and 1DV inlet boundary condition simulations have similar, positive, correlation with Spearman's Rank correlation coefficients of 0.584 ($p << 0.01$) and 0.448 ($p << 0.01$) while the Womersley inlet flow simulations shows a smaller, though still positive Spearman's Rank correlation coefficient of 0.162 ($p = 0.089$). Figure 6.8(c) suggests there is still noise present in the data between 0.06 and 0.1 m/s of the Womersley inlet flow models. The Womersley inlet flow method produces the least accurate simulations of AAA velocity and both 3DV and 1DV models have a similar level of accuracy. There are limits to what can be inferred from a Spear-

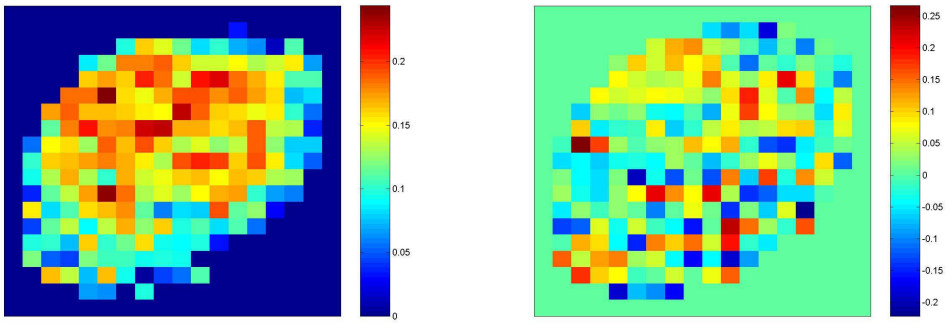

(a) T/t=0.1 (b) T/t=1

Figure 6.7: *Unfiltered PC-MRI velocity data (m/s) in axial direction during systole and diastole*

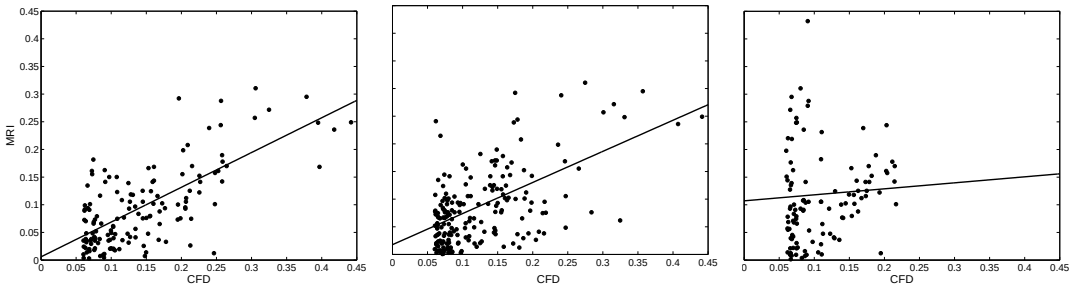

(a) 3DV (b) 1DV (c) Womersley inlet flow

Figure 6.8: *Scatterplots of CFD against MRI midplane velocity data for all samples in which CFD velocity is greater than 0.06m/s*

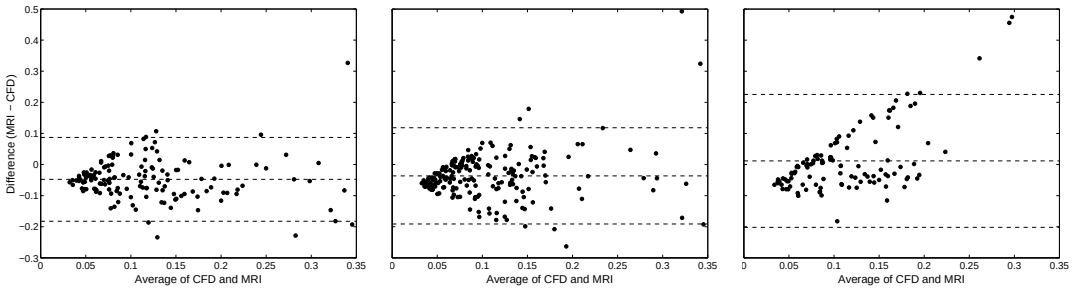

(a) 3DV (b) 1DV (c) Womersley inlet flow

Figure 6.9: *Bland-Altman plots of CFD against MRI midplane velocity data for all samples in which CFD velocity is greater than 0.06m/s*

man's Rank correlation coefficient as the null hypothesis assumes zero correlation and, as both the simulated and MRI data measure the same physiological variable, some degree of positive correlation is expected. Even a perfect agreement with MR data does not guarantee physiological accuracy as a degree of error is associated with obtaining PC-MRI, and the unfiltered data shows the introduction of further noise through the use of fixed velocity encoding. Bland-Altman plots allow an analysis of the variance in difference between simulated and imaging data.

The Womersley inlet flow model has the least mean velocity difference between MRI and CFD (0.0119m/s with 95% confidence intervals of -0.008 to 0.0317 m/s). This does not infer that it is the most accurate method as it was shown to have the largest variation in data with the limits of agreement between 0.221 and -0.197 m/s. Variation is the more relevant factor here since a simulation with large mean difference but insignificant variation from MR data indicates a constant difference in results and so a correction factor can be used to provide agreement. Correcting the data in this way becomes harder to justify with increasing variation. Figure 6.9 indicates 2 subgroups in the data, a set with error proportional to average velocity, possibly related to noise in the lower velocity data and a more stable set with a lower average difference. The mean velocity differences between MRI and CFD for the 3DV and 1DV model are -0.0477 m/s (95% confidence intervals of -0.0367 to -0.05 m/s) and -0.0364 (95% confidence intervals of -0.0257 to -0.0471 m/s). A difference of around 0.01 m/s is unlikely to indicate significant differences in haemodynamics during systole where velocities exceed 0.2m/s, but may be more significant during diastole when flow velocities are generally lower than 0.05 m/s. Both 3DV and 1DV models have less variability between MRI and CFD data than the Womersley inlet flow model (limits of agreement of 0.0844 to -0.1797 for the 3DV and 0.1152 to -0.188 for the 1DV). The lower variability of the 3DV model suggests that using all three velocity components at the inlet produces the simulations most likely to be accurate when compared with one direction and Womersley flow profiles. While it proved to be the more accurate model in this study, the 3DV model has a standard deviation of 0.0674 m/s which is high even in systolic flow conditions. Data in both the 3DV and 1DV Bland-Altman plots is arranged in an arrowhead shape which portrays the variability increasing with average velocity for average velocities of less than 0.15 m/s. This effect may be due to the presence of noise in the MR data at lower velocities.

By maintaining a constant velocity encoding value well above peak systolic velocity, the SNR of PC-MRI data is diminished at low velocities making comparisons of radial flow velocities

impractical. Filtering data points in which the CFD data is lower than 0.06 m/s removes much of this noise. Comparisons of velocity filtered data show that Womersley inlet flow simulations have limited correlation with PC-MRI data and a high degree of variability in difference between CFD and PC-MRI data. 3DV and 1DV inlet boundary condition simulations share a similar, positive, correlation with MRI data though the 3DV method gives the least variation in difference between simulated and PC-MRI data. While the 3DV model may be the most consistent with MR data, the variability in data is still relatively high.

6.4 Discussion

In Chapter 5, CFD simulations of patient AAAs were compared in order to assess the differences in haemodynamics observed by adding increasing levels of complexity to the inlet boundary conditions. While differences in flow velocities and structure were observed between methods, the most physiologically realistic scenario cannot be identified without comparing the simulated results with a validated method of blood velocity measurement. Mid-cavity cross-sections of PC-MRI velocity data were obtained for comparison with CFD simulations. Data from the CFD simulations with low velocity flow corresponded with regions of low signal to noise ratio in the MR data so comparison of data was carried out using only data points in which simulated velocity was above 0.06 m/s.

Womersley inlet flow models result in large variations in difference and poor correlation between simulated and MRI data. The simplification of haemodynamics and differences caused by centreline velocity assumptions seen in Chapter 5 have been shown to be physiologically unrealistic. The scale of the deviation from PC-MRI data suggests that the assumption of inlet Womersley flow profiles is inadequate for effective simulation of AAA disease. The difference in variation of CFD and MRI data between simulations with 3 and 1 components of inlet velocity are more subtle due to the similarity in haemodynamic trends shown in Chapter 5. The 3DV models exhibited the least variation between simulated and MRI data and so can be assumed to be the most consistent with physiological flow. The choice of boundary condition method often involves a compromise between the accuracy of the simulation and the effort required in obtaining inlet data. To acquire three components of velocity from PC-MRI data, three separate scans are required. Achieving these extra scans is not always possible given time, funding and patient participation restraints. The required accuracy depends on the motives for simulation. This study has shown that if general trends in haemodynamics are required then velocity data

in the head to foot direction only may be sufficient. Simulations in which a higher order of accuracy are necessary, such as the flow-particle behaviour simulated in this study require the most accurate inlet boundary conditions available which has been shown in this study to be the 3DV model.

PC-MRI uses velocity encoding to prevent aliasing of the data. Higher velocity encoding sensitivity values prevent velocity artefacts produced through aliasing but decreases the phase shift leading to a decrease in SNR [124]. The low SNR observed in low velocity flows in this study is likely to be the result of using a fixed velocity encoding range for each component of velocity throughout the cardiac cycle. Setting a conservative fixed value for velocity encoding sensitivity prevents aliasing in axial flow during systole but increases noise in the lower velocity flows. A study by Greil et al [55] show that the effects of low SNR are cancelled out when all pixels are averaged to give accurate flow rate, but the influence of noise becomes more important when spatial velocity profiles are required. Johnson and Markl [64] describe the challenge in obtaining the optimum velocity encoding protocol as more complex parameters lead to longer scanning times. They trial the use of 5-point balanced flow encoding.

Low SNR is also present in the inlet PC-MRI data, particularly during diastole and in the radial flow velocities of the 3DV model. This study shows that changes in the radial components of the inlet velocity boundary conditions result in a difference in downstream haemodynamics and so applying a velocity encoding scaled by the magnitude of velocity may result in further differences in AAA haemodynamics. Using 3 components of inlet velocity in simulations has been shown to be the most consistent method of simulation and so by removing some of the noise present in the radial directions this accuracy may be further improved.

6.5 Conclusions

As the amount of information contained in AAA inlet velocity boundary conditions decreases, changes in simulated downstream haemodynamics occur leading to increased deviation from physiological flow as measured via PC-MR imaging. This shift is less significant between simulations with three components of velocity and axial velocity only than between axial only and Womersley inlet flow profile simulations. Future investigations applying a variable velocity encoding range, scaled by estimated maximum velocity may increase the SNR present in lower velocity flows and allow for a more detailed analysis of radial velocities.

Chapter 7
Patient Specific Near Wall Particle Residence Time Modelling

7.1 Introduction

In Chapter 4, the application of a NWPRT model in simplified AAA geometries revealed defined peaks in areas where monocyte infiltration is most likely. These peaks shift in magnitude and position depending on the size of the aneurysm cavity and the vortex dynamics present. In this chapter the WSS-limited NWPRT model developed in Chapter 4 is applied to simulated monocytes seeded into flow in the patient-specific geometries used in Chapters 5 and 6 with three directional inlet velocity boundary conditions taken from PC-MR data. While the patient-specific geometries are more complex, the formation and dissipation of vortices which appear to control the motion of monocytes in flow has been shown to be present. The areas with the highest potential physiological impact, are sections of the AAA with high peak NWPRT where monocytes are statistically most likely to enter the vessel wall and, conversely, sections of low or zero NWPRT where monocytes are extremely unlikely to enter the wall.

7.2 Methods

The patient-specific geometries and finite volume meshes used here are identical to those of patients 1 to 3 described in Chapters 5 and 6. Fluent was used for solving the equations of flow and particle motion as described previously. Each of the 3 geometries feature a fine boundary layer of volumes and extended outlets though no extension of the inlet is required. The three-directional inlet velocity boundary condition based on PC-MR data as described in Chapter 5 was applied to each geometry and each simulated for three full cardiac cycles before seeding with particles. The properties of the monocyte particles and the variables of the DPM used to track their motion, including near wall lift and drag forces, remain as described in Chapter 4. Monocytes were seeded into the flow from the beginning of the fourth pulsatile cycle with particles injected 1cm downstream of the inlet to minimise particle escape due to retrograde

Patient	$\lvert\overline{WSS}\rvert_{TA}$	$\overline{WSS_{TA}}$	$\overline{NWPRT/mm}$
1	5.81	0.57	4.95
2	0.6	3.5×10^{-4}	0.27
3	2.9	0.15	9.85

Table 7.1: *Average WSS and NWPRT values*

flow at the inlet. Monocytes were seeded at each $\Delta t = T/200$ timestep over one full cardiac cycle allowing the monocytes to spread throughout the AAA. The WSS-limited NWPRT model was initiated at the start of the fifth cycle and residence times recorded over 6 full cycles.

7.3 Results

Large peaks in NWPRT are localised at the neck and the bifurcation points of all patients. NWPRT within the centre of the AAA cavity is generally an order of magnitude less than the inlet and outlet peaks. Monocyte infiltration is therefore most likely at the neck and around the bifurcation point of the aneurysms and least likely in the cavity centre. There is more variation in NWPRT between the geometries with magnitudes skewed towards the distal end in patient 1 (figure 7.1), the proximal end in the wider patient 2 (figure 7.2) and various, smaller, peaks throughout the cavity in patient 3 (figure 7.3) . The NWPRT results of particles injected into straight tube models studied in Chapter 4 (figure 4.13(a)) suggest large residence time values located close to the injection plane may be an artefact caused by particles moving immediately to the wall upon injection.

Peaks in NWPRT tend to localise at, or slightly downstream of, peaks in WSS though not all peaks in WSS localise with peaks in NWPRT. For example, the large fluctuation in WSS 7cm upstream from the bifurcation point in patient 2 (figure 7.2) does not match any significant peak in residence time. In patients 1 and 2 there appears to be a qualitative correlation between the scale of NWPRT and the size of the peak in WSS. This relationship does not appear to hold for patient 3 as the largest peak in NWPRT is aligned with a relatively small change in WSS (figure 7.3). Fluctuations in WSS are therefore insufficient predictors of the position and magnitude of NWPRT and monocyte adhesion probability.

Between geometries there is a significant difference in the average residence time per millimeter (see table 7.1). Patient 2 has a significantly smaller mean time averaged WSS magnitude than the other patients as well as a much smaller average residence time. From a study of 3 patients

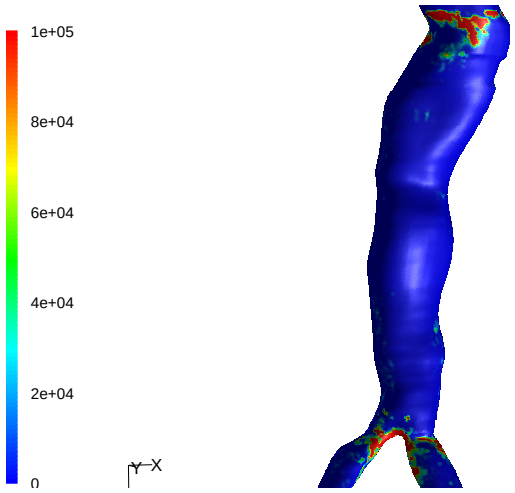

(a) Contours of NWPRT

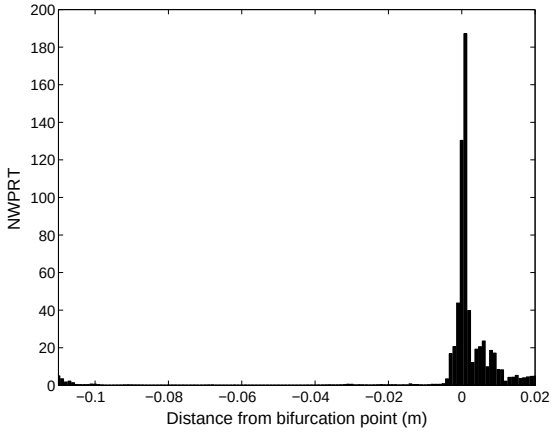

(b) Histogram of NWPRT at 1mm intervals along axial direction

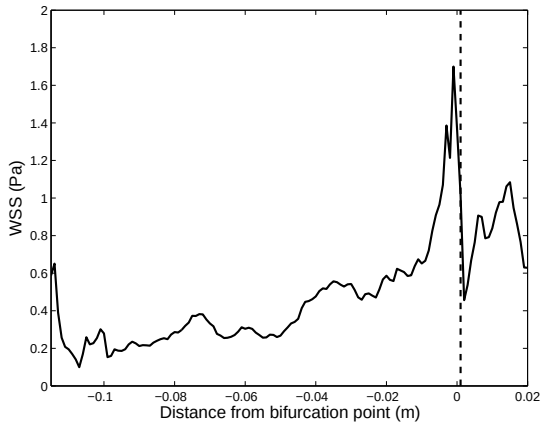

(c) Time averaged WSS. Dashed lines are aligned with peaks in NWPRT

Figure 7.1: *Contours (a) of NWPRT and plots of NWPRT (b) and time averaged WSS (c) in patient 1 after 6 cycles*

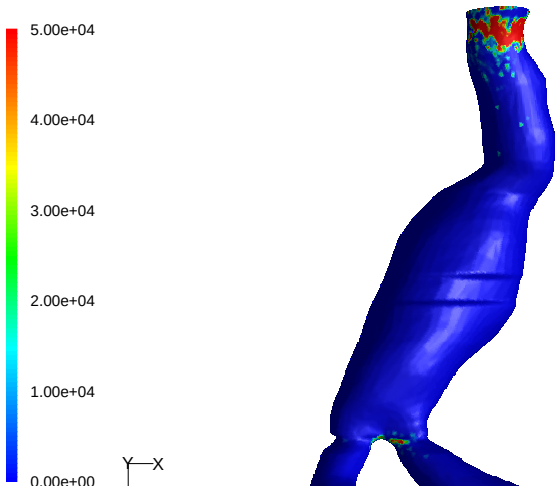

(a) Contours of NWPRT

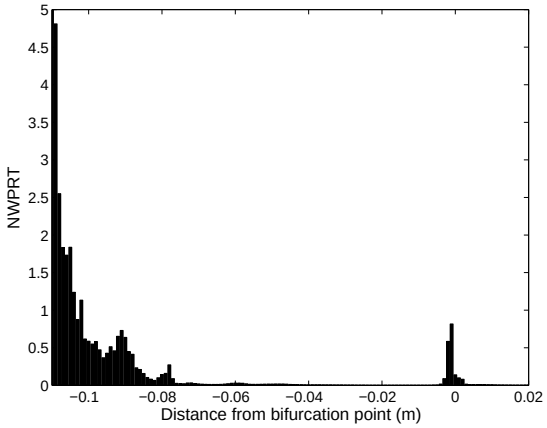

(b) Histogram of NWPRT at 1mm intervals along axial direction

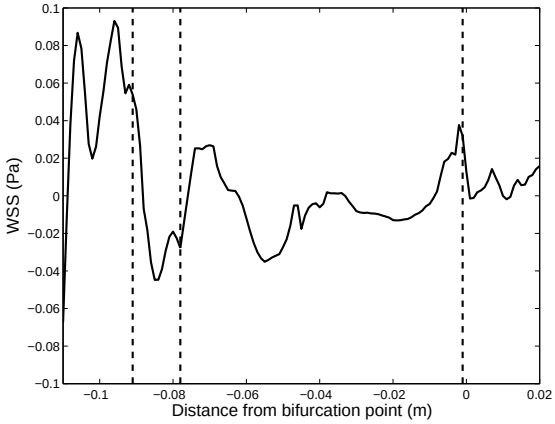

(c) Time averaged WSS. Dashed lines are aligned with peaks in NWPRT

Figure 7.2: *Contours (a) of NWPRT and plots of NWPRT (b) and time averaged WSS (c) in patient 2 after 6 cycles*

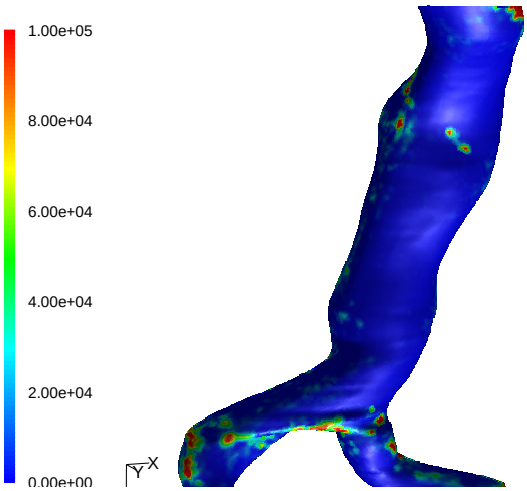

(a) Contours of NWPRT

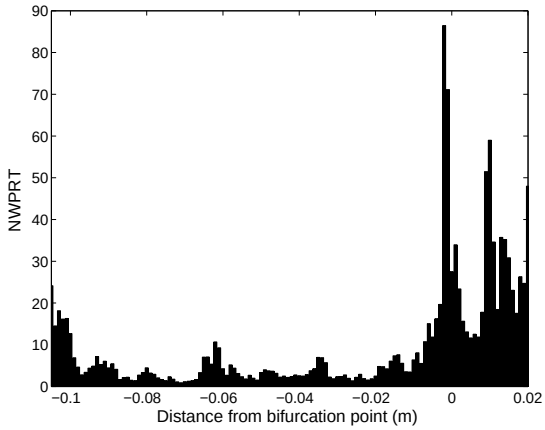

(b) Histogram of NWPRT at 1mm intervals along axial direction

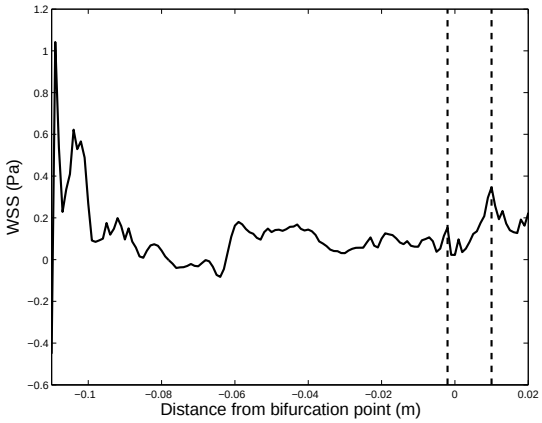

(c) Time averaged WSS. Dashed lines are aligned with peaks in NWPRT

Figure 7.3: *Contours (a) of NWPRT and plots of NWPRT (b) and time averaged WSS (c) in patient 3 after 6 cycles*

it is not statistically significant to claim a correlation between low magnitude WSS and low residence times.

Despite the differences in aneurysm dimensions between the three patients, the general trends in residence times are shared between all geometries with high NWPRT at the neck and bifurcation point of the AAA and lower residence times within the cavity. There are however significant differences in mean residence times between patients. Peaks in residence time generally colocate with peaks in WSS, though trends and magnitude of WSS alone do not appear to be a sufficient indicator of residence time.

7.4 Discussion

Vallabhaneni et al [171] propose the hypothesis that inflammation in AAA occurs in discrete hotspots which in turn causes heterogeneous patterns in wall degradation and therefore wall weaknesses. In this study, monocyte residence times in simulated patient specific AAAs show that there are indeed discrete regions in which monocytes are significantly more likely to attach to the lumen and areas where attachment is extremely unlikely. Cell attachment was shown to be most likely in regions at the neck and bifurcation point of the aneurysm, irrespective of the shape of the geometry, with attachment unlikely at the cavity centre.

In Chapter 4, peaks in the residence times of inflammatory cells were observed to correlate with spikes in time averaged axial WSS which, in simplified models, indicate regions of vortex dissipation. As in the simplified models, this study shows that peaks in cell residence times are located at points immediately downstream of spikes in axial WSS. This may show cell adherence is controlled by vortex behaviour in patient specific aneurysms, though the complex secondary flows observed in patient specific models make vortex behaviour harder to define. While the probability of monocyte attachment is associated with regions of peak WSS, profiles of WSS alone are insufficient for determining where regions of high residence time will occur.

The general trends in peak monocyte residence time are preserved in different aneurysm geometries though the magnitude of these peak residence times and the average residence times in an aneurysm were shown to vary significantly. Physiologically this may mean that inflammation is less prevalent in some AAAs than others. This may be caused by the shape of the geometry, the dynamics of the inlet flow or a combination of the two. This study showed that an AAA with significantly lower average particle residence times also had significantly lower

WSS magnitudes. The size of this study does not provide statistical significance and further trials would be required to assess any correlation between WSS magnitude and cell residence time. Inhibition of cell adhesion at low WSS would be significant since low WSS conditions are generally thought [81, 164, 189] to be preferential for leukocyte adhesion.

This study simulates the probability of inflammatory cell adhesion to the lumen. The migration of cells once they enter the interstitial tissue beyond the endothelial lining is beyond the scope of this investigation but will play a role in the final destination of macrophages within the AAA wall. The trafficking of interstitial leukocytes is controlled via chemotactic gradients [49]. While this is a complex procedure on a cellular level, statistical modelling of macrophage accumulation may be an area for future investigation. Physiological data may be used to assess the probability of a macrophage residing in a given radius. This will enable the NWPRT model used in this investigation to be extended to determine the probability of inflammation throughout the AAA wall.

In order to develop the techniques used in this study for clinical use, the simulated residence time results must be validated against *in vivo* measurements of macrophage accumulation. *In vivo* data can be obtained by applying contrast agents to a variety of scanning techniques. The PET contrast agent ^{18}F-FDG has been used previously as an indirect marker of vessel inflammation [75, 135]. Combined PET/CT images give a visualisation of the spatial distribution and the magnitude of inflammation. For macrophages specifically, MRI contrast agents SPIO and USPIO may be useful tools have been used to quantify monocyte recruitment in atherosclerotic lesions [91] and feasibility studies have been conducted on murine AAA models [170]. If the results of simulated monocyte attachment correlate with regions of *in vivo* macrophage accumulation then NWPRT models can be used as a non-invasive method of determining the hotspots of inflammation. This information could then be used to quantify the magnitude and distribution of wall weaknesses and could potentially be incorporated into a model of aneurysm rupture risk prediction. Significant differences between the simulated and observed accumulation of inflammatory cells would suggest that cells are transported to the site of inflammation via an alternative mechanism. This may be due the migration of cells between the point of entry and their destination or through cells entering the wall through an 'outside-in' pathway whereby the inflammatory cells do not originate in the bulk aortic flow, reaching the adventitia through a network of microvessels.

Whether a correlation is present or not, validation of simulated results against *in vivo* observa-

tions will elucidate the mechanisms by which macrophages reach the site of inflammation in the aneurysm wall.

7.5 Conclusions

Numerical simulations of monocyte residence times in patient specific AAA models show discrete regions in which the probability of cell adhesion is high. These regions are located at the neck and bifurcation point of the aneurysm and tend to be located immediately downstream of peaks in axial WSS indicating that secondary flow features have a significant influence on monocyte adhesion. Attachment was found to be unlikely throughout the centre of the cavity. Further investigation is required to determine whether average WSS affects the average magnitude of cell residence times.

Residence time models do not account for the migration of macrophages within the vessel wall. In future investigations, a probabilistic model can be added which accounts for this movement.

Simulated results must be compared against *in vivo* observations of macrophage accumulation in order to validate the numerical findings. Validation may determine the pathway in which inflammatory cells reach their destination within the aortic wall in AAA disease.

Chapter 8
Final Conclusions and Future Work

8.0.1 Conclusions

AAA rupture remains a major cause of death in the elderly, accounting for 1.5% of the total mortality in males over 55 years old [23]. Despite improvements in surgical techniques and endovascular stenting, the mortality rate for emergency AAA repair remains high while the post rupture AAA mortality rate is up to 90%, including patients who do not reach hospital [150]. A method of rupture prediction is required to prevent unnecessary surgery while ensuring that intervention occurs before the aneurysm ruptures. Aneurysm size and growth rate are the current clinical indicators of rupture which require frequent monitoring and have been shown to be inefficient in many cases. One of the underlying mechanisms responsible for the breakdown of the wall itself is inflammation. It has been suggested that inflammation occurs in specific focal areas in the AAA wall causing 'hotspots' of wall degradation and remodelling. Identifying the distribution and intensity of these hotspots may lead to a clinical indicator of AAA wall weakness and thus improve rupture risk prediction. In this study numerical models were developed which simulate haemodynamics and the probability and distribution of monocyte adhesion to the lumen in generic and patient-specific AAAs. The aims of the study were to develop the process of numerical modelling through novel investigations of turbulence models and inlet boundary conditions, to elucidate the behaviour of monocytes in AAA pathology and to work towards a clinical indicator of AAA rupture risk based on inflammation-driven wall weakness.

In Chapter 2, generic AAA geometries were calibrated to ensure cycle independence and appropriate order of accuracy and optimum grid and timestep sizes were obtained via convergence investigations. A fine boundary layer was applied near the wall to account for shear stresses and flow dynamics on the scale of a single monocyte.

A transition to turbulent flow has previously been observed in experimental AAAs during the end of systole. Despite this, there have been no previous investigations into the use of turbulence models in numerical simulations of AAA.

In Chapter 3, the RNG $\kappa-\epsilon$ model was found to over simplify secondary flow in both steady and

pulsatile flows to an unacceptable degree and so should be avoided for modelling AAA flow. The $\kappa - \omega$ and LES models predicted peak WSS with more accuracy than the laminar model in steady flow. In pulsatile flow the $\kappa - \omega$ and the LES model with no turbulent perturbations at the inlet produced similar WSS profiles while the LES models in which inlet turbulence was simulated produced significant differences in haemodynamics during the deceleration phase. The changes in haemodynamics caused by the addition of inlet turbulence were not affected by the intensity of the perturbations, suggesting that the spatial distribution of secondary flow at the inlet has significant effects on downstream flow. Using $\kappa - \omega$ and LES models did not significantly increase the simulation times in these models when compared to laminar models. If information on inlet turbulence is unavailable, both the $\kappa - \omega$ and no inlet perturbation LES models are viable for AAA modelling. If inlet perturbations can be quantified the vortex method inlet perturbation LES model is required.

In Chapter 4, the haemodynamics of generic aneurysm geometries were found to be characterised by the formation, translation and dissipation of annular vortices. Regions of high monocyte residence times were expressed in discrete bands along the AAA walls in the axial direction with large regions of very low or zero residence time throughout the cavity. The regions of high adhesion probability were aligned with peaks in WSS associated with vortex dissipation. This suggests that the distribution of discrete hotspots of monocyte adherence is controlled by vortex behaviour. The bands of high residence time move downstream as the maximum aneurysm diameter increases until a critical diameter of around 1.8 times the inlet diameter above which the bands move upstream and the overall residence time of monocytes increases exponentially. If this were to happen *in vivo*, fully developed AAAs with large cavity sizes may create a positive feedback effect as the higher numbers of monocytes entering the wall cause greater degradation.

The protocol for obtaining haemodynamics and monocyte residence time was applied to patient specific models. There is no previous literature detailing which velocity inlet boundary condition method is most appropriate for modelling AAAs and so an inlet boundary condition investigation was conducted in Chapters 5 and 6.

Applying Womersley inlet flow profiles created much more linear flow than using spatially varying inlet velocities. In some cases, assumptions in calculating centreline velocity were found to lead to significant errors in mean inlet velocity during diastolic flow. Simulations with one and three components of inlet velocity produced similar axial velocities and WSS distributions though differed significantly in terms of the secondary and oscillatory nature of

flow and often in the magnitude of WSS and oscillatory shear. Spiral flow was prominent in the axial inlet boundary condition simulation. Applying Womersley inlet velocity profiles removed much of this spiral flow, while adding radial velocity vectors at the inlet created more complex flow dynamics which reduced the magnitude of spiral flow.

In Chapter 6, the boundary condition methods were validated through comparison of simulated mid-cavity velocities with PC-MR data. At low velocities PC-MR data exhibited low SNR resulting in a high degree of error when comparing with simulated data. At higher velocities, the Womersley inlet velocity profiles deviated the most from physiological flow while the three component inlet velocity deviated the least. There was less difference between one and three component models of inlet velocity than between the one component and Womersley inlet flow model.

Chapters 5 and 6 show that Womersley flow models should only be used if the general trends in axial velocity and WSS are required and should not be used to ascertain values of WSS or secondary flow magnitude. If Womersley inlet flow is applied, care should be taken to ensure centreline velocity is representative of the mean inlet velocity.

Similarities in haemodynamics between models with one and three components of inlet velocity mean that using only axial velocity may be sufficient to obtain trends in velocity magnitude and patterns of WSS distribution. The differences in secondary flow prediction and WSS and oscillatory shear magnitudes between the methods mean that simulations which rely on accurate secondary flow modelling or obtaining accurate WSS magnitudes, such as the particle tracking used in this study, require the use of radial as well as axial components of inlet velocity.

In Chapter 7, initial studies of monocyte residence times in patients showed the relationship between the probablility of particle adhesion and haemodynamics was the same in *in vivo* and simplified AAAs, suggesting that the idealised model used in this thesis is reasonable. All patient simulations showed discrete regions at the neck and bifurcation point of the aneurysm at which the probability of monocyte adhesion is high with larger areas throughout the cavity centre where adhesion probability is unlikely. The regions of high residence time are located immediately downstream of regions with peaks in axial WSS suggesting that secondary flow has a significant effect on the distribution of monocyte adhesion.

This study has shown that monocytes are likely to adhere to the lumen in discrete hotspots, with large regions in which adhesion is unlikely. The patterns in adhesion distribution were found to

be dictated by the behaviour of secondary flow in the aneurysm. In simplified AAA geometries, a critical diameter was found above which the average near wall cell residence time increased exponentially.

8.0.2 Future Work

The complexities involved in the simulation of any biological system mean that it is necessary to make various assumptions in order to achieve feasible simulation times. This study assumed rigid walled geometries throughout and so further investigation is required to assess the affects of wall motion on monocyte adhesion probability.

The comparison of simulated CFD results with PC-MRI data was hampered by a high degree of noise present at regions of low velocity flow due to a high velocity encoding sensitivity. Applying a variable velocity encoding range, scaled by estimated flow velocity may increase the SNR in low velocity PC-MR data sufficiently to allow comparison. Recent investigations have proposed methods of solving this problem without significantly affecting the duration of scan time [64].

The migration of macrophages from within the intima of the vessel wall to their final destination is beyond the scope of this investigation. To gain a holistic view of monocyte/macrophage inflammation, the results of the residence time models can be linked with statistical models of monocyte migration within the wall based on physiological data.

A tentative link between the mean time-averaged WSS and mean magnitude of residence time was found in patient-specific simulations though further study is required to assess whether this trend is statistically significant.

This work represents the first steps towards a rupture risk prediction model based on inflammatory wall degradation. To assess the clinical relevance of the predicted trends in monocyte adhesion found in this study, the results must be validated against *in vivo* data. Regions of inflammatory activity and monocyte accumulation within the aortic wall can be mapped through the use of contrast agents such as FDG in PET/CT scanning and SPIO and USPIO in MR scans. A study comparing numerical predictions of monocyte adherence with imaging data of inflammatory activity in patients will determine the relevance of using numerical prediction in defining regions of inflammation in AAA disease. A correlation between simulated and *in vivo* imaging results would mean numerical modelling is a viable method of predicting

inflammation-mediated wall weakness. Significant differences in results would suggest that inflammatory cells reach their destination through a radically different mechanism than the traditional model and so future research must focus on discovering the origin and methods of transportation of cells before numerical modelling can be applied.

Appendix A
Grid Convergence Indices

Table A.1 shows the GCI for WSS at the cavity midpoint and a point 0.038m downstream of the midpoint calculated using $p = 2$ and a value of p derived from Roache et al [138] (equation 2.19).

T/t=0, z=0m		T/t=0, z=0.038m		T/t=0.08, z=0m		T/t=0.08, z=0.038m	
GCI_{12}, $p = 2$	GCI_{12}, $p = 1.04$	GCI_{12}, $p = 2$	GCI_{12}, $p = -1.3$	GCI_{12}, $p = 2$	GCI_{12}, $p = 0.76$	GCI_{12}, $p = 2$	GCI_{12}, $p = 1.64$
34%	95%	8.7%	44%	8.3 %	14%	4.2%	4%

Table A.1: *WSS GCI for model $D = 2.1$ in pulsatile flow with $p = 2$ and p derived from equation 2.19*

At the end of diastole ($T/t = 0$) the GCI obtained using the derived p are unfeasibly large. Changes in flow direction with grid refinement at the sample regions may cause unrealistic values of p and so the value of $p = 2$ was used throughout [139].

Appendix B
NWPRT Models

Histograms of NWPRT against distance from cavity centre for axisymmetric AAA models $D = 1.3d$ to $D = 2.9d$ with no WSS-limiter applied (see Chapter 4). Applying the WSS-limiter tends to decrease the magnitude of the proximal peak in NWPRT. In the case of the $D = 2.1d$, applying the limiter splits the large peak in NWPRT into 2 seperate peaks.

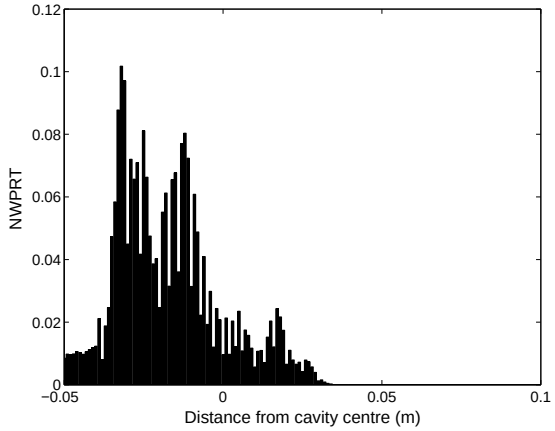

Figure B.1: *Histogram of NWPRT (no WSS-limiter) against distance from cavity centre for* $D = 1.3d$*.*

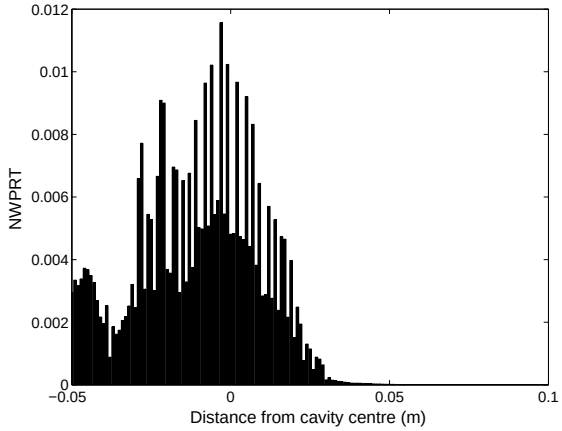

Figure B.2: *Histogram of NWPRT (no WSS-limiter) against distance from cavity centre for* $D = 1.5d$*.*

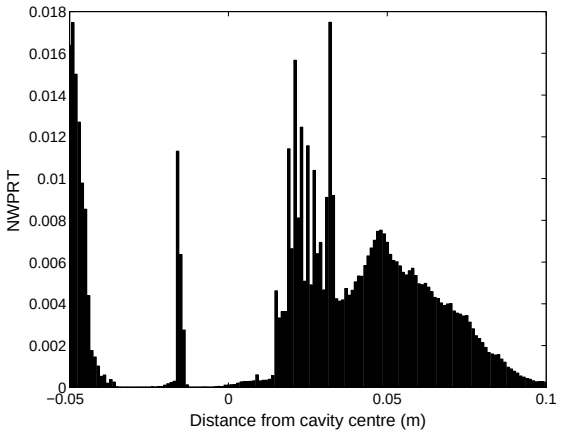

Figure B.3: *Histogram of NWPRT (no WSS-limiter) against distance from cavity centre for* $D = 1.8d$*.*

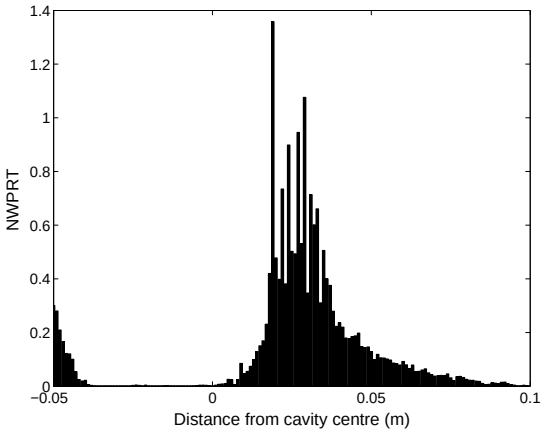

Figure B.4: *Histogram of NWPRT (no WSS-limiter) against distance from cavity centre for* $D = 2.1d$*.*

Appendix C
Comparison of CFD and MRI data

Scatterplots and Bland-Altman plots comparing CFD simulated results with PC-MRI data for anterior-posterior velocity at the midsection of the aneurysm in patient 1 (figure C.1 and C.2) show that, with the left to right component of velocity, there appears to be no correlation between simulated and imaged data for any of the CFD inlet boundary condition methods.

Bland-Altman plots of CFD against MRI in the anterior-posterior direction (figure C.3) show good correlation during higher velocity systolic flow but no correlation during diastolic flow.

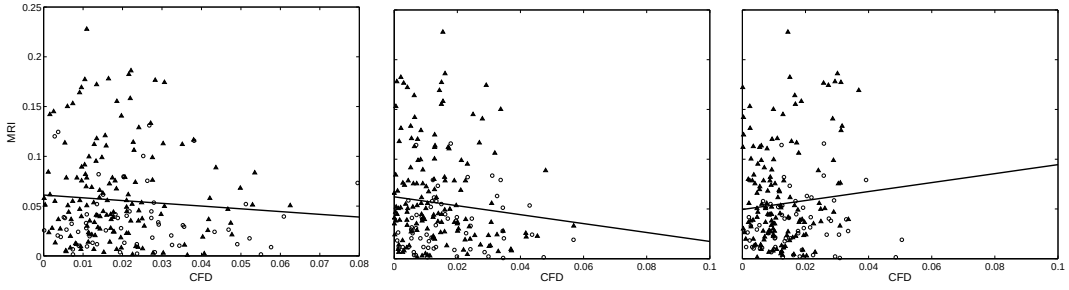

(a) 3DV (b) 1DV (c) Womersley inlet flow

Figure C.1: *Scatterplots of CFD against MRI midplane velocity data in anterior-posterior direction of patient 1. Systolic data is represented by circles, diastolic by black triangles*

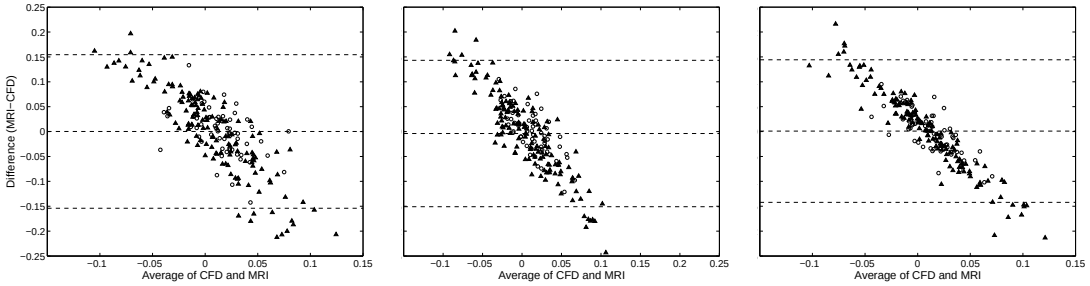

(a) 3DV (b) 1DV (c) Womersley inlet flow

Figure C.2: *Bland-Altman plots of CFD against MRI midplane velocity data in anterior-posterior direction of patient 1. Systolic data is represented by circles, diastolic by black triangles*

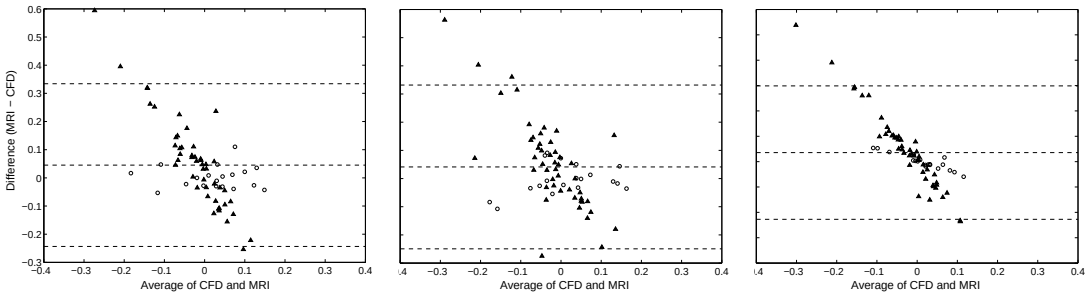

(a) 3DV (b) 1DV (c) Womersley inlet flow

Figure C.3: *Bland-Altman plots of CFD against MRI midplane velocity data in anterior-posterior direction of patient 3. Systolic data is represented by circles, diastolic by black triangles*

Bibliography

[1] R Adolph, DA Vorp, DL Steed, MW Webster, MV Kameneva, and SC Watkins. ”Cellular content and permeability of intraluminal thrombus in abdominal aortic aneurysm”. *Journal of Vascular Surgery*, 25(5):916–926, 1997.

[2] K Affeld, AJ Reininger, J Gaddischke, K Grunert, S SchmidtT, and F Thiele. ”Fluid mechanics of the stagnation point flow chamber and its platelet deposition”. *Artificial Organs*, 19(7):597–602, 1995.

[3] L Ai and K Vafai. ”A coupling model for macromolecule transport in a stenosed arterial wall”. *International Journal of Heat and Mass Transfer*, 49(9-10):1568–1591, 2006.

[4] CL Asbury, JW Ruberti, EI Bluth, and RA Peattie. ”Experimental investigation of steady flow in rigid models of abdominal aortic aneurysms”. *Annals of Biomedical Engineering*, 23(1):29–39, 1995.

[5] H Bengtsson and D Bergqvist. ”Ruptured abdominal aortic aneurysm: a population-based study”. *Journal of Vascular Surgery*, 18(1):74–80, 1993.

[6] JF Blanchard, HK Armenian, R Peeling, PP Friesen, CX Shen, and RC Brunham. ”The relation between Chlamydia pneumoniae infection and abdominal aortic aneurysm: Case-control study”. *Clinical Infectious Diseases*, 30(6):946–947, 2000.

[7] JM Bland and DG Altman. ”Statistical methods for assessing agreement between two methods of clinical measurement”. *Lancet*, 1(8476):307–310, 1986.

[8] D Bluestein, C Guttierez, M Londono, and RT Schoephoerster. ”vortex shedding in steady flow through a model of an arterial stenosis and its relevance to mural platelet deposition”. *Annals of Biomedical Engineering*, 27(6):763–773, 1999.

[9] D Bluestein, L Niu, RT Schoephoerster, and MK Dewanjee. ”Steady flow in an aneurysm model: Correlation between fluid dynamics and blood platelet deposition”. *Journal of Biomechanical Engineering-Transactions of the ASME*, 118(3):280–286, 1996.

[10] K Bluestein, Dand Dumont, M De Beule, J Ricotta, P Impellizzeri, B Verhegghe, and P Verdonck. ”Intraluminal thrombus and risk of rupture in patient specific abdominal

aortic aneurysm - FSI modelling". *Computer Methods in Biomechanics and Biomedical Engineering*, 12(1):73–81, 2009.

[11] M Bonert, RL Leask, J Butany, CR Ethier, JG Myers, KW Johnston, and M Ojha. "The relationship between wall shear stress distributions and intimal thickening in the human abdominal aorta". *Biomedical Engineering Online*, 2, 2003.

[12] E Boutsianis, M Guala, U Olgac, S Wildermuth, K Hoyer, Y Ventikos, and D Poulikakos. "CFD and PTV steady flow investigation in an anatomically accurate abdominal aortic aneurysm". *Journal of Biomechanical Engineering*, 131(1):0011008, 2009.

[13] CM Brophy, JM Reilly, GJ Smith, and MD Tilson. "the role of inflammation in nonspecific abdominal aortic aneurysm disease". *Annals of Vascular Surgery*, 5(3):229–233, 1991.

[14] JR Buchanan, C Kleinstreuer, S Hyun, and GA Truskey. "hemodynamics simulation and identification of susceptible sites of atherosclerotic lesion formation in a model abdominal aorta". *Journal of Biomechanics*, 36(8):1185 – 1196, 2003.

[15] R Budwig, D Elger, H Hooper, and J Slippy. "Steady Flow in Abdominal Aortic Aneurysm Models". *Transactions of the ASME*, 115(4A):418–423, 1993.

[16] VD Butty, K Gudjonsson, P Buchel, VB Makhijani, Y Ventikos, and D Poulikakos. "residence times and basins of attraction for a realistic right internal carotid artery with two aneurysms". *Biorheology*, 39(3-4):387–393, 2002.

[17] AL Bylock and RG Gerrity. "Visualization of monocyte recruitment into atherosclerotic arteries using fluorescent labelling". *Atherosclerosis*, 71(1):17–25, 1988.

[18] CG Caro, TJ Pedley, RC Schroter, and WA Seed. *"The Mechanics of the Circulation"*. Oxford University Press, 1978.

[19] JR Cebral, PJ Yimb, R Lhnera, O Sotoa, H Marcosb, and PL Choykeb. "New Methods for Computational Fluid Dynamics Modeling of Carotid Artery from Magnetic Resonance Angiography". *Proceedings of the SPIE*, 4321:177–187, 2001.

[20] CP Cheng, D Parker, and CA Taylor. "Quantification of wall shear stress in large blood vessels using lagrangian interpolation functions with cine phase-contrast magnetic resonance imaging". *Annals of Biomedical Engineering*, 30(8):1020–1032, 2002.

[21] P Cherukat and JB McLaughlin. ”The inertial lift on a rigid sphere in a linear shear flow field near a flat wall”. *Journal of Fluid Mechanics*, 263:1–18, 1994.

[22] JJ Chiu, CN Chen, PL Lee, CT Yang, HS Chuang, S Chien, and S Usami. ”Analysis of the effect of disturbed flow on monocytic adhesion to endothelial cells”. *Journal of Biomechanics*, 36(12):1883–1895, 2003.

[23] E Choke, G Cockerill, WRW Wilson, S Saved, J Dawson, I Loftus, and MM Thompson. ”a review of biological factors implicated in abdominal aortic aneurysm rupture”. *European Journal of Vascular and Endovascular Surgery*, 30(3):227–244, 2005.

[24] RA Close, GR Duckwiler, and F Vinuela. ”Fluid equations applied to blood flow measurement using digital videodensitometry”. *Investigative Radiology*, 27(7):504–509, 1992.

[25] KP Conway, J Byrne, M Townsend, and IF Lane. ”Prognosis of patients turned down for conventional abdominal aortic aneurysm repair in the endovascular and sonographic era: Szilagyi revisited?”. *Journal of Vascular Surgery*, 33(4):752–757, 2001.

[26] RG Cox and S Hsu. ”the lateral migration of solid particles in a laminar flow near a plane”. *International Journal of Multiphase Flow*, 3(3):201 – 222, 1977.

[27] RH Cox.

[28] CT Crowe, M Sommerfeld, and Y Tsuji. *Multiphase flows with droplets and particles*. CRC Press, Florida, 1998.

[29] VG Daniels, PR Wheater, and HG Burkitt. *Functional histology: A text and colour atlas*. Churchill Livingstone, Edinburgh, 1979.

[30] PF Davies. ”Mechanisms involved in endothelial responses to hemodynamic forces”. *Atherosclerosis*, 131(Suppl. S):S15–S17, 1997.

[31] PF Davies, A Remuzzi, EJ Gordon, CF Dewey, and MA Gimbrone. ”Turbulent fluid shear stress induces vascular endothelial cell turnover in vitro”. *Proceedings of the National Academy of Sciences of the USA*, 83(7):2114–2117, 1986.

[32] V Deplano, Y Knapp, E Bertrand, and E Gaillard. ”Flow behaviour in an asymmetric compliant experimental model for abdominal aortic aneurysm”. *Journal of Biomechanics*, 40(11):2406–2413, 2007.

[33] E Di Martino, S Mantero, F Inzoli, G Melissano, D Astore, R Chiesa, and R Fumero. ”biomechanics of abdominal aortic aneurysm in the presence of endoluminal thrombus: Experimental characterisation and structural static computational analysis”. *European Journal of Vascular and Endovascular Surgery*, 15(4):290–299, 1998.

[34] ES Di Martino, A Bohra, JP Vande Geest, N Gupta, MS Makaroun, and DA Vorp. ”Biomechanical properties of ruptured versus electively repaired abdominal aortic aneurysm wall tissue”. *Journal of Vascular Surgery*, 43(3):570–576, 2006.

[35] ES Di Martino, G Guadagni, A Fumero, G Ballerini, R Spirito, P Biglioli, and A Redaelli. ”Fluid-structure interaction within realistic three-dimensional models of the aneurysmatic aorta as a guidance to assess the risk of rupture of the aneurysm”. *Medical Engineering & Physics*, 23(9):647 – 655, 2001.

[36] PB Dobrin and R Mrkvicka. ”failure of elastin or collagen as possible critical connective tissue alterations underlying aneurismal dilatation”. *Cardiovascular Surgery*, 2:484–488, 1994.

[37] CJ Egelhoff, RS Budwig, DF Elger, TA Khraishi, and KH Johansen.

[38] JL Eliason, KK Hannawa, G Ailawadi, I Sinha, JW Ford, MP Deogracias, KJ Roelofs, DT Woodrum, TL Ennis, PK Henke, JC Stanley, RW Thompson, and GR Upchurch. ”Neutrophil depletion inhibits experimental abdominal aortic aneurysm formation”. *Circulation*, 112(2):232–240, 2005.

[39] H Faxen. ”The validity range of the Stokes-Oseen resistance formula - Explanation of several discrepancies found by J Weyssenhoff”. *Annalen Der Physik*, 63(22):581–584, 1920.

[40] MF Fillinger, ML Raghavan, SP Marra, JL Cronenwett, and FE Kennedy. ”In vivo analysis of mechanical wall stress and abdominal aortic aneurysm rupture risk”. *Journal of Vascular Surgery*, 36(3):589–597, 2002.

[41] EA Finol and CH Amon. (”blood flow in abdominal aortic aneurysms: Pulsatile flow hemodynamics”.

[42] EA Finol and CH Amon. ”Flow Dynamics in Anatomical Models of Abdominal Aortic Aneurysms: Computational Analysis of Pulsatile Flow”. *Acta Cientfica Venezolana*, 54(1):43–49, 2003.

[43] V Fontaine, MP Jacob, X Houard, P Rossignol, D Plissonnier, E Angles-Cano, and JB Michel. ”Involvement of the mural thrombus as a site of protease release and activation in human aortic aneurysms”. *American Journal of Pathology*, 161(5):1701–1710, 2002.

[44] ND Forester, SM Cruickshank, DJA Scott, and SR Carding. ”Functional characterization of T cells in abdominal aortic aneurysms”. *Immunology*, 115(2):262–270, 2005.

[45] L Formaggia, D Lamponi, and A Quarteroni. ”One-dimensional models for blood flow in arteries”. *Journal of Engineering Mathematics*, 47(3):251–276, 2004.

[46] KH Fraser. *”Computational Estimation of Haemodynamics and Tissue Stresses in Abdominal Aortic Aneurysms”*. PhD thesis, The University of Edinburgh, 2007.

[47] R Frayne, DA Steinman, CR Ethier, and BK Rutt. ”Accuracy of MR phase contrast velocity measurements for unsteady flow”. *Journal of Magnetic Resonance Imaging*, 5(4):428–431, 1995.

[48] LJ Frazin, MJ Vonesh, KB Chandran, T Shipkowitz, AS Yaacoub, and DD McPherson. ”Confirmation and initial documentation of thoracic and abdominal aortic helical flow - An ultrasound study”. *ASAIO Journal*, 42(6):951–956, 1996.

[49] P Friedl and B Weigelin. ”Interstitial leukocyte migration and immune function”. *Nature Immunology*, 9(9):960–969, 2008.

[50] S Fukuda, T Yasu, DN Predescu, and GW Schmid-Schonbein. ”Mechanisms for regulation of fluid shear stress response in circulating leukocytes”. *Circulation Research*, 86(1):E13–E18, 2000.

[51] PD Gatehouse, J Keegan, LA Crowe, S Masood, RH Mohiaddin, KF Kreitner, and DN Firmin. ”Applications of phase-contrast flow and velocity imaging in cardiovascular MRI”. *European Radiology*, 15(10):2172–2184, 2005.

[52] AJ Goldman, RG Cox, and H Brenner. ”Slow viscous motion of a sphere parallel to a plane wallII Couette flow”. *Chemical Engineering Science*, 22(4):653–660, 1967.

[53] PJ Gough, IG Gomez, PT Wille, and EW Raines. ”Macrophage expression of active MMP-9 induces acute plaque disruption in apoE-deficient mice”. *Journal of Clinical Investigation*, 116(1):59–69, 2006.

[54] RM Greenhalgh and JT Powell. ”Endovascular repair of abdominal aortic aneurysm”. *New England Journal of Medicine*, 358(5):494–501, 2008.

[55] G Greil, T Geva, SE Maier, and AJ Powell. ”Effect of acquisition parameters on the accuracy of velocity encoded cine magnetic resonance imaging blood flow measurements”. *Journal of Magnetic Resonance Imaging*, 15(1):47–54, 2002.

[56] M Grigioni, C Daniele, U Morbiducci, C Del Gaudio, G D'Avenio, A Balducci, and V Barbaro. A mathematical description of blood spiral flow in vessels: application to a numerical study of flow in arterial bending. *Journal of Biomechanics*, 38(7):1375–1386, 2005.

[57] SS Hans, O Jareunpoon, M Balasubramaniam, and GB Zelenock. ”size and location of thrombus in intact and ruptured abdominal aortic aneurysms”. *Journal of Vascular Surgery*, 41(4):584–588, 2005.

[58] CM He and MR Roach. ”The composition and mechanical properties of abdominal aortic aneurysms”. *Journal of Vascular Surgery*, 20(1):6–13, 1994.

[59] MT Hinds, YJ Park, SA Jones, DP Giddens, and BR Alevriadou. ”Local hemodynamics affect monocytic cell adhesion to a three-dimensional flow model coated with E-selectin”. *Journal of Biomechanics*, 34(1):95–103, 2001.

[60] GA Holzapfel, TC Gasser, and RW Ogden. ”A New Constitutive Framework for Arterial Wall Mechanics and a Comparative Study of Material Models”. *Journal of Elasticity*, 61(1):1 – 48, 2000.

[61] PR Hoskins and D Hardman. ”Three-dimensional imaging and computational modelling for estimation of wall stresses in arteries”. *British Journal of Radiology*, 82(Sp. Iss. 1):S3–S17, 2009.

[62] JG Houston, SJ Gandy, DG Sheppard, JB Dick, JJF Belch, and PA Stonebridge. ”Two-dimensional flow quantitative MRI of aortic arch blood flow patterns: Effect of age, sex, and presence of carotid atheromatous disease on prevalence of spiral blood flow”. *Journal of Magnetic Resonance Imaging*, 18(2):169–174, 2003.

[63] TK Hsiai, SK Cho, PK Wong, M Ing, A Salazar, A Sevanian, M Navab, LL Demer, and CM Ho. ”Monocyte recruitment to endothelial cells in response to oscillatory shear stress”. *FASEB Journal*, 17(12):1648–1657, 2003.

[64] KM Johnson and M Markl. ”Improved SNR in Phase Contrast Velocimetry With Five-Point Balanced Flow Encoding”. *Magnetic Resonance in Medicine*, 63(2):349–355, 2010.

[65] JH Jung, A Hassanein, and RW Lyczkowski. ”Hemodynamic computation using multiphase flow dynamics in a right coronary artery”. *Annals of Biomedical Engineering*, 34(3):393–407, 2006.

[66] T Karino and HL Goldsmith. ”Flow behaviour of blood cells and rigid spheres in an annular vortex”. *Philosophical Transactions of the Royal Society of London. Series B-Biological Sciences”*, 279(967):413–&, 1977.

[67] VS Kashyap, TD Reil, WS Moore, TX Hoang, HA Gelabert, RE Byrns, LJ Ignarro, and JA Freischlag. ”Acute arterial thrombosis causes endothelial dysfunction: a new paradigm for thrombolytic therapy”. *Journal of Vascular Surgery*, 34(2):323–329, 2001.

[68] DA Katz and JL Cronenwett. ”The cost-effectiveness of early surgery versus watchful waiting in the management of small abdominal aortic aneurysms”. *Journal of Vascular Surgery*, 19(6):980–991, 1994.

[69] M Kazi, J Thyberg, P Religa, J Roy, P Eriksson, U Hedin, and J Swedenborg. ”influence of intraluminal thrombus on structural and cellular composition of abdominal aortic aneurysm wall”. *Journal of Vascular Surgery*, 38(6):1283–1292, 2003.

[70] DB Khismatullin and GA Truskey. ”Three-dimensional numerical simulation of receptor-mediated leukocyte adhesion to surfaces: Effects of cell deformability and viscoelasticity”. *Physics of Fluids*, 17(3), 2005.

[71] MB Kim and IH Sarelius. ”Role of shear forces and adhesion molecule distribution on P-selectin-mediated leukocyte rolling in postcapillary venules”. *American Journal of Physiology-Heart and Circulatory Physiology*, 287(6):H2705–H2711, 2004.

[72] MC Kim, JH Nam, and CS Lee. ”Near-wall deposition probability of blood elements as a new hemodynamic wall parameter”. *Annals of Biomedical Engineering*, 34(6):958–970, 2006.

[73] S-E Kim and D Choudhury. ”A Near-Wall Treatment Using Wall Functions Sensitized to Pressure Gradient”. *Separated and Complex Flows*, 217:281–318, 1995.

[74] U Kose, S de Putter, R Hoogeveen, and M Breeuwer. Computational fluid dynamics of abdominal aortic aneurysms with patient-specific inflow boundary conditions. *Proceedings of the SPIE*, 6143:D1432–D1432, 2006.

[75] CW Kotze, LJ Menezes, R Endozo, AM Groves, PJ Ell, and SW Yusuf. "Increased Metabolic Activity in Abdominal Aortic Aneurysm Detected by 18F-Fluorodeoxyglucose (F-18-FDG) Positron Emission Tomography/Computed Tomography (PET/CT)". *European Journal of Vascular and Endovascular Surgery*, 38(1):93–99, 2009.

[76] DN Ku. "Blood flow in arteries". *Annual Review of Fluid Mechanics*, 29:399–434, 1997.

[77] DN Ku, DP Giddens, CK Zarins, and S Glagov. "Pulsatile flow and atherosclerosis in the human carotid bifurcation. Positive correlation between plaque location and low oscillating shear stress". *Arteriosclerosis*, 5(3):293–302, 1985.

[78] MJ Kunov, DA Steinman, and CR Ethier. "Particle volumetric residence time calculations in arterial geometries". *Journal of Biomechanical Engineering-Transactions of the ASME*, 118(2):158–164, 1996.

[79] BE Launder and DB Spalding. "The Numerical Computation of Turbulent Flows". *Computer Methods in Applied Mechanics and Engineering*, 3:269–289, 1974.

[80] MB Lawrence, EL Berg, EC Butcher, and TA Springer. "Rolling of lymphocytes and neutrophils on peripheral node addressin and subsequent arrest on ICAM-1 in shear flow". *European Journal of Immunology*, 25(4):1025–1031, 1995.

[81] MB Lawrence, LV McIntire, and SG Eskin. "Effect of flow on polymorphonuclear leukocyte/endothelial cell adhesion". *Blood*, 70(5):1284–1290, 1987.

[82] MB Lawrence and TA Springer. "Leukocytes roll on a selectin at physiological flow-rates: Distinction from and prerequisite for adhesion through integrins". *CELL*, 65(5):859–873, MAY 31 1991.

[83] FA Lederle, SE Wilson, GR Johnson, DB Reinke, FN Littooy, CW Acher, DJ Ballard, LM Messina, IL Gordon, EP Chute, WC Krupski, and D Bandyk. "Immediate repair compared with surveillance of small abdominal aortic aneurysms". *New England Journal of Medicine*, 346(19):1437–1444, 2002.

[84] AJ Lee, FGR Fowkes, MN Carson, GC Leng, and PL Allan. ”Smoking, atherosclerosis and risk of abdominal aortic aneurysm”. *European Heart Journal*, 18(4):671–676, 1997.

[85] H Leong-Poi, J Christiansen, AL Klibanov, S Kaul, and JR Lindner. ”Noninvasive assessment of angiogenesis by ultrasound and microbubbles targeted to alpha(v)-integrins”. *Circulation*, 107(3):455–460, 2003.

[86] AS Les, SC Shadden, CA Figueroa, JM Park, MM Tedesco, RJ Herfkens, RL Dalman, and CA Taylor. ”Quantification of Hemodynamics in Abdominal Aortic Aneurysms During Rest and Exercise Using Magnetic Resonance Imaging and Computational Fluid Dynamics”. *Annals of Biomedical Engineering*, 38(4):1288–1313, 2010.

[87] Z Li and C Kleinstreuer. ”fluid-structure interaction effects on sac-blood pressure and wall stress in a stented aneurysm”. *Journal of Biomechanical Engineering*, 127(4):662–671, 2005.

[88] Z Li and C Kleinstreuer. ”A comparison between different asymmetric abdominal aortic aneurysm morphologies employing computational fluid-structure interaction analysis”. *European Journal of Mechanics B-=Fluids*, 26(5):615–631, 2007.

[89] P Libby, PM Ridker, and A Maseri. ”Inflammation and atherosclerosis”. *Circulation*, 105(9):1135–1143, 2002.

[90] JS Lindholt, H Fasting, EW Henneberg, and L Ostergaard. ”A review of Chlamydia pneumoniae and atherosclerosis”. *European Journal of Vascular and Endovascular Surgery*, 17(4):283–289, 1999.

[91] S Litovsky, M Madjid, A Zarrabi, SW Casscells, JT Willerson, and M Naghavi. ”Superparamagnetic iron oxide-based method for quantifying recruitment of monocytes to mouse atherosclerotic lesions in vivo - Enhancement by tissue necrosis factor-alpha, interleukin-1 beta, and interferon-gamma”. *Circulation*, 107(11):1545–1549, 2003.

[92] Xiao Liu, Fang Pu, Yubo Fan, Xiaoyan Deng, Deyu Li, and Shuyu Li. :A numerical study on the flow of blood and the transport of LDL in the human aorta: the physiological significance of the helical flow in the aortic arch”. *American Journal of Physiology-Heart and Circulatory Physiology*, 297(1):H163–H170, 2009.

[93] Q Long, XY Xu, M Bourne, and TM Griffith. "Numerical study of blood flow in an anatomically realistic aorto-iliac bifurcation generated from MRI data". *Magnetic Resonance in Medicine*, 43(4):565–576, 2000.

[94] PW Longest. *"Computational analysis of transient particle hemodynamics with applications to femoral bypass graft designs"*. PhD thesis, North Carolina State University, 2002.

[95] PW Longest, C Kleinstreuer, and JR Buchanan. "Efficient computation of micro-particle dynamics including wall effects". *Computers & Fluids*, 33(4):577–601, 2004.

[96] PW Longest, C Kleinstreuer, GA Truskey, and JR Buchanan. Relation between near-wall residence times of monocytes and early lesion growth in the rabbit aorto-celiac junction. *Annals of Biomedical Engineering*, 31(1):53–64, 2003.

[97] E Loth. "numerical approaches for motion of dispersed particles, droplets and bubbles". *Progress in Energy and Combustion Science*, 26(3):161 – 223, 2000.

[98] J Lotz, C Meier, A Leppert, and M Galanski. "Cardiovascular flow measurement with phase-contrast MR imaging: Basic facts and implementation". *Radiographics*, 22(3):651–671, 2002.

[99] K Maiellaro and WR Taylor. "The role of the adventitia in vascular inflammation". *Cardiovascular Research*, 75(4):640–648, 2007.

[100] A Maier, MW Gee, C Reeps, HH Eckstein, and WA Wall. "impact of calcifications on patient-specific wall stress analysis of abdominal aortic aneurysms". *Biomechanics and Modeling in Mechanobiology*, 9(5):511–521, 2010.

[101] Alberto Marzo, Pankaj Singh, Philippe Reymond, Nikos Stergiopulos, Umang Patel, and Rodney Hose. "Influence of inlet boundary conditions on the local haemodynamics of intracranial aneurysms". *Computer Methods in Biomechanics and Biomedical Engineering*, 12(4):431–444, 2009.

[102] MR Maxey and JJ Riley. "Equation of motion for a small rigid sphere in a nonuniform flow". *Physics of Fluids*, 26(4):883–889, 1983.

[103] JB McLaughlin. "Inertial migration of a small sphere in linear shear flows". *Journal of Fluid Mechanics*, 224:261–274, 1991.

[104] C Migliorini, YH Qian, HD Chen, EB Brown, RK Jain, and LL Munn. ”Red blood cells augment leukocyte rolling in a virtual blood vessel”. *Biophysical Journal*, 83(4):1834–1841, 2002.

[105] R Mittal, SP Simmons, and HS Udaykumar. ”Application of large-eddy simulation to the study of pulsatile flow in a modeled arterial stenosis”. *Journal of Biomechanical Engineering-Transactions of the ASME*, 123(4):325–332, 2001.

[106] P Moin and K Mahesh. ”Direct numerical simulation: A tool in turbulence research”. *Annual Review of Fluid Mechanics*, 30:539–578, 1998.

[107] P Moin and M Wang. ”Wall modeling for large-eddy simulation of turbulent boundary layers”. In Meier, GEA and Sreenivasan, KR, editor, *IUTAM Symposium on One Hundred Years of Boundary Layer Research*, volume 129 of *Solid Mechanics and its Applications*, pages 269–278, 2006.

[108] NI Moldovan and T Asahara. ”Role of blood mononuclear cells in recanalization and vascularization of thrombi: Past, present, and future”. *Trends in Cardiovascular Medicine*, 13(7):265–269, 2003.

[109] JE Moore and DN Ku. ”Pulsatile velocity measurements in a model of the human abdominal aorta under resting conditions”. *Journal of Biomechanical Engineering-Transactions of the ASME*, 116(3):337–346, 1994.

[110] JE Moore and DN Ku. ”Pulsatile velocity measurements in a model of the human abdominal aorta under simulated exercise and postprandial conditions”. *Journal of Biomechanical Engineering-Transactions of the ASME*, 116(1):107–111, 1994.

[111] U Morbiducci, R Ponzini, G Rizzo, M Cadioli, A Esposito, F De Cobelli, A Del Maschio, FM Montevecchi, and A Redaelli. ”In Vivo Quantification of Helical Blood Flow in Human Aorta by Time-Resolved Three-Dimensional Cine Phase Contrast Magnetic Resonance Imaging”. *Annals of Biomedical Engineering*, 37(3):516–531, 2009.

[112] SA Morsi and AJ Alexander. ”an investigation of particle trajectories in two-phase flow systems”. *Journal of Fluid Mechanics*, 55(2):193 – 208, 1972.

[113] LK Mostafa, DB Jones, and DH Wright. ”Mechanism of the induction of angiogenesis by human neoplastic lymphoid tissue: studies employing bovine aortic endothelial cells in vitro”. *Journal of Pathology*, 132(3):207–216, 1980.

[114] KS Moulton, K Vakili, D Zurakowski, M Soliman, C Butterfield, E Sylvin, KM Lo, S Gillies, K Javaherian, and J Folkman. ”Inhibition of plaque neovascularization reduces macrophage accumulation and progression of advanced atherosclerosis”. *Proceedings of the National Academy of Sciences of the USA*, 100(8):4736–4741, 2003.

[115] WR Mower, WJ Quinones, and SS Gambhir. ”Effect of intraluminal thrombus on abdominal aortic aneurysm wall stress”. *Journal of Vascular Surgery*, 26(4):602–608, 1997.

[116] MJ Mulligan-Kehoe. ”The vasa vasorum in diseased and nondiseased arteries”. *American Journal of Physiology-Heart and Circulatory Physiology*, 298(2):H295–H305, 2010.

[117] T Nagel, N Resnick, WJ Atkinson, CF Dewey, and MA Gimbrone. ”Sheer stress selectively Up-regulates intercellular-adhesion molecule-1 expression in cultured human vascular endothelial-cells”. *Journal of Clinical Investigation*, 94(2):885–891, 1994.

[118] NA N’Dri, W Shyy, and R Tran-Soy-Tay. ”Computational modeling of cell adhesion and movement using a continuum-kinetics approach”. *Biophysical Journal*, 85(4):2273–2286, 2003.

[119] SC Nicholls, JB Gardner, MH Meissner, and KH Johansen. ”Rupture in small abdominal aortic aneurysms”. *Journal of Vascular Surgery*, 28(5):884–888, 1998.

[120] WW Nichols and MF O’Rourke. *”McDonald’s Blood Flow in Arteries: Theoretical, Experimental and Clinical Principles”*. Hodder Arnold, 5 edition, 2005.

[121] P Norman, M Le, C Pearce, and K Jamrozik. ”Infrarenal aortic diameter predicts all-cause mortality”. *Arteriosclerosis Thrombosis and Vascular Biology*, 24(7):1278–1282, 2004.

[122] S Oyre, EM Pedersen, S Ringgaard, P Boesiger, and WP Paaske. ”In vivo wall shear stress measured by magnetic resonance velocity mapping in the normal human abdominal aorta”. *European Journal of Vascular and Endovascular Surgery*, 13(3):263–271, 1997.

[123] EM Pedersen, S Oyre, M Agerbaek, IB Kristensen, S Ringgaard, P Boesiger, and WP Paaske. ”Distribution of early atherosclerotic lesions in the human abdominal aorta correlates with wall shear stresses measured in vivo”. *European Journal of Vascular and Endovascular Surgery*, 18(4):328–333, 1999.

[124] Shimakawa A Enzmann DR Pelc NJ, Herfkens RJ. ”Effect of acquisition parameters on the accuracy of velocity encoded cine magnetic resonance imaging blood flow measurements”. *Phase contrast cine magnetic resonance imaging*, 7(4):229–254, 1991.

[125] E Petersen, F Wagberg, and KA Angquist. ”Proteolysis of the abdominal aortic aneurysm wall and the association with rupture”. *European Journal of Vascular and Endovascular Surgery*, 23(2):153–157, 2002.

[126] R H Phibbs. ”distribution of leukocytes in blood flowing through arteries”. *Amateur Journal of Physiology*, 210(5):919–925, 1966.

[127] PJ Polverini, RS Cotran, MA Gimbrone, and ER Unanue. ”Activated macrophages induce vascular proliferation”. *Nature*, 269(5631):804–806, 1977.

[128] JT Powell, AR Brady, LC Brown, JF Forbes, FGR Fowkes, RM Greenhalgh, CV Ruckley, SG Thompson, and UK Small Aneurysm Trial Participants. ”Mortality results for randomised controlled trial of early elective surgery or ultrasonographic surveillance for small abdominal aortic aneurysms”. *Lancet*, 352(9141):1649–1655, 1998.

[129] ML Raghavan, J Kratzberg, EM Castro de Tolosa, MM Hanaoka, P Walker, and ES da Silva. Regional distribution of wall thickness and failure properties of human abdominal aortic aneurysm. *Journal of Biomechanics*, 39(16):3010–3016, 2006.

[130] ML Raghavan and DA Vorp. ”Toward a biomechanical tool to evaluate rupture potential of abdominal aortic aneurysm: identification of a finite strain constitutive model and evaluation of its applicability”. *Journal of Biomechanics*, 33(4):475–482, 2000.

[131] ML Raghavan, MW Webster, and DA Vorp. ”Ex vivo biomechanical behavior of abdominal aortic aneurysm: Assessment using a new mathematical model”. *Annals of Biomedical Engineering*, 24(5):573–582, 1996.

[132] QM Ramadan, O Hamid, and KO Lim. ”Steady flow visualization in a rigid model of the aortic-renal junction: application to atherosclerosis”. *Physica Medica*, 19(4):295–303, 2003.

[133] G Rappitsch and K Perktold. ”Computer simulation of convective diffusion processes in large arteries”. *Journal of Biomechanics*, 29(2):207–215, 1996.

[134] I Raynal, P Prigent, S Peyramaure, A Najid, C Rebuzzi, and C Corot. ”Macrophage endocytosis of superparamagnetic iron oxide nanoparticles - Mechanisms and comparison of Ferumoxides and Ferumoxtran-10”. *Investigative Radiology*, 39(1):56–63, 2004.

[135] C Reeps, M Essler, J Pelisek, S Seidl, H-H Eckstein, and B-J K. ”Increased 18F-fluorodeoxyglucose uptake in abdominal aortic aneurysms in positron emission/computed tomography is associated with inflammation, aortic wall instability, and acute symptoms”. *Journal of Vascular Surgery*, 48(2):417–423, 2008.

[136] EL Ritman and A Lerman. ”The dynamic vasa vasorum”. *Cardiovascular Research*, 75(4):649–658, 2007.

[137] KD Rizas, N Ippagunta, and M D Tilson, III. ”Immune Cells and Molecular Mediators in the Pathogenesis of the Abdominal Aortic Aneurysm”. *Cardiology in Review*, 17(5):201–210, 2009.

[138] PJ Roache. ”Perspective: a method for uniform reporting of grid refinement studies”. *Journal of Fluids Engineering Transactions of the ASME*, 116(3):405–413, 1994.

[139] PJ Roache. ”Quantification of uncertainty in computational fluid dynamics”. *Annual Review of Fluid Mechanics*, 29:123–160, 1997.

[140] MB Robertson, U Kohler, PR Hoskins, and I Marshall. ”Quantitative analysis of PC MRI velocity maps: pulsatile flow in cylindrical vessels”. *Magnetic Resonance Imaging*, 19(5):685–695, 2001.

[141] SI Rubinow and JB Keller. ”The transverse force on a spinning sphere moving in a viscous fluid”. *Journal of Fluid Mechanics*, 11(3):447–459, 1961.

[142] PG Saffman. ”The Lift on a Small Sphere in a Slow Shear Flow”. *Journal of Fluid Mechanics*, 22:385–400, 1965.

[143] N Sakalihasan, R Limet, and OD Defawe. ”Abdominal aortic aneurysm”. *Lancet*, 365(9470):1577–1589, 2005.

[144] A-V Salsac, SR Sparks, J-M Chomaz, and JC Lasheras. ”Evolution of the wall shear stresses during the progressive enlargement of symmetric abdominal aortic aneurysms”. *Journal of Fluid Mechanics*, 560:19–51, 2006.

[145] H Schlichting. *Boundary-Layer Theory*. McGraw-Hill, New York, 7 edition, 1979.

[146] RAP Scott, NM Wilson, HA Ashton, and DN Kay. "Is surgery necessary for abdominal aortic aneurysm less than 6 cm in diameter?". *Lancet*, 342(8884):1395–1396, 1993.

[147] A Scotti, C Meneveau, and DK Lilly. "Generalized Smagorinsky model for anisotropic grids". *Physics of Fluids A-Fluid Dynamics*, 5(9):2306–2308, 1993.

[148] CM Scotti and EA Finol. "Compliant biomechanics of abdominal aortic aneurysms: A fluid-structure interaction study". *Computers & Structures*, 85(11-14, Sp. Iss. SI):1097–1113, 2007.

[149] P Segers, N Stergiopulos, N Westerhof, P Wouters, P Kolh, and P Verdonck. "Systemic and pulmonary hemodynamics assessed with a lumped-parameter heart-arterial interaction model". *Journal of Engineering Mathematics*, 47(3-4):185–199, 2003.

[150] E Sho, M Sho, K Hoshina, H Kimura, TK Nakahashi, and RL Dalman. "Hemodynamic forces regulate mural macrophage infiltration in experimental aortic aneurysms". *Experimental and Molecular Pathology*, 76(2):108–116, 2004.

[151] E Sho, M Sho, H Nanjo, K Kawamura, H Masuda, and R Dalman. "hemodynamic regulation of cd34(+) cell localization and differentiation in experimental aneurysms". *Arteriosclerosis Thrombosis and Vascular Biology*, 76(2):108–116, 2004.

[152] R Skalak and S Chien. *Handbook of Bioengineering*. McGraw-Hill, New York, 1987.

[153] P Spalart and S Allmaras. "a one-equation turbulence model for aerodynamic flows". Technical report, American Institute of Aeronautics and Astronautics, 1992.

[154] DK Stangeby and CR Ethier. "Computational analysis of coupled blood-wall arterial LDL transport". *Journal of Biomechanical Engineering-Transactions of the ASME*, 124(1):1–8, 2002.

[155] D Steinberg, JC Khoo, CK Glass, W Palinski, and F Almazan. "A new approach to determining the rates of recruitment of circulating leukocytes into tissues: Application to the measurement of leukocyte recruitment into atherosclerotic lesions". *Proceedings of the National Academy of Sciences of the USA*, 94(8):4040–4044, 1997.

[156] DA Steinman. "Image-based computational fluid dynamics modeling in realistic arterial geometries". *Annals of Biomedical Engineering*, 30(4):483–497, APR 2002.

[157] DA Steinman, CR Ethier, and BK Rutt. "Combined analysis of spatial and velocity displacement artifacts in phase contrast measurements of complex flows". *Journal of Magnetic Resonance Imaging*, 7(2):339–346, 1997.

[158] PA Stonebridge, C Buckley, A Thompson, J Dick, G Hunter, JA Chudek, JG Houston, and JJF Belch. "Non spiral and spiral (helical) flow patterns in stenoses - In vitro observations using spin and gradient echo magnetic resonance imaging (MRI) and computational fluid dynamic modeling". *International Angiology*, 23(3):276–283, 2004.

[159] PA Stonebridge, PR Hoskins, PL Allan, and JFF Belch. "Spiral laminar flow in vivo". *Clinical Science*, 91(1):17–21, 1996.

[160] CH Sun, C Migliorini, and LL Munn. Red blood cells initiate leukocyte rolling in postcapillary expansions: A lattice Boltzmann analysis. *Biophysical Journal*, 85(1):208–222, 2003.

[161] C Sunderkotter, K Steinbrink, M Goebeler, R Bhardwaj, and C Sorg. "Macrophages and angiogenesis". *Journal of Leukocyte Biology*, 55(3):410–422, 1994.

[162] FPP Tan, A Borghi, RH Mohiaddin, NB Wood, S Thom, and XY Xu. Analysis of flow patterns in a patient-specific thoracic aortic aneurysm model. *Computers & Structures*, 87(11-12, Sp. Iss. SI):680–690, 2009.

[163] BT Tang, CP Cheng, MT Draney, NM Wilson, PS Tsao, RJ Herfkens, and CA Taylor. "Abdominal aortic hemodynamics in young healthy adults at rest and during lower limb exercise: quantification using image-based computer modeling". *American Journal of Physiology-Heart and Circulatory Physiology*, 291(2):H668–H676, 2006.

[164] AD Taylor, S Neelamegham, JD Hellums, CW Smith, and SI Simon. "Molecular dynamics of the transition from L-selectin- to beta(2)-integrin-dependent neutrophil adhesion under defined hydrodynamic shear". *Biophysical Journal*, 71(6):3488–3500, 1996.

[165] CA Taylor, CP Cheng, LA Espinosa, BT Tang, D Parker, and RJ Herfkens. "In vivo quantification of blood flow and wall shear stress in the human abdominal aorta during lower limb exercise". *Annals of Biomedical Engineering*, 30(3):402–408, 2002.

[166] CA Taylor, TJR Hughes, and CK Zarins. "Finite element modeling of blood flow in arteries". *Computer Methods in Applied Mechanics and Engineering*, 158(1-2):155–196, MAY 25 1998.

[167] JB Thomas, JS Milner, and DA Steinman. ”On the influence of vessel planarity on local hemodynamics at the human carotid bifurcation”. *Biorheology*, 39(3-4):443–448, 2002.

[168] GJ Todd and JJ Derose. ”Retroperitoneal approach for repair of inflammatory aortic aneurysms”. *Annals OF Vascular Surgery*, 9(6):525–534, 1995.

[169] Z Touat, V Ollivier, JP Dai, MG Huisse, A Bezeaud, U Sebbag, T Palombi, P Rossignol, O Meilhac, MC Guillin, and JB Michel. ”Renewal of mural thrombus releases plasma markers and is involved in aortic abdominal aneurysm evolution”. *American Journal of Pathology*, 168(3):1022–1030, 2006.

[170] GH Turner, AR Olzinski, RE Bernard, K Aravindhan, RJ Boyle, MJ Newman, SD Gardner, RN Willette, PJ Gough, and BM Jucker. ”Assessment of Macrophage Infiltration in a Murine Model of Abdominal Aortic Aneurysm”. *Journal of Magnetic Resonance Imaging*, 30(2):455–460, 2009.

[171] SR Vallabhaneni, GL Gilling-Smith, TV How, SD Carter, JA Brennan, and PL Harris. Heterogeneity of tensile strength and matrix metalloproteinase activity in the wall of abdominal aortic aneurysms. *Journal of Endovascular Therapy*, 11(4):494–502, 2004.

[172] SS Varghese and SH Frankel. ”Numerical modeling of pulsatile turbulent flow in stenotic vessels”. *Journal of Biomechanical Engineering-Transactions of the ASME*, 125(4):445–460, 2003.

[173] SS Varghese, SH Frankel, and PF Fischer. ”Direct numerical simulation of stenotic flows. Part 1. Steady flow”. *Journal of Fluid Mechanics*, 582:253–280, 2007.

[174] SS Varghese, SH Frankel, and PF Fischer. ”Direct numerical simulation of stenotic flows. Part 2. Pulsatile flow”. *Journal of Fluid Mechanics*, 582:281–318, 2007.

[175] P Vasseur and RG Cox. ”The lateral migration of spherical particles sedimenting in a stagnant bounded fluid”. *Journal of Fluid Mechanics*, 80:561–591, 1977.

[176] A Vieli, U Moser, S Maier, D Meier, and P Boesiger. ”Velocity profiles in the normal human abdominal aorta: a comparison between ultrasound and magnetic resonance data”. *Ultrasound in Medicine and Biology*, 15(2):113–119, 1989.

[177] DA Vorp, PC Lee, DHJ Wang, MS Makaroun, EM Nemoto, S Ogawa, and MW Webster. ”association of intraluminal thrombus in abdominal aortic aneurysm with local hypoxia and wall weakening”. *Journal of Vascular Surgery*, 34(2):291–299, 2001.

[178] DA Vorp, ML Raghavan, and MW Webster. ”Mechanical wall stress in abdominal aortic aneurysm: Influence of diameter and asymmetry”. *Journal of Vascular Surgery*, 27(4):632–639, 1998.

[179] DHJ Wang, M Makaroun, MW Webster, and DA Vorp. ”Mechanical properties and microstructure of intraluminal thrombus from abdominal aortic aneurysm”. *Journal of Biomechanical Engineering-Transactions of the ASME*, 123(6):536–539, 2001.

[180] DHJ Wang, MS Makaroun, MW Webster, and DA Vorp. ”effect of intraluminal thrombus on wall stress in patient-specific models of abdominal aortic aneurysm”. *Journal of Vascular Surgery*, 36(3):598–604, 2002.

[181] Q Wang, KD Squires, M Chen, and JB McLaughlin. On the role of the lift force in turbulence simulations of particle deposition. *International Journal of Multiphase Flow*, 23(4):749–763, 1997.

[182] HJ Weiss. ”Flow-related platelet deposition on subendothelium”. *Thrombosis and Haemostasis*, 74(1):117–122, 1995.

[183] DC Wilcox. ”umerical study of separated turbulent flows”. *AIAA Journal*, 13(5):555–556, 1975.

[184] DW Wilcox. *Turbulence Modeling For CFD*. DCW Industries, La Canada, 3 edition, 2006.

[185] WRW Wilson, M Anderton, EC Choke, J Dawson, IM Loftus, and MM Thompson. Elevated plasma MMP1 and MMP9 are associated with abdominal aortic aneurysm rupture. *European Journal of Vascular and Endovascular Surgery*, 35(5):580–584, 2008.

[186] WRW Wilson, M Anderton, EC Schwalbe, JL Jones, PN Furness, PRF Bell, and MM Thompson. ”Matrix metalloproteinase-8 and-9 are increased at the site of abdominal aortic aneurysm rupture”. *Circulation*, 113(3):438–445, 2006.

[187] H Wolinsky and S Glagov. ”Comparison of abdominal and thoracic aortic medial structure in mammals”. *Circulation Research*, 25(6):677–&, 1969.

[188] JR Womersley. ”method for the calculation of velocity, rate of flow and viscous drag in arteries when the pressure gradient is known”. *Journal of Physiology*, 127:553–563, 1955.

[189] GS Worthen, LA Smedly, MG Tonnesen, D Ellis, NF Voelkel, JT Reeves, and PM Henson. ”Effects of shear-stress on adhesive interaction between neutrophils and cultured endothelial-cells”. *Journal of Applied Physiology*, 63(5):2031–2041, 1987.

[190] V Yakhot and SA Orszag. ”Renormalization Group Analysis of Turbulence: I. Basic Theory.”. *Journal of Scientific Computing*, 1(1):1–56, 1986.

[191] TH Yip and SCM Yu. ”Cyclic transition to turbulence in rigid abdominal aortic aneurysm models”. *Fluid Dynamics Research*, 29(2):81–113, 2001.

[192] JB Young and TJ Hanratty. ”Trapping of solid particles at a wall in a turbulent flow”. *AIChE Journal*, 37(10):1529–1536, 1991.

[193] L Zhao, MPW Moos, R Grabner, F Pedrono, JJ Fan, B Kaiser, N John, S Schmidt, R Spanbroek, J Lotzer, L Huang, JS Cui, DJ Rader, JF Evans, AJR Habenicht, and CD Funk. ”the 5-lipoxygenase pathway promotes pathogenesis of hyperlipidemia-dependent aortic aneurysm”. *Nature Medicine*, 10(9):966–973, 2004.

Publications

Hoskins PR, Hardman D, Three-dimensional imaging and computational modelling for estimation of wall stresses in arteries *British Journal of Radiology. 82:S3-S17, 2009*

Hardman D, Hoskins P.R, Easson W.J, Haemodynamics of Patient-Specific AAA using 3-D PC-MRI Velocity Boundary Conditions *Bioengineering 09* (Sept. 2009, Oxford). Oral presentation.

Hardman D, Hoskins P.R, Easson W.J, Computation of the distribution of monocyte deposition in abdominal aortic aneurysm disease. *World Congress on Medical Physics and Biomedical Engineering* (Sept. 2009, Munich). Paper and oral presentation.

Hardman D, Hoskins P.R, Easson W.J Computation of the distribution of monocyte deposition in abdominal aortic aneurysm disease and comparison with wall shear stress. *4th International Symposium on Biomechanics in Vascular Biology and Cardiovascular Disease* (Apr. 2009, Rotterdam). Poster.

Hardman D, Hoskins P.R, Easson W.J Modelling leukocyte adhesion in abdominal aortic aneurysm disease using CFD. *Scottish Cardiovascular Forum* (Jan. 2009, Inverness). Oral presentation.

Hardman D, Hoskins P.R, Easson W.J Computation of the distribution of monocyte deposition in abdominal aortic aneurysm disease. *Bioengineering 08 Symposium* (Sept. 2008, Imperial College, London). Oral presentation.

Hardman D, Hoskins P.R, Monocyte tracking in abdominal aortic aneurysms using computational fluid dynamics *Edinburgh University Centre for Cardiovascular Science symposium* (Feb. 2008, Edinburgh). Poster